Research Topics

Human-in-the-loop system design and control adaptation for behavior-assistant robots

Edited by
Yuquan Leng, Ningbo Yu, Bi Zhang, Benyan Huo
and Xu Jin

Published in
Frontiers in Neuroscience

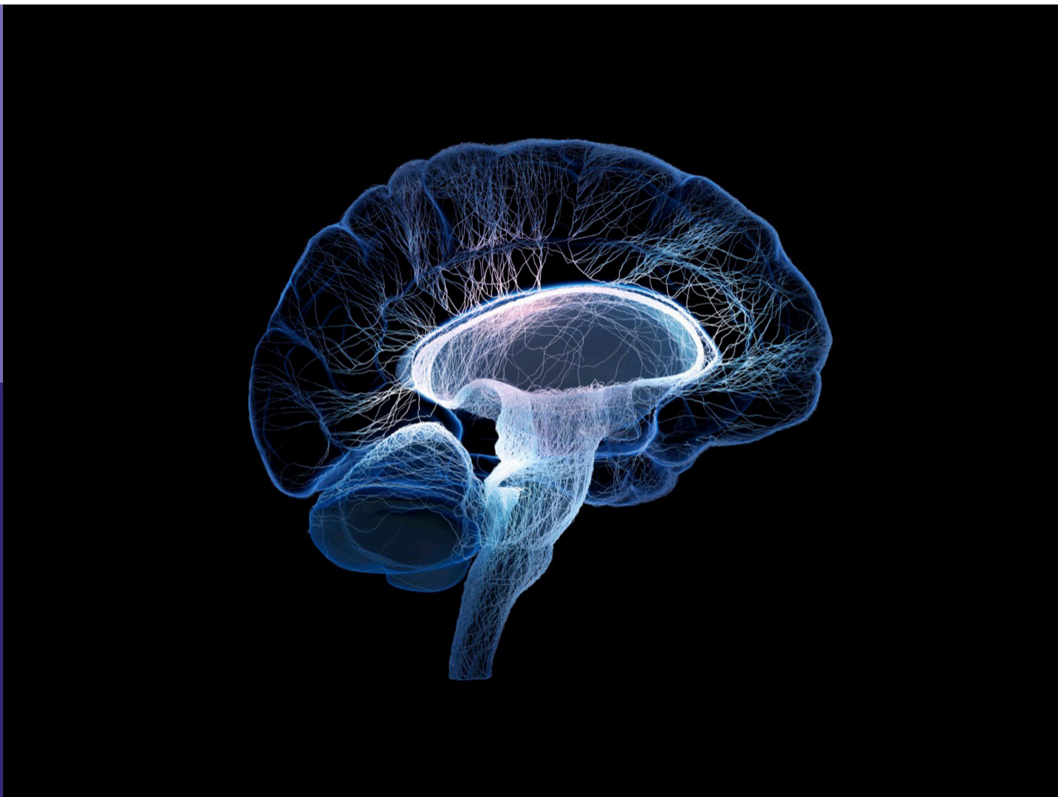

ISSN 1664-8714
ISBN 978-2-8325-4985-8
DOI 10.3389/978-2-8325-4985-8

About Frontiers

Frontiers is more than just an open access publisher of scholarly articles: it is a pioneering approach to the world of academia, radically improving the way scholarly research is managed. The grand vision of Frontiers is a world where all people have an equal opportunity to seek, share and generate knowledge. Frontiers provides immediate and permanent online open access to all its publications, but this alone is not enough to realize our grand goals.

Frontiers journal series

The Frontiers journal series is a multi-tier and interdisciplinary set of open-access, online journals, promising a paradigm shift from the current review, selection and dissemination processes in academic publishing. All Frontiers journals are driven by researchers for researchers; therefore, they constitute a service to the scholarly community. At the same time, the *Frontiers journal series* operates on a revolutionary invention, the tiered publishing system, initially addressing specific communities of scholars, and gradually climbing up to broader public understanding, thus serving the interests of the lay society, too.

Dedication to quality

Each Frontiers article is a landmark of the highest quality, thanks to genuinely collaborative interactions between authors and review editors, who include some of the world's best academicians. Research must be certified by peers before entering a stream of knowledge that may eventually reach the public - and shape society; therefore, Frontiers only applies the most rigorous and unbiased reviews. Frontiers revolutionizes research publishing by freely delivering the most outstanding research, evaluated with no bias from both the academic and social point of view. By applying the most advanced information technologies, Frontiers is catapulting scholarly publishing into a new generation.

What are Frontiers Research Topics?

Frontiers Research Topics are very popular trademarks of the *Frontiers journals series*: they are collections of at least ten articles, all centered on a particular subject. With their unique mix of varied contributions from Original Research to Review Articles, Frontiers Research Topics unify the most influential researchers, the latest key findings and historical advances in a hot research area.

Find out more on how to host your own Frontiers Research Topic or contribute to one as an author by contacting the Frontiers editorial office: frontiersin.org/about/contact

Human-in-the-loop system design and control adaptation for behavior-assistant robots

Topic editors
Yuquan Leng – Southern University of Science and Technology, China
Ningbo Yu – Nankai University, China
Bi Zhang – Shenyang Institute of Automation, Chinese Academy of Sciences (CAS), China
Benyan Huo – Zhengzhou University, China
Xu Jin – University of Kentucky, United States

Citation
Leng, Y., Yu, N., Zhang, B., Huo, B., Jin, X., eds. (2024). *Human-in-the-loop system design and control adaptation for behavior-assistant robots*. Lausanne: Frontiers Media SA. doi: 10.3389/978-2-8325-4985-8

Table of contents

04 Editorial: Human-in-the-loop system design and control adaptation for behavior-assistant robots
Bi Zhang, Yuquan Leng, Benyan Huo, Ningbo Yu and Xu Jin

07 Research status of elderly-care robots and safe human-robot interaction methods
Donghui Zhao, Xingwang Sun, Bo Shan, Zihao Yang, Junyou Yang, Houde Liu, Yinlai Jiang and Yokoi Hiroshi

23 Adaptive control for shape memory alloy actuated systems with applications to human–robot interaction
Enming Shi, Xu Zhong, Tian Wang, Xiaoguang Li, Chunguang Bu and Xingang Zhao

37 Automatic rehabilitation assessment method of upper limb motor function based on posture and distribution force
Jing Bai, Guocheng Li, Xuanming Lu and Xiulan Wen

52 Design and motion control of exoskeleton robot for paralyzed lower limb rehabilitation
Zhiyong Zhu, Lingyan Liu, Wenbin Zhang, Cong Jiang, Xingsong Wang and Jie Li

68 3D-CAM: a novel context-aware feature extraction framework for neurological disease classification
Yuhan Ying, Xin Huang, Guoli Song, Yiwen Zhao, XinGang Zhao, Lin Shi, Ziqi Gao, Andi Li, Tian Gao, Hua Lu and Guoguang Fan

77 Improving wheelchair user sitting posture to alleviate lumbar fatigue: a study utilizing sEMG and pressure sensors
Zizheng Huang, Jianwei Cui, Yuanbo Wang and Siji Yu

86 Adaptive fuzzy control for tendon-sheath actuated bending-tip system with unknown friction for robotic flexible endoscope
Fan Ren, Xiangyu Wang, Ningbo Yu and Jianda Han

98 The effect of electromyographic feedback functional electrical stimulation on the plantar pressure in stroke patients with foot drop
Xiaoting Li, Hanting Li, Yu Liu, Weidi Liang, Lixin Zhang, Fenghua Zhou, Zhiqiang Zhang and Xiangnan Yuan

110 Multi-layer CNN-LSTM network with self-attention mechanism for robust estimation of nonlinear uncertain systems
Lin Liu, Jun Feng, Jiwei Li, Wanxin Chen, Zhizhong Mao and Xiaowei Tan

124 MF-Net: multi-scale feature extraction-integration network for unsupervised deformable registration
Andi Li, Yuhan Ying, Tian Gao, Lei Zhang, Xingang Zhao, Yiwen Zhao, Guoli Song and He Zhang

frontiers | Frontiers in Neuroscience

TYPE Editorial
PUBLISHED 24 May 2024
DOI 10.3389/fnins.2024.1418331

Editorial: Human-in-the-loop system design and control adaptation for behavior-assistant robots

Bi Zhang[1]*, Yuquan Leng[2], Benyan Huo[3], Ningbo Yu[4] and Xu Jin[5]

[1]State Key Laboratory of Robotics, Shenyang Institute of Automation, Chinese Academy of Science (CAS), Shenyang, China, [2]Department of Mechanical and Energy Engineering, Southern University of Science and Technology, Shenzhen, China, [3]School of Electrical and Information Engineering, Zhengzhou University, Zhengzhou, China, [4]College of Artificial Intelligence, Nankai University, Tianjin, China, [5]Department of Mechanical and Aerospace Engineering, University of Kentucky, Lexington, KY, United States

KEYWORDS

editorial, human-in-the-loop system, behavior-assistant robots, adaptation, safety

OPEN ACCESS

EDITED AND REVIEWED BY
Michela Chiappalone,
University of Genoa, Italy

*CORRESPONDENCE
Bi Zhang
✉ zhangbi@sia.cn

RECEIVED 16 April 2024
ACCEPTED 15 May 2024
PUBLISHED 24 May 2024

CITATION
Zhang B, Leng Y, Huo B, Yu N and Jin X (2024) Editorial: Human-in-the-loop system design and control adaptation for behavior-assistant robots. *Front. Neurosci.* 18:1418331.
doi: 10.3389/fnins.2024.1418331

Editorial on the Research Topic
Human-in-the-loop system design and control adaptation for behavior-assistant robots

With the progress and development of human-robot systems, the coordination among humans, robots, and environments has become increasingly sophisticated. In this Research Topic, we focus on an important field in robotics and automation disciplines, which is defined as behavior-assistant robots [i.e., rehabilitation robots, assistive robots (Zhang et al., 2024), homecare robots (Zhao et al.) and so on]. The emergence of robot-assisted daily behaviors is gradually becoming a part of social life, which improves weak motor abilities, enhances physical functionalities, and enables various other benefits. For effective operation of a behavior-assistant robot, one successful strategy is human-in-the-loop (HIL) control architecture (Zhang et al., 2017). Integration of perception, actuation, and control technologies forms a HIL system.

Multimodal information-based pattern recognition is an important pathway to obtain human motion intention. Intelligent wheelchair is a common rehabilitation device, which is indispensable for people with limited mobility. Huang et al. utilized surface electromyography (sEMG) and pressure sensors to improve wheelchair user sitting posture and alleviate lumbar muscle fatigue. The results could provide more scientific guidance and suggestions for the daily use of wheelchairs. Lower limb rehabilitation robots, including both rigid exoskeleton (Sankai and Sakurai, 2018) and exosuit (Nuckols et al., 2021), are crucial devices for stroke or spinal cord injury patients. A key factor of rehabilitation robots is to estimate continuous joint motions based on sEMG and thus to ensure unhindered human-robot interaction. Liu et al. proposed a multilayer CNN-LSTM network incorporating the self-attention mechanism, which extracted and learnt the periodic and trend characteristics of sEMG signals, and realized the accurate autoregressive prediction of human motion information. The results had shown that it is applicable for both healthy and hemiplegic individuals under non-ideal sEMG conditions. Deformable registration also plays a fundamental role for image-assisted analysis. Li A. et al. proposed a novel registration network called multi-scale feature extraction-integration network, which utilized global and local features in images. This algorithm has the potential to predict displacement fields with high accuracy. These bio-machine interfaces expand information dimensions, improve modeling precision, and promote connections with the human nervous system, which are crucial for enhancing robot intelligence technologies.

Safety of HIL systems is a considerable gap to be bridged before advanced technologies could be widely applied in clinical rehabilitation settings. Rehabilitation assessment provides a basis for formulating treatment programs and judging effects. It is conducted based on the level of function, degree of damage, and recovery of stroke patients; however, it is subjective, time-consuming, and non-uniform for clinicians. Bai et al. proposed an automatic rehabilitation assessment method for hemiplegic upper limb motor function, which could allow for automated measurement of 30 items within the Fugl-Meyer scale. Experiments with 17 participants had demonstrated a significant correlation between the results of the automated assessment system and those of the physician's assessment. For real-time human-robot interaction, a monitoring system incorporating supervised loop is anticipated to effectively counter uncertainties arising from recognition inaccuracies. Zhu et al. proposed a novel exoskeleton robotic system with remote monitoring function for lower limb rehabilitation, the force and motion of which were analyzed in detail to implement closed-loop control. The results had shown that the exoskeleton robot has satisfactory assistance performance. In sum, the integration of fault-tolerance control and neural supervised loop exhibits potential for HIL systems, which implements a switching mechanism for predefined state events ensuring safe command over robots, enabling long-term closed-loop stability.

HIL systems also face challenges from environmental factors. How to realize the adaptation of the robotic systems and to robustly cope with uncertainties, is another interesting Research Topic. Tendon-sheath mechanisms (i.e., cable-driven actuation or smart material actuation) have attracted widespread interests due to flexibility, safety, and dexterity. These salient features guarantee a comfortable and user-friendly human-robot-environment interaction. Shi et al. proposed an adaptive control method by describing a SMA actuator as a gray-box model. The adaptation algorithm was built upon the multi-innovation concept and incorporated a dead-zone weighted factor, aiming to reduce computational complexities and enhance robustness properties. The experimental results of a SMA actuated hand rehabilitation robot had achieved higher position tracking accuracy. Ren et al. dealt with the precise modeling of non-linear friction, and proposed a novel fuzzy control scheme for the Euler-Lagrange dynamics model of tendon-sheath mechanisms, which achieved satisfactory tracking performance and provided more accurate friction compensation. Both of these methods are model-free control and have no strict requirement for the dynamics model, which could help improve human-robot locomotion adaptations, and thus exhibit potential applications in human-robot-environment interaction within the field of HIL based neural rehabilitation training.

Results from clinical practice have demonstrated the practicality and reliability of HIL systems. Li X. et al. analyzed the effect of electromyographic feedback functional electrical stimulation (FES) on the changes in the plantar pressure of drop foot patients. This case-control study enrolled 34 stroke patients with foot drop during a 4 weeks' treatments in a Rehabilitation Center at hospital. Compared with the control group, the advantages of FES were more significantly reflected in the improvement of gait speed, the step length symmetry index, and the enhancement of propulsive force. The results indicated that integrating FES with robot is more effective than basic rehabilitation training for stroke patients with foot drop. Ying et al. dealt with the classification problem of some neurological diseases such as Parkinson's Disease and Multiple System Atrophy, and proposed a novel feature extraction framework called 3D-CAM for computer-aided diagnosis. The dataset for this study was obtained from the Neurology Outpatient Department of a hospital, covering patient data from July 2020 to August 2023. Both studies provide new ideas for diagnosis and treatment of neurological diseases by using a more general HIL concept for clinical applications.

Author contributions

BZ: Writing – original draft, Writing – review & editing. YL: Writing – original draft, Writing – review & editing. BH: Writing – original draft, Writing – review & editing. NY: Writing – original draft, Writing – review & editing. XJ: Writing – original draft, Writing – review & editing.

Funding

The author(s) declare that financial support was received for the research, authorship, and/or publication of this article. The work of BZ was supported in part by the National Natural Science Foundation of China under Grant Nos. 62103406, 62333007, and U22A2067. The work of YL was supported in part by the National Natural Science Foundation of China under Grant No. 52175272. The work of BH was supported in part by the National Natural Science Foundation of China under Grant No. 62103376. The work of NY was supported in part by the Science and Technology Program of Tianjin under Grant No. 21JCZDJC00170. The work of XJ was supported in part by the United States National Science Foundation under Grant Nos. 2131802 and 2336189. Any opinions, findings, and conclusions or recommendations expressed in this material are those of the authors and do not necessarily reflect the views of the National Science Foundation.

Conflict of interest

The authors declare that the research was conducted in the absence of any commercial or financial relationships that could be construed as a potential conflict of interest.

Publisher's note

References

Nuckols, R. W., Lee, S., Swaminathan, K., Orzel, D., Howe, R. D., and Walsh, C. J. (2021). Individualization of exosuit assistance based on measured muscle dynamics during versatile walking. *Sci. Robot*. 6:eabj1362. doi: 10.1126/scirobotics.abj1362

Sankai, Y., and Sakurai, T. (2018). Exoskeletal cyborg-type robot. *Sci. Robot*. 3:eaat3912. doi: 10.1126/scirobotics.aat3912

Zhang, B., Shuai, M., Han, B., Li, S., Liu, L. Q., and Zhao, X. G. (2024). Assistive robots for Beijing Winter Paralympic torch relay: accessible technologies to restore human functionality. *Innovation* 5:100556. doi: 10.1016/j.xinn.2023.100556

Zhang, J. J., Fiers, P., Witte, K. A., Jackson, R. W., Poggensee, K. L., Atkeson, C. G., et al. (2017). Human-in-the-loop optimization of exoskeleton assistance during walking. *Science* 356, 1280–1284. doi: 10.1126/science.aal5054

frontiers | Frontiers in Neuroscience

TYPE Review
PUBLISHED 30 November 2023
DOI 10.3389/fnins.2023.1291682

OPEN ACCESS

EDITED BY
Ningbo Yu,
Nankai University, China

REVIEWED BY
Mengze Li,
Zhejiang Lab, China
Zhu Jun Wang,
Shenyang Aerospace University, China

*CORRESPONDENCE
Junyou Yang
✉ junyouyang@sut.edu.cn

RECEIVED 10 September 2023
ACCEPTED 14 November 2023
PUBLISHED 30 November 2023

CITATION
Zhao D, Sun X, Shan B, Yang Z, Yang J, Liu H, Jiang Y and Hiroshi Y (2023) Research status of elderly-care robots and safe human-robot interaction methods.
Front. Neurosci. 17:1291682.
doi: 10.3389/fnins.2023.1291682

Research status of elderly-care robots and safe human-robot interaction methods

Donghui Zhao[1,2], Xingwang Sun[1], Bo Shan[1], Zihao Yang[1], Junyou Yang[1]*, Houde Liu[2], Yinlai Jiang[3] and Yokoi Hiroshi[3]

[1]School of Electrical Engineering, Shenyang University of Technology, Shenyang, China, [2]Tsinghua Shenzhen International Graduate School, Tsinghua University, Shenzhen, China, [3]Department of Mechanical Engineering and Intelligent Systems, University of Electro-Communications, Tokyo, Japan

Faced with the increasingly severe global aging population with fewer children, the research, development, and application of elderly-care robots are expected to provide some technical means to solve the problems of elderly care, disability and semi-disability nursing, and rehabilitation. Elderly-care robots involve biomechanics, computer science, automatic control, ethics, and other fields of knowledge, which is one of the most challenging and most concerned research fields of robotics. Unlike other robots, elderly-care robots work for the frail elderly. There is information exchange and energy exchange between people and robots, and the safe human-robot interaction methods are the research core and key technology. The states of the art of elderly-care robots and their various nursing modes and safe interaction methods are introduced and discussed in this paper. To conclude, considering the disparity between current elderly care robots and their anticipated objectives, we offer a comprehensive overview of the critical technologies and research trends that impact and enhance the feasibility and acceptance of elderly care robots. These areas encompass the collaborative assistance of diverse assistive robots, the establishment of a novel smart home care model for elderly individuals using sensor networks, the optimization of robot design for improved flexibility, and the enhancement of robot acceptability.

KEYWORDS

elderly-care robots, nursing mode, safe interaction methods, practicality, acceptability

1 Introduction

According to the latest data from the United Nations, the global population is expected to reach 8 billion by 15 November 2022. The global population will likely grow to around 8.5 billion by 2030 and 9.7 billion by 2050. Concurrently, the elderly population is expected to rise from 771 million in 2022 to 994 million in 2030 and 1.6 billion in 2050. The proportion of individuals aged 65 and over is projected to increase from 9.7% in 2022 to 11.7% in 2030 and further to 16.4% in 2050 (United Nations Department for Economic and Social Affairs, 2023). Moreover, the number of frail elderly individuals unable to engage in physical activity is anticipated to surpass 440 million by 2021 (World Health Organization, 2022). This global aging phenomenon and a low birth rate are increasing the demand for elderly care services. However, statistics from 2019 indicate that the number of nursing staff dedicated to elderly care accounted for only 9% of the professional nursing staff, totaling approximately 15 million individuals worldwide (United Nations, 2019). This glaring disparity between the demand for nursing care and the available resources has become a pressing global issue (Wu et al., 2021). Consequently, the World

Health Organization (WHO) and all United Nations Member States approved the "United Nations Decade of Healthy Aging" project in 2020, which emphasizes the provision and accessibility of long-term care for older persons as one of its key areas of focus for the next decade (Arias-Casais et al., 2022). To address these challenges, leveraging robotic nursing technology to effectively and safely attend to the daily needs of the frail elderly population represents a promising solution. This approach helps to bridge the gap between demand and resources and enhances the well-being of elderly individuals with compromised functional abilities.

The field of elderly care has witnessed the emergence of elderly-care robots, which can effectively assist and replace manual caregiving in meeting the daily life needs of elderly individuals. These robots have the potential to alleviate the burden on families and society in providing elderly care, as well as address the critical shortage of nursing staff (Vercelli et al., 2018). Furthermore, they offer promising prospects for improving the quality of life for individuals with compromised functional abilities and contribute to social stability and development (Pilotto et al., 2018). In contrast to traditional service robots (Gonzalez-Aguirre et al., 2021; Lee, 2021) and auxiliary robots (Alboul et al., 2023) that provide a wide range of services for different types of humans or families in various industries, elderly-care robots are tailored to meet the unique needs and challenges of the elderly. However, frail elderly individuals often experience motor function issues such as osteoporosis and muscle weakness. However, frail elderly often experience motor function issues such as osteoporosis and muscle weakness. Additionally, the decline in language, limb, and emotional expression further complicates the accurate conveyance of nursing intentions from elderly individuals with weak functional abilities. This presents significant challenges for delivering appropriate nursing to this particular group, necessitating a high level of expertise in nursing practices. The shortage of nursing staff, coupled with the demanding nature of nursing requirements, has given rise to the development of the robotic nursing industry. The growing demand for high-performance elderly-care robots has provided unprecedented opportunities and challenges.

2 Elderly-care robots and their various nursing modes

The elderly-care robot integrates advanced robotics technology with the specific needs of elderly care, enabling accurate, safe, and intelligent nursing to enhance the well-being and level of care for frail elderly. Over the past decade, many countries have implemented significant policies to promote the development of the elderly-care robot industry. Over the past decade, numerous countries have implemented tremendous policies to encourage the development of the elderly-care robot industry. For instance, the National Science Foundation (NSF) funded $37 million in 2016 to support fundamental research on companion robots and home care robots (Bekey and Yuh, 2008). The European Union's civil robot research and development program, SPARC, allocated 700 million euros from 2014 to 2020 to develop key technologies for robots to address the challenges of an aging society (Huet and Mastroddi, 2016). In 2016, Japan introduced the "Five-Year Plan for Care Robots" into the national "2016 Revitalization Strategy," investing 100 billion yen to support research into robotic technologies for elderly care. This research covered various aspects, including transfers, toileting, monitoring, bathing, communication, and rehabilitation (Neumann, 2016). The development of high-performance elderly-care robots holds significant importance in light of the global elderly-care landscape. (1) Medical assistant function: Designed to assist with medical tasks with almost no social characteristics, such as human physiological index monitoring and auxiliary analysis. (2) Daily living assistance and rehabilitation training function: Aims to assist frail elderly with simple daily living and care tasks, including feeding, walking, mobility, turning over, postural support, toileting, sleep care, dressing and undressing, and some rehabilitation training tasks. (3) Life companion and emotional interaction function: Enhances the quality of life of elderly individuals through voice communication and companionship. In practical elderly care settings, the integration of these three functions aims to achieve the following objectives:

- Enhancing the autonomy and behavioral abilities of elderly individuals, enabling them to live in a comfortable environment while preserving their dignity.
- Ensuring the safety and companionship of elderly individuals, maintaining their health and mobility, and promoting a healthy lifestyle.
- Effectively distributing caregiving tasks among nursing staff, families, and healthcare organizations, thus optimizing resource allocation and efficiency.

Based on the medical assistant function, daily living assistance and rehabilitation training function, as well as life companion and emotional interaction function of elderly-care robots, and the varying emphases of these functions, we categorize elderly-care robots into three main types: intelligent robots based on medical functionality and physiological index monitoring, life-assisted nursing robots, and companion robots based on emotional interaction and behavior monitoring. The purpose of this classification is to better meet the diverse needs of the elderly and the complexity of real-life elderly care scenarios.

2.1 Intelligent robots based on medical functionality and physiological index monitoring

Addressing specific physiological, motor, and cognitive impairments in some elderly individuals, the system aims to complement and enhance medical services based on physiological monitoring and analysis while respecting user privacy. This strengthens the autonomy of elderly individuals and improves their physical and cognitive conditions (Heerink et al., 2006; Stefanie et al., 2017; Etemad-Sajadi and Gomes Dos Santos, 2019).

Personal AAL (Personal Ambient Assisted Living; Corcella et al., 2019) and Emerald (Rincon et al., 2019) are examples of systems that remotely measure physiological indicators using high-precision wearable sensors. These systems automatically generate visual health recommendations while assessing the users' health status. Additionally, the system can provide early intervention for elderly individuals living in the home environment, effectively assess and minimize the long-term impact of various factors on health, and encourage elderly individuals to maintain an active and healthy lifestyle (Alsulami et al., 2017, 2022;

Almalki et al., 2022). PHAROS (Physical Assistant Robot System) combines the Pepper robot (Figure 1A) and a motion expert system to analyze users' motion states during daily training using deep learning methods (Costa et al., 2018; Martinez-Martin et al., 2019). It provides real-time posture correction and positive feedback to encourage and enhance users' initiative. The system offers personalized training sets and programs, compares the degree of decline based on certified clinical guidelines, and notifies healthcare professionals of potential physical issues. IMBTMMS (Intelligent Mobile Body Temperature Monitoring and Management System; Cui et al., 2021) is designed for elderly care settings. It regularly processes body temperature, heart rate, and blood oxygen data, providing real-time and continuous monitoring, prediction, alerting, and management services. The system's implementation in nursing homes has achieved large-scale index monitoring and data management, significantly alleviating staff shortages during epidemics and reducing the risk of cross-infection. In summary, Personal AAL and Emerald utilize wearable sensors to assess the health status and physical activity of the elderly, while PHAROS employs visual input to analyze motion states. Proper sensor placement is crucial for accurate measurement results, and ensuring correct order becomes challenging when frail elderly individuals are responsible for sensor installation. Furthermore, these technologies primarily support and assist medical staff rather than directly replacing them. Therefore, medical staff need access to comprehensive physical activity data and daily assessment reports to utilize these systems effectively.

Castillo et al. proposed a robot (Figure 1B) for guiding the rehabilitation of language apraxia (Castillo et al., 2018). The model parameters are trained using oral motion information from standardized elderly individuals. Subsequently, the system captures oral motion and utilizes deep learning methods to evaluate key points, ensuring the correct execution of the treatment regimen. With the assistance of professionals, the system improves muscle movement planning, sequencing, and coordination to produce speech ultimately. Regarding cognitive aspects, CoME effectively analyzes the development.

process of mild cognitive impairment by detecting early signs of abnormal user behavior (COME, 2021). It offers cognitive games, monitors health status, provides recommendations for maintaining a healthy lifestyle, and offers guidance on daily activities, chores, and relevant knowledge for the elderly. MyMemory is a mobile augmented memory system that combines schedules and games to help individuals with traumatic brain injury recover from autobiographical memory deficits (Chang et al., 2018). Clinical research indicates that the system aids in recovering autobiographical memory deficits among elderly individuals. In the systems mentioned above, nursing staff receive personalized reports regarding platform usage, the health status of elderly individuals, and their overall progress. Moreover, professional nursing staff can create tutorials to guide relatives and non-professional caregivers in completing assistance tasks. These systems significantly contribute to treating specific conditions such as mild cognitive impairment, traumatic brain injury, or language apraxia. However, the technologies employed in these systems require the supervision of medical professionals. They are limited to use during formal treatment periods, hindering elderly individuals from independently pursuing physical health and improvement at home. To enhance the versatility of such systems, StayFitLonger (Perez-Marcos et al., 2018) proposes a solution that operates without the supervision of medical professionals. This integrated system combines physical and cognitive training for elderly individuals, offering gamified activities and personalized exercises through mobile devices. It allows users to engage in more extended periods of activity. Additionally, virtual reality technology provides assistance and instructions during exercises, encouraging active participation among elderly individuals. The platform aims to empower elderly individuals to use it autonomously at home and provides various exercise modes based on their flexibility and injury levels.

2.2 Life-assisted nursing robots

The care of frail elderly individuals demands a high degree of specialization and remains primarily reliant on manual caregiving. This approach not only entails significant caregiving complexity and intensity but also places substantial reliance on the service proficiency of caregivers. With the development of assistive robots, rehabilitation robots, and human-robot interaction technologies, life-assisting nursing robots and their key technologies are emerging. These robots must adapt to users' physiological differences and living conditions, enabling them to safely operate in a user-centric environment and provide secure assistance to frail elderly individuals in mobility, household tasks, rehabilitation training, and various daily life demands. In general, these robots can be categorized into three main types: robots for autonomous assistive tasks, rehabilitation robots in elderly care scenarios, and multifunctional nursing robots based on human-robot interaction.

2.2.1 Robots for autonomous assistive tasks

Robots for autonomous assistive tasks can autonomously complete repetitive service or nursing tasks without human intervention. They can help elderly individuals deliver medicines and items, automatically

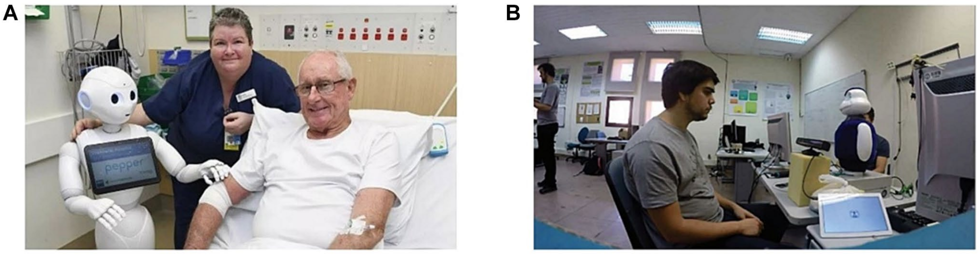

FIGURE 1
Intelligent robots based on medical functionality and physiological index monitoring. **(A)** PHAROS. **(B)** Mini.

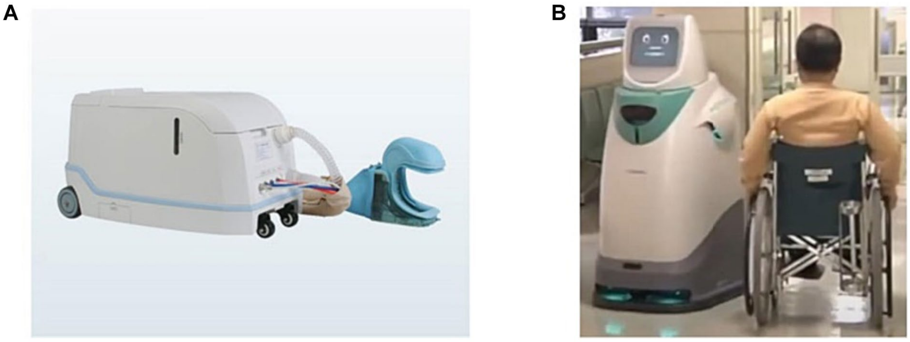

FIGURE 2
Robots for autonomous assistive tasks. **(A)** XFCS-A. **(B)** HOSPI-R.

clean excrement, dehumidify, purify, and other functions (Christoforou et al., 2020).

The XFCS-A (Qian et al., 2010) nursing robot (Figure 2A) is primarily employed to assist elderly individuals or long-term bedridden patients in defecation. At the same time, cleaning steps such as warm water washing, warm air drying, and negative ion purification are performed on the user's buttocks. This robot has gained significant popularity in hospitals and homes due to its convenience, safety, and reliability. In 2005, Toshiba Corporation of Japan developed the HOSPI-R series of home care robots (Panasonic's Autonomous Delivery Robot - HOSPI(R), 2023; Figure 2B), which includes functions such as drug delivery and risk status identification. These robots comprehend user instructions through voice and visual systems, autonomously follow the user, and assess potential risk states in the surrounding environment, providing timely prompts to the operator. To address concerns related to drug or liquid overflow caused by robot acceleration or deceleration, various storage methods for liquids and solids, as well as buffer devices, have been devised to enhance the safety of the drug transportation process (Mertz, 2012). Yanshan University has invented a bidirectional transfer nursing robot. This innovation enables the transfer of frail elderly from hospital beds to stretcher workshops, effectively reducing the labor intensity of nursing staff and avoiding the secondary damage to the user caused by the traditional transfer method (Wang et al., 2016a,b). Additionally, Shenyang University of Technology has developed an intelligent toilet robot with autonomous movement and slip risk identification, as well as an intelligent wheelchair robot capable of adjusting the user's seating posture (Yu, 2019). To enhance the safety and flexibility of these robots' usage for elderly individuals with weakened functions, a highly robust follow-up control method has been proposed for the intelligent toilet robot. This involves designing seating trajectories and postures based on the principles of user motion engineering, calculating the control rate of the intelligent toilet robot accordingly, and providing optimal seating postures for users with varying levels of mobility.

2.2.2 Rehabilitation robots in elderly care scenarios

Rehabilitation robots in elderly care scenarios are crucial in assisting frail elderly with rehabilitation training functions in hospitals, nursing homes, homes, and other scenarios.

In the late 20th century, developed countries began to focus on the development of nursing bed robots, which are mainly used for various operations such as rehabilitation training, turning, and defecation of long-term bedridden elderly (Chen, 2016). These nursing bed robots provide upper and lower limb rehabilitation training and muscle massage functions, promoting bone rehabilitation and improving limb blood circulation for individuals whose limbs cannot stretch due to prolonged bedridden conditions. The nursing bed robots also offer vital signs monitoring capabilities and assist nursing staff with real-time user monitoring through camera configurations (Zhang et al., 2006). Notable examples include the intelligent nursing bed developed by Metrocare based on ergonomic principles and motion planning principles (Xin and Zhang, 2010), the integrated nursing bed robot with bed and wheelchair switching function developed by Devicelink Company (Luo, 2005), and the Gakusho series rehabilitation nursing bed robot developed by Matsushita Electric Company and Paramount Bed Company in Japan (Shi, 2014). In recent years, China has made significant progress in the field of rehabilitation nursing bed robots. Li Zhenqing et al. has developed a multifunctional nursing robot bed capable of addressing the high-efficiency nursing needs of long-term bedridden patients, including rehabilitation training, sitting, turning, eating, reading, writing, excretion, and entertainment (Li et al., 2012). Shanghai University of Technology has also developed a nursing bed robot that assists elderly individuals with back support, leg bending, turning over, and excreting. The system provides two nursing modes: active control and passive control. Furthermore, Zhang Hua et al. have invented a nursing bed integrated with a bathroom system, serving as an intelligent transportation tool while meeting the various daily care demands of families and hospitals (Zhang et al., 2011).

Intelligent assistive systems that facilitate proper standing and walking training for elderly with declining lower limb function have significant implications for the recovery of lower limb motor function and overall physical health. The renowned PAMM (Personal Aid for Mobility and Monitoring) system, developed by the Massachusetts Institute of Technology, consists of an intelligent walking machine and a smart walking stick device. The system utilizes force sensors as the primary input interface to drive the active wheel at the base of the system, which provides walking assistance to users (Dubowsky et al., 2000). To address the inconvenience of wearing devices, Honda has designed an intelligent lower limb assist system. This mechanical device, worn on the hip, assists elderly individuals with insufficient muscle strength by improving walking speed, increasing walking distance, enhancing gait uniformity, and monitoring the user's heartbeat to adjust walking speed (Kusuda, 2009) automatically. Shenyang University of Technology and Kochi University of

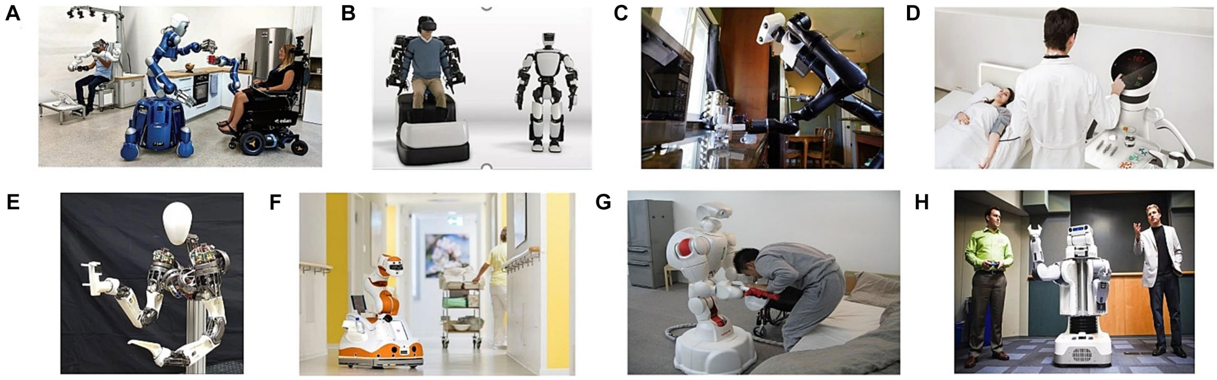

FIGURE 3
Multifunctional nursing robots based on human-robot interaction with a humanoid structure. **(A)** EDAN and Justin. **(B)** T-HR3. **(C)** Busboy. **(D)** Care-O-bot 4. **(E)** LIMS2-AMBIDEX. **(F)** Lio. **(G)** TWENDY-ONE. **(H)** PR2.

Technology in Japan have collaborated to develop a walking rehabilitation training robot for home care scenarios. This robot offers active training, passive training, and active-passive hybrid training modes. Equipped with an integrated omnidirectional mobile platform, it can operate within small indoor spaces without requiring a turning radius. The robot incorporates various interactive modes such as touch screen interaction, automatic navigation, and control based on the user's walking direction and speed intentions, considering the exercise habits of frail elderly (Zhao et al., 2017). Compared to the steps involved in repeatedly placing and calibrating electrodes during rehabilitation training using a multi-channel EMG acquisition system, Zhao Xingang proposed a hand motion recognition system based on single-channel EMG signal decomposition. This system significantly improves motion recognition accuracy by 10% while enhancing operation convenience and user comfort. Its applications extend to daily sign language recognition, prosthetic hand control, and hand rehabilitation robot control (Zhao X. et al., 2019). Furthermore, Bai Jing from Southeast University proposed an autonomous home rehabilitation training and evaluation system based on workspace measurement. This system provides three-dimensional spatial image information, two-dimensional image information, and quantitative data to evaluate training outcomes, providing specific and easily understandable visual feedback for patients. The system overcomes the limitations of conventional treatment methods, enabling users to independently complete home rehabilitation training and evaluation without the supervision of a doctor (Bai et al., 2018). Various studies on indoor rehabilitation robots in elderly care scenarios have also been conducted by the Institute of Automation of the Chinese Academy of Sciences, Beijing University of Technology, Harbin Institute of Technology, and Huazhong University of Science and Technology.

2.2.3 Multifunctional nursing robots based on human-robot interaction

Multifunctional nursing robots based on human-robot interaction play a significant role in assisting nursing staff by effectively improving nursing ability and efficiency. The German space agency has developed the home care robot ecosystem SMILE (Vogel et al., 2021), which consists of the wheelchair robot EDAN, the humanoid robot Justin, and the tactile remote control device HUG (Figure 3A). EDAN integrates a force-controlled light manipulator with a five-finger intelligent hand, controllable via joystick, EMG signal, or EEG signal, to assist individuals with motor dysfunction. Justin is a robot with a wheeled chassis and a humanoid upper body equipped with a four-finger gripper. The humanoid upper body features two arms capable of executing various tasks, including making coffee, mopping tables, rinsing cups, and sweeping floors. The tactile remote control device HUG enables the remote control operation of EDAN and Justin. The system offers various operating modes with different levels of autonomy. TRI (Toyota Research Institute) has developed the T-HR3 (Figure 3B), a humanoid robot capable of safely supporting human activities at home or in medical institutions (Toyota Research Institute, 2021). Additionally, TRI has introduced the Busboy (Figure 3C), a new generation of home care robots that can perform relatively complex humanoid tasks. Busboy learns various household activities through human teachings, such as grasping objects and opening/closing doors, instead of being directly programmed for fixed tasks. Notably, the robot effectively links observed transactions with previous learning actions, enabling adaptive autonomous actions when encountering specific objects or scenes, even with slight task variations. To address the care needs of lonely, frail elderly, a Robotic home assistant, "care-o-bot," has been developed (Hans et al., 2002). This series of robots not only performs a range of housework tasks but also provides emotional comfort through various interactive methods. The latest generation, Care-O-bot 4 (Figure 3D), supports a modular design, allowing users to configure it according to their preferences, resulting in improved quality and efficiency of care (Kittmann et al., 2015). The dual-arm robot LIMS2-AMBIDEX, based on tendon-driven technology, has been developed by KoreaTech in South Korea (Kim et al., 2018; Figure 3E). Each arm features seven degrees of freedom, and to reduce the inertia of the end effector, the corresponding drivers are positioned on the shoulder joint, utilizing a line drive transmission scheme. The design achieves an extremely lightweight structure of 2.63 kg below the shoulder joint, ensuring the safety and high-speed precision of dual-arm operations.

The Swiss F&P Robot Company has developed a multifunctional artificial intelligence (AI) nursing robot called Lio (Miseikis et al., 2020; Figure 3F), which integrates various capabilities such as walking, grasping, cognitive nursing, emotional support, disability assistance, rehabilitation therapy, patrolling, and delivery of living items. Lio has been successfully deployed in numerous nursing homes in Germany

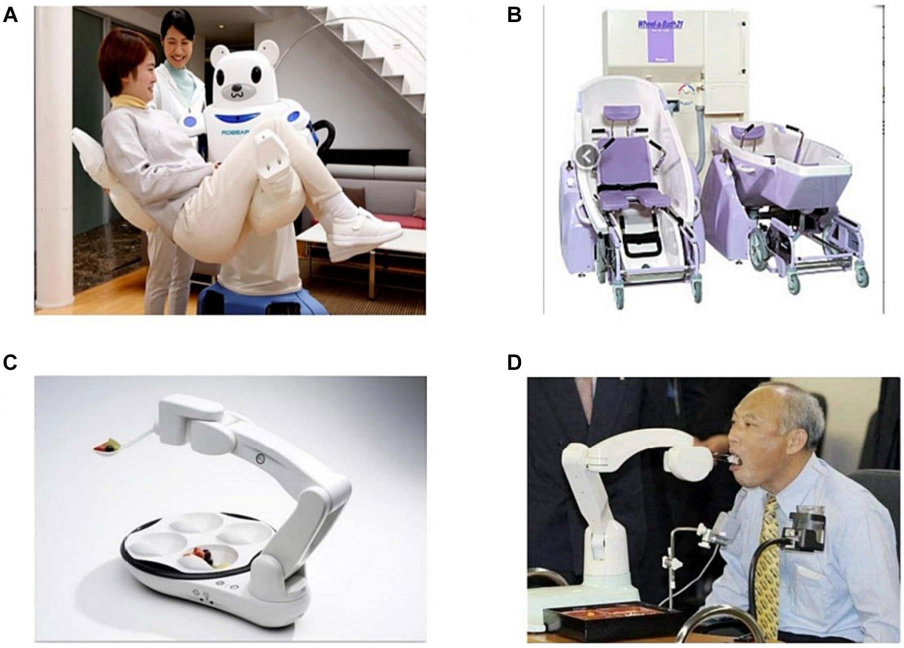

FIGURE 4
Multifunctional nursing robots based on human-robot interaction for special behaviors. **(A)** Robear. **(B)** Bishamon. **(C)** Obi. **(D)** My Spoon.

and Switzerland, effectively assisting nursing staff in providing targeted services. Lio is a nursing robot that efficiently assists the nursing staff in providing targeted services and is ideally suited for nursing homes, hospitals, nursing centers, and private residences. In 2007, Waseda University in Japan introduced a mobile-based multifunctional nursing robot named "TWENDY-ONE" (Hargrove et al., 2007; Vallery et al., 2008; Negro et al., 2016; Figure 3G). With 13 sensors on its hand, including a six-axis force sensor on its fingertips and distributed pressure sensors on its palm surface, TWENDY-ONE can perform delicate movements and provide a more human-like touch sensation through soft skin on its palm surface. Its arm is equipped with a high-power output driver that combines high-power.

output with a mechanical impedance mechanism, enabling it to perform precise grabbing and lifting tasks for patients. The Georgia Institute of Technology has developed the PR2 (Personal Robot 2) life behavior assistance robot (Rusu et al., 2009; Figure 3H). This system features two 7-degree-of-freedom anthropomorphic arms with a wrist equipped with a 6-axis force/torque sensor. The PR2 robot can autonomously assist bedridden users in body wiping tasks. The system includes an operator selection interface that allows autonomous selection of areas that require cleaning, including the upper arm, forearm, thigh, and calf (King et al., 2010). In the process of nursing, the repeated and repeated transfer services of the frail elderly bring excessive physical burden to the nursing staff, resulting in the majority of nursing staff in nursing homes suffering from chronic lumbar diseases. At the same time, most of the transfer assistive devices represented by traditional lifts are inconvenient to use, time-consuming and laborious and have low penetration rates. To this end, the RIBA series of robots have been developed to realize the safe and convenient transfer of lower limb disabled elderly in their living space. The third-generation Robear robots (Tak et al., 2010; Figure 4A) facilitate the safe and convenient transfer of lower limb disabled elderly within their living spaces. By analyzing posture, force, speed, acceleration, comfort, and other physical data, these robots can predict potentially dangerous behavior during the movement of the frail elderly. The robots are equipped with joint torque sensors and intelligent electronic rubber skin on their arms and chest, enabling them to accurately sense contact forces below 1 N and better understand the intentions of elderly individuals during mobile operations, ensuring patient health and safety (RIBA-II, 2021). The University of Pittsburgh has developed an assisted nursing robot that provides comfortable mobile assistance to users (Fan et al., 2018). Clinical experiments have demonstrated that this robot effectively reduces physiological and psychological pressure on nursing staff, thereby reducing overall management costs. Guo Shijie of Hebei University of Technology has developed a humanoid back-hugging mobile nursing robot with a three-degree-of-freedom chest mechanism to support the user's chest during transfers (Guo et al., 2019). By imitating human back movements, this robot enables safe and efficient mobility and toileting for the frail elderly. The study integrates factors affecting mobility comfort into the human-robot system model, optimizing robot mechanisms and motion trajectories to effectively address the challenges faced by elderly individuals during mobility. Harbin Institute of Technology has determined the configuration and performance indicators of large-load manipulators based on the requirements of mobile tasks (Wu, 2020). They have successfully developed a two-degree-of-freedom joint system.

using multi-stage deceleration techniques, accompanied by the design of a compact six-degree-of-freedom manipulator. Combined with impedance control methods, these manipulators can lift paralyzed elderly individuals out of hospital beds. The robotic arm also features tactile perception and proximity sensing capabilities on its surface, ensuring safe and reliable nursing tasks through the proposed active and passive safety control methods. Zhejiang

University and Yanshan University have developed a variety of transfer nursing robots that assist bedridden elderly individuals and people with lower limb disabilities in leaving hospital beds and moving conveniently. These robots include functions such as automatic folding, all-around automatic walking, automatic lifting, automatic toilet opening, and width adjustment. Furthermore, Jiang Yinlai and Zhao Donghui have invented a walking support robot with auxiliary standing and walking functions, effectively achieving safe and flexible standing assistance based on ergonomic principles in the standing process and intelligent wheelchair robot integration. Additionally, they have developed a multi-channel close-range sensor and a flexible control method based on human motion gait (Zhao, 2020). Significant research efforts have been made worldwide to enhance the mobility of elderly and disabled individuals through intelligent wheelchairs and their multimodal interaction technologies. Notable examples include the Wheelesley autonomous wheelchair robot (Yanco, 1998), the TAO Aicle intelligent wheelchair from Japan (Matsumoto et al., 2006), the Connie intelligent company KSI intelligent elderly function electric wheelchair, the RoboChair intelligent wheelchair developed by the Institute of Automation of the Chinese Academy of Sciences, the "Jiaolong" intelligent wheelchair developed by Shanghai Jiaotong University (Zhang, 2015), and the multimodal control wheelchair developed by Chongqing University of Posts and Telecommunications (Luo et al., 2012). These intelligent wheelchairs offer advanced features, such as multimodal human-robot interaction, efficient path planning, dynamic obstacle avoidance, and autonomous navigation, which greatly improve the mobility of elderly and disabled individuals. In Japan, the Bishamon care wheelchair bathing robot (He et al., 2019; Figure 4B) integrates an adjustable bathtub and an upper and lower separable wheelchair, significantly enhancing bathing efficiency and nursing care. Henan University of Science and Technology has developed a nursing robot bathroom system (Cheng, 2015), which includes bathing mechanisms and a robot that integrates auxiliary standing, friction, and shampoo mechanisms. This system assists users in standing and provides efficient cleaning services, ensuring a comfortable bathing experience.

Li et al. have developed a nursing shampoo robot that effectively addresses the safety control problem associated with existing shampoo robots while ensuring efficient cleaning of the user's home (Li et al., 2017). In the domain of feeding assistance for frail elderly, notable robots include the Obi robot that helps disabled individuals eat unassisted by Design Robot Company in the United States (Automation, 2021; Figure 4C), the My Spoon meal-assistance robot by SECOM Company in Japan (Ishii, 2003; Figure 4D), and the intelligent feeding assistive robot developed by the University of Shanghai for Science and Technology (Xu et al., 2020). These innovative solutions provide effective auxiliary feeding schemes for frail elderly. Furthermore, Google's Liftware Level anti-shake spoon has demonstrated its benefits for Parkinson's patients by offering a stable grip and improving the eating experience (Liftware, 2021). Additionally, Krati has addressed the assistive dressing needs of frail elderly individuals s through the development of a deep learning-based framework. This framework accurately predicts clothing categories and identifies spatial coordinates for grip points, thereby streamlining the clothing operation process. Promising results have been achieved in fabric type detection and precise grasping point determination.

2.3 Companion robots based on emotional interaction

Companion robots based on emotional interaction have social and companionship capabilities, effectively assisting elderly individuals in addressing psychological and emotional problems such as isolation, emotion, stress, and loneliness, thereby improving their well-being. With continuous innovations in human-robot interaction (Goodrich and Schultz, 2007), behavior detection (Mohebbi, 2020), and autonomous navigation technologies (Marder-Eppstein et al., 2010), increasingly advanced socially interactive robots have emerged (Fong et al., 2003; Breazeal, 2004).

Within the scope of Horizon 2020, the European Union's research and innovation framework program, numerous projects focused on elderly nursing services, including ENRICHME, SOCRATES, RADIO, and STREAMS, have been approved. Research indicates that older users are more receptive to robots that resemble pets or babies in both appearance and behavior (Breazeal and Scassellati, 2000). Consequently, various companion robots with pet-like or baby-like appearances have been developed to engage with frail elderly individuals daily. Notably, PARO, a seal-shaped robot (Figure 5A), incorporates tactile feedback, voice interaction, and posture perception to elicit positive emotions in users through real-time responsive behaviors such as head and flipper movements (Sabanovic et al., 2013; Hung et al., 2019; Chen et al., 2022). PARO has found utility in several nursing homes. NeCoRo robots, designed to resemble cats, are capable of expressing emotions like satisfaction, surprise, and happiness while responding appropriately to user emotions and actions (Nakashima et al., 2010). Clinical trials conducted in nursing homes show that NeCoRo effectively assists residents in improving communication and comfort among elderly individuals. AIBO, another companion robot, has been used in several clinical studies on the acceptability of geriatric care (Fujita, 2004). Participants exhibited a high degree of dependence on AIBO and reported reduced feelings of loneliness. Clinical experiments have further revealed that robot-assisted activities can help alleviate loneliness and enhance the activity and emotional state of patients with Alzheimer's disease. MARIO (Figure 5B) alleviates the challenges of loneliness and dementia in elderly individuals through the development of companion robots (MARIO, 2021). A clinical study of MARIO has revealed various factors affecting its acceptability, including facial appearance, knowledge of user preferences, practicality, and the ability to connect users with their family and friends (Casey et al., 2016). The Jibo social robot (Figure 5C) conducted a three-week "facilitating social interaction experiment" on 19 participants in an assisted living community in California (Jibo, 2023). By utilizing natural language processing techniques to provide information pertaining to daily activities obtained from the internet, Jibo enabled remote nursing staff to establish a sense of telepresence within the user's home (Roy et al., 2000). Many nursing studies have highlighted the significant influence of emotional, behavioral, and environmental factors on the nursing experience of elderly individuals (Hirsch et al., 2000). In conclusion, social robots have demonstrated their effectiveness in enhancing user engagement and fostering social connections. Nevertheless, these advancements also shed light on users' concerns regarding security, privacy, and the collective apprehensions surrounding social robotics.

Based on completing the accompanying behavior, the robot can provide extensible behaviors such as feeding reminders, abnormal behavior recognition, and entertainment activities.

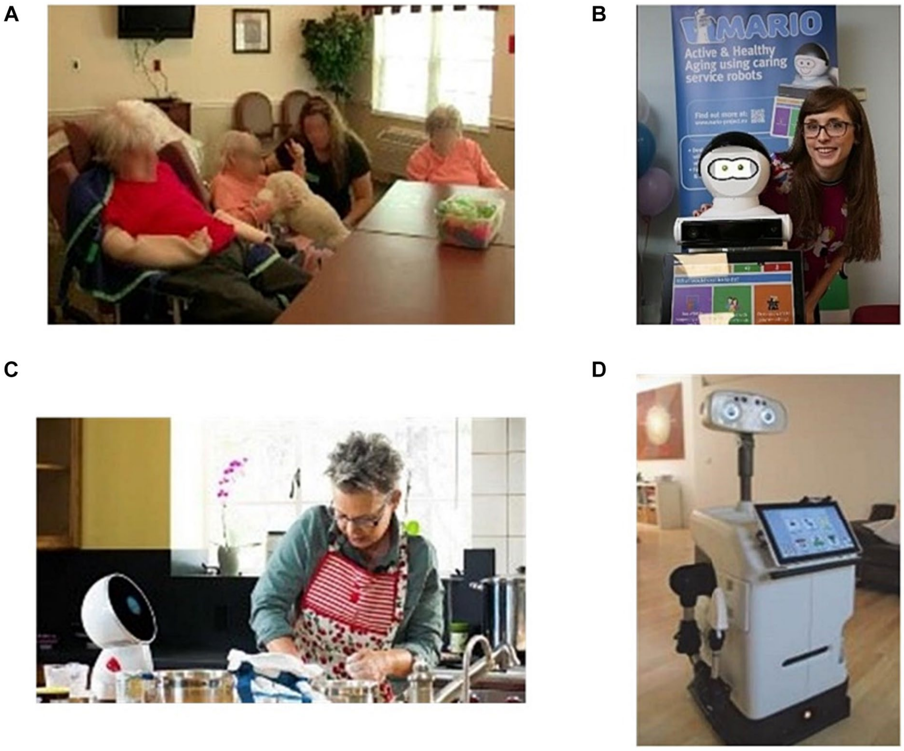

FIGURE 5
Companion robots based on emotional interaction. **(A)** PARO. **(B)** MARIO. **(C)** Jibo. **(D)** HOBBIT.

Mabu, a personal healthcare companion robot, was introduced in 2015 ((My Website, 2023)). This robot engages in social interactions with elderly individuals and creates personalized conversations for each user based on classical psychological models of behavior, helping to address issues related to chronic diseases, such as medication intake. Stevie, developed by Trinity College Dublin (McGinn et al., 2020), interacts with elderly individuals through a combination of sensory data, including gestures, speech, and facial expressions, with high acceptability. Mabu and Stevie robots are primarily employed in reminder scenarios and do not include behavior monitoring or data collection and analysis systems. The HOBBIT project, funded by the European Union, aims to develop a socially assistive robot (Figure 5D) capable of tasks such as picking up and carrying, emergency recognition, fitness planning, and reminders while ensuring the safety of elderly individuals (Bajones et al., 2018). The project introduces.

the concept of interactive care, enabling the robot to learn the user's habits and preferences to adapt its behavior. ZORA presents two commercial robot solutions (Zorarobotic, 2021). ZoraRobot, based on the Nano platform, integrates healthcare applications that assist elderly individuals in interactive therapy and entertainment activities and have been introduced in nursing homes and retirement communities in the United States. Zorabot, on the other hand, is based on the Pepper robot platform and incorporates medical applications, providing functions such as visiting, greeting and returning, inquiries, and medical assistance. Blue Frog has developed a robot named BUDDY (BUDDY, 2021), which enhances care for elderly individuals by providing companionship and assistance in their daily activities. For instance, it can remind them to take medication, make appointments, deliver items, or detect abnormal behaviors such as falls. In the European Union's 7th Research Framework Programme (FP7), several elderly care projects combine robotics technology with ambient intelligence to achieve panoramic semantic integration for assisted home care, facilitating independent living for elderly individuals (Saunders et al., 2013). The CompanionAble project effectively addresses the social integration and home care challenges faced by elderly individuals with chronic cognitive impairment in Europe (Badii et al., 2009). The GiraffPlus project combines sensor networks to provide a remote-controlled robot for monitoring activities within the home environment. The project particularly emphasizes the emotional aspect of user interaction to meet their needs and capabilities (Coradeschi et al., 2014). The Mobiserv system comprises a socially interactive robot, wearable smart clothing, and a smart home environment, aiming to support the daily lives of elderly individuals with comprehensive care services focused on health, nutrition, happiness, and safety, thereby improving their quality of life and care efficiency (Nani et al., 2010; Esposito et al., 2014).

Regarding cognitive assistance, LIZA (Le and Wartschinski, 2018) has emerged as a widely adopted cognitive companion that enhances older adults' reasoning and decision-making abilities through continuous human-robot interaction. This system employs natural language interaction based on 66 topic texts to impart knowledge to elderly individuals about one or more subjects. By posing synthesized questions and adapting to the individual needs of elderly individuals during each interaction, LIZA autonomously and subconsciously corrects its guidance criteria. Furthermore, social assistance robots (Andriella et al., 2018) have also found extensive applications in cognitive assistance. Through efficient interactions, these robots encourage elderly individuals to grasp specific tasks or engage in cognitive exercises such as the Syndrom-Kurztest neuropsychological battery (SKT). They exhibit adaptability to the diverse responses of different older adults and provide support and assistance at multiple levels of interaction.

In summary, current companion robot technologies are predominantly focused on specific domains. In comprehensive elderly care scenarios, multiple systems must collaborate to provide comprehensive support, which poses challenges in effectively managing these systems and accurately monitoring the health conditions of elderly individuals. Moreover, using visual sensors in home care scenarios raises privacy concerns. Therefore, it is necessary to establish appropriate regulations to address the ethical and technological boundaries, aiming to minimize threats to the privacy of elderly individuals. Furthermore, the issue of acceptance by the elderly population presents a significant challenge in the widespread adoption of robotics in elderly care. The difficulty in operating high-tech products and the gap between social experiences and expectations contribute to the resistance among some elderly individuals to utilize such technologies. Research shows (Sixsmith, 2013) that the acceptance of robots depends not only on the personalized functionalities they offer, such as entertainment, status enhancement, and tangible benefits, but also on the inherent characteristics of individuals, including age, needs, gender, technological experience, cognitive abilities, education, culture, roles, expectations, attitudes toward robots, and the inherent characteristics of robots, such as safety, usability, intelligence, appearance, human likeness, facial expressions, physical size, gender, personality, and adaptability (Young et al., 2009; Frennert et al., 2012). Therefore, effectively handling the practicality and social aspects while satisfying the essential performance requirements and catering to the individual differences of users is crucial to the successful deployment of companion robot technologies in elderly care scenarios and to enhance acceptance among the elderly population.

3 Safe interaction methods

The safe human-robot interaction method is one of the most critical research areas in elderly care scenarios. This technology encompasses collision protection between users and robots within shared spaces while comprehensively considering various ways in which harm can be inflicted upon frail elderly individuals, from physical contact to psychological effects. This paper comprehensively describes four aspects of safe interaction methods: control methods, motion planning, behavior prediction, and psychological factors.

3.1 Control-based safe interaction methods

Control strategies are commonly used to achieve safe human-robot interaction, without the need for complex predictive models or planning strategies, while still demonstrating high system robustness. Among these, safety improvements in human-robot interaction can be split into two distinct phases: pre-collision safety and post-collision safety.

Pre-collision safety control methods are measures taken before an actual collision between humans and robots occurs. These methods can be achieved by ensuring collision avoidance as a primary objective or by constraining critical parameters of the robot. For instance, collision prevention can be achieved by limiting the robot's speed or energy, using defined safety zones, maintaining tracking separation distances, guiding the robot away from humans, and other methods. The common approach involves controlling safe human-robot interaction by setting thresholds for key system parameters, such as joint velocity, energy, or force exerted by the robot. One method combines a force threshold-based foot motion control strategy with an improved robot body center of mass motion for enhanced performance when walking on uneven terrain (Heinzmann and Zelinsky, 2003). Another approach by Broquere et al. utilizes piecewise cubic polynomial chains to construct trajectory chains that limit jerk, acceleration, and velocity for pre-collision safety control (Broquere et al., 2008). While these methods may be overly conservative without imminent collision threats, they provide pre-collision safety by globally constraining the robot's motion without relying on accurate and robust detection and tracking of human positions. Another method of pre-collision control involves decelerating or stopping the robot by utilizing safety zones or separation distances to prevent collisions. This method uses depth sensors to estimate the distance between the robot and static or moving obstacles. It combines real-time distance measurements with estimated obstacle velocities to adopt a repulsive vector-based collision avoidance controller (Buizza Avanzini et al., 2014). De Luca et al. also propose a method utilizing a distributed distance sensor and optimization of robot body sensor node positions for safety (Flacco et al., 2012). Compared to threshold-based methods, this method offers greater flexibility but also requires robust and low-latency tracking of humans within a given space. Incorporating risk criteria and field computation into control algorithms can prevent robot collisions. For instance, potential field methods define repulsive vector fields that guide robot motion, adjusting the trajectory based on changing dynamic environmental factors to ensure safety during complex behaviors (Khatib, 1986; Kovács et al., 2016). This method allows for more intricate collision avoidance beyond adjusting the robot's speed. However, the method's effectiveness depends on the strategy employed in constructing the potential field. In elderly care scenarios, customizing strategies involve factors beyond separation distances, such as approach direction, emotional states, and human gaze direction. Therefore, in the case of unexpected or unpredictable contact, post-collision control methods minimize harm by switching to different control strategies, differentiating between intentional and unintentional contact, and allowing safe physical contact when necessary to achieve effective collaboration. The first step in implementing post-collision control methods for safe human-robot interaction is to detect whether a collision has occurred. Sharkawy et al. propose a collision detection method based on a multi-layer feed-forward neural network, utilizing robot position and joint torque sensors for detecting collisions between operators and robots, applicable to any robot equipped with joint torque sensors (Sharkawy et al., 2020). Geravand et al. present another method using motor current measurements for detection and response, eliminating the need for torque sensors (Geravand et al., 2013). This system is designed for robots with closed-loop structures, capable of distinguishing between intentional collisions and switching the robot into a collaboration modality upon collision detection. Golz et al. propose a method utilizing machine learning and physical contact models to distinguish between intentional and unintentional robot collision detection, employing non-linear support vector machines for classification by observing real collision data and extracting a set of features. As interaction scenarios become more complex, effectively distinguishing between intentional and unintentional contact in collision detection systems becomes critical to ensuring safe interactions. When intentional contact is recognized, the robot must accurately infer the user's collaborative intent and provide optimal support actions during the interaction rather than simply minimizing damage by avoiding collisions or switching control. Luca and Flacco proposed an inference framework based on user gestures and speech to determine whether users intend to enter a collaboration modality and specify body-specific parts where robot contact is allowed or prohibited, such as the user's head (De Luca and Flacco, 2012). Additionally, these frameworks can effectively estimate interaction forces at contact points and control the robot to ensure that they do not exceed predetermined thresholds. In elderly care scenarios, collaborative contact requires specific consideration of the actual contact points and monitoring and limiting the effects of forces during an interaction.

3.2 Motion planning-based safe interaction methods

Motion planning-based safe interaction methods employ robot path planning and motion planning to avoid collisions and ensure safety. In the process of motion planning, human-related constraints, such as separation distances and human gaze directions, are directly incorporated into the motion planner's cost functions and objective functions to actively avoid collisions and generate comfortable and user-acceptable motions, thereby achieving optimal motion planning strategies in closed-loop scenarios. Motion planning takes a more proactive approach than control-based methods to ensure interaction safety. Research has shown that, in some instances, traditional control methods for collision avoidance may result in lower safety and efficiency compared to perception-based motion planning methods and may negatively impact the user's psychological safety (Lasota et al., 2014). Furthermore, motion planning algorithms incorporating safety operators apply to almost any robotic platform, such as manipulator manipulation and robotic navigation, demonstrating good functional generality and portability. These algorithms primarily include planners based on human closure constraints and motion planners based on geometric and task constraints. Compared to threshold-based control methods, the parameters of motion planners can minimize risk operators throughout the motion process rather than just approaching safety thresholds. Several motion planning algorithms have been developed that take human constraints into account. For instance, for scenarios involving human-carrying mobile platforms, Morales et al. developed the HCoPP (Human Comfort Path Planner), which takes into account user preferences, such as the desired distance from walls when walking in corridors and visibility at corners while approaching turns, to design driving paths that provide a comfortable and pleasant experience for the user (Morales et al., 2015). In the spatial zones of human-robot collaboration, due to the inherent uncertainty in user behavior, motion planning strategies need to consider the ability for rapid re-planning based on geometric and task constraints. Interaction safety zones and buffer zones can be encoded using geometric constraints, while additional information guiding the robot's motion can be modeled using task constraints, such as leveraging previous observations to predict the occurrence of future events. By hierarchically encoding task constraints and geometric constraints and combining them, complex search spaces can be efficiently traversed, effectively eliminating illogical solutions and local optima, thereby accelerating computation speed Combined Task and Motion Planning for Mobile Manipulation (Wolfe et al., 2021).

3.3 Perception and prediction-based safe interaction methods

Accurate perception and prediction of each other's behaviors and actions are crucial to ensure safe interaction between human users and robots in scenarios involving mutual proximity, contact, and dynamic interaction. This capability needs to be extended to all members of multi-robot systems involved in assistive behaviors alongside users. Perception of human activity states encompasses the perception and prediction of actions. In pursuit of this goal, research focuses primarily on behavior analysis by analyzing the underlying features of motion signal sensors, physiological signal sensors, visual sensors, and depth sensors.

In the field of elderly care, robots need to monitor and discriminate the behavior of elderly individuals in indoor environments, such as homes, which is crucial for enhancing safe interaction. These behaviors include behavior monitoring, fall detection, abnormal behavior detection, and medication monitoring, which significantly improve the safety of assisted living in homes. For instance, in designing applications for the frail elderly, an effective and common method for fall detection involves utilizing the three-dimensional depth data from depth cameras to determine the distance from the human centroid to the ground and to analyze the vibration characteristics. However, the robustness of traditional global visual sensors is compromised when there are occlusions between users and robots. A fall recognition algorithm based on a set-source filter can effectively identify various abnormal gaits, including falls and dragging gaits (Zhao D. et al., 2019). Activity prediction using image data has been explored by Azorin-Lopez et al., where they establish normalized activity vectors to describe RGB (Red Green, and Blue) interaction data, eliminating dependence on time or event sequences (Azorin-Lopez et al., 2014). Shah et al. utilize a time-series analysis method, defining multivariate Gaussian distributions for each motion time step based on tracked human arm degrees of freedom (Perez-D'Arpino and Shah, 2015). The system utilizes the learned model for Bayesian classification of the initial phase of motion to predict the direction of a person's movement and select the robot's action with minimal interference. Intention recognition is a prerequisite for achieving safe human-robot interaction, particularly for frail elderly. Intention recognition can be accomplished through explicit and implicit methods. Explicit methods directly convey the robot's intent and planned behavior through language, visual cues, auditory signals, and other explicit means. In cases where explicit expression of motion goals is not desired, the implicit method implicitly embeds subtle cues through action performances to convey motion intentions. By combining these methods in specific elderly care scenarios, human-robot behavior becomes more predictable, allowing for more effective motion planning and ensuring safe interaction. Intention recognition needs to be specifically defined in conjunction with particular tasks and can involve the recognition of individual action switches, transitions between multiple discrete actions, and continuous information. These methods have been applied in research on facial recognition-based user emotion detection, language recognition, action intention recognition, and cognitive emotion regulation methods, providing a solid research foundation for human-robot interaction technology in the context of elderly care scenarios (Li, 2013; Liu, 2015; Liu et al., 2016; Lu, 2017). Particularly in the domain of action intention recognition, various applications include control of prosthetic grasping, dexterous manipulation of prosthetics, control of brain-computer interfaces, and assistance in standing and walking. These motion signal perception-based studies mainly utilize position sensors, angle sensors, and force sensors to capture the motion state of the user's limb joints, which are then fed back to the control unit to form a closed-loop control system. This approach enables smooth control, significantly improving precision and accuracy and preventing secondary injuries. For instance, Xu Wenxia et al. propose a multi-sensor fusion-based motion control method for assistive walking robots that can adapt to users' walking intentions, predict potential falls during usage, and take corresponding fall prevention strategies. The effectiveness of this method is demonstrated through experiments (Xu et al., 2016). Another technique for human action prediction does not directly infer sensor data but represents discrete actions or task steps in a labeled form. Task models are used to infer actions taken and combined with sequence matching and probability recognition methods for prediction. In this regard, the objective of perception systems is action detection. Nikolaidis et al. encode human-robot collaborative tasks based on Markov decision processes and accurately predict the outcome of human actions (Nikolaidis and Shah, 2013). They subsequently propose a hybrid observable Markov decision process (Nikolaidis et al., 2015). In this work, the system clusters action sequences, learns reward functions for each cluster through inverse reinforcement learning from joint action demonstrations, and automatically learns user models. The robot then utilizes these models to predict user types for anticipating user behavior and executing appropriate expected behaviors.

In order to create a safe, comfortable, and natural assistive environment or rehabilitation training system for elderly individuals, research on perception and prediction between robots and elderly individuals play a crucial role. This research not only identifies the current states of elderly individuals and robots but also facilitates interaction between them. It can construct a closed-loop control system, improve the control accuracy of the system, and use the information of force and position to realize the compliant control of the robot. In addition, the research of perception and prediction can also be used as an evaluation signal to participate in the evaluation and calibration of rehabilitation robot performance (Lloyd and Besier, 2003; Balbinot and Favieiro, 2013). Accurate perception combined with high-quality control methods can create a safe and comfortable care and rehabilitation environment for elderly individuals, significantly improving nursing safety and nursing efficiency.

3.4 Psychological factor analysis based safe interaction methods

Enhancing psychological safety is a key factor in users' acceptance of elderly-care robots. Maintaining psychological safety means ensuring that users subjectively perceive their interactions with the robot as safe without causing any psychological discomfort or stress, whether due to the robot's actions, appearance, speech, posture, social behavior, or other attributes. Previous research has shown that relying solely on physical safety measures is insufficient to improve users' sense of safety and comfort (Lasota and Shah, 2015). Therefore, in human-robot interaction, a crucial method for ensuring psychological safety is appropriately adjusting the robot's behavior, which can be categorized into adjustments based on robot characteristics and social factors characteristics. Researchers commonly evaluate the effectiveness of psychological safety through three evaluation methods: questionnaire surveys, physiological indicators, and behavioral indicators.

Research on adjustments based on robot features focuses primarily on psychological safety factors by modifying various parameters of robot motion, such as speed, acceleration, or the degree of proximity to human characteristics, to make human-robot interaction more comfortable. Previous studies have quantified user comfort during human-robot interaction by establishing human comfort models. For instance, dynamic comfort models have been developed to enhance the comfort of the interaction process by adjusting parameters such as robot speed and distance from the user (Wang et al., 2018). Sisbot and Alami found that physical safety alone is insufficient to achieve user-acceptable human-robot interaction and that any behavior that could cause fear or discomfort in humans must be avoided. Therefore, they developed a safety-compliant motion planner (Sisbot and Alami, 2012). Mainprice et al. generated reactive actions that satisfy human comfort by introducing interaction constraints in the motion planner (Mainprice et al., 2011). Additionally, it is necessary to consider research and adjustments related to robot features and understand the influence of social factors (Haring et al., 2013; Costanza et al., 2014; Obaid et al., 2016). Factors such as different robot postures, appearance design, and different types of background sounds can affect user comfort. Another method to enhance interaction safety through psychological factors is to adhere to social norms, including considering the influence of cultural and personality differences. It is essential to translate social habits observed in human interactions into methods for interacting with robots and to consider the impact of robots violating social conventions on users' psychological safety. Researchers such as Joosse have found that users are highly sensitive to the extent to which robots respect social norms when invading personal space, and their reactions to robot invasions of personal space can be even more potent than those of humans (Joosse et al., 2013). A six-week clinical study by Walters assessed participants' behavioral preferences when interacting with robots in a home environment. The results showed that even without safety hazards, robot failures directly increased the expected distance between humans and robots. Furthermore, studies have revealed that compared to the distances at which users willingly approach robots, they allow robots to approach them at greater distances within physically constrained areas. Ghazali et al. found that users tend to trust robots with human facial features more, and most users exhibit higher psychological reactions when interacting with opposite-sex robots (Ghazali et al., 2018). Furthermore, studies have indicated that users from different cultural backgrounds have varying standards for appropriate proximity when robots move toward a group of people, and user differences in traits, culture, and experiences can influence behavioral preferences (Joosse et al., 2014).

4 Future development directions of elderly-care robots

4.1 Multi-heterogeneous nursing robot system and their collaborative control technology

Due to the strong individual variations in physical conditions among frail elderly individuals, the development of rigid-flexible coupled robots for the care of frail elderly and their human-robot collaboration is gradually becoming a new trend in achieving universal high-quality elderly care. Rigid-flexible coupled robot systems, by seamlessly combining flexible actuation and transmission with rigid support and execution capabilities, can effectively simulate human nursing processes and compensate for the shortage of staff nursing. This provides a new safe, efficient, and accurate robotic nursing solution. To address the deficiencies in contextualization and functionality in daily life, there is a need to establish an overall system for a variety of heterogeneous elderly care service robots tailored to complex caregiving scenarios, alongside a robust communication system. Furthermore, it is crucial to develop task planning and collaborative control methods customized for specific application scenarios, assisting users in achieving safe and smooth state transitions to support continuous activities in daily life. Additionally, optimizing the structure and nursing modes of elderly-care robots based on the analysis of human motion functions and human factors engineering is an essential direction for the future development of nursing robots, ensuring a balance between safety and adaptability in assisting daily living.

4.2 Establishing a new model of smart home care for elderly individuals based on robotic nursing systems and sensor networks

Compared to health care, nutrition, social interaction, and other daily living support services provided by adult day care centers, long-term care facilities, and nursing homes, elderly individuals prefer to live in their own homes and enjoy the sense of familiarity, self-confidence, independence, and sense of accomplishment brought about by self-care activities. Therefore, establishing a home care model that meets specific user needs, combined with intelligent home sensor networks and robotic nursing technologies, can provide users with context-aware ubiquitous computing applications and home automation services. What's more, this technology is a future development trend. The framework of home-based elderly care systems should possess adaptability to efficiently cater to the diverse needs of the elderly population with individual differences. It should correctly manage sensor network systems, elderly smart systems with medical and metric monitoring, life-assisted nursing robots, and companion robots based on emotional interaction. Additionally, standardized data communication methods and cloud management systems need to be established to realize a new model of smart home-based elderly care.

4.3 Future directions for the safety of interactive control and compliance of frail elderly in complex scenarios

Considering the physiological characteristics of frail elderly, such as decreased continuity, stability, and susceptibility to misleading signals in their diminished motor functions, rigid robot operation based solely on experience can easily lead to unnoticed secondary damage or even life-threatening hazards. The extraordinary physical conditions of frail elderly and their demands for nursing safety impose strict requirements on the safety and compliance of nursing robots. It is essential to combine foundational theories and key technologies from the fields of medicine, information, and mechanics to enhance the compliance and safety of robot operations. Simultaneously, for specific caregiving tasks, selecting effective intent recognition carrier signals for frail elderly individuals and effectively combining their respective advantages, establishing a method for synchronized acquisition of multi-source signals, feature extraction, uniform representation, and joint recognition is crucial. This method enhances the estimation accuracy and stability of human intent and target information, enabling efficient information exchange between frail elderly individuals and caregiving robots, and is a key component in the development of caregiving robots for frail elderly individuals. Moreover, designing efficient control techniques, establishing mappings between intent and interfaces, and incorporating collaborative task constraints while integrating elderly individuals as part of the closed-loop control system, allows robots to adapt to the intentions of elderly individuals, ensuring high fault tolerance and compliance in their responses. This addresses essential issues in nursing robots. To further enhance robots' safety and caregiving capabilities, it is imperative to integrate the physiological characteristics of frail elderly individuals and break through the core technologies of human-robot coupling dynamics, service robot design, intention recognition for frail elderly, and human-robot coordinated control. This will establish a new principle and theoretical framework for rigid-flexible coupled robots tailored for frail elderly care.

4.4 Exploring the critical issues of robotic nursing technology, acceptability, and ethics

The development of robotic technologies for elderly nursing brings benefits to frail elderly but also raises concerns regarding privacy rights, interpersonal interaction, quality of care, acceptability, and ethical considerations between the elderly and nursing robots. Key ethical dilemmas include striking a balance between the need for supervision and privacy protection, the potential misguidance caused by one-sided emotional bonds with elderly individuals, restrictions on elderly individuals' behaviors due to the autonomy of nursing robots, the insufficient acceptability resulting from the objectification risks in robot nursing services, and concerns about the deterioration of interpersonal skills in elderly individuals. Therefore, it is necessary to establish effective, ethical principles considering the differences between robot technology and human ethics while meeting the principles of specificity, flexibility, and safety to ensure that elderly-care robots can truly enter and benefit every household.

5 Conclusion

In summary, the application prospects of elderly-care robots in assisting the frail elderly in daily living assistance, nursing, and rehabilitation training are extensive, making it one of the most challenging research areas in robotics. Over the past 30 years, elderly-care robots have gradually transitioned from laboratory research to clinical applications, giving rise to a significant number of distinctive life-assisted nursing robots, companion robots based on emotional interaction, and intelligent robots based on medical functionality and physiological index monitoring. This progression has greatly advanced both the research and application levels in this field. Given that frail elderly individuals have direct physical contact with robots, the methods for safe human-robot interaction are crucial scientific issues affecting interaction performance. Utilizing motion control, motion planning, prediction methods, and psychological factors are essential means and core technologies for achieving safe human-robot interaction strategies. Future research will focus on the collaborative assistance of heterogeneous assistive robots, the establishment of home-based elderly care models based on robots and sensor networks, the optimization of robot flexibility design, and the improvement of robot acceptance. These efforts will ultimately enhance the level of service and nursing provided by elderly-care robots.

Author contributions

DZ: Funding acquisition, Project administration, Supervision, Writing – review & editing, Conceptualization, Resources. XS: Writing – original draft, Investigation. BS: Data curation, Investigation, Methodology, Writing – review & editing. ZY: Formal analysis, Investigation, Validation, Writing – review & editing. JY: Conceptualization, Project administration, Supervision, Writing – review & editing. HL: Formal analysis, Supervision, Validation, Writing – review & editing. YJ: Writing – review & editing. YH: Funding acquisition, Project administration, Supervision, Writing – review & editing.

Funding

The author(s) declare financial support was received for the research, authorship, and/or publication of this article. This work was supported by Shenzhen Science Fund for Distinguished Young Scholars: RCJC20210706091946001, National Key Research and Development Program of China: 2022YFB4701400/4701402, the General Project of Liaoning Provincial Department of Education: LJKZ0124 and the Natural Science Foundation of Liaoning Province: 2021-BS-152.

Conflict of interest

The authors declare that the research was conducted in the absence of any commercial or financial relationships that could be construed as a potential conflict of interest.

Publisher's note

References

Alboul, L., Dimitrova, M., Lekova, A., Kaburlasos, V. G., and Mitrouchev, P. (2023). Editorial: emerging technologies for assistive robotics: current challenges and perspectives. *Front Robot AI* 10:1288360. doi: 10.3389/frobt.2023.1288360

Almalki, M., Alsulami, M. H., Alshdadi, A. A., Almuayqil, S. N., Alsaqer, M. S., Atkins, A. S., et al. (2022). Delivering digital healthcare for elderly: a holistic framework for the adoption of ambient assisted living. *Int. J. Environ. Res. Public Health* 19:16760. doi: 10.3390/ijerph192416760

Alsulami, M. H., Atkins, A. S., Campion, R. J., and Alaboudi, A. A. (2017). An enhanced conceptual model for using ambient assisted living to provide a home proactive monitoring system for elderly Saudi Arabians. In: *2017 IEEE/ACS 14th International Conference on Computer Systems and Applications (AICCSA) (Hammamet: IEEE)*, 1443–1449.

Alsulami, M. H., Atkins, A. S., Sorour, A. S., and Campion, R. J. (2022). "CHAPTER 3—ageing population supported by ambient-assisted living in the Kingdom of Saudi Arabia" in *Smart home technologies and services for geriatric rehabilitation*. eds. M.-A. Choukou and S. Syed-Abdul (San Jose, California, USA: Academic Press), 43–78.

Andriella, A., Alenyà, G., Hernández-Farigola, J., and Torras, C. (2018). Deciding the different robot roles for patient cognitive training. *Int J Hum Comput Stud* 117, 20–29. doi: 10.1016/j.ijhcs.2018.03.004

Arias-Casais, N., Amuthavalli Thiyagarajan, J., Rodrigues Perracini, M., Park, E., Van Den Block, L., Sumi, Y., et al. (2022). What long-term care interventions have been published between 2010 and 2020? Results of a WHO scoping review identifying long-term care interventions for older people around the world. *BMJ Open* 12:e054492. doi: 10.1136/bmjopen-2021-054492

Automation, E. (2021). Meet obi, a robot that helps disabled individuals eat unassisted. Available at: https://meetobi.com/ (Accessed 6 May 2023).

Azorin-Lopez, J., Saval-Calvo, M., Fuster-Guillo, A., and Oliver-Albert, A. (2014). A predictive model for recognizing human behaviour based on trajectory representation. In *2014 international joint conference on neural networks (IJCNN)* (Beijing, China: IEEE), 1494–1501.

Badii, A., Etxeberria, I., Huijnen, C., Maseda, M., Dittenberger, S., Hochgatterer, A., et al. (2009). CompanionAble: graceful integration of mobile robot companion with a smart home environment. *Geron* 8:181. doi: 10.4017/gt.2009.08.03.008.00

Bai, J., Song, A., Li, H., and Xu, B. (2018). Evaluation system of upper limb rehabilitation training for stroke patients at home based on workspace measurement. *Chin J Sci Instru* 39, 74–81. doi: 10.19650/j.cnki.cjsi.J1702932

Bajones, M., Fischinger, D., Weiss, A., Wolf, D., Vincze, M., De La Puente, P., et al. (2018). Hobbit: providing fall detection and prevention for the elderly in the real world. *J Robot* 2018, 1–20. doi: 10.1155/2018/1754657

Balbinot, A., and Favieiro, G. (2013). A neuro-fuzzy system for characterization of arm movements. *Sensors* 13, 2613–2630. doi: 10.3390/s130202613

Bekey, G., and Yuh, J. (2008). The status of robotics. *IEEE Robot. Automat. Mag.* 15, 80–86. doi: 10.1109/M-RA.2007.907356

Breazeal, C. (2004). *Designing sociable robots*. Cambridge, Massachusetts, United States: MIT Press.

Breazeal, C., and Scassellati, B. (2000). Infant-like social interactions between a robot and a human caregiver. *Adapt. Behav.* 8, 49–74. doi: 10.1177/105971230000800104

Broquere, X., Sidobre, D., and Herrera-Aguilar, I. (2008). Soft motion trajectory planner for service manipulator robot. In *2008 IEEE/RSJ international conference on intelligent robots and systems* (Nice: IEEE), 2808–2813.

BUDDY (2021). The companion robot. Available at: http://www.bluefrogrobotics.com/news/buddy-a-innorobo/ (Accessed 6 May 2023).

Buizza Avanzini, G., Ceriani, N. M., Zanchettin, A. M., Rocco, P., and Bascetta, L. (2014). Safety control of industrial robots based on a distributed distance sensor. *IEEE Trans. Contr. Syst. Technol.* 22, 2127–2140. doi: 10.1109/TCST.2014.2300696

Casey, D., Felzmann, H., Pegman, G., Kouroupetroglou, C., Murphy, K., Koumpis, A., et al. (2016). "What people with dementia want: designing MARIO an acceptable robot companion" in *Computers Helping People with Special Needs*. eds. Miesenberger Klaus, A Bühler, Model for Human Comfort, Penaz Petr (Cham: Springer), 318–325.

Castillo, J. C., Álvarez-Fernández, D., Alonso-Martín, F., Marques-Villarroya, S., and Salichs, M. A. (2018). Social robotics in therapy of apraxia of speech. *J Healthc Engineer* 2018, 7075290–7075211. doi: 10.1155/2018/7075290

Chang, C., Hinze, A., Bowen, J., Gilbert, L., and Starkey, N. (2018). Mymemory: a mobile memory assistant for people with traumatic brain injury. *Int J Hum Comput Stud* 117, 4–19. doi: 10.1016/j.ijhcs.2018.02.006

Chen, M. (2016). Research and development of control system of nursing robot bed. Master's thesis. Shanghai University of Engineering Science.

Chen, S.-C., Jones, C., and Moyle, W. (2022). The impact of engagement with the PARO therapeutic robot on the psychological benefits of older adults with dementia. *Clin. Gerontol.* 0, 1–13. doi: 10.1080/07317115.2022.2117674

Cheng, C. (2015). *Research on the bathroom ystem of nursing robot based on ergonomics*. Master's thesis. Harbin Institute of Technology.

Christoforou, E. G., Avgousti, S., Ramdani, N., Novales, C., and Panayides, A. S. (2020). The upcoming role for nursing and assistive robotics: opportunities and challenges ahead. *Front Digit Health* 2:585656. doi: 10.3389/fdgth.2020.585656

COME (2021). Alpplication for healthier self-management of seniors. Available at: http://come-aal.eu/. (Accessed 6 May 2023).

Coradeschi, S., Cesta, A., Cortellessa, G., Coraci, L., Galindo, C., Gonzalez, J., et al. (2014). "GiraffPlus: a system for monitoring activities and physiological parameters and promoting social interaction for elderly" in *Human-computer systems interaction: Backgrounds and applications 3 advances in intelligent systems and computing*. eds. Z. S. Hippe, J. L. Kulikowski, T. Mroczek and J. Wtorek (Cham: Springer International Publishing), 261–271.

Corcella, L., Manca, M., Nordvik, J. E., Paternò, F., Sanders, A.-M., and Santoro, C. (2019). Enabling personalisation of remote elderly assistance. *Multimed. Tools Appl.* 78, 21557–21583. doi: 10.1007/s11042-019-7449-z

Costa, A., Martinez-Martin, E., Cazorla, M., and Julian, V. (2018). Pharos—physical assistant robot system. *Sensors* 18:2633. doi: 10.3390/s18082633

Costanza, E., Fischer, J. E., Colley, J. A., Rodden, T., Ramchurn, S. D., and Jennings, N. R. (2014). Doing the laundry with agents: a field trial of a future smart energy system in the home. In *Proceedings of the SIGCHI Conference on Human Factors in Computing Systems* (Toronto Ontario Canada: ACM), 813–822.

Cui, C., Wang, C., Dong, X., and An, Z. (2021). Intelligent Mobile body temperature monitoring & management system for nursing home. In *2021 IEEE 6th International Conference on Computer and Communication Systems* (ICCCS) (Chengdu, China: IEEE), 812–818.

De Luca, A., and Flacco, F. (2012). Integrated control for pHRI: collision avoidance, detection, reaction and collaboration. In *2012 4th IEEE RAS & EMBS International Conference on Biomedical Robotics and Biomechatronics (BioRob)* (Rome, Italy: IEEE), 288–295.

Dubowsky, S., Genot, F., Godding, S., Kozono, H., Skwersky, A., Haoyong, Y., et al. (2000). PAMM—a robotic aid to the elderly for mobility assistance and monitoring: a "helping-hand" for the elderly. In *Proceedings 2000 ICRA. Millennium conference. IEEE international conference on robotics and Automation*. Symposia proceedings (cat. No.00CH37065) (San Francisco, CA, USA: IEEE), 570–576.

Esposito, R., Cavallo, F., Marcellini, F., Bevilacqua, R., Felici, E., and Dario, P. (2014). *Robot-era project: Preliminary results of robotic services in smart environments with elderly people* (Bucharest, Romania: AAL Forum).

Etemad-Sajadi, R., and Gomes Dos Santos, G. (2019). Senior citizens' acceptance of connected health technologies in their homes. *Int. J. Health Care Qual. Assur.* 32, 1162–1174. doi: 10.1108/IJHCQA-10-2018-0240

Fan, Z., Meng, L., Chen, T. Q., Li, J., and Mitchell, I. M. (2018). Learning motion predictors for smart wheelchair using autoregressive sparse Gaussian process. In *2018 IEEE international conference on robotics and Automation (ICRA)* (Brisbane, QLD: IEEE), 713–718.

Flacco, F., Kroger, T., De Luca, A., and Khatib, O. (2012). A depth space approach to human-robot collision avoidance. In *2012 IEEE international conference on robotics and Automation* (Saint Paul, MN: IEEE), 338–345.

Fong, T., Nourbakhsh, I., and Dautenhahn, K. (2003). Infant-like social interactions between a robot and a human. *Robot. Auton. Syst.* 42, 143–166. doi: 10.1016/S0921-8890(02)00372-X

Frennert, S., Östlund, B., and Eftring, H. (2012). "Would granny let an assistive robot into her home?" in *Social robotics lecture notes in computer science*. eds. S. S. Ge, O. Khatib, J.-J. Cabibihan, R. Simmons and M.-A. Williams (Berlin, Heidelberg: Springer Berlin Heidelberg), 128–137.

Fujita, M. (2004). On activating human communications with pet-type robot AIBO. *Proc. IEEE* 92, 1804–1813. doi: 10.1109/JPROC.2004.835364

Geravand, M., Flacco, F., and De Luca, A. (2013). Human-robot physical interaction and collaboration using an industrial robot with a closed control architecture. In *2013 IEEE international conference on robotics and Automation* (Karlsruhe, Germany: IEEE), 4000–4007.

Ghazali, A. S., Ham, J., Barakova, E. I., and Markopoulos, P. (2018). Effects of robot facial characteristics and gender in persuasive human-robot interaction. *Front. Robot. AI* 5:73. doi: 10.3389/frobt.2018.00073

Gonzalez-Aguirre, J. A., Osorio-Oliveros, R., Rodríguez-Hernández, K. L., Lizárraga-Iturralde, J., Morales Menendez, R., Ramírez-Mendoza, R. A., et al. (2021). Service robots: trends and technology. *Appl. Sci.* 11:10702. doi: 10.3390/app112210702

Goodrich, M. A., and Schultz, A. C. (2007). People detection and mapping system for a mobile robpeople detection and mapping system for a mobile rob. *FNT in Human-Computer Interaction* 1, 203–275. doi: 10.1561/1100000005

Guo, S., Yi, Y., and Liu, Y.Hebei University of Technology. (2019). Human body posture recognition system for back-hugging mobile nursing robot. Chinese patent CN 109910024A.

Hans, M., Graf, B., and Schraft, R. D. (2002). Robotic home assistant care-O-bot: past-present-future. In *Proceedings. 11th IEEE international workshop on robot and human interactive communication* (Berlin, Germany: IEEE), 380–385.

Hargrove, L. J., Englehart, K., and Hudgins, B. (2007). A comparison of surface and intramuscular myoelectric signal classification. *IEEE Trans. Biomed. Eng.* 54, 847–853. doi: 10.1109/TBME.2006.889192

Haring, K. S., Watanabe, K., and Mougenot, C. (2013). The influence of robot appearance on assessment. In *2013 8th ACM/IEEE International Conference on Human-Robot Interaction (HRI)* (Tokyo, Japan: IEEE), 131–132.

He, Z., Yuan, F., Chen, D., and Wang, M. (2019). Ergonomic Design of Multi-functional Bathing Robot. In: *2019 IEEE International Conference on Real-time Computing and Robotics (RCAR)* (Irkutsk, Russia: IEEE), 580–585.

Heerink, M., Krose, B., Evers, V., and Wielinga, B. (2006). The influence of a Robot's social abilities on acceptance by elderly users. In: *ROMAN 2006—the 15th IEEE international symposium on robot and human interactive communication* (Hatfield: IEEE), 521–526.

Heinzmann, J., and Zelinsky, A. (2003). Quantitative safety guarantees for physical human-robot interaction. *Int J Robot Res* 22, 479–504. doi: 10.1177/02783649030227004

Hirsch, T., Forlizzi, J., Hyder, E., Goetz, J., Kurtz, C., and Stroback, J. (2000). The ELDer project: social, emotional, and environmental factors in the design of eldercare technologies. In *Proceedings on the 2000 conference on universal usability—CUU '00* (Arlington, Virginia, United States: ACM Press), 72–79.

Huet, C., and Mastroddi, F. (2016). Autonomy for underwater robots—a European perspective. *Auton. Robot.* 40, 1113–1118. doi: 10.1007/s10514-016-9605-x

Hung, L., Liu, C., Woldum, E., Au-Yeung, A., Berndt, A., Wallsworth, C., et al. (2019). The benefits of and barriers to using a social robot PARO in care settings: a scoping review. *BMC Geriatr.* 19:232. doi: 10.1186/s12877-019-1244-6

Ishii, S. (2003). Meal-assistance robot "my spoon.". *J Robot Soc Japan* 21, 378–381. doi: 10.7210/jrsj.21.378

Jibo, (2023). *ROBOTS: Your Guide to the World of Robotics*. Available at: https://robotsguide.com/robots/jibo (Accessed November 20, 2023).

Joosse, M. P., Poppe, R. W., Lohse, M., and Evers, V. (2014). Cultural differences in how an engagement-seeking robot should approach a group of people. In *Proceedings of the 5th ACM international conference on collaboration across boundaries: culture, distance & technology* (Kyoto Japan: ACM), 121–130.

Joosse, M., Sardar, A., Lohse, M., and Evers, V. (2013). BEHAVE-II: the revised set of measures to assess users' attitudinal and behavioral responses to a social robot. *Int J of Soc Robotics* 5, 379–388. doi: 10.1007/s12369-013-0191-1

Khatib, O. (1986). "Real-time obstacle avoidance for manipulators and Mobile robots" in *Autonomous robot vehicles*. eds. I. J. Cox and G. T. Wilfong (New York, NY: Springer New York), 396–404.

Kim, Y.-J., Kim, J.-I., and Jang, W. (2018). Quaternion joint: dexterous 3-DOF joint representing quaternion motion for high-speed safe interaction. In *2018 IEEE/RSJ international conference on intelligent robots and systems (IROS)* (Madrid: IEEE), 935–942.

King, C.-H., Chen, T. L., Jain, A., and Kemp, C. C. (2010). Echnology for long-term care in 2010 *IEEE/RSJ International Conference on Intelligent Robots and Systems* (Taipei: IEEE), 319–324.

Kittmann, R., Fröhlich, T., Schäfer, J., Reiser, U., Weißhardt, F., and Haug, A. (2015). "Let me Introduce Myself: I am Care-O-bot 4, a Gentleman Robot," in *Let me Introduce Myself: I am Care-O-bot 4, a Gentleman Robot* (Berlin, Germany: De Gruyter), 223–232. doi: 10.1515/9783110443929-024

Kovács, B., Szayer, G., Tajti, F., Burdelis, M., and Korondi, P. (2016). A novel potential field method for path planning of mobile robots by adapting animal motion attributes. *Robot. Auton. Syst.* 82, 24–34. doi: 10.1016/j.robot.2016.04.007

Kusuda, Y. (2009). In quest of mobility – Honda to develop walking assist devices. *Industr Robot* 36, 537–539. doi: 10.1108/01439910910994597

Lasota, P. A., Rossano, G. F., and Shah, J. A. (2014). Toward safe close-proximity human-robot interaction with standard industrial robots. In *2014 IEEE international conference on Automation science and engineering (CASE)* (Taipei: IEEE), 339–344.

Lasota, P. A., and Shah, J. A. (2015). Analyzing the effects of human-aware motion planning on close-proximity human-robot collaboration. *Hum. Factors* 57, 21–33. doi: 10.1177/0018720814565188

Le, N.-T., and Wartschinski, L. (2018). A cognitive assistant for improving human reasoning skills. *Int J Hum Comput Stud* 117, 45–54. doi: 10.1016/j.ijhcs.2018.02.005

Lee, I. (2021). Service robots: a systematic literature review. *Electronics* 10:2658. doi: 10.3390/electronics10212658

Li, C. (2013). The research and design on human facial recognizing system of service robot. Master's thesis. Lanzhou university of technology.

Li, Z., Li, J., and Li, Z.Kangli Medical Equipment Technology Co., Ltd. (2012). Robot nursing bed. Chinese patent CN 202459018U.

Li, Q., Liu, R., Yuan, H., Song, Y., and Fang, Y., (2017). Nursing shampoo robot. Chinese patent CN 201721132158X.

Liftware, L. (2021). 5 awesome inventions to reduce troublesome parkinson's tremors. Available at: http://parkinsonslife.eu/5-awesome-inventions-to-reduce-troublesome-parkinsons-tremors/ (Accessed 6 May 2023).

Liu, X. (2015). Service robot's affective computing based on facial expression cognition. Doctoral thesis. University of Science and Technology Beijing.

Liu, J., Zhang, S., and Sun, Y. (2016). Technology and system of service robots for smart home and intelligent life. *Integrat Technol* 5, 38–46.

Lloyd, D. G., and Besier, T. F. (2003). An EMG-driven musculoskeletal model to estimate muscle forces and knee joint moments in vivo. *J. Biomech.* 36, 765–776. doi: 10.1016/S0021-9290(03)00010-1

Lu, D. (2017). Task understanding for service robots. Doctoral thesis. University of University of Science and Technology of China.

Luo, Y. (2005). The treatment principle and common faults of CLINITRONII suspension bed. *Chin Med J Peking* 94:62. doi: 10.3969/j.issn.1003-8868.2005.08.062

Luo, Y., Xie, H., and Zhang, Y. (2012). Design and implementation of intelligent wheelchair gesture control system based on Kinect sensor. *Robot* 34, 110–113 119. doi: 10.3724/SP.J.1218.2012.00110

Mainprice, J., Akin Sisbot, E., Jaillet, L., Cortes, J., Alami, R., and Simeon, T. (2011). Planning human-aware motions using a sampling-based costmap planner. In 2011 *IEEE international conference on robotics and Automation* (Shanghai, China: IEEE), 5012–5017.

Marder-Eppstein, E., Berger, E., Foote, T., Gerkey, B., and Konolige, K. (2010). Designing sociable robots. In *2010 IEEE international conference on robotics and Automation* (Anchorage, AK: IEEE), 300–307.

MARIO (2021). Managing active and healthy aging with use of caring service robots. Available at: http://www.mario-project.eu/portal/ (Accessed 6 May 2023).

Martinez-Martin, E., Costa, A., and Cazorla, M. (2019). Pharos 2.0—a physical assistant robot system improved. *Sensors* 19:4531. doi: 10.3390/s19204531

Matsumoto, O., Komoriya, K., Toda, K., Goto, S., Hatase, T., and Nishimura, H. (2006). Autonomous traveling control of the "TAO Aicle" Intelligent wheelchair. In *2006 IEEE/RSJ international conference on intelligent robots and systems* (Beijing, China: IEEE), 4322–4327.

McGinn, C., Bourke, E., Murtagh, A., Donovan, C., Lynch, P., Cullinan, M. F., et al. (2020). Meet Stevie: a socially assistive robot developed through application of a 'design-thinking' approach. *J. Intell. Robot. Syst.* 98, 39–58. doi: 10.1007/s10846-019-01051-9

Mertz, L. (2012). The next generation of exoskeletons: lighter, cheaper devices are in the works. *IEEE Pulse* 3, 56–61. doi: 10.1109/MPUL.2012.2196836

Miseikis, J., Caroni, P., Duchamp, P., Gasser, A., Marko, R., Miseikiene, N., et al. (2020). Lio-a personal robot assistant for human-robot interaction and care applications. *IEEE Robot Automat Lett* 5, 5339–5346. doi: 10.1109/LRA.2020.3007462

Mohebbi, A. (2020). Human-robot interaction in rehabilitation and assistance: a review. *Curr Robot Rep* 1, 131–144. doi: 10.1007/s43154-020-00015-4

Morales, Y., Watanabe, A., Ferreri, F., Even, J., Ikeda, T., Shinozawa, K., et al. (2015). Including human factors for planning comfortable paths. In *2015 IEEE international conference on robotics and Automation (ICRA)* (Seattle, WA, USA: IEEE), 6153–6159.

My Website (2023). Available at: https://cataliahealth.com/ (Accessed November 21, 2023).

Nakashima, T., Fukutome, G., and Ishii, N. (2010). Healing effects of pet robots at an elderly-care facility. In *2010 IEEE/ACIS 9th international conference on computer and information science* (Yamagata, Japan: IEEE), 407–412.

Nani, M., Caleb-Solly, P., Dogramadgi, S., Fear, C., and Heuvel, H. (2010). *MOBISERV: An integrated intelligent home environment for the provision of health, nutrition and mobility services to the elderly*. The 4th Companion Robotics Institute (Brussels).

Negro, F., Muceli, S., Castronovo, A. M., Holobar, A., and Farina, D. (2016). Multi-channel intramuscular and surface EMG decomposition by convolutive blind source separation. *J. Neural Eng.* 13:026027. doi: 10.1088/1741-2560/13/2/026027

Neumann, D. (2016). *Human assistant robotics in Japan—challenges and opportunities for European companies*. Tokyo: EU–Japan Centre for Industrial Cooperation.

Nikolaidis, S., Ramakrishnan, R., Gu, K., and Shah, J. (2015). Efficient model learning from joint-action demonstrations for human-robot collaborative tasks. In *Proceedings of the Tenth Annual ACM/IEEE International Conference on Human-Robot Interaction* (Portland Oregon USA: ACM), 189–196.

Nikolaidis, S., and Shah, J. (2013). Human-robot cross-training: computational formulation, modeling and evaluation of a human team training strategy. In *2013 8th ACM/IEEE International Conference on Human-Robot Interaction (HRI)* (Tokyo, Japan: IEEE), 33–40.

Obaid, M., Sandoval, E. B., Zlotowski, J., Moltchanova, E., Basedow, C. A., and Bartneck, C. (2016). Stop! That is close enough. How body postures influence human-robot proximity. In *2016 25th IEEE international symposium on robot and human interactive communication (RO-MAN)* (New York, NY, USA: IEEE), 354–361.

Panasonic's Autonomous Delivery Robot - HOSPI(R) (2023). *Panasonic Newsroom Global*. Available at: https://news.panasonic.com/global/topics/5001 (Accessed November 21, 2023).

Perez-D'Arpino, C., and Shah, J. A. (2015). Fast target prediction of human reaching motion for cooperative human-robot manipulation tasks using time series classification. In *2015 IEEE international conference on robotics and Automation (ICRA)* (Seattle, WA, USA: IEEE), 6175–6182.

Perez-Marcos, D., Bieler-Aeschlimann, M., and Serino, A. (2018). Virtual reality as a vehicle to empower motor-cognitive neurorehabilitation. *Front. Psychol.* 9:2120. doi: 10.3389/fpsyg.2018.02120

Pilotto, A., Boi, R., and Petermans, J. (2018). Technology in geriatrics. *Age Ageing* 47, 771–774. doi: 10.1093/ageing/afy026

Qian, Z., Cao, H., and Zhang, G.Xinfeng Medical Device Co., Ltd. (2010). Nursing machine (XFCS-A). Chinese patent CN 301500132S.

RIBA-II (2021). The next generation care-giving robot. Available at: http://www.riken.jp/en/pr/press/2011/20110802_2/ (Accessed 6 May 2023).

Rincon, J. A., Costa, A., Carrascosa, C., Novais, P., and Julian, V. (2019). EMERALD—exercise monitoring emotional assistant. *Sensors* 19:1953. doi: 10.3390/s19081953

Roy, N., Baltus, G., Fox, D., Gemperle, F., Goetz, J., Hirsch, T., et al. (2000). *Towards personal service robots for the elderly Workshop on Interactive Robots and Entertainment*. 25, 184.

Rusu, R. B., Sucan, I. A., Gerkey, B., Chitta, S., Beetz, M., and Kavraki, L. E. (2009). Real-time perception-guided motion planning for a personal robot. In *2009 IEEE/RSJ International Conference on Intelligent Robots and Systems* (St. Louis, MO: IEEE), 4245–4252.

Sabanovic, S., Bennett, C. C., Chang, W.-L., and Huber, L. (2013). PARO robot affects diverse interaction modalities in group sensory therapy for older adults with dementia. In *2013 IEEE 13th International Conference on Rehabilitation Robotics (ICORR)* (Seattle, WA: IEEE), 1–6.

Saunders, J., Burke, N., Koay, K., and Dautenhahn, K. (2013). A user friendly robot architecture for re-ablement and co-learning in a sensorised home. *Assist Technol Res Series* 33, 49–58. doi: 10.3233/978-1-61499-304-9-49

Sharkawy, A.-N., Koustoumpardis, P. N., and Aspragathos, N. (2020). Human–robot collisions detection for safe human–robot interaction using one multi-input–output neural network. *Soft. Comput.* 24, 6687–6719. doi: 10.1007/s00500-019-04306-7

Shi, C. (2014). The dynamic optimization and a new structure of the nursing bed robot. Master's thesis. Dalian Jiaotong University.

Sisbot, E. A., and Alami, R. (2012). A human-aware manipulation planner. *IEEE Trans. Robot.* 28, 1045–1057. doi: 10.1109/TRO.2012.2196303

Sixsmith, A. (2013). *Technologies for active aging*. New York: Springer.

Stefanie, B., Thorsten, K., Schall, A., Saskia, R., Stefanie, S., Ziyon, K., et al. (2017). Acceptance of social robots by Elder people: does psychosocial functioning matter? *Int. J. Soc. Robot.* 9, 293–307. doi: 10.1007/s12369-016-0392-5

Tak, S. H., Benefield, L. E., and Mahoney, D. F. (2010). Learning motion predictors for smart wheelchair using autoregressive sparse gaussian proce. *Res. Gerontol. Nurs.* 3, 61–72. doi: 10.3928/19404921-20091103-01

Toyota Research Institute (2021). T-HR3 and busboy. Available at: https://www.tri.global/our-work/robotics/ (Accessed 6 May 2023).

United Nations (2019). *World population prospects 2019: highlights*. New York (US): United Nations Department for Economic and Social Affairs.

United Nations Department for Economic and Social Affairs (2023). *World population prospects 2022: Summary of results*. S.l.: United Nations.

Vallery, H., Veneman, J., van Asseldonk, E., Ekkelenkamp, R., Buss, M., and van Der Kooij, H. (2008). Compliant actuation of rehabilitation robots. *IEEE Robot Automat Magaz* 15, 60–69. doi: 10.1109/MRA.2008.927689

Vercelli, A., Rainero, I., Ciferri, L., Boido, M., and Pirri, C. F. (2018). Robots in elderly care. *DigitCult. Sci J Digit Cult*, 2, 37–50. doi: 10.4399/97888255088954

Vogel, J., Leidner, D., Hagengruber, A., Panzirsch, M., Bauml, B., Denninger, M., et al. (2021). An ecosystem for heterogeneous robotic assistants in caregiving: Core functionalities and use cases. *IEEE Robot. Automat. Mag.* 28, 12–28. doi: 10.1109/MRA.2020.3032142

Wang, H., He, X., Liu, Z., Yu, H., Hu, G., Zhang, Y., et al., (2016a). Modular transfer nursing robot. Chinese patent CN 106625707B.

Wang, H., Jie, L., Niu, J., Liu, Z., He, X., Li, D., et al., (2016b). Bidirectional transfer nursing robot. Chinese patent CN 106580602B.

Wang, W., Liu, N., Li, R., Chen, Y., and Jia, Y. (2018). "HuCoM: a model for human comfort estimation in personalized human-robot collaboration. In volume 2: control and optimization of connected and automated ground vehicles; dynamic systems and control education; dynamics and control of renewable energy systems; energy harvesting; energy systems; estimation and identification" in *Intelligent transportation and vehicles; manufacturing; mechatronics; modeling and control of IC engines and Aftertreatment systems; modeling and control of IC engines and powertrain systems; modeling and Management of Power Systems* (Atlanta, Georgia, USA: American Society of Mechanical Engineers), V002T23A006.

Wolfe, J., Marthi, B., and Russell, S. (2021). Combined task and motion planning for Mobile manipulation. *ICAPS* 20, 254–257. doi: 10.1609/icaps.v20i1.13436

World Health Organization (2022). *Global report on health equity for persons with disabilities*. Geneva: World Health Organization.

Wu, J. (2020). Design and active-passive safety control of nursing task-oriented heavy-duty manipulator. Master's thesis. Harbin Institute of Technology.

Wu, D., Gao, X., Xie, Z., and Xu, Z. (2021). What long-term care interventions have been published between 2010 and 2020? Results of a WHO scoping review identifying long-term care interventions for older people around the world. *IJERPH* 18:389. doi: 10.3390/ijerph18020389

Xin, S. J., and Zhang, H. H. (2010). The dynamic optimization and a new structure of the nursing bed robot. *KEM* 426–427, 352–355. doi: 10.4028/www.scientific.net/KEM.426-427.352

Xu, W., Huang, J., An, J., Wang, Y., and Tao, C. (2016). Research on walking-aid robot motion control with both compliance and safety. *Chin J Sci Instru* 42, 1859–1873. doi: 10.16383/j.aas.2016.c160163

Xu, P., Yu, H., and Shi, P. (2020). Development a smart feeding assistive robot for eating assist. *Comput Engineer Softw* 41, 56–59. doi: 10.3969/j.issn.1003-6970.2020.09.015

Yanco, H. A. (1998). "Wheelesley: A robotic wheelchair system: Indoor navigation and user interface," in *Assistive Technology and Artificial Intelligence (Springer*, Berlin, Heidelberg: Springer-Verlag), 256–268. doi: 10.1007/BFb0055983

Young, J. E., Hawkins, R., Sharlin, E., and Igarashi, T. (2009). Toward acceptable domestic robots: applying insights from social psychology. *Int J of Soc Robotics* 1, 95–108. doi: 10.1007/s12369-008-0006-y

Yu, C. (2019). Research on human-machine cooperation control system of excretion support robot. Master's thesis. Shenyang University of Technology. Master's thesis. Henan University of Science and Technology.

Zhang, J. (2015). Design and implementation of obstacle avoidance and target tracking system for intelligent wheelchair. Master's thesis. Shanghai Jiao Tong University.

Zhang, H., Bai, J., and Zhou, Z. (2011). Robot nursing bed. Chinese patent CN102429795B.

Zhang, T., Xie, C., and Li, L. (2006). Research on tele-monitoring system and control Sytem of intelligent nursing bed based on network. In *2006 6th world congress on intelligent control and Automation* (Dalian, China: IEEE), 9434–9438.

Zhao, D. (2020). Interaction method of multiple welfare-robots oriented to safe transfer tasks. Doctoral thesis. Shenyang University of Technology.

Zhao, D., Yang, J., Okoye, M. O., and Wang, S. (2019). Walking assist robot: a novel non-contact abnormal gait recognition approach based on extended set membership filter. *IEEE Access* 7, 76741–76753. doi: 10.1109/ACCESS.2019.2922258

Zhao, D., Yang, J., Wang, Y., and Wang, Y. (2017). Fuzzy system based on the rule evolution strategy for directional intention identification of walking. *Chin J Sci Instru* 38, 2615–2625. doi: 10.3969/j.issn.0254-3087.2017.11.001

Zhao, X., Yao, J., Ma, L., Zhang, B., Xu, Z., and Zhao, M. (2019). A control method of hand rehabilitation robot based on Semg. Chinese patent CN 111973388A.

Zorarobotic (2021). Zora. Available at: https://www.zorarobotics.be/ (Accessed 6 May 2023).

frontiers | Frontiers in Neuroscience

TYPE Original Research
PUBLISHED 31 January 2024
DOI 10.3389/fnins.2024.1337580

Adaptive control for shape memory alloy actuated systems with applications to human–robot interaction

Enming Shi[1,2,3], Xu Zhong[4], Tian Wang[5]*, Xiaoguang Li[6], Chunguang Bu[1,2] and Xingang Zhao[1,2,3]*

[1]State Key Laboratory of Robotics, Shenyang Institute of Automation, Chinese Academy of Sciences, Shenyang, Liaoning, China, [2]Institutes for Robotics and Intelligent Manufacturing, Chinese Academy of Sciences, Shenyang, Liaoning, China, [3]University of Chinese Academy of Sciences, Beijing, China, [4]Medical Engineering Department, Affiliated Hospital of Yangzhou University, Yangzhou, Jiangsu, China, [5]The Fourth Affiliated Hospital of China Medical University, Shenyang, China, [6]School of Intelligent Manufacturing, Huzhou College, Zhejiang, China

Introduction: Shape memory alloy (SMA) actuators are attractive options for robotic applications due to their salient features. So far, achieving precise control of SMA actuators and applying them to human-robot interaction scenarios remains a challenge.

Methods: This paper proposes a novel approach to deal with the control problem of a SMA actuator. Departing from conventional mechanism models, we attempt to describe this nonlinear plant using a gray-box model, in which only the input current and the output displacement are measured. The control scheme consists of the model parameters updating and the control law calculation. The adaptation algorithm is founded on the multi-innovation concept and incorporates a dead-zone weighted factor, aiming to concurrently reduce computational complexities and enhance robustness properties. The control law is based on a PI controller, the gains of which are designed by the pole assignment technique. Theoretical analysis proves that the closed-loop performance can be ensured under mild conditions.

Results: The experiments are first conducted through the Beckhoff controller. The comparative results suggest that the proposed adaptive PI control strategy exhibits broad applicability, particularly under load variations. Subsequently, the SMA actuator is designed and incorporated into the hand rehabilitation robot. System position tracking experiments and passive rehabilitation training experiments for various gestures are then conducted. The experimental outcomes demonstrate that the hand rehabilitation robot, utilizing the SMA actuator, achieves higher position tracking accuracy and a more stable system under the adaptive control strategy proposed in this paper. Simultaneously, it successfully accommodates hand rehabilitation movements for multiple gestures.

Discussion: The adaptive controller proposed in this paper takes into account both the computational complexity of the model and the accuracy of the control results, Experimental results not only demonstrate the practicality and reliability of the controller but also attest to its potential application in human-machine interaction within the field of neural rehabilitation.

KEYWORDS

adaptive control, SMA actuator, gray-box model, robustness, hand rehabilitation robots

EDITED BY
Benyan Huo,
Zhengzhou University, China

REVIEWED BY
Yu Dang,
Nankai University, China
Shuchen Ding,
Suzhou University of Science and Technology, China

*CORRESPONDENCE
Tian Wang
✉ wangtian@cmu.edu.cn
Xingang Zhao
✉ zhaoxingang@sia.cn

RECEIVED 13 November 2023
ACCEPTED 04 January 2024
PUBLISHED 31 January 2024

CITATION
Shi E, Zhong X, Wang T, Li X, Bu C and Zhao X (2024) Adaptive control for shape memory alloy actuated systems with applications to human−robot interaction. *Front. Neurosci.* 18:1337580. doi: 10.3389/fnins.2024.1337580

1 Introduction

Shape memory alloy (SMA) actuators present numerous advantageous features, including excellent volume output ratios, low driving voltages, and noiseless and clean actuations (Shi et al., 2017). These attributes render SMA actuators appealing choices for rehabilitation robotic systems. The inherent shape memory effects of SMAs allow them to revert to predefined shapes upon proper heating. Nevertheless, these effects introduce nonlinearities, parameter uncertainties, and hysteresis into the control problem (Wiest and Buckner, 2014). As of now, achieving precise control of SMA actuators remains an unresolved and highly relevant challenge, serving as the primary motivation for this study.

In the literature, a particularly intuitive approach involves the design of controllers based on mechanism models. Romano and Tannuri (2009) exemplified this approach by creating a mechanical actuator using SMA. The mechanism model, derived from experimental setups, encompasses a thermal model, a phase transformation model, and a description of the mechanical properties and dynamics of the system. Elahinia and Ashrafiuon (2002) developed a sliding mode control (SMC) method based on a mechanism model. Given that this control law necessitates full state feedback, the extended Kalman filter is employed to update the unmeasurable states. In Ashrafiuon and Jala (2009), this approach was implemented in a three-degrees-of-freedom robotic manipulator. Zakerzadeh and Sayyaadi (2013) investigated hysteresis behaviors and integrated a feed-forward controller into an adaptive controller, relying on the inverse of the hysteresis model. Riccardi et al. (2013) addressed magnetic SMA actuators, introducing a novel technique to compensate for hysteresis nonlinearity. In a related context, Pai et al. (2017) proposed a force control strategy grounded in the mechanism model. Despite the contributions, mechanism model-based controllers have limitations: (a) the structures of mechanism models are often very complex; (b) updating model parameters recursively is quite challenging, and they typically remain fixed for online implementation; (c) the inverse hysteresis models are also very intricate and lack adaptability.

As an alternative, neural network models have attracted attention due to their approximation accuracy and structural flexibility. Tai and Ahn (2010) introduced a model for an SMA actuator based on radial basis function neural networks, with parameters updated through online learning. Nikdel et al. (2014) compared the neural model predictive control method with the SMC approach. In a related context, Son and Anh (2015) proposed an adaptive feed-forward neural network model to compensate for hysteresis nonlinearity. The model proposed by Son and Anh (2015) is constructed by integrating multi-layer perceptron neural networks with a linear model. Tai and Ahn (2012) combined the advantages of a direct adaptive controller with neural network approximations, showcasing effectiveness in compensating for hysteresis and ensuring reliable robustness. In a related context, Wiest and Buckner (2014) tackled antagonistic SMA systems using a hysteretic recurrent neural network. Meanwhile, Pan et al. (2017) focused on a novel SMA actuator designed with reduced total stiffness and increased compliance. Neural networks are utilized to model this nonlinear plant. The effectiveness of the adaptive observer-based output-feedback controller in handling load changes is demonstrated. However, despite these merits, several key issues still need to be addressed: (a) online training of neural networks may face challenges associated with local minima; (b) conducting robust stability analysis for systems based on neural networks has proven to be difficult; (c) controllers based on neural networks often involve significant computational complexities and may be impractical for specific applications.

On the other hand, the pseudoelasticity and shape memory effect (SME) of SMA hold significant application value in neurology and neuromuscular rehabilitation applications (Pittaccio et al., 2015). Specifically, pseudoelasticity has been proposed in various studies, including limb positioning and gait rehabilitation (Viscuso et al., 2009; Deberg et al., 2014; Mataee et al., 2015). In these studies, the adaptability, deformability, and nonlinear mechanical properties of SMA are considered effective in addressing clinical issues associated with spasticity and paralysis. Similarly, SME can provide the foundational characteristics for the design of neural rehabilitation devices, including quasi-constant stress levels and a larger range of deformation, and these parameters can be manipulated through thermomechanical processing for structural design and repair (Pittaccio et al., 2015). SME also enables the SMA to integrate the sensor with actuator which can simplify the structure (Wang et al., 2021). In addition, SMA actuators are frictionless, quiet, corrosion-resistant, offer an extended fatigue life, and demonstrate high damping and resistivity (Kumbhar et al., 2017; Shariat et al., 2017). These characteristics reduce actuator complexity, size, and weight. Therefore, several research teams have employed SMA in wearable rehabilitation devices and have devised corresponding system control algorithms. Serrano et al. (2018) introduced an SMA-actuated wrist-based exoskeleton with a lightweight and comfortable design. Additionally, Serrano et al. (2023) developed a flexible exo-glove powered by SMA, capable of executing complex gestures. Jeong et al. proposed a wrist exoskeleton robot driven by SMA springs, featuring a high contraction strain capacity. However, its coil structure is complex, and despite the establishment of a complicated thermodynamic model, the accuracy of the model remains unsatisfactory (Jeong et al., 2019, 2022). Wang et al. (2021) presented a flexible hand motion device powered by SMA wires. This device controls the angle of the robot finger joints by adjusting the duty cycle of the PWM pulses. However, the study does not delve into the robustness considerations of the robot system. Xie et al. (2023) embedded SMA into a conformal material and proposed a hand rehabilitation wearable glove actuated by an SMA-based Soft Composite Structure (SSCS). This structure is characterized by simple actuation and a large force-to-weight ratio. However, its precision in the motion control of the hand is noted to be imprecise. Lai et al. (2023) introduced a hybrid actuator combining a flexible actuator and an SMA spring actuator, integrated into a soft glove. This configuration offers a larger workspace and enhanced output force. However, there is potential for improvement in the tracking accuracy of the control system and the anti-interference capability. Considering the above set of research results, it is clear that ensuring model simplicity and improving the accuracy of control results are extremely challenging issues. They directly affect the overall control effectiveness and practicality of the actuator.

To this end, this paper proposes describing a SMA actuator using a gray-box model. This simple model comprises a first-order discrete linear model and unmodeled dynamics, leveraging measurements of the actuator's input current and output displacement as data-driven components. Only two model parameters are updated online, resulting in a low computational burden. To enhance system robustness and reject disturbances, a novel identification algorithm with a dead-zone weighted factor is introduced. Robust estimation of unmodeled dynamics is necessary, as it can be directly compensated by an adaptive control law. In line with the adaptations, the proportional and differential gains of the PI control law are updated online based on a pre-specified stable characteristic polynomial. The overall adaptive control algorithms are explicit and have been successfully implemented in both the Beckhoff controller and the embedded system. More interestingly, this method proves to be applicable for handling load variations and rejecting disturbances. Furthermore, the integration of the SMA actuator into the hand rehabilitation robot system allows for position tracking experiments and hand rehabilitation training. These experiments are conducted based on the data-driven modeling method and the robust adaptive control strategy proposed in this paper. The most important contribution of this paper is that, oriented to the SMA actuator, a comprehensive method of control system design is proposed, which takes into account both the model computational complexity problem and the control accuracy problem, tries to give a more reasonable solution, and makes this adaptive control technology effectively applied in the rehabilitation robot system.

This paper is organized as follows: the problem formulation and the adaptive controller are proposed in Section 2, the experiments and results are presented in Section 3, a brief summary is given in Section 4, and the closed-loop stability is analyzed in Appendix.

2 Methods

2.1 SMA characteristics

The SME of SMA wires refers to the fact that the unconstrained deformed alloy wire material can be restored to its original shape under the condition of external temperature change (Airoldi et al., 1991). On a microscopic level, the shape memory properties of a SMA wire are caused by changes in its own structure. SMA wires have two main crystal states, a martensitic phase at low temperatures, when the SMA wires have a monoclinic crystal shape inside; The other is the austenite phase at high ambient temperatures, when the material exhibits a cubic crystal structure internally; In addition to these two states, SMA wires also have an R-phase state at intermediate temperatures, when the material has an internal monoclinic crystal structure. The essence of SME is the migration of highly ordered “militarization” of crystal atoms within the SMA wire (Lagoudas and Dimitris, 2008), from monoclinic to cubic crystal structure, and the deformation of the SMA wire is achieved by the change of countless such microcrystal structures, a process known as the martensitic phase transition, as shown in Figure 1.

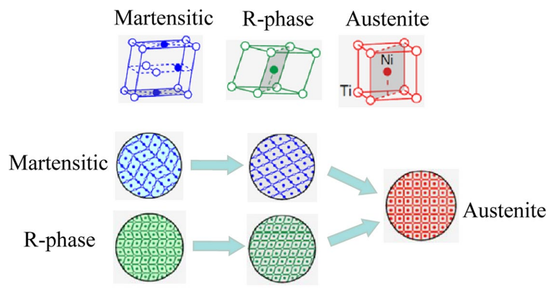

FIGURE 1
Microstructural changes in shape memory alloys.

There are many types of constituent materials of shape memory alloy wires, and the different properties of different materials lead to differences in the shape memory function of SMAs, and researchers have categorized the SME into three types according to the differences in the shape memory function: the single-pass memory effect, the two-pass memory effect, and the whole-pass memory effect (Wu et al., 1996). The SMA wires used in this study were dual-range memory effect SMA wires. Dual-range SMA wires have a shape memory effect when they are deformed and processed, and they change back to their original shape when heated to a certain temperature, and then regain their length when cooled. Different heat treatments during processing also have a great influence on the SMA wires. Figure 2 shows the deformation and temperature curves of SMA wires selected with the same diameter and phase transition temperatures of 70 and 90°C, respectively, in the process of heating and cooling. As depicted in the figure, it is evident that the temperature of deformation increases with the higher temperature of the heat treatment.

2.2 Gray-box model description

Plenty of research has demonstrated a fact that it is almost impossible to precisely capture the nonlinear dynamics of SMA actuators during a relatively wide range. An alternative idea to address the unmodeled dynamics is to compensate the negative effects in the subsequent control problem, rather than copy with it directly in the modeling problem.

In other words, for the modeling aspect of this work, the aim is to approximately capture the main dynamic property of this actuator, based on a computationally efficient model. Later, the adaptive controller will ensure the robust stability despite the unmodeled dynamics.

Let the single-input-single-output SMA actuator be described as a discrete-time nonlinear dynamical system in the following form:

$$y(t+1)=\phi\left[y(t),\ldots,y(t+1-n_a),u(t),\ldots,u(t+1-n_b)\right] \quad (1)$$

where the system output $y(t)$ is the displacement of the SMA wire (unit: m); the system input $u(t)$ is the current signal (unit: A); n_a and n_b are unknown system orders; $\phi[\cdot]$ is a nonlinear function. The origin can be assumed as an equilibrium point.

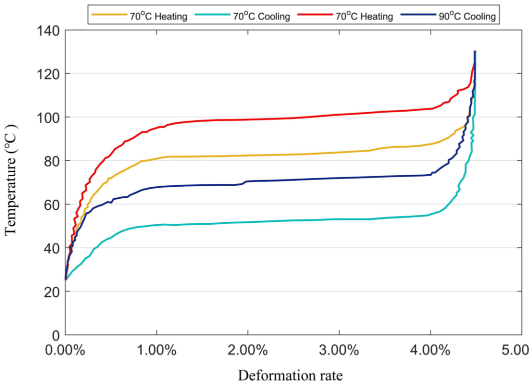

FIGURE 2
Deformation rate of SMA at different phase transition temperatures.

By using Taylor's formula around the origin, the nonlinear system (Equation 1) can be equivalently expressed as a first-order linear model together with unmodeled dynamics:

$$A\left(z^{-1}\right)y\left(t\right)=B\left(z^{-1}\right)u\left(t\right)+\zeta\left(t\right) \tag{2}$$

where $A\left(z^{-1}\right)$ and $B\left(z^{-1}\right)$ are polynomials in the time delay operator $z^{-1}\left\{e.g.z^{-1}u\left(t\right)=u\left(t-1\right)\right\}$ which are defined as:

$$A\left(z^{-1}\right)=1+a_1z^{-1}$$

$$B\left(z^{-1}\right)=b_1z^{-1}$$

where a_1 and b_1 are the uncertain system parameters; $\zeta(t)$ is the unmodeled dynamics, which is unknown and varies due to temperature changes, load variations or other factors.

The system Equation (2) can be written as a compact form

$$y\left(t\right)=\varphi^T\left(t\right)\theta+\zeta\left(t\right) \tag{3}$$

where the parameter vector θ and the regressor vector $\varphi(t)$ are defined as follows:

$$\theta=\left[a_1,b_1\right]^T \tag{4}$$

$$\varphi\left(t\right)=\left[-y\left(t-1\right),u\left(t-1\right)\right]^T \tag{5}$$

Regardless of $\zeta(t)$, the prediction model is considered as:

$$y\left(t+1\right)\triangleq\varphi^T\left(t+1\right)\hat{\theta}\left(t\right) \tag{6}$$

with $\hat{\theta}\left(t\right)$ defined as the estimation of θ:

$$\hat{\theta}\left(t\right)=\left[\hat{a}_1\left(t\right),\hat{b}_1\left(t\right)\right]^T \tag{7}$$

We can approximately capture the main dynamic property of the nonlinear plant by the discrete linear model (Equation 6). Inevitably, there exist modeling errors based on this simple model. But it will be proved in the Appendix that the unmodeled dynamics can be compensated by the proposed PI controller.

2.3 An adaptive control strategy

The utilized PI controller is written as:

$$u\left(t\right)=u\left(t-1\right)+k_P\left[\varepsilon\left(t\right)-\varepsilon\left(t-1\right)\right]+k_I\varepsilon\left(t\right) \tag{8}$$

where k_p and k_I are the proportional and integral gains, and $\varepsilon\left(t\right)=y^*\left(t\right)-y\left(t\right)$ with $y^*\left(t\right)$ defined as the reference.

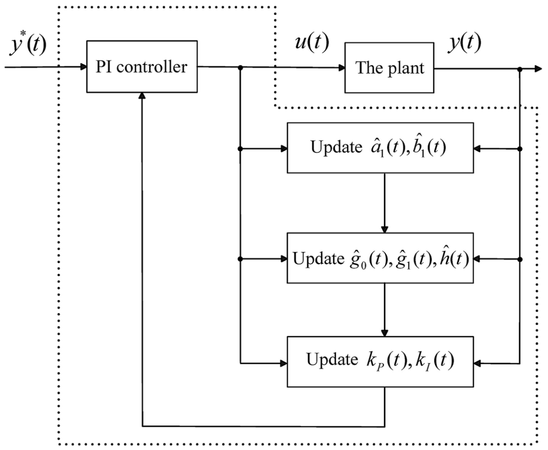

FIGURE 3
The adaptive PI control scheme.

It is desired that the system output tracks the reference, and the robust stability is ensured under uncertainties. The adaptive PI control scheme is briefly depicted in Figure 3, which consists of online parameter adaptation and control law calculation.

2.3.1 Control law for deterministic systems

The above control law can be written in the following form:

$$H\left(z^{-1}\right)u\left(t\right)=G\left(z^{-1}\right)\varepsilon\left(t\right) \tag{9}$$

where $H\left(z^{-1}\right)=h\left(1-z^{-1}\right)$ and $G\left(z^{-1}\right)=g_0+g_1z^{-1}$. Note that the proportional and differential gains in Equation (8) are chosen by the following relation Equation (10).

$$\begin{cases} k_P+k_I=\dfrac{g_0}{h} \\ -k_P=\dfrac{g_1}{h} \end{cases} \tag{10}$$

An effective technique to design the polynomials $H\left(z^{-1}\right)$ and $G\left(z^{-1}\right)$ is based on the pole assignment concept (Goodwin and Sin, 1984).

Applying the controller Equation (8) and combining Equation (3) with Equation (9) yield the closed-loop Equation (11).

$$\begin{aligned}&\left[A\left(z^{-1}\right)H\left(z^{-1}\right)+B\left(z^{-1}\right)G\left(z^{-1}\right)\right]y\left(t+1\right)\\&=B\left(z^{-1}\right)G\left(z^{-1}\right)y^*\left(t\right)+H\left(z^{-1}\right)\zeta\left(t\right)\end{aligned} \tag{11}$$

Let the closed-loop characteristic polynomial be defined as $T\left(z^{-1}\right)=t_0+t_1z^{-1}+t_2z^{-2}$, which has stable poles.

When $A\left(z^{-1}\right)$ and $B\left(z^{-1}\right)$ are completely known, to ensure the closed-loop stability, the polynomials $H\left(z^{-1}\right)$ and $G\left(z^{-1}\right)$ should be designed based on:

$$T\left(z^{-1}\right)=A\left(z^{-1}\right)H\left(z^{-1}\right)+B\left(z^{-1}\right)G\left(z^{-1}\right) \tag{12}$$

From Equations (2), (9), and (12), the coefficients are:

$$h=t_0, g_0=\frac{t_1+t_0-a_1t_0}{b_1}, g_1=\frac{t_2+a_1t_0}{b_1} \tag{13}$$

Further based on Equation (10), the proportional and differential gains k_p and k_I are designed as follows:

$$k_P=-\frac{t_2+a_1t_0}{b_1t_0}, k_I=\frac{t_1+t_2+t_0}{b_1t_0} \tag{14}$$

The above analysis is carried out based on the deterministic model. However, such an assumption is unrealistic for the SMA actuator. Actually, the parameters a_1 and b_1 of the gray-box model are uncertain, and it is difficult to offline choose fixed and appropriate k_p and k_I to ensure the closed-loop stability during the whole operating range. A more reasonable treatment seems to estimate $A\left(z^{-1}\right)$ and $B\left(z^{-1}\right)$ recursively, to update $H\left(z^{-1}\right)$ and $G\left(z^{-1}\right)$ online, and then to calculate k_p and k_I.

2.3.2 Online adaptation algorithm

This subsection presents an online adaptation algorithm for uncertain parameters. Recursive least squares (RLS) algorithm has a fast convergence rate. However, it has high computational complexities, especially when it is applied to the Beckhoff IPC programming. On the other hand, recursive stochastic gradient (RSG) algorithm is more favorable to model adaptations, but it leads to a much slower convergence rate. To this end, a novel recursive estimator will be introduced, which has a similar form as the RSG algorithm, but possesses a similar convergence rate as the RLS algorithm.

The parameter identification will be carried out based on Equation (3). We first impose an assumption on this system.

Assumption 1: The unmodeled dynamics ζ(t) satisfies

$$\left|\zeta(t)\right|\le\Delta \tag{15}$$

where the bound Δ is user-designed.

> Remark 1: This condition is commonly used to improve the robustness performance (Goodwin and Sin, 1984). The unmodeled dynamics can be treated as a bounded disturbance, and the parameter estimation can reject some continuous perturbations. The bound Δ is easy to design according to the control performance.

Then the uncertain parameter estimation vector $\hat{\theta}(t)$ can be updated by the following modified recursive multi-innovation stochastic gradient identification algorithm (Zhang et al., 2008) with a novel dead-zone weighted factor:

$$E(t)=\left[e(t),e(t-1),\ldots,e(t-p+1)\right]^T \tag{16}$$

$$\Phi(t)=\left[\varphi(t),\varphi(t-1),\ldots,\varphi(t-p+1)\right] \tag{17}$$

$$e(t)=y(t)-\varphi^T(t)\hat{\theta}(t-1) \tag{18}$$

$$r(t)=r(t-1)+\left\|\Phi(t)\right\|_2^2 \tag{19}$$

$$\lambda(t)=\begin{cases}1-\dfrac{\sqrt{p\Delta}}{\left\|E(t)\right\|_2}, \text{if } \left\|E(t)\right\|_2>\sqrt{p\Delta}\\ 0, \text{otherwise}\end{cases} \tag{20}$$

$$\hat{\theta}(t)=\hat{\theta}(t-1)+\frac{\varepsilon\lambda(t)\Phi(t)E(t)}{r(t)} \tag{21}$$

where p is the dimension of the extended signals, which is designed by the user; r(0)=1; e(t) is the model error; E(t) is the extended model error; Φ(t) is the extended regressor vector; λ(t) is a nonnegative weighted factor; ε is a user-designed adaptation gain and satisfies 0 < ε ≤ 2 (*Lemma 1* will explain the reason).

> Remark 2: It is seen that when p = 1, the algorithm becomes a RSG one. Ding and Chen (2006) proved that when p increases, the convergence rate of a multi-innovation-based identification algorithm tends to an RLS one. To make a tradeoff between the convergence rate and the computational complexities, we will select p = 3. More interestingly, the update of each parameter can be separated and written in one dimensional form, such as
>
> $$\hat{a}_1(t)=\hat{a}_1(t-1)-\left[\sum_{n=0}^{2}y(t-n-1)e(t-n)\right]\cdot\varepsilon\lambda(t)/r(t).$$

2.3.3 Control law update

Based on Equation (7), the estimated polynomials at instant t can be defined as:

$$\hat{A}\left(t,z^{-1}\right)=1+\hat{a}_1(t)z^{-1} \tag{22}$$

$$\hat{B}\left(t,z^{-1}\right)=\hat{b}_1(t)z^{-1} \tag{23}$$

In order to adaptively design the proportional and differential gains k_p and k_I for the PI control Equation (8), a modified relationship is as follows:

$$\hat{H}\left(t,z^{-1}\right)u(t)=\hat{G}\left(t,z^{-1}\right)\varepsilon(t) \tag{24}$$

where $\hat{H}\left(t,z^{-1}\right)$ and $\hat{G}\left(t,z^{-1}\right)$ are used in place of $H\left(z^{-1}\right)$ and $G\left(z^{-1}\right)$. These two polynomials are defined as:

$$\hat{H}\left(t,z^{-1}\right)=\hat{h}(t)\left(1-z^{-1}\right) \tag{25}$$

$$\hat{G}\left(t,z^{-1}\right)=\hat{g}_0(t)+\hat{g}_1(t)z^{-1} \tag{26}$$

It is desired that the polynomials $\hat{H}\left(t,z^{-1}\right)$ and $\hat{G}\left(t,z^{-1}\right)$ satisfy the following relation:

$$T\left(z^{-1}\right)=\hat{A}\left(t,z^{-1}\right)\hat{H}\left(t,z^{-1}\right)+\hat{B}\left(t,z^{-1}\right)\hat{G}\left(t,z^{-1}\right) \quad (27)$$

where $T\left(z^{-1}\right)=t_0+t_1z^{-1}+t_2z^{-2}$ is a pre-specified characteristic polynomial with stable poles.

Now that the estimates $\hat{a}_1(t)$ and $\hat{b}_1(t)$ are obtained, then the coefficients $\hat{h}(t)$, $\hat{g}_0(t)$, and $\hat{g}_1(t)$ can be updated based on the relation Equation (28):

$$\hat{h}(t)=t_0,\ \hat{g}_0(t)=\frac{t_1+t_0-\hat{a}_1(t)t_0}{\hat{b}_1(t)},\ \hat{g}_1(t)=\frac{t_2+\hat{a}_1(t)t_0}{\hat{b}_1(t)} \quad (28)$$

Similar to Equation (10), now the proportional and differential gains in Equation (8) are chosen by the following relation:

$$\begin{cases} k_P+k_I=\dfrac{\hat{g}_0(t)}{\hat{h}(t)} \\ -k_P=\dfrac{\hat{g}_1(t)}{\hat{h}(t)} \end{cases} \quad (29)$$

which means that k_p and k_I should be designed as:

$$k_P=-\frac{t_2+\hat{a}_1(t)t_0}{\hat{b}_1(t)t_0},\ k_I=\frac{t_1+t_2+t_0}{\hat{b}_1(t)t_0} \quad (30)$$

From Equation (30), it is found that $\hat{b}_1(t)$ appears in the denominator. In order to ensure the smoothness of the control law, we impose a constrain on $\hat{b}_1(t)$:

$$\hat{b}_1(t)=\begin{cases} \hat{b} & if\ \hat{b}_1(t)\le\hat{b} \\ \hat{b}_1(t) & else \end{cases} \quad (31)$$

where $\hat{b}$ is a pre-specified upper bound. It is noted that such treatment has no negative effect on the convergence or stability properties (Chen et al., 2001).

The proposed PI controller can be implemented as follows:

Step 1: Update $\hat{a}_1(t)$ and $\hat{b}_1(t)$ by Equations (16)–(21);
Step 2: Calculate $\hat{h}(t)$, $\hat{g}_0(t)$ and $\hat{g}_1(t)$ by Equation (28);
Step 3: Calculate k_p and k_I by Equation (30);
Step 4: Calculate $u(t)$ by Equation (8);
Step 5: Let $t=t+1$ and apply $u(t)$ to the plant.

2.4 Human–robot interaction control framework

The integration of voluntary participation and mechanical assistance in robot-assisted rehabilitation for hand rehabilitation is also crucial. Therefore, a SMA actuator-based rehabilitation robotic system is needed to not only perform motion-guided training for functional rehabilitation of patients with impaired hand function, but also to assist and collaborate with the patient's preserved motor abilities to achieve on-demand assistance. Therefore, collaboration and interaction between the patient and the rehabilitation robot during human–robot interaction is a major challenge for the control system. To address this challenge, we plan to propose a fusion human–robot-environment interaction control framework that incorporates multi-level control research techniques. The framework for human–robot-environment cohesive interaction control strategy is shown in Figure 4.

The intention for motion is generated by the user themselves, requiring the recognition of human intent. User states include the body's posture, velocity, and the physical interactions between the user, environment, and devices. The external environment comprises spatial features and terrain, which the controller can also perceive and take into consideration. At the high level, the controller needs to perceive human intent, recognize mental thoughts, and perform pattern recognition for gesture activities such as clenching fists or bending fingers. In the mid-level, the user's intent is translated into the desired state of the device by adjusting controller gains, switching models, or tuning model parameters. At the low level, the device's controller and specific control algorithms are responsible for realizing the desired device state and achieving compliant motion control of the hand rehabilitation robot. Finally, the SMA actuators-based hand rehabilitation robot executes control commands to achieve hand rehabilitation for the user. The hand rehabilitation robot system could also provide artificial sensory feedback in combination with pre-set electrical stimulation, etc.

In the research conducted in this paper, our proposed adaptive control method focuses on robust adaptive control at the low level controller of the SMA actuator-based hand rehabilitation robots. This method ensures stability and practicality during human–robot interactions. The experimental verification process will be presented in the following sections. It is worth pointing out that in our proposed control framework for human–robot interaction, the research methods related to mid-level and high-level control are already relatively mature. For instance, our research team has proposed a continuous estimation method for upper limb multi-joint motions based on sEMG (Ding et al., 2016). Moreover, deep learning has recently been widely applied in sEMG signal recognition and gesture classification (Xiong et al., 2021). In addition, some research teams have proposed methods for electrode shifts estimation and adaptive correction, applying them to enhance the robustness of sEMG recognition in hand rehabilitation processes (Li et al., 2020). Besides, a benchmark dataset of sEMG in non-ideal conditions (SeNic) has also been introduced to investigate the robustness of gesture recognition based on surface electromyographic signals in practical applications (Zhu et al., 2022). In summary, extensive research has been conducted on mid-level and high-level control for hand neurorehabilitation. Therefore, due to space constraints, we will not elaborate further on this aspect.

3 Experiments and results

3.1 Experimental validation on the SMA actuator-based platform

3.1.1 The experimental set-up

The experimental platform diagram of the SMA actuator is depicted in Figure 5, and the experimental set-up is presented in

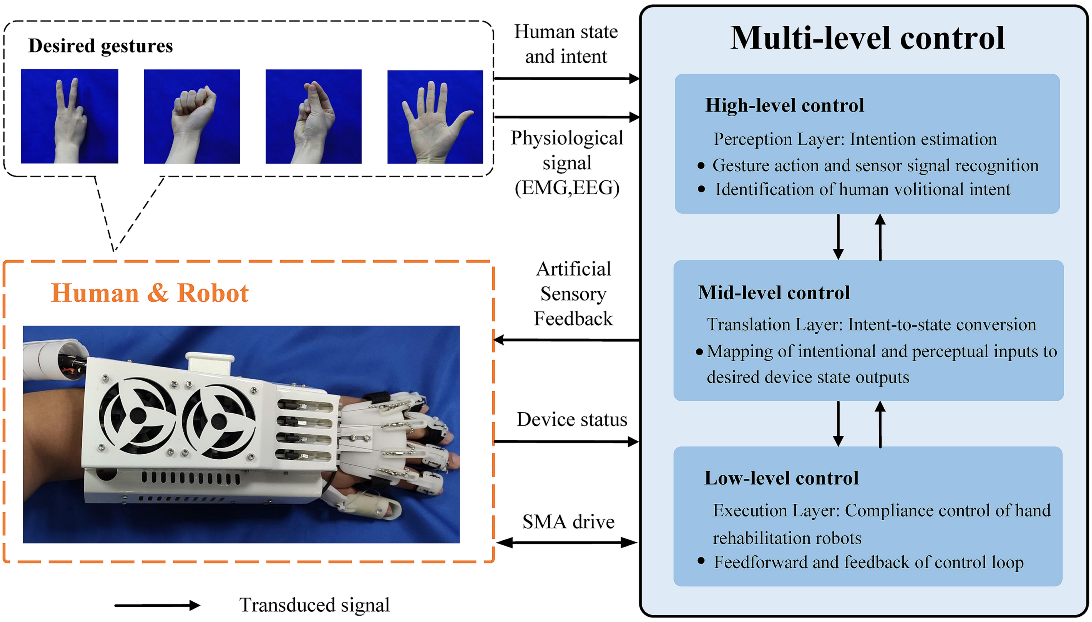

FIGURE 4
A framework for human–robot-environment interaction control strategy.

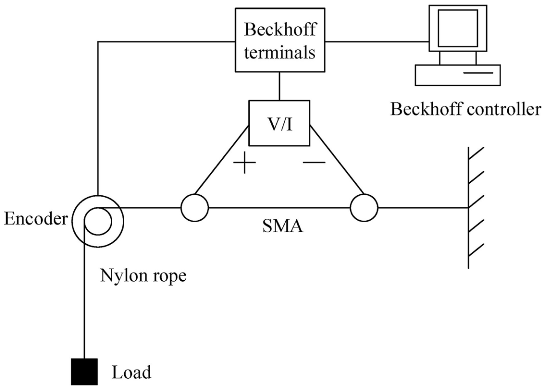

FIGURE 5
The experimental platform diagram of the SMA actuator.

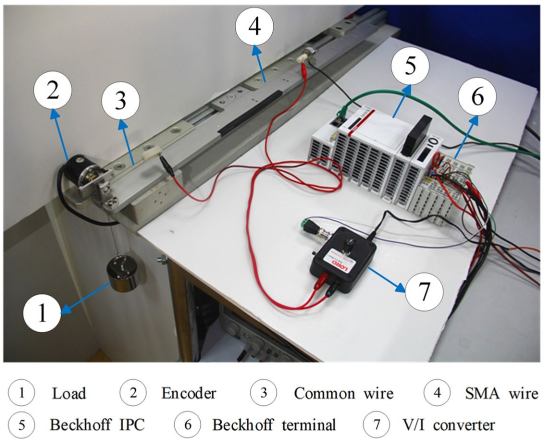

FIGURE 6
The experimental set-up of the SMA actuated system.

Figure 6. The structure of this SMA actuated system is similar to the one in Romano and Tannuri (2009) but without a cooling device. The SMA wire is the Flexinol actuator wire which is produced by Dynalloy, Inc. For this type of wire, the diameter is 0.25 mm, the length is 340 mm, the deformations are up to about 4%, and the Austenite start temperature is 90°C. In this experiment, the system output is the displacement (unit: m) and the input signal is the current (unit: A), which is constrained to the range 0 ~ 0.4. The control current applied to the SMA actuator is obtained from a V/I converter. The SMA wire then generates significant strains in response to the temperature changes caused by the current heating effect. The displacement of the SMA wire is measured by a high precision encoder. The Beckhoff EtherCAT terminals are used for the transformation and conversion of data, and the sample frequency is 200 Hz. The load is fixed as 500 g for the set-point tracking experiment, but varies for the other experiments.

To describe this nonlinear plant, two groups of models have been considered in previous studies (Nikdel et al., 2014; Pai et al., 2017; Pan et al., 2017), namely, mechanism models or neural networks models. However, there exist some inevitable drawbacks in each group. The objective of this work is to find an alternative way to simultaneously address the computational burden and the unmodeled dynamics issues.

3.1.2 PI controllers design

The proposed adaptive PI controller is applied to this plant. Before the control implementation, some offline identifications have been carried out in the Matlab software. The purpose of the offline procedure is to probe the main dynamic properties of this nonlinear

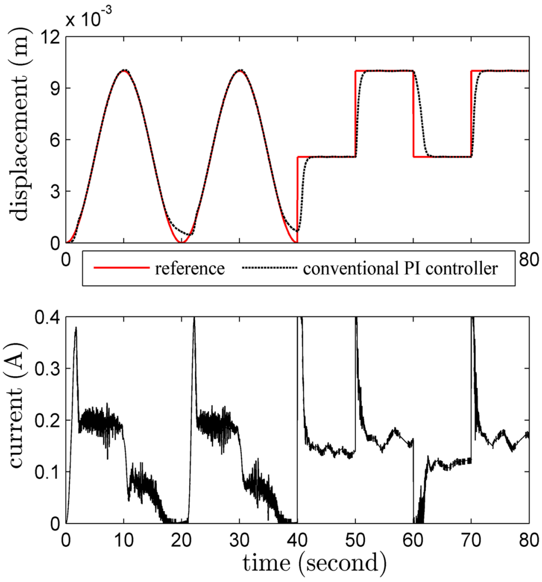

FIGURE 7
Set-point tracking results by the conventional PI scheme.

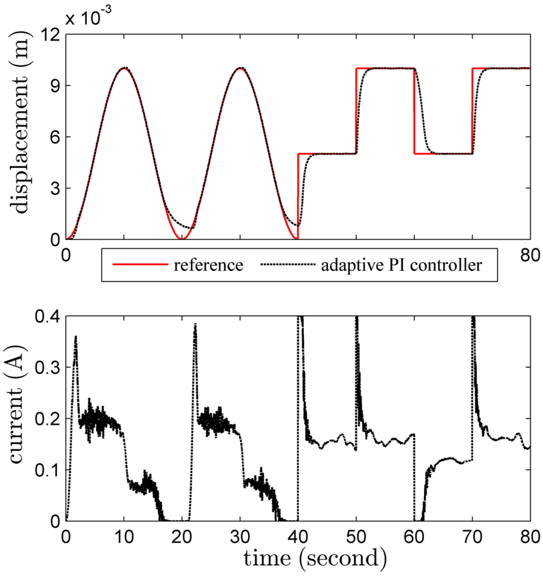

FIGURE 8
Set-point tracking results by the adaptive PI scheme.

plant. Based on some groups of input–output data around different operating points, an RLS algorithm is used to identify the parameters of the model Equation (6). Then some groups of convergent parameter estimates are obtained. Based on these estimates and other input–output data, we have also conducted the model test experiment. Finally, the best prediction model is selected as $y(t+1) = 0.9923\,y(t) + 0.001\,u(t)$. Meanwhile, the obtained results are used as initial conditions for the controller design. For the proposed PI control method, the initialization is $\hat{\theta}(0) = [-0.9923, 0.001]^T$, the multi-innovation length is $p = 3$, the gain is $\varepsilon = 1$, the bound is $\Delta = 0.00012$, the characteristic polynomial is pre-specified as $T(z^{-1}) = 1 - 1.44z^{-1} + 0.445z^{-2}$, and the constrain is $\hat{b} = 0.001$.

As a comparison, the conventional fixed-gains PI controller is applied to this plant as well. The proportional and differential gains k_p and k_I are pre-specified as $k_p = 500$ and $k_p = 5$.

3.1.3 Set-point tracking

The load is fixed as 500 g in this test. Sinusoidal trajectory and square-wave trajectory are both considered. The set-point tracking results of these methods are shown in Figures 7, 8.

The performance of the adaptive PI controller is better than the conventional PI one, especially for the milder control input. It is obvious that the adaptive PI controller can accurately track the reference trajectory with a slowly changing reference trajectory. In addition, the overshoot and oscillation of the adaptive PI controller are more satisfactory. Interestingly, the unmodeled dynamics has been gradually compensated by the adaptive PI controller, which can verify Theorem 1 in Appendix.

3.1.4 Load variations

An additional load with 200 g is imposed on this actuator at 90th second, and removed at 105th second. Another heavier load with 300 g is added at 120th second, and removed at 135th second. The regulation results are shown in Figures 9, 10.

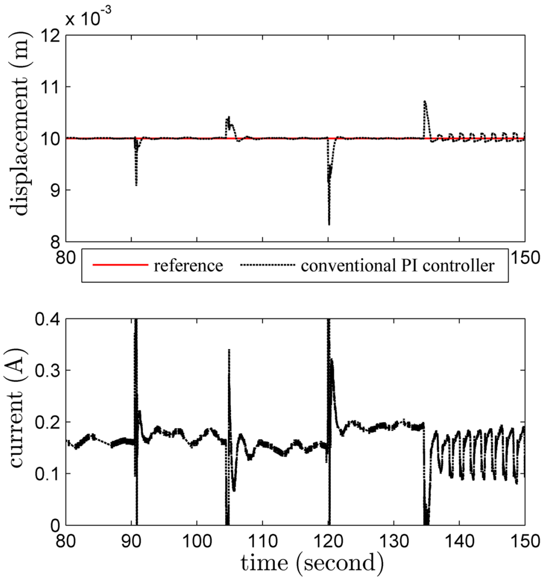

FIGURE 9
Regulation results under load variations by the conventional PI scheme.

The conventional PI controller leads to unattractive results under uncertainties induced by load variations. Worse still, the system becomes unstable after 135th second. Obviously, thanks to the online adaptation, the adaptive PI controller can ensure satisfactory robust stability despite of severe uncertainties.

3.1.5 Disturbance rejection

We further test the disturbance rejection ability. An unknown instantaneous vertical force is suddenly imposed on the load at 160th second, and then an unknown instantaneous lateral force is suddenly

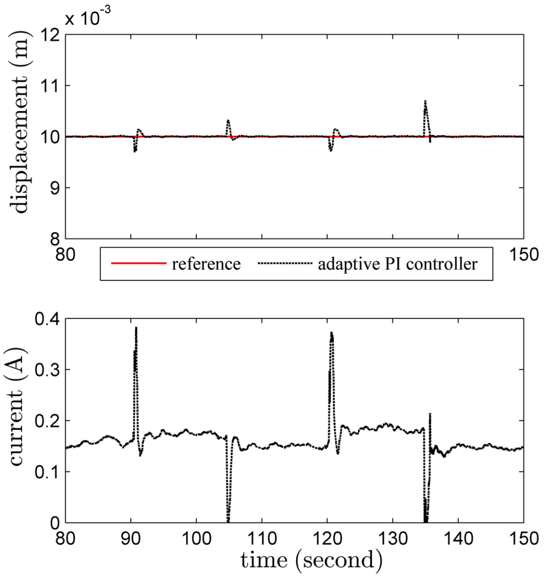

FIGURE 10
Regulation results under load variations by the adaptive PI scheme.

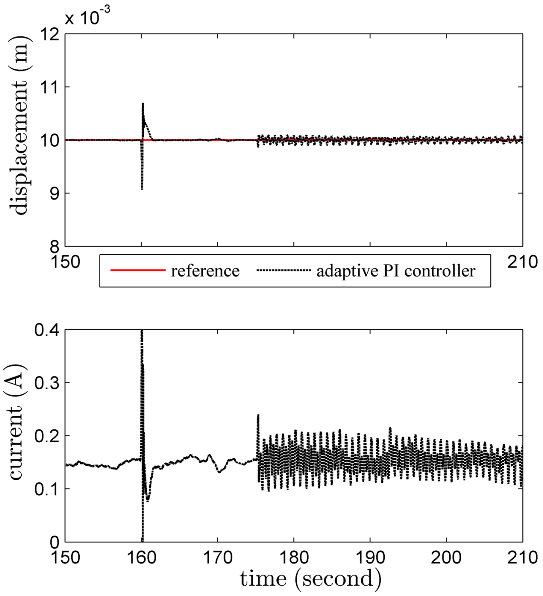

FIGURE 11
Regulation results under non-Gaussian by the adaptive PI scheme.

added at 175th second. The disturbance rejection result of the proposed adaptive PI controller is shown in Figure 11.

The result shows that the proposed adaptive PI controller is reliable under non-Gaussian stochastic noise, which is ensured by the dead-zone weighted factor Equation (20). Though the control input varies a lot, the system output stays within a small region.

3.1.6 Summary

For robotic applications, plenty of issues (i.e., modeling error, load variations and stochastic noise) may cause uncertainties. The proposed adaptive PI controller can address these issues in a computationally efficient manner. During the whole operation, the proportional and differential gains k_p and k_I are updated according to the current working conditions, as shown in Figure 12. Most interestingly, it is seen that when the system suffers from severe uncertainties, especially around 135th and 160th seconds, the updated gains can address the negative effects timely.

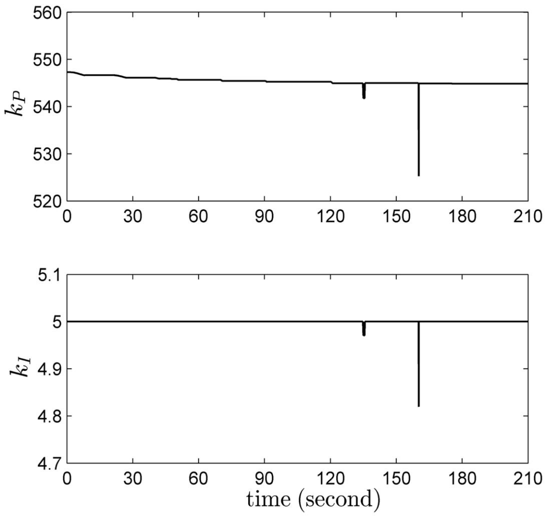

FIGURE 12
The online updates of the proportional and differential gains.

3.2 Experiments on SMA actuator-based hand rehabilitation robot system

3.2.1 The experimental set-up

After verifying the driving principle of SMA and the proposed adaptive PI control algorithm, we designed an actuator mechanism based on SMA and integrated it into a hand rehabilitation robot system to form an SMA-based hand rehabilitation robot system platform, which is suitable for hand rehabilitation training of hemiplegic patients. In this hand rehabilitation robot, each finger is controlled by an individual SMA actuator, and the entire robot comprises five identical SMA actuators. The SMA actuator is primarily comprised of six components, as shown in the left part of Figure 13A. This includes the installation of a pulley device on the main plate of the actuator, winding a shape memory alloy wire around the pulley, connecting the shape memory alloy wire to the output wire and the preloaded pulley through connecting members, and incorporating a wiring mechanism on the actuator's main plate for ease of wiring. Additionally, a displacement feedback mechanism is established to enhance control over the shape memory alloy wire. A prototype SMA actuator was fabricated and assembled using 3D printing technology, as shown in the right part of Figure 13A. To prevent short-circuiting of the wiring mechanism with the shape memory alloy filament, a layer of Teflon tape with insulating and high-temperature-resistant properties was applied to the copper sheet of the wiring mechanism.

After the hand rehabilitation robot system based on SMA actuator is built, the movement of the hand rehabilitation robot is controlled in

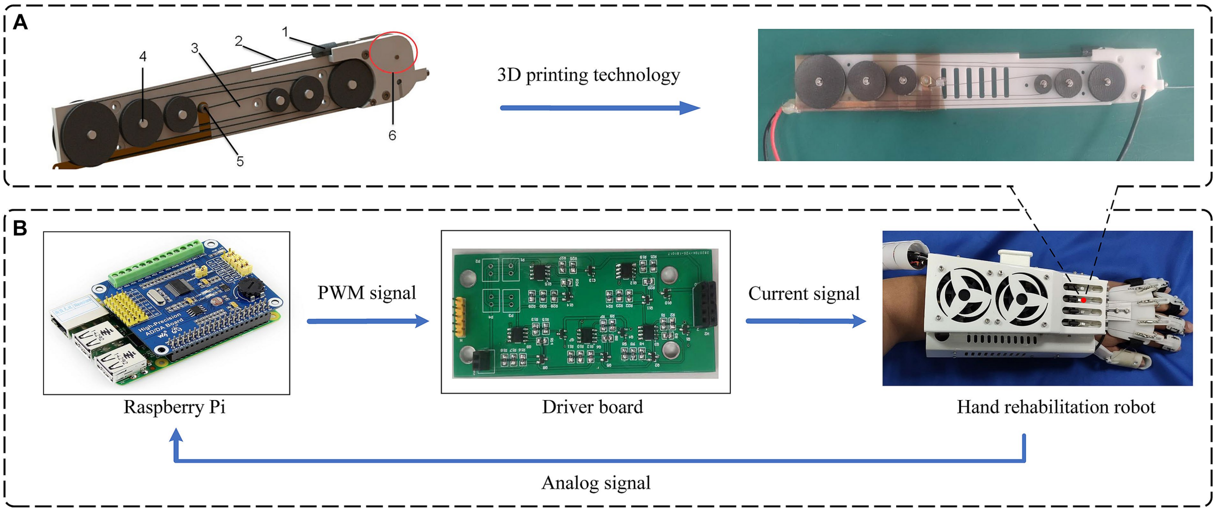

FIGURE 13
Hand rehabilitation robotic system based on SMA actuator. **(A)** SMA actuator structure diagram: 1- Connection, 2- SMA Wires, 3- Actuator body plate, 4- Pulley mechanism, 5- Wiring mechanism, 6- Displacement feedback mechanism. **(B)** System hardware integration framework for hand rehabilitation robot.

the form of sending commands from the upper computer to the lower computer, so as to assist the patient in rehabilitation training. The framework of the hardware system is shown in Figure 13B.

3.2.2 Position tracking experiments of hand rehabilitation robot system based on adaptive PI control

In this subsection, the control core utilizes the Raspberry Pi, and the SMA is subjected to heating signals dispatched to the controller, causing it to contract and deform, thereby propelling the movement of the rehabilitation hand. In this experiment, the SMA actuator of the index finger part of the hand rehabilitation robot is selected as the control object, and based on the adaptive PI control algorithm proposed in this paper to track the position response curve of the SMA actuator under the step signal as well as the sinusoidal signal. For comparative analysis, the PID control law (Khalil, 1996) is utilized as a reference algorithm. Meanwhile, in order to be able to visually compare and analyze the control effects of the two control algorithms, the errors of the SMA actuator-based hand rehabilitation robotic system will be compared when it reaches the steady state under the two control algorithms, respectively. The actual results of the robot system tracking the step and sinusoidal signals and the steady state error results are shown in Figure 14.

From the experimental results in Figure 14A, it can be seen that under the adaptive PI control algorithm, the desired value of the hand rehabilitation robot system is set to 4 mm at 2 s, and the system responds at 2.4 s, reaches the desired position at about 3 s, and maintains stability thereafter, with almost no deviation. Meanwhile, the response times of the two control algorithms are basically the same, but the hand rehabilitation robotic system does not produce overshooting and has a smaller steady state error when the step signal is tracked under the adaptive PI control algorithm. Consequently, for reference trajectories represented by step signals, the hand rehabilitation robot system demonstrates superior control performance under the adaptive PI control algorithm proposed in this paper. Examining the experimental outcomes in Figure 14B, it is observed that the hand rehabilitation robotic system adeptly tracks sinusoidal signals. While the response times of the SMA actuator system remain consistent under both algorithms, the adaptive PI algorithm proposed in this paper achieves more accurate position tracking with less error when tracking sinusoidal signals. Thus, for various signal amplitudes, the methodology presented in this paper enables the SMA actuator-based hand rehabilitation robotic system to approach the target position with reduced overshooting and a smaller steady-state error. These experiments substantiate the reliability and accuracy of the proposed methodology, affirming the safety of the SMA actuator-based hand rehabilitation robot in assisting subjects during the rehabilitation training process.

3.2.3 Experiments on hand rehabilitation training with different gestures

We oriented the SMA actuator-based hand rehabilitation robotic system platform to conduct the hand passive rehabilitation training experiments on subjects with different gestures, and the training process is shown in Figure 15. The hand rehabilitation exercises are divided into five movements, which are thumb extension/flexion, index extension/flexion, index and middle finger extension/flexion, three fingers extension/flexion and hand open/close. During the hand gesture rehabilitation training experiment with the SMA actuator-based hand rehabilitation robot system, a complete single flexion-extension training cycle takes a total of 12 s. Throughout this process, spanning from 0 to 4 s, the SMA contracts upon heating and powering, propelling the fingers to their maximum extended position. Subsequently, from 4 to 12 s, the SMA undergoes cooling facilitated by a fan on the outer shell of the hand rehabilitation robot, causing the hand to return to its initial state. Importantly, this mechanism satisfies the requirements of passive rehabilitation training for multiple gestures in patients with hand hemiplegia, demonstrating an optimal control effect. This experiment effectively establishes the reliability and precision of the SMA actuator-based hand rehabilitation robotic system for subject-specific rehabilitation training under the adaptive PI control strategy. It is worth noting that, due to space limitations,

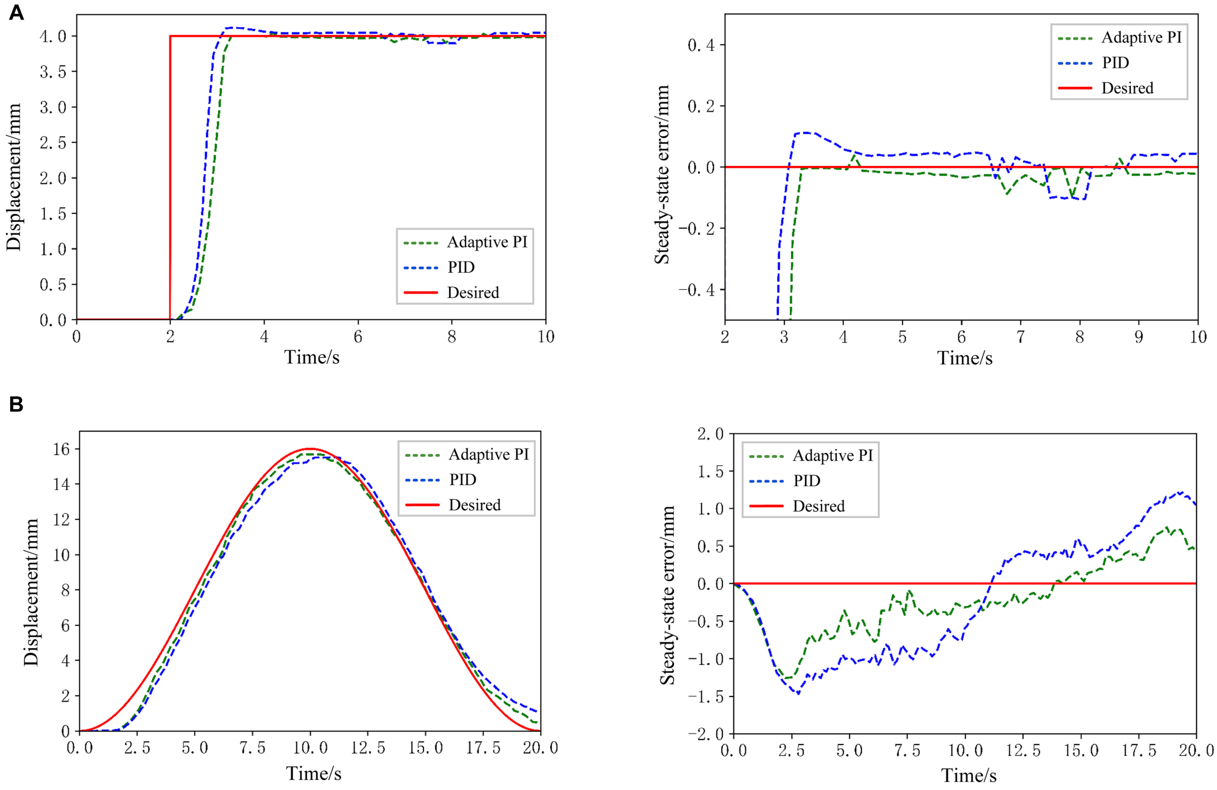

FIGURE 14
(A) Position tracking result and system steady state error for step signal tracking. **(B)** Position tracking result and system steady state error for and sinusoidal signal tracking.

our experiments only focused on the low-level robust adaptive control of hand rehabilitation robots based on SMA actuators. We did not conduct experiments related to neural rehabilitation control involving mid-level and high-level controllers. This aspect will be addressed in our future research.

4 Discussion and conclusion

This paper presents an innovative adaptive PI control strategy tailored for SMA actuators. Utilizing a simplified gray-box model, the primary dynamic properties of the plant are approximated. An efficient adaptive algorithm is then introduced to iteratively update the model parameters. Subsequently, a PI control law is proposed, with gains calculated through the pole assignment technique, ensuring closed-loop stability under mild conditions. Notably, the strategy exhibits robustness, particularly in the face of load variations and continuous disturbances. The proposed adaptive control algorithm is well-defined and has been initially experimentally validated on a Beckhoff controller. Finally, the SMA actuator is designed, fabricated and integrated into a hand rehabilitation robot system, and the position tracking experiments of the SMA actuator based on the proposed adaptive PI control strategy are conducted to verify the stability and accuracy of the proposed control algorithm. Meanwhile, rehabilitation training for several different gestures was conducted for subjects to verify the reliability of the hand rehabilitation robot system based on the SMA actuator.

From another perspective, the control method proposed in this paper exhibits closed-loop stability. Additionally, it is based on several foundational assumptions and theorems, as mentioned in Equation (15) and Theorem 1. The assumption in Equation (15) implies treating unmodeled dynamics as bounded disturbances, and parameter estimation can reject certain continuous disturbances. From the practical application standpoint in the field of hand rehabilitation robotics, disturbances within bounds refer to slow temperature changes in the rehabilitation environment or subtle vibrations in the load. Disturbances beyond bounds refer to severe shaking of the load or significant parameter drift. Furthermore, regarding Equation (A20) in Theorem 1, in actual rehabilitation scenarios, especially in hand rehabilitation, the rehabilitation goals and environment are relatively stable systems not subject to large-scale fluctuations. Therefore, Equation (A20) is satisfied according to the practical needs of rehabilitation. For Equation (A21), in practical applications, for the safety of patients, the reference trajectory of rehabilitation equipment changes slowly and has a small range during the hand rehabilitation process. Therefore, we believe that (Equation A21) can be satisfied in practical applications. In summary, from the perspective of practical applications in the rehabilitation field, our system complies with Theorem 1, demonstrating rationality and reliability.

For control issues of SMA actuators, the systematic method derived in this work probably is the simplest adaptive controller so far, which takes into account the model computational complexity as well as the accuracy of the control results, and the controller has good

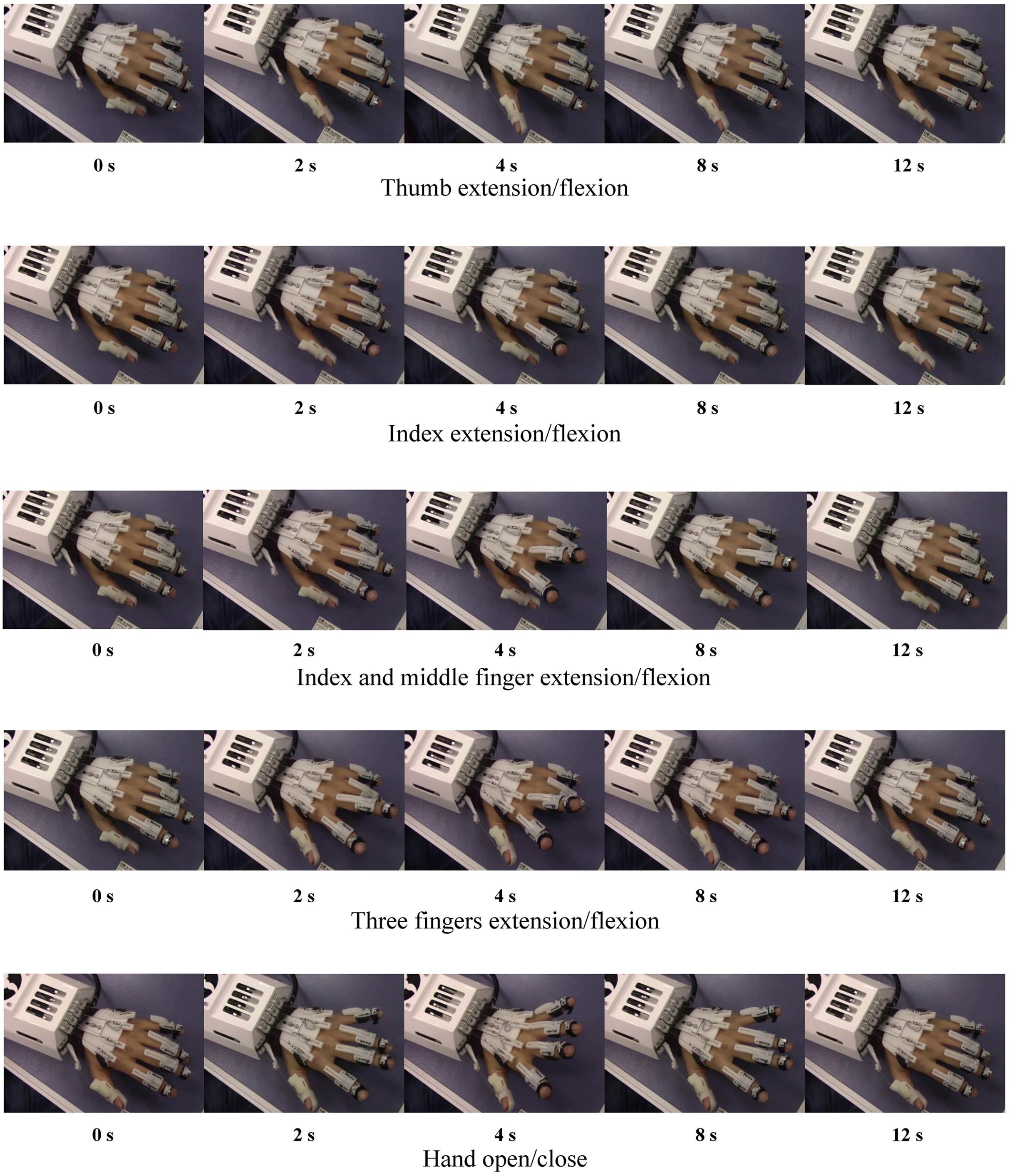

FIGURE 15
Passive rehabilitation of the hand with different gestures.

practicability and reliability. In the future, we expect that the theoretical achievements we have obtained can be further applied to a broader range of rehabilitation robotic devices.

Data availability statement

The raw data supporting the conclusions of this article will be made available by the authors, without undue reservation.

Ethics statement

The studies involving humans were approved by the Research Ethics Committee of the Shenyang Institute of Automation. The studies were conducted in accordance with the local legislation and institutional requirements. The participants provided their written informed consent to participate in this study. The animal study was approved by the Research Ethics Committee of the Shenyang

Institute of Automation. The study was conducted in accordance with the local legislation and institutional requirements. Written informed consent was obtained from the individual(s) for the publication of any potentially identifiable images or data included in this article.

Author contributions

ES: Conceptualization, Formal analysis, Methodology, Validation, Writing – original draft. XZ: Data curation, Investigation, Methodology, Writing – original draft. TW: Project administration, Resources, Visualization, Writing – review & editing. XL: Funding acquisition, Project administration, Supervision, Writing – review & editing. CB: Resources, Software, Supervision, Writing – review & editing. XZ: Conceptualization, Funding acquisition, Project administration, Resources, Writing – review & editing.

Funding

The author(s) declare financial support was received for the research, authorship, and/or publication of this article. This work was partly supported by the National Natural Science Foundation of China under grant numbers U22A2067, 62103406, and 62333007, and also supported by the Applied Basic Research Program Project of Liaoning Province under grant number 2022JH2/101300102, as well as by the Huzhou Science and Technology Project under grant number 2023YZ39 (Corresponding authors: XZ and TW).

Conflict of interest

The authors declare that the research was conducted in the absence of any commercial or financial relationships that could be construed as a potential conflict of interest.

The author(s) declared that they were an editorial board member of Frontiers, at the time of submission. This had no impact on the peer review process and the final decision.

Publisher's note

Supplementary material

The Supplementary material for this article can be found online at: https://www.frontiersin.org/articles/10.3389/fnins.2024.1337580/full#supplementary-material

References

Airoldi, G., Riva, G., Ranucci, T., and Vicentini, B. (1991). Electric transport properties of a NiTi shape memory alloy under applied stress. *MRS Online Proc. Libr. Arch.* 246, 277–281. doi: 10.1557/PROC-246-277

Ashrafiuon, H., and Jala, V. R. (2009). Sliding mode control of mechanical systems actuated by shape memory alloy. *ASME J. Dyn. Syst. Meas. Control.* 131, 101–116. doi: 10.1115/1.3023121

Chen, X. K. (2006). Adaptive sliding mode control for discrete-time multi-input multi-output systems. *Automatica* 42, 427–435. doi: 10.1016/j.automatica.2005.10.008

Chen, X. K., Fukuda, T., and Young, K. D. (2001). Adaptive quasi-sliding-mode tracking control for discrete uncertain input-output systems. *IEEE Trans. Ind. Electron.* 48, 216–224. doi: 10.1109/41.904582

Deberg, L., Taheri Andani, M., Hosseinipour, M., and Elahinia, M. (2014). An SMA passive ankle foot orthosis: design, modeling, and experimental evaluation. *Smart Mater. Res.* 11:572094. doi: 10.1155/2014/572094

Ding, F., and Chen, T. W. (2006). Performance analysis of multi-innovation gradient type identification methods. *Automatica* 43, 1–14. doi: 10.1016/j.automatica.2006.07.024

Ding, Q., Han, J., and Zhao, X. (2016). Continuous estimation of human multi-joint angles from sEMG using a state-space model. *IEEE Trans. Neural Syst. Rehabil. Eng.* 25, 1518–1528. doi: 10.1109/TNSRE.2016.2639527

Elahinia, M. H., and Ashrafiuon, H. (2002). Nonlinear control of a shape memory alloy actuated maniputor. *ASME J. Dyn. Syst. Meas. Control.* 124, 566–575. doi: 10.1115/1.1501285

Fu, Y., and Chai, T. Y. (2011). Indirect self-tuning control using multiple models for non-affine nonlinear systems. *Int. J. Control.* 84, 1031–1040. doi: 10.1080/00207179.2011.588960

Goodwin, G. C., and Sin, K. S. (1984). *Adaptive filtering, prediction and control.* Englewood Cliffs, New Jersey: Prentice Hall.

Jeong, J., Hyeon, K., Han, J., Park, C. H., Ahn, S. Y., Bok, S. K., et al. (2022). Wrist assisting soft wearable robot with stretchable coolant vessel integrated SMA muscle. *IEEE/ASME Trans. Mechatr.* 27, 1046–1058. doi: 10.1109/TMECH.2021.3078472

Jeong, J., Yasir, I. B., Han, J., Park, C. H., Bok, S. K., and Kyung, K. U. (2019). Design of Shape Memory Alloy-Based Soft Wearable Robot for assisting wrist motion. *Appl. Sci.* 9:4025. doi: 10.3390/app9194025

Khalil, H. K. (1996). Adaptive output feedback control of nonlinear systems represented by input-output models. *IEEE Trans. Autom. Control* 41, 177–188. doi: 10.1109/9.481517

Kumbhar, S. B., Chavan, S. P., and Gawade, S. S. (2017). Adaptive tuned vibration absorber based on magnetorheological elastomer-shape memory alloy composite. *Mech. Syst. Signal Process.* 100, 208–223. doi: 10.1016/j.ymssp.2017.07.027

Lagoudas, ., Dimitris, C., ed. (2008). *Shape memory alloys: modeling and engineering applications*. Berlin: Springer Science & Business Media.

Lai, J., Song, A., Shi, K., Ji, Q., Lu, Y., and Li, H. (2023). Design and evaluation of a bidirectional soft glove for hand rehabilitation-assistance tasks. *IEEE Trans. Med. Robot. Bion.* 5, 730–740. doi: 10.1109/TMRB.2023.3292414

Li, Z., Zhao, X., Liu, G., Zhang, B., Zhang, D., and Han, J. (2020). Electrode shifts estimation and adaptive correction for improving robustness of sEMG-based recognition. *IEEE J. Biomed. Health Inform.* 25, 1101–1110. doi: 10.1109/JBHI.2020.3012698

Mataee, M. G., Taheri Andani, M., and Elahinia, M. (2015). Adaptive ankle–foot orthoses based on superelasticity of shape memory alloys. *J. Intell. Mater. Syst. Struct.* 26, 639–651. doi: 10.1177/1045389X14544145

Nikdel, N., Nikdel, P., Badamchizadeh, M. A., and Hassanzadeh, I. (2014). Using neural network model predictive control for controlling shape memory alloy-based manipulators. *IEEE Trans. Ind. Electron.* 61, 1394–1401. doi: 10.1109/TIE.2013.2258292

Pai, A., Riepold, M., and Trächtler, A. (2017). Model-based precision control and force control of SMA actuators with a clamping application. *Mechatronics* 50, 303–320. doi: 10.1016/j.mechatronics.2017.08.011

Pan, Y. P., Guo, Z., Li, X., and Yu, H. Y. (2017). Output-feedback adaptive neural control of a compliant differential SMA actuator. *IEEE Trans. Control Syst. Technol.* 25, 2202–2210. doi: 10.1109/TCST.2016.2638958

Pittaccio, S., Garavaglia, L., Ceriotti, C., and Passaretti, F. (2015). Applications of shape memory alloys for neurology and neuromuscular rehabilitation. *J. Funct. Biomater.* 6, 328–344. doi: 10.3390/jfb6020328

Riccardi, L., Naso, D., Turchiano, B., and Janocha, H. (2013). Adaptive control of positioning systems with hysteresis based on magnetic shape memory alloys. *IEEE Trans. Control Syst. Technol.* 21, 2011–2023. doi: 10.1109/TCST.2012.2222645

Romano, R., and Tannuri, E. A. (2009). Modeling, control and experimental validation of a novel actuator based on shape memory alloys. *Mechatronics* 19, 1169–1177. doi: 10.1016/j.mechatronics.2009.03.007

Serrano, D., Copaci, D., Arias, J., Moreno, L. E., and Blanco, D. (2023). SMA-based soft Exo-glove. *IEEE Robot. Automat. Lett.* 8, 5448–5455. doi: 10.1109/LRA.2023.3295994

Serrano, D., Copaci, D. S., Moreno, L., and Blanco, D. (2018). SMA based wrist exoskeleton for rehabilitation therapy. In 2018 IEEE/RSJ international conference on intelligent robots and systems (IROS). 2018 IEEE/RSJ international conference on intelligent robots and systems (IROS) (Madrid, IEEE), 2318–2323.

Shariat, B. S., Meng, Q., Mahmud, A. S., Wu, Z., Bakhtiari, R., Zhang, J., et al. (2017). Functionally graded shape memory alloys: design, fabrication and experimental evaluation. *Mater. Des.* 124, 225–237. doi: 10.1016/j.matdes.2017.03.069

Shi, Z. Y., Tian, J. W., Luo, R. D., Zhao, G., and Wang, T. M. (2017). Multifeedback control of a shape memory alloy actuator and a trial application. *IEEE Trans. Syst. Man Cybern. Syst.* 48, 1106–1119. doi: 10.1109/TSMC.2016.2641465

Son, N. N., and Anh, H. P. H. (2015). Adaptive displacement online control of shape memory alloys actuator based on neural networks and hybrid differential evolution algorithm. *Neurocomputing* 166, 464–474. doi: 10.1016/j.neucom.2015.03.032

Tai, N. T., and Ahn, K. Y. (2010). A RBF neural network sliding mode controller for SMA actuators. *Int. J. Control. Autom. Syst.* 8, 1296–1305. doi: 10.1007/s12555-010-0615-8

Tai, N. T., and Ahn, K. Y. (2012). Output feedback direct adaptive controller for a SMA actuator with a Kalman filter. *IEEE Trans. Control Syst. Technol.* 20, 1081–1091. doi: 10.1109/TCST.2011.2158435

Viscuso, S., Pittaccio, S., Caimmi, M., Gasperini, G., Pirovano, S., Villa, E., et al. (2009). Pseudoelastic nitinol-based device for relaxation of spastic elbow in stroke patients. *J. Mater. Eng. Perform.* 18, 805–813. doi: 10.1007/s11665-009-9418-6

Wang, Y., Zheng, S., Pang, J., Li, S., and Li, J. (2021). Design and experiment of a hand movement device driven by shape memory alloy wires. *J. Robot.* 2021, 1–13. doi: 10.1155/2021/6611581

Wiest, J. H., and Buckner, G. D. (2014). Indirect intelligent sliding mode control of antagonistci shape memory alloy actuators using hysteretic recurrent neural networks. *IEEE Trans. Control Syst. Technol.* 22, 921–929. doi: 10.1109/TCST.2013.2272420

Wu, S. K., Lin, H. C., and Yen, Y. C. (1996). A study on the wire drawing of TiNi shape memory alloys. *Mater. Sci. Eng. A.* 215, 113–119. doi: 10.1016/09021-5093(96)10369-5

Xie, Q., Meng, Q., Yu, W., Wu, Z., Xu, R., Zeng, Q., et al. (2023). Design of a SMA-based soft composite structure for wearable rehabilitation gloves. *Front. Neurorobot.* 17:1047493. doi: 10.3389/fnbot.2023.1047493

Xiong, D., Zhang, D., Zhao, X., and Zhao, Y. (2021). Deep learning for EMG-based human-machine interaction: a review. *IEEE/CAA J. Automat. Sin.* 8, 512–533. doi: 10.1109/JAS.2021.1003865

Zakerzadeh, M. R., and Sayyaadi, H. (2013). Precise position control of shape memory alloy actuator using inverse hysteresis model and model reference adpative control system. *Mechatronics* 23, 1150–1162. doi: 10.1016/j.mechatronics.2013.10.001

Zhang, J., Ding, F., and Shi, Y. (2008). Self-tuning control based on multi- innovation stochastic gradient parameter estimation. *Syst. Control Lett.* 58, 69–75. doi: 10.1016/j.sysconle.2008.08.005

Zhu, B., Zhang, D., Chu, Y., Gu, Y., and Zhao, X. (2022). SeNic: an open source dataset for sEMG-based gesture recognition in non-ideal conditions. *IEEE Trans. Neural Syst. Rehabil. Eng.* 30, 1252–1260. doi: 10.1109/TNSRE.2022.3173708

frontiers | Frontiers in Neuroscience

TYPE Original Research
PUBLISHED 19 February 2024
DOI 10.3389/fnins.2024.1362495

OPEN ACCESS

EDITED BY
Yuquan Leng,
Southern University of Science and Technology, China

REVIEWED BY
Liquan Guo,
Chinese Academy of Sciences (CAS), China
Mengyi Zhang,
Nanjing Tech University, China

*CORRESPONDENCE
Jing Bai
✉ baijing@njit.edu.cn

RECEIVED 28 December 2023
ACCEPTED 30 January 2024
PUBLISHED 19 February 2024

CITATION
Bai J, Li G, Lu X and Wen X (2024) Automatic rehabilitation assessment method of upper limb motor function based on posture and distribution force.
Front. Neurosci. 18:1362495.
doi: 10.3389/fnins.2024.1362495

Automatic rehabilitation assessment method of upper limb motor function based on posture and distribution force

Jing Bai[1,2]*, Guocheng Li[3], Xuanming Lu[1,2] and Xiulan Wen[3]

[1]Industrial Technology Research Institute of Intelligent Equipment, Nanjing Institute of Technology, Nanjing, China, [2]Jiangsu Provincial Engineering Laboratory of Intelligent Manufacturing Equipment, Nanjing, China, [3]Automation Department, Nanjing Institute of Technology, Nanjing, China

The clinical rehabilitation assessment methods for hemiplegic upper limb motor function are often subjective, time-consuming, and non-uniform. This study proposes an automatic rehabilitation assessment method for upper limb motor function based on posture and distributed force measurements. Azure Kinect combined with MediaPipe was used to detect upper limb and hand movements, and the array distributed flexible thin film pressure sensor was employed to measure the distributed force of hand. This allowed for the automated measurement of 30 items within the Fugl-Meyer scale. Feature information was extracted separately from the affected and healthy sides, the feature ratios or deviation were then fed into a single/multiple fuzzy logic assessment model to determine the assessment score of each item. Finally, the total score of the hemiplegic upper limb motor function assessment was derived. Experiments were performed to evaluate the motor function of the subjects' upper extremities. Bland-Altman plots of physician and system scores showed good agreement. The results of the automated assessment system were highly correlated with the clinical Fugl-Meyer total score ($r=0.99$, $p<0.001$). The experimental results state that this system can automatically assess the motor function of the affected upper limb by measuring the posture and force distribution.

KEYWORDS
rehabilitation assessment, upper limb, posture, distributed force, fuzzy logic

1 Introduction

With the acceleration of social aging, the incidence of stroke is gradually increasing. The death and disability rate of stroke is extremely high, and 70% of the survivors have varying degrees of disability (Garro et al., 2021). Motor disorders of the limbs significantly reduce patients' quality of life and cause considerable suffering. The plasticity of the nervous system has been demonstrated by research (Turon et al., 2018). Early intervention in the early stages of the disease has the potential to reduce the severity of disability and significantly improve the patient's quality of life (Meng et al., 2023). Rehabilitation assessment is based on the level of function, degree of damage, and recovery of stroke patients. It provides a scientific basis for formulating rehabilitation treatment programs, evaluating patients' functional changes, and judging treatment effects and prognosis.

However, the commonly used clinical methods to assess upper limb motor function after stroke are mainly qualitative or semi-quantitative, including active mobility rating (AMR), ARAT-Brunnstrom, Fugl–Meyer rating (FMA), Barthel index, Wolf motor function test (WMFT), and so on (Wolf et al., 1989; Sanford et al., 1993; Sardari et al., 2023). The degree of limb impairment is mainly evaluated subjectively through manual measurement of angle and force information by physicians using protractors and dynamometers. The traditional scale-based assessment has been widely accepted in the medical field (Du et al., 2022), but there are still some shortcomings:

(1) The assessment mechanism is subjective, leading to variation in results. Longitudinal results for the same patient cannot be compared, let alone between different patients. (2) There is no established uniform assessment system among hospitals. (3) The process is also time-consuming. Research on quantitative automatic rehabilitation assessment methods based on automated information technology can improve the standardization of rehabilitation medical technology, reduce assessment and testing time, and alleviate the burden on rehabilitation physicians. Research into automated information technology-based rehabilitation assessment methods could improve the standardization of rehabilitation medical technology, reduce assessment testing time and relieve the burden on rehabilitation professionals.

Modern devices for automatic assessment of upper limb motion function mainly include wearable sensors, rehabilitation robots and visual motion capture systems (Ona Simbana et al., 2019). Wearable sensors mainly include inertial measurement Unit (IMU), surface electromyography (sEMG) sensor, data glove, etc. Oubre et al. (2020) used two wearable inertial sensors on the wrist and the sternum to estimate upper-limb impairment, and proposed an unsupervised clustering algorithm and a supervised regression model to estimate FMA scores. Ueyama et al. (2023) automated the FMA with 9-axis motion sensors and measured 23 FMA upper-limb items. Pan et al. (2021) proposed an evaluation method for upper limb motor function in stroke patients with five features by using the inertial sensor and sEMG sensor. Li C. et al. (2022) used data glove and Thalmic Myo armband to assess the hand motor function quantitatively. Dutta et al. (2022) developed a data glove housing 6 flex sensors, 3 force sensors, and a motion processing unit to evaluate the grasp ability of stroke patients. There is also related research on robot rehabilitation assessment. Moon et al. (2023) proposed a method for evaluating upper limb motor performance with robot based on a normal reaching movement model. However, patients need to wear the IMU and attach the sEMG sensor to their skin. Wearable IMUs are prone to displacement, and stroke may cause hand contractures in some patients, making data gloves difficult to wear. Additionally, sEMG signals are weak, random, and susceptible to interference from muscle status, skin sweat, and the environment. Robots are expensive and beyond the reach of the average family.

In terms of visual motion capture systems, VICON (Oxford, United Kingdom) is an optical motion capture system, that has become the gold standard for motion analysis (Van Crombrugge et al., 2022), but it is relatively expensive. Infrared imaging devices are also used to assess hand function (Fang et al., 2019). Kinect can visually capture three-dimensional motion and has been used in many motion analysis studies due to its comfort, low cost, easy installation, and suitability for home or community hospitals.

Bai and Song (2019) used Kinect V1 and IMU sensors to evaluate 15 FMA items, and automatically evaluated the upper limb combined with the reachable workspace of each subject. Motion measurement sensors, such as inertial and visual sensors (Ambros-Antemate et al., 2022; Francisco-Martínez et al., 2022), are unable to assess changes in stiffness. To quantify joint stiffness, force measurement is a more appropriate method. Lee et al. (2016, 2018) used Kinect v2 and force sensing resistor sensors, and developed a rule-based binary logic classification algorithm, to realize an automated FMA system for upper extremity motor function assessment. Li Y. et al. (2022) proposed an automated evaluation system composed with RealSense D435, Leap Motion and Force Sensitive Resistors.

Bai proposed less automatic motion protocol (only 15 items). Lee uses Kinect v2 sensor, resulting in inaccurate and unstable hand posture measurement, and inaccurate forearm pronation/pronation tracking. The scheme proposed by Yue Li uses three different types of sensors, and the detection system is complex. The accuracy of RealSense D435 human posture measurement can be affected by the position of the hand attitude measurement sensor and its affiliated platform. Furthermore, these studies utilized a single force sensing resistor sensor to measure hand grasping ability, which only measures thumb and index finger force and may not accurately reflect force at other hand positions.

Regarding evaluation methods, the researchers suggest utilizing machine learning techniques for data processing (Chung et al., 2022). Eichler et al. (2018) developed a multi-camera tracking system with SVM and Random Forest to evaluate the motion of stroke patients. Kim et al. (2020) proposed a method to judge the severity of elbow spasm. Machine learning algorithm was used to analyze the acceleration and rotation attributes of the affected elbow joint, and the degree of spasm was classified. Miao et al. (2021) proposed to adopt smartphone and Kinect sensor to collect upper limb movement data and use the long short-term memory neural network to evaluate upper limb movement function. Deb et al. (2022) adapt spatio-temporal GCN for the assessment of rehabilitation exercises. However, implementing machine learning, particularly deep learning, in clinical practice is challenging due to the need for extensive labeled data.

To address the issues with the previous studies, this study proposes a new approach that utilizes the array distributed flexible thin film pressure sensor (DFPS) and Azure Kinect for Upper Extremity FMA (FMA-UE) automation. Azure Kinect combined with MediaPipe can improve the accuracy of upper limb and hand posture recognition. Additionally, the DFPS is used to refine hand joint stiffness measurements. The fuzzy logic-based assessment method is adopted to avoid the problem of reliance on large amounts of labeled data.

The block diagram of the automatic rehabilitation assessment system of upper limb motor function based on posture and distributed force measurement is shown in Figure 1. The assessment protocol is presented to the subjects through a display screen. The DFPS and Azure Kinect are connected to the computer via USB. Azure Kinect combined with MediaPipe automatically recognizes the subject's upper limb and hand joint positions, which are used to calculate information like motion angles under each assessed movement within the FMA scale. DFPS is used to measure force information in the hand during different gripping modes. Next, feature information is extracted for both the affected and healthy upper limbs and hands.

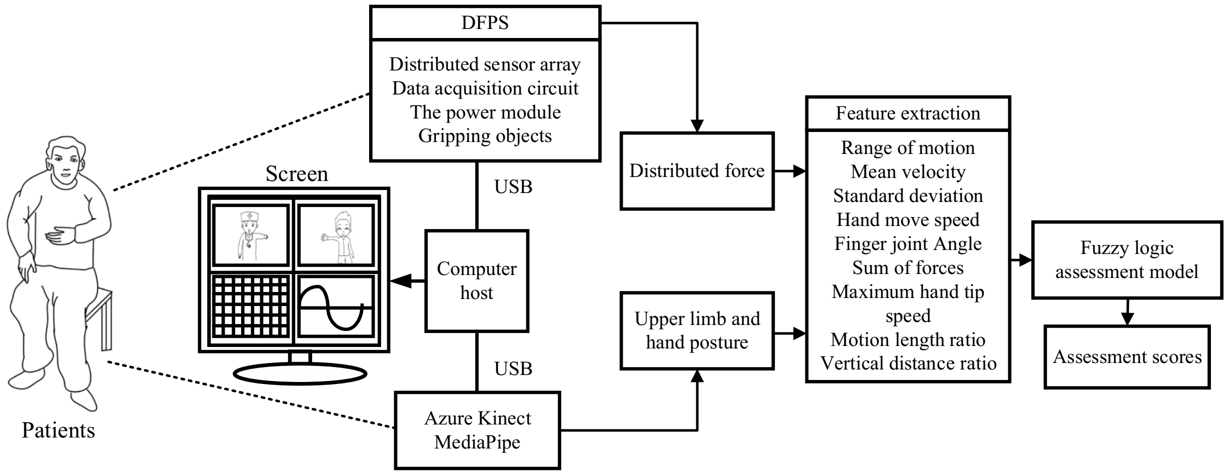

FIGURE 1
Automatic rehabilitation assessment system of upper limb motor function based on posture and distribution force.

The ratio or deviation is then calculated and input into a single/multiple fuzzy logic assessment model to derive assessment scores for each item in automated FMA-UE scale. Finally, the total assessment scores for the upper limbs are calculated.

2 Methods

2.1 Automatic FMA-UE

The Fugl–Meyer assessment is a widely used method for clinically evaluating post-stroke motor dysfunction. It consists of 33 items for assessing upper extremity motor function, including 18 for shoulder-arm motor function, 12 for wrist-hand motor function, and 3 for coordination. The scoring criteria for the Fugl–Meyer upper extremity motor function assessment are: the assessment is scored out of 66 points, with 2 points awarded for complete completion of each item, 1 point for partial completion, and 0 points for failure to complete. The FMA-UE score is used to classify the severity of hemiplegia, with scores below 32 indicating severe hemiplegia, scores between 32 and 57 indicating moderate hemiplegia, and scores between 58 and 66 indicating mild hemiplegia (Gladstone et al., 2002).

The FMA-UE is a detailed scale closely related to the functions required for daily living activities. It can visually and quickly reflect abnormal movement patterns, making it a comprehensive assessment. However, the clinical test is lengthy, tedious, and subjective. To effectively assess the motor function of the upper extremity in post-stroke patients, automating as many items as possible in the FMA-UE program is necessary. This study improved the testing method of the scale to enable automated measurement of upper limb motor function in stroke patients.

The method proposed in this paper contains 30 items (F1–F30) for automation, as shown in the "FMA-UE Item" column in the Table 1. Only the two items shown in grey are not included, namely the "Reflex activity" and the "Normal reflex activity," as they require a small hammer to tap the muscles. All automatic evaluations are summarized into 21 sets of actions as shown in the "Motion" column. The actions M16–M20 (M16 is hook grasp., M17 is lateral pinch, M18 is Pincer grasp., M19 is cylinder grasp., M20 is Sphere grasp) adopt the DFPS, and other actions are measured using Azure Kinect combined with MediaPipe (AKM). The column "Feature" in the table indicates the feature information extracted for each item.

2.2 System design

In this study, an automated FMA-UE upper limb motor function assessment system is proposed, including an Azure Kinect and a set of DFPS. The RGBD camera combined with MediaPipe enables motion and posture tracking of the upper limbs and hands. Azure Kinect Depth Camera integrates a depth sensor, a spatial microphone array, a video camera, and a direction sensor to achieve depth recognition based on the TOF principle, which can realize three-dimensional tracking of the human body and identify the position information of 32 joints (Wei et al., 2022). MediaPipe is an open-source machine learning application development framework developed by Google. MediaPipeHands is a high-fidelity hand and finger tracking solution. It uses machine learning to infer the 3D coordinates of 21 joints of a hand from a single frame.

MediaPipe uses color image to recognize human motion information. Azure Kinect's collection of human joint points includes depth image information. Therefore, the color image and depth image need to be aligned initially. The camera can capture three types of data simultaneously, namely RGB images (three-channel images), depth images (single-channel grayscale maps), and color 3D point clouds. The device calibration data is retrieved before the coordinate system conversion can be performed. Then the 3D points of the source coordinate system are converted into the 3D points of the target coordinate system using the external calibration of the camera, and the corresponding 2D pixel coordinates are calculated using the target camera's internal calibration to align the depth image and color image for subsequent hand tracking and upper limb joint tracking.

The DFPS comprises a sensing element, an array scanning module, a signal acquisition and processing module, and a power supply module. A piezoresistive tactile sensor is used as the sensing element, based on the semiconductor piezoresistive effect. The

TABLE 1 Target FMA-UE items.

Category		Motion	FMA-UE item	Sensors	Feature symbol	Feature
Shoulder/elbow	Reflex activity		(1) Flexors data	N/A		
			(2) Extensors	N/A		
	Flexor synergy	M1	(3) Shoulder elevation	AKM	F1	ROM, MV, SD
			(4) Shoulder retraction	AKM	F2	
			(5) Shoulder abduction (≥90°)	AKM	F3	
			(6) Shoulder external rotation	AKM	F4	
			(7) Elbow flexion	AKM	F5	
			(8) Forearm supination	AKM	F6	
	Extensor synergy	M2	(9) Shoulder adduction/internal rotation	AKM	F7	
			(10) Elbow extension	AKM	F8	
			(11) Forearm pronation	AKM	F9	
	Volitional movement mixing synergies	M3	(12) Hand to lumbar spine	AKM	F10	Hand-to-hip motion length ratio
		M4 + M5	(13) Shoulder flexion 0–90° with the elbow fully extended	AKM	F11	ROM, MV, SD of M4 and M5
		M6 + M7 + M8	(14) Forearm pronation/supination with the elbow 90°and shoulder 0°	AKM	F12	ROM, MV, SD of M6–M8
	Volitional movement with little or no synergy	M9 + M5 + M6	(15) Shoulder abduction 0–90° with elbow fully extended and forearm pronation	AKM	F13	ROM, MV, SD of M5, M8, and M9
		M10 + M5	(16) Shoulder flexion 90–180° with elbow fully extended	AKM	F14	ROM, MV, SD of M10, and M5
		M5 + M6+ M11	(17) Forearm pronation/supination with the elbow fully extended and shoulder 30°–90°	AKM	F15	ROM, MV, SD of M5, M8, and M11
	Normal reflex activity		(18) Biceps, triceps, finger flexors	N/A		
Wrist/hand	Wrist stability	M12 + M7 + M8	(19) Wrist stability at 15° dorsiflexion with elbow 90°and shoulder 0°	AKM	F16	ROM, MV, SD of M12, M7, and M8
		M13 + M7	(20) Repeated wrist flexion and extension (WFE) with elbow 90°	AKM	F17	ROM, MV, SD of M13 and M7
		M12 + M5 + M11	(21) Wrist stability at 15° dorsiflexion with elbow 0° and shoulder 30°	AKM	F18	ROM, MV, SD of M12, M5, and M11
		M12 + M5 + M11	(22) Repeated wrist flexion and extension with elbow 0° and shoulder 30°	AKM	F19	ROM, MV, SD of M12, M5 and M11
		M13 + M5 + M11	(23) Circumduction with elbow 0° and shoulder 30°	AKM	F20	ROM, MV, SD of M5 and M11
	Hand	M14	(24) Mass flexion	AKM	F21	Max angle and MV
		M15	(25) Mass extension	AKM	F22	
		M16	(26) Hook grasp	DFPS	F23	Total force per sensing unit
		M17	(27) Lateral pinch	DFPS	F24	
		M18	(28) Pincer grasp	DFPS	F25	
		M19	(29) Cylinder grasp	DFPS	F26	
		M20	(30) Sphere grasp	DFPS	F27	
Coordination/speed		M21	(31) Finger-nose tremor	AKM	F28	The MV and MA of the fingertips
			(32) Finger-nose dysmetria	AKM	F29	Vertical distance ratio, motion length ratio
			(33) Finger-nose speed	AKM	F30	V and t

N/A, not applicable. The gray part is not included in this automated FMA-UE. Motion represents all movements; there are 20 motion tasks in total. F1–F20 represent the feature symbol. FMA-UE item represents the item included in this automated FMA-UE. AK means Azure Kinect, DFPS means the Array Distributed Flexible Thin Film Pressure Sensor. ROM means Range of motion, MV represents mean velocity, SD means the standard deviation.

principle of piezoresistive tactile sensors is that the electrical resistivity of the elastomer material varies with the magnitude of the pressure, which converts the pressure signals on the contact surfaces into electrical signals. The array scan module performs periodic scans of the sensor array and stabilizes the power supply and battery voltage. The TPS62046 is used in the voltage regulator part to convert the 5 V DC power supply to 3.3 V. The scanning circuit utilizes the CD4052 analog multi-switch to cyclically supply power to the sensing unit, access the voltage divider circuit for voltage division, and transmit the resistive voltage division value of the sensing unit to the signal acquisition and processing module. The STM32 microcontroller module acquires the voltage value of the sensing unit for data interpretation and outputs the measurement results to the computer through USB to serial port. The sensor is then calibrated using the calibration device to establish the relationship between voltage and pressure.

2.3 Data processing

Prior to feature extraction, the raw data of the measured postural signals were filtered by a fourth-order Butterworth low-pass filter with a cut-off frequency of 12 Hz to remove artefacts caused by the patient's voluntary movement and gravity during the measurement (Ren et al., 2020).

In order to enable doctors to quickly use the automatic evaluation method proposed in this study, the description of limb movements adopts the method in rehabilitation medicine, based on the standards defined by the International Society of Biomechanics (ISB) (Wu et al., 2005). The Standardization and Terminology Committee (STC) of the ISB proposes a definition of a joint coordinate system (JCS) for each joint (Da Gama et al., 2016). In this paper, only the coordinates of the right joints are presented, and the left joint is the mirror image of the right (with respect to the sagittal plane $z = -z$).

The coordinate system for the thorax is defined as follows: the Y_T axis is a unit vector from the spine chest (SC) to the neck, the ISB conventionally uses the X-axis turned away from the body and pointing directly anterior to the body, and the Z_T axis is a unit vector perpendicular to the X_T and Y_T axes, which can be computed by the cross product between them. The coordinate system for the right shoulder joint (CS) is also defined. For that purpose, Y_S is used as the unit vector from ER towards SR, and Z_S as the vector perpendicular to the plane formed by X_S and Y_S. The flexion/extension, adduction/abduction and internal/external rotation angles of the shoulder joint can be solved using the Euler angles of the rotation matrices of the two coordinate systems. The angles of flexion and extension of the wrist joint and the anterior and posterior rotation of the forearm can also be solved. The elbow flexion angle is defined as the angle between the upper arm and the forearm, which can be determined using the flexion angle vector. F1 and F2 can be calculated using the shoulder-neck (SN) vector with respect to the horizontal and frontal planes, respectively.

The range of motion (ROM), mean velocity (MV), and standard deviation (SD) are selected as the eigenvalues for item (3–11). ROM is defined as the difference between the maximum and minimum angle of motion, MV represents the average velocity, and SD is the standard deviation of the unaffected side and the affected side. To ensure consistency across individuals, the healthy side data is used as the standard. The standard deviation (δ) between the unaffected and healthy side for the same motion is calculated using Eq. 1.

$$\delta = \sqrt{\frac{\sum_{i=1}^{n} \Delta d_i^2}{n}} \tag{1}$$

where n is the sampling frequency of each action, and Δd is the deviation between the unaffected and healthy side. The target symbol F1-F9 can extract the ROM, MV and SD of each action as feature information.

Item (12) extracts the hand-to-hip motion length ratio α (Eq. 2) as characteristic values F10.

$$\alpha = \min \frac{d_{\mathrm{AHC}}}{d_{\mathrm{OHC}}} \tag{2}$$

where d_{OHC} is the distance from the original position of the hand to the center of the hip, d_{AHC} is the distance from the actual position of the hand to the center of the hip.

As shown in Table 1, item (13), (16), and (20) each contain two sub-motions, the ROM and MV and SD of each sub-motions should be extracted as F11, F14 and F17 separately. Item (14), (15), (17), (19), and (21)–(23) each contain three sub-motions. The ROM and MV and SD of each sub-motions (F12, F13, F15, F16, and F18–F20) need to be extracted separately.

Aligning the color image and depth image using Azure Kinect calibration function. Then, aligning the wrist joint position and fingertip position recognized by MediaPipe and Azure Kinect, respectively. The coordinates of other hand joints are transformed simultaneously. This allows for tracking of hand joint positions and capturing of hand posture.

The bending angle of the finger joints was calculated by determining the maximum value of the finger's bending angle and the MV to judge the Mass flexion (F21) and Mass extension (F22). Figure 2 shows the calculation of the bending angle of the finger joints. Panel (A) displays the ordinal number of the 21 key points of the hand, while panels (B) and (C) show the schematic of the thumb and index finger bending vector pinch angles, respectively. The thumb fingertip joint point 4 and joint point 3 form vector 3_4. The joint point 2 and wrist origin point (joint point 0) form vector 0_2. The angle between vector 3_4 and vector 0_2 is calculated according to Eq. 3.

$$\theta = \arccos\left(\frac{(x_4 - x_3)(x_0 - x_2) + (y_4 - y_3)(y_4 - y_2)}{\sqrt{(x_4 - x_3)^2 + (y_4 - y_3)^2} \times \sqrt{(x_0 - x_2)^2 + (y_0 - y_2)^2}} \right) \tag{3}$$

The angle between vector 0_6, consisting of joints 0 and 6, and vector 7_8, consisting of joints 7 and 8, represents the degree of curvature of the index finger as shown in Figure 2B. The curvature of each finger is represented by the angle between two vectors. Specifically, the degree of curvature of the middle finger is represented by the angle between vector 0_9 and vector 10_12, the degree of curvature of the ring finger is represented by the angle between vector 0_13 and vector 14_16, and the degree of curvature of the little finger

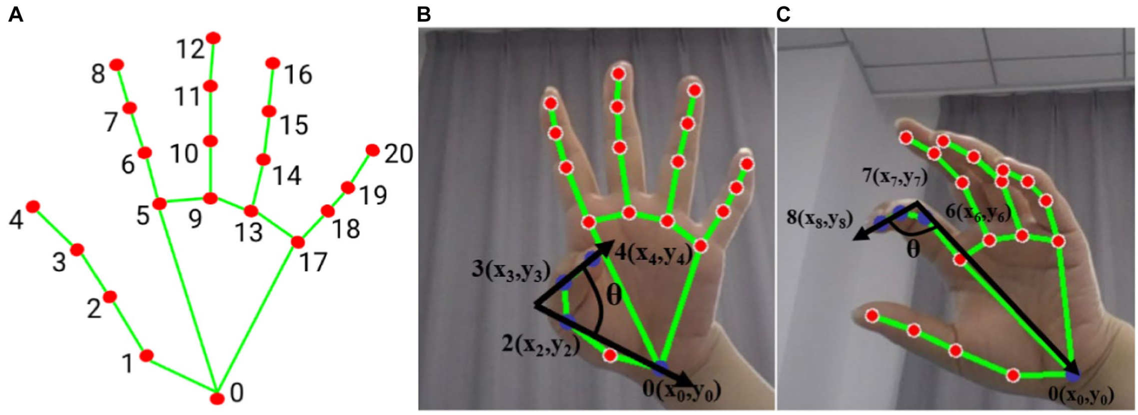

FIGURE 2
Hand posture **(A)** hand node serial number, **(B)** thumb flexion vector angle (blue dot marked as used joint), **(C)** index finger flexion vector angle (blue dot marked as used joint).

is represented by the angle between vector 0_17 and vector 18_20. The motion of the thumb and the average of the remaining four fingers are treated as separate sub-motion, and the following evaluator takes the maximum averaged angle and the averaged velocity as eigenvalues (F21 and F22).

In item 26–30, DFPS is used to measure hand grip force, and a certain threshold is set for effective gripping, and the threshold in this study is set as the minimum force to be detected by the DFPS. Due to the different handles, the positions of the force on the DFPS are different. Hook grasp., cylinder grasp and Sphere grasp exert force on the whole palm, while lateral pinch mainly exerts force on thumb and index finger, and Pincer grasp exerts force on thumb, index finger and middle finger. Therefore, it is not feasible to calculate the grip strength only by the sum of the thumb and index finger. This study proposes to calculate the total grip force of the hand (affected side/healthy side) by calculating the sum of the forces of each sensing unit in the inductive area (F23–F27).

Coordination and velocity [item (31)–(33)] (Huo et al., 2020): based on the measured fingertip data, the velocity and acceleration of the fingertip can be obtained, and average velocity and average acceleration are analyzed as feature (F28) for tremor classification. The characteristics of finger-nose dysmetria (F29) are mainly manifested in two aspects, namely, the ratio of the horizontal distance from the fingertip position to the left and right shoulder joints β, and the fingertip-to-nose movement length ratio γ as shown in Eq. 4.

$$\gamma = \frac{\Delta d}{d_{FON}} \tag{4}$$

where Δd represents the distance from the real-time position of the fingertip to the nose in the vertical direction, d_{FON} is the distance from the original position of the fingertip to the nose in the vertical direction. The hands are naturally placed at the sides of the body as the original position. The greater the movement length ratio, the better the patient's ability to control the affected limb. The characteristic of finger-nose speed (F30) is mainly expressed by the maximum value of the movement time and the speed of the hand movement.

2.4 Assessment method

There is no obvious standard boundary for the classification of patients' motor function grades, and the clinician's assessment method is fuzzy. The use of fuzzy mathematical methods for assessment and analysis appears to align more naturally with objective facts. Therefore, this study proposes a multi-group fuzzy inference system for rehabilitation assessment (FISRA) based on the experience of rehabilitation physicians. To standardize the assessment system, the movement information of the healthy limb is collected simultaneously with the affected limb. The ratio/deviation of the sum of the movement/distributed force on the affected side to that on the healthy side is used as the eigenvalue to design the assessment method for the grades of the affected limb. It is important to note that joint movement and force application criteria differ for each subject.

The inputs to FISRA were the ratio of affected side ROM (AROM) to healthy side ROM (HROM), the ratio of affected side MV (AMV) to healthy side MV (HMV), and the SD. The trapezoidal membership function is adopted, as shown in Eq. 5. The output represents the assessment score using the triangular membership function, as shown in Eq. 6. As Elbow flexion in item (10), the FISRA inputs are AROM/HROM, AMV/HMV and SD, using trapezoidal membership function. and the output is rehabilitation assessment score, using triangular membership function. The assessment level is lower when the average speed AMV is slower, the AMV/HMV is smaller, and the SD is larger. Conversely, the assessment level is higher when the AROM/HROM is larger, the average speed AMV is higher, the AMV/HMV is larger, and the SD is smaller.

$$f(x) = \begin{cases} 0 & (x \le a) \\ \dfrac{x-a}{b-a} & (a \le x \le b) \\ 1 & (b \le x \le c) \\ \dfrac{d-x}{d-c} & (c \le x \le d) \\ 0 & (x \ge d) \end{cases} \tag{5}$$

$$f(x)=\begin{cases}0 & (x\le e)\\ \dfrac{x-e}{f-e} & (e\le x\le f)\\ \dfrac{g-x}{g-f} & (f\le x\le g)\\ 0 & (x\ge g)\end{cases} \tag{6}$$

For item (12) Hand to lumbar spine, the extracted feature is the length ratio α of the hand to hip movement. The input is the length ratio of the affected side to the length ratio of the healthy side (Eα/Hα). A trapezoidal affiliation function is used. The greater the Eα/Hα, the greater the distance from the hand to the hip on the affected side, and the lower the assessment score.

For the items containing multiple sub-motions, each sub-motion is fuzzy evaluated first, and a separate FISRA is established. Then the evaluation results of multiple sub-motions are combined to evaluate the motor function score of the affected upper limb, as shown in Eq. 7.

$$Ra=\begin{cases}0 \ \exists\ FIS_i=0\\ 1 \quad else\\ 2\ \forall\ FIS_i=2\end{cases} \tag{7}$$

(a) If the score of multiple sub-motion is 2, the final evaluation score is 2.
(b) If one of the multiple sub-motion scores is 0, the motion evaluation score for that action is 0.
(c) All other assessments were scored 1.

Item (13), (16), and (20) each have two actions. For example, (13) involves shoulder flexion 0–90° with the elbow fully extended including sub-motion M4 and M5. The features of the two sub-motions are extracted, FIS1 and FIS2 are used for evaluation, and the AROM/HROM, AMV/HMV and SD of each sub-motion are input into the model, the two evaluation scores are output respectively, and then the results of the two FIS are processed according to Eq. 7, as shown in Figure 3.

Items 14, 15, 17, 19, and 21–23 contain three sub-motions respectively, then three FISs are adopted. The AROM/HROM, AMV/HMV and SD of each sub-motion are input into a model respectively, the three evaluation scores are output, and then the results of the three FISs are processed according to Eq. 7.

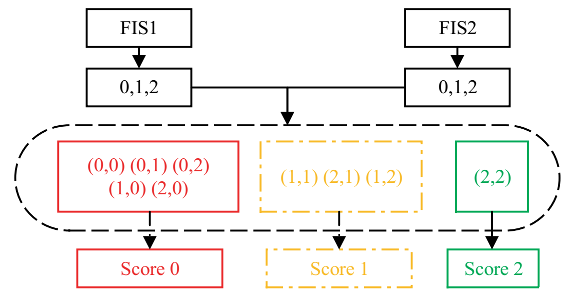

FIGURE 3
Two sets of FIS.

Item (24) and (25) contains the motion of five fingers. Two FISs are used for the average results of the thumb and the other four fingers, respectively. The ratio of the maximum bending angle of the affected side to the maximum bending angle of the healthy side (AAngle/HAngle) and the AMV/HMV are input into each FIS, and then the evaluation scores are output. The larger the AAngle/HAngle, the larger the MV, the higher the evaluation score. Then the results of the two FIS are processed according to Eq. 7.

In item (26)–(30), the feature extracted by each item is the sum of the forces of the sensing unit. The input of the FIS is the sum of the distributed forces on the affected side to the healthy side (AFsum/HFsum). The greater the AFsum/HFsum, the higher the level of hand motor function. The lower the AFsum/HFsum, and the lower the level of hand motor function.

In the process of fingertip pointing to the nose in action 31, the ratio of the movement characteristics of the fingertip on the affected side to those on the unaffected side is calculated, AMV/HMV and AMA/HMA are input into each FIS to obtain the final assessment score. For item 32 finger-nose dysmetria, the characteristics of the affected side/unaffected side are calculated. The vertical distance Aβ of the affected side is divided by the vertical distance Hβ of the unaffected side. The movement length ratio of the affected side Aγ is divided by the movement length ratio of the unaffected side Hγ. These values are input into the FIS to obtain the assessment score. For item 33 speed, the ratio of AVmax (maximum velocity) on the affected side to HVmax on the healthy side is calculated and inputted into FIS. Then, the evaluation grade is obtained.

FIS adopts Mamdani fuzzy inference method, which is obtained by Cartesian product of fuzzy set. The defuzzification method is “centroid” to transform the fuzzy conclusion into a specific and accurate output process.

2.5 Human-computer interaction

Interactive virtual environment can improve the enthusiasm and attention of patients. Based on previous research and the doctor’s recommendations, this study designed a human machine interface for assessing upper limb motor function. It includes motion-teaching videos, virtual feedback scenarios, and the distributed force sensor results, as shown in Figure 4.

The rehabilitation assessment teaching video is recorded by experienced rehabilitation physicians, including 20 actions (M1–M21) proposed in 2.1 Automatic FMA-UE. A part of the remaining time is set aside after each action, to ensure that the patient has enough time to complete the action. The patient’s appearance was neglected during illness. This study is based on the concept of paying attention to the patient’s mental health. The feedback video does not show the patient’s real image to protect the patient’s privacy. Instead, it uses an avatar to provide the patient with mirror feedback, display the subject’s movement posture, and show the subject’s real posture through a small window. In the virtual scene, arrows are added to indicate the direction of movement, and the voice is added to prompt the action content. Appropriate encouragement is given according to the patient’s completion (e.g., very good, come on, you are awesome, etc.) to further enhance the patient’s motivation to participate in the

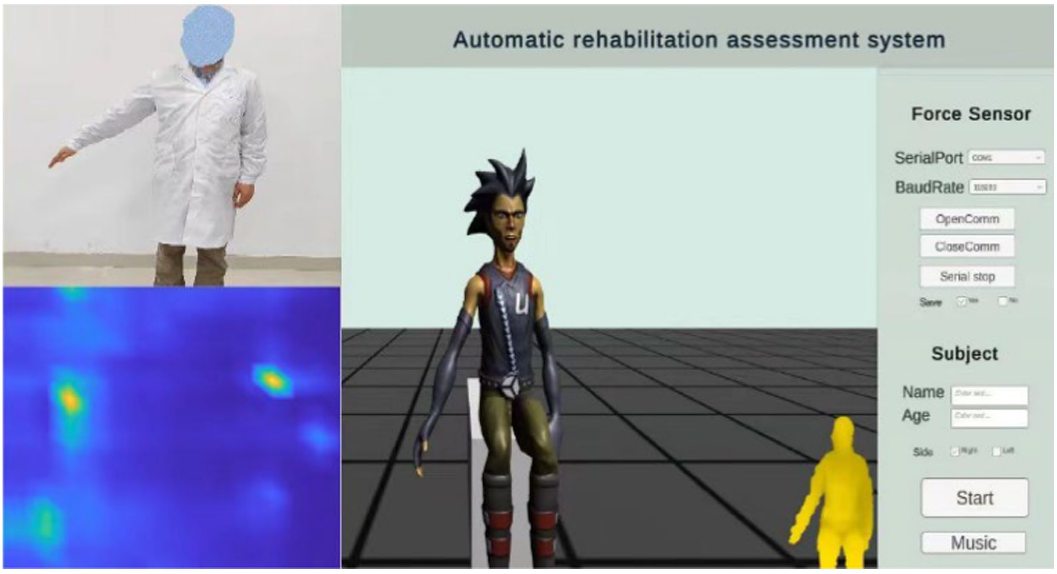

FIGURE 4
Human machine interface.

assessment of the movement for optimal exercise performance. At the same time, the scene is equipped with soothing background music to help relieve the patient's mood.

The specific operating procedures are as follows: First, enter the patient's name and age, select the affected side, and click the Start button. The video teaching starts, the patient imitates the movements demonstrated by the doctor, and Azure Kinect synchronously collects the patient's postural information, mainly including postural measurements of items (3–17), (19–25) and (31–33). Music can be played simultaneously by clicking the Music button to create a favorable environment. Pause the video at the end of the pose acquisition. Then select the appropriate serial port, set the baud rate 115,200, and click to continue playing the video. Combine the video instruction to capture the force information of the items (26–30), click the save button to save the force information, switch the serial port using the pause button, and click the finish button when the acquisition is complete.

FIGURE 5
Experimental platforms.

3 Experiments and results

3.1 Experiment setup

The experimental equipment of the rehabilitation evaluation system mainly includes a computer, a monitor, an Azure Kinect, a tripod and a grasping tool attached with a distributed sensor [cylinder (diameter: $d = 1$ cm, $d = 3$ cm, $d = 5$ cm), ball, slice], as shown in Figure 5. The subjects sat on a chair without armrests, with the Azure Kinect placed 1.5 m directly in front of them, so that the subjects were in the center of the best visual field of the camera, and the grip tools attached with distributed sensors were placed on the table next to the subjects. According to the size of human palm, 16 rows and 16 columns DFPS is selected. Two hundred fifty-six sensing units are distributed in the square of 150 mm × 150 mm, and the size of each induction unit is 7.5 mm × 7.5 mm.

While the subject performed various movements according to Table 1, the Azure Kinect in combination with the MediaPipe measured the posture information of each joint of the upper limb and the hand on both the affected and the healthy side. The values of each feature used for the evaluation were then calculated. DFPS is attached to the gripping tool to measure the distributed force of the hand. During the hook grasp (26), the DFPS was attached to a cylinder with a 3 cm diameter. The subject's hand was hooked to grasp the device with maximum force in the way of carrying a purse. The forces of both the healthy hand and the affected hand were measured. For the lateral pinch (27), DFPS was attached to the slice and placed between the thumb and index finger. The other four fingers were pinched together with the thumb to pinch the DFPS with the maximum force. The measured result was lateral pinch force. For the Pincer grasp (28), the DFPS was attached to the 1 cm-diameter cylinder. The measured hand grasps the device as if holding a pencil to measure the force. For the cylinder grasp (29), the DFPS is attached to a 5 cm diameter cylinder, and the hand grasps the device in the manner of holding a cup. For the Sphere grasp (30), the DFPS is attached to the spherical object and the device is held in the hand for force measurement. The cylindrical grasping and hook grasping posture are shown in Figure 6, panel (A) is the hand grasps the cylinder of the 5 cm in a cylindrical shape, panel (B) is the hand grasps 3 cm cylinder in the form of a hook.

3.2 Participant and protocol

Participants included 17 stroke patients (10 males, 7 females; Age: 58 ± 16.5 years) and 1 healthy subject, no severe cognitive impairment (MMSE score >15), and able to maintain a chair-sitting position. Patients with a Fugl–Meyer score below 10 were excluded due to the severity of their post-stroke condition, which hindered the collection of signals from the affected limb. Prior to data collection, all patients underwent evaluation by a rehabilitation technician and were tested for cognitive impairment. The patient's statistical information is shown in the Table 2.

In this study, an experienced rehabilitation physician demonstrated and recorded each action of automatic Fugl–Meyer. They also provided a detailed explanation for each action. Before each data collection, the experimenter explained the experiment process to the patient. Then, they played the evaluation action video, and left enough time for the patient to practice the action. Finally, the experiment was conducted. Each subject was evaluated 6 times, each time at an interval of 10 min, to reduce the impact of the previous exercise on the next one. Both the affected and healthy limbs were tested with the same movements. It should be noted that the experiment will be stopped as soon as the subject reports any uncomfortable sensations. To reduce the influence of uncertain factors, four better results were selected for each patient. These results were used as the original data for the rehabilitation evaluation. A total of 72 groups of data were obtained.

3.3 Statistical analysis

To evaluate the accuracy of the proposed assessment method in this research, Bland–Altman analysis was applied to assess the agreement between the assessment results of this system (SFMA) and those of the rehabilitation physicians (RPFMA) Bland–Altman analysis calculates the limits of agreement between the two measurements, which are then visualized graphically.

Pearson correlation analyses were performed between the subjects' SFMA and the total FMA-UE score (TFMA) to evaluate whether the SFMA score of the 30-item motor assessment method proposed in this research could replace the TFMA of the 33 upper extremity movements in the FMA-UE scale.

4 Results

4.1 Posture measurement results

The partial results of the posture measurements are shown in Figure 7. Sub-figure (A) shows the results of the 15th item for a subject with a Fugl–Meyer score of 75. This item consists of a total of three movements. The graph displays the shoulder abduction angle (red solid line) with a maximum of approximately 34°, the elbow angle (blue dotted line) with a measured range of 0–2°, indicating that the elbow is in a state of straightening, and the angle for forearm rotation forward (green dotted line) with a range of 1–19°, indicating poor forward rotation ability. The results suggest that the subject is only able to partially complete the movement, and forward rotation of the forearm is essentially impossible. The fuzzy controller took AROM/HROM (ROM Ratio), AMV/HMV (MV Ratio), and SD as inputs and Rehabilitation Assessment Levels as output. Both inputs and outputs used three affiliation functions: low, medium, and high. The domains of ROM Ratio, MV Ratio, and SD were [0, 1], and the domain of the output was [0, 2]. The three inputs were represented as trapezoidal subordination functions with parameters [−0.4 −0.1 0.1 0.4], [0.1 0.4 0.6 0.9] and [0.6 0.9 1.1 1.4]. The output utilized three triangular membership functions for

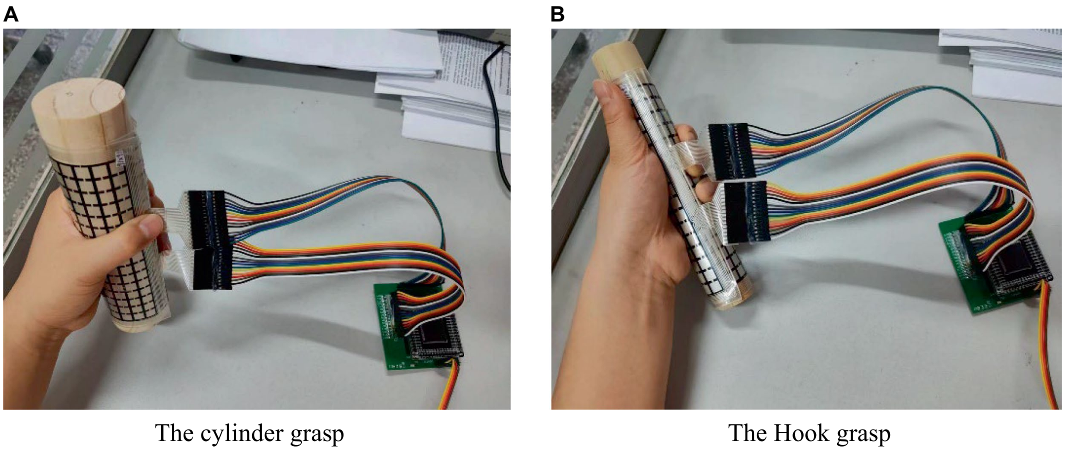

FIGURE 6
Measuring method of distributed force, **(A)** the cylinder grasp, **(B)** the hook grasp.

TABLE 2 The patient's statistical information.

Subject	Gender	Affected side	Etiology	Time since stroke (month)	FME-UE
S1	M	R	Ischemic	1	35
S2	M	R	Hemorrhagic	3	29
S3	M	L	Ischemic	7	14
S4	M	L	Ischemic	1	16
S5	M	L	Hemorrhagic	2	27
S6	F	L	Hemorrhagic	13	53
S7	F	R	Hemorrhagic	4	25
S8	F	L	Ischemic	1	38
S9	F	R	Ischemic	5	42
S10	M	R	Ischemic	7	31
S11	M	R	Hemorrhagic	5	57
S12	M	L	Ischemic	2	20
S13	M	R	Hemorrhagic	1	41
S14	F	R	Hemorrhagic	3	47
S15	F	L	Ischemic	4	57
S16	F	L	Hemorrhagic	2	28
S17	F	L	Hemorrhagic	1	60

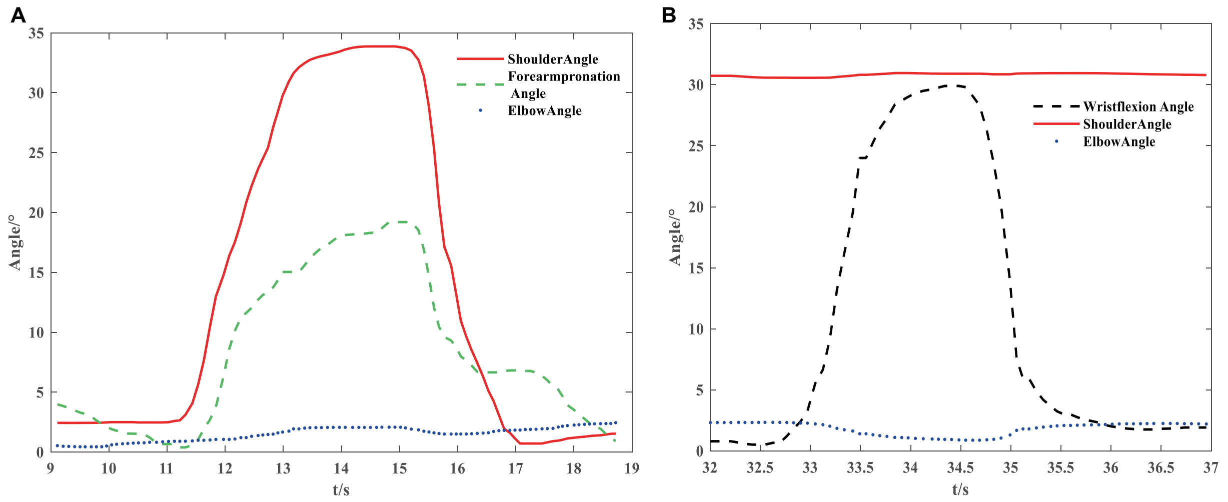

The results of item 15

The results of item 21

FIGURE 7
Posture measurement result, **(A)** the results of item 15, **(B)** the results of item 21.

affiliation with parameters [0 0 1], [0 1 2] and [1 2 2]. The fuzzy rule is illustrated in Figure 8. The FISRA scored the shoulder abduction angle with 1 point, the elbow angle with 2 points, and the forward forearm rotation with 1 point. The final assessment result was 1 point, which was consistent with the doctor's assessment.

Subfigure (B) displays the results of the 21st test maneuver for a subject with a Fugl–Meyer score of 82. The maneuver consisted of three total movements. The graph displays the wrist dorsiflexion angle (black dotted line) with a maximum of approximately 30°. The elbow angle (blue dotted line) is measured within the range of 0–3°, indicating a straightened elbow joint. The joint forward flexion angle (red solid line) is at an angle of about 31°, indicating better completion of the subject's wrist dorsiflexion. The FISRA scored 2 for wrist dorsiflexion, elbow joint angle, and shoulder joint angle. The final assessment result for this movement was also 2, which was consistent with the doctor's assessment.

4.2 Distributed pressure measurement results

The results of the healthy hand were mirrored to facilitate comparison with the affected side. This put the fingers of the affected and healthy sides in the same approximate area. Figure 9 displays the distributed pressure measured by the cylindrical grasping device. Sub-figure (A) shows the maximum force information (Force1) when grasping the cylinder with the healthy hand. The force points of the thumb, index, middle, ring and little fingers are clearly visible, with maximum forces of 12.2 ± 1.3 N, 7.6 ± 1.2 N, 6.3 ± 1.6 N, 4.1 ± 2.0 N, and 3.6 N ± 2.6, respectively. Together with the force information for the rest of the hand, the total combined force of the hand is 68.2 ± 5.7 N.

Sub-figure (B) shows the maximum force information (Force2) when the affected hand grasps the 5 cm cylinder. This figure only shows the force information of the thumb, middle finger and ring finger. The maximum forces of these finger are 5.1 ± 2.7 N, 4.5 ± 1.5 N, 3.4 N ± 1.3 N, respectively. The total force of the palm sensing unit is 24.8 N. It shows that the patient's index finger does not produce force information. Upon reviewing the patient's medical records, it was found that the patient has motor dysfunction of the index finger joint

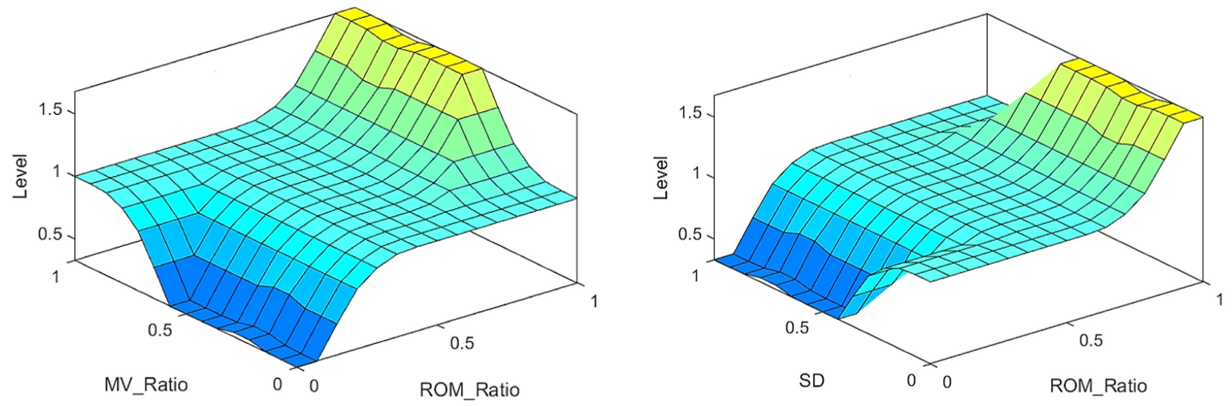

FIGURE 8
Fuzzy rules.

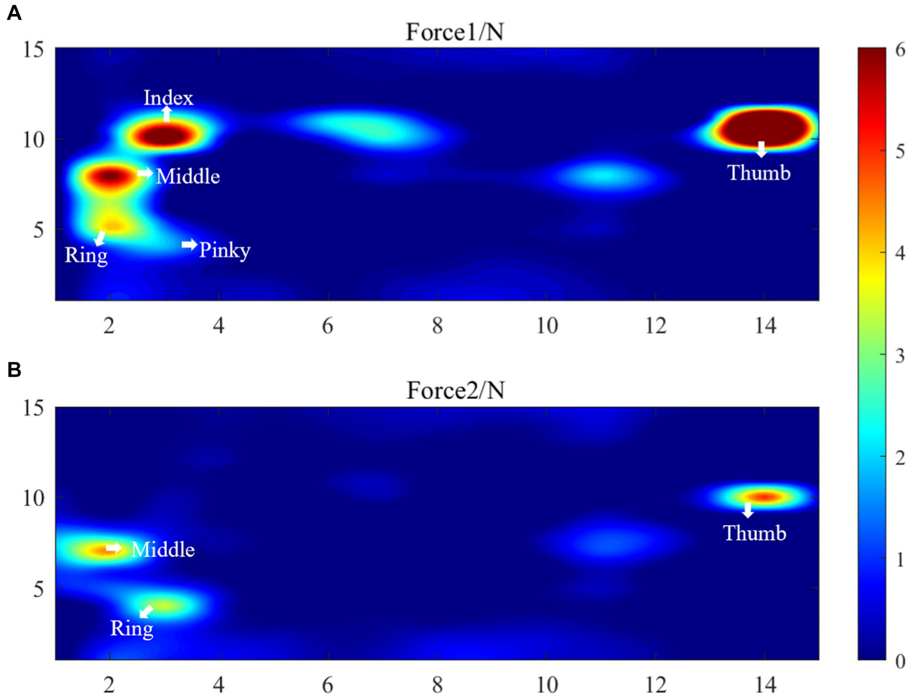

FIGURE 9
Distributed pressure measurement results, **(A)** Force1 (the maximum force information Force1 when grasping the cylinder with the healthy hand), **(B)** Force2 (the maximum force information Force2 when the affected hand grasps the 5 cm cylinder).

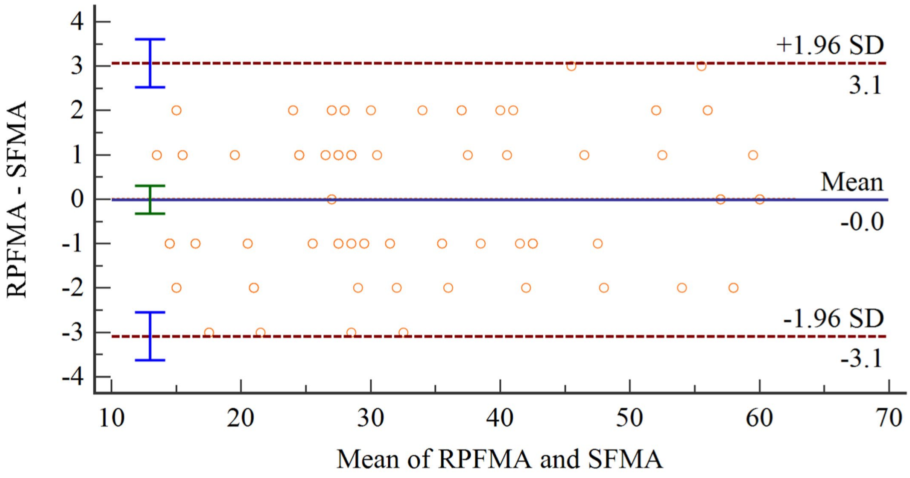

FIGURE 10
The Bland–Altman plot of the two assessment results.

on the affected side. The patient's cylindrical grip motor function score on the affected side was assessed as 1 by FISRA, which was consistent with the physician's evaluation.

4.3 Statistical analysis results

The Shapiro–Wilk test was used to test the difference between SFMA and TFMA and ensure a normal distribution. Then Bland–Altman diagram was used to analyze the consistency of the two groups of data. As shown in Figure 10, the abscissa represents the average value of the two sets of data. The ordinate represents the difference between the two groups of data. The upper and lower brown horizontal dashed lines represent the upper and lower limits of 95% consistency. The middle blue solid line represents the average difference. The orange dotted line represents the average difference of 0. The arithmetic mean is −0.0102, 95% confidence interval (CI) is −0.3249 to 0.3054. As can be seen from the figure, there is no point outside the 95% CI, so the consistency between the two evaluation methods is good.

The SFMA mean (SFMAM) of each subject was calculated, and a total of 18 data sets were obtained. The Pearson correlation analysis between SFMAM and TFMA of the subjects' upper limbs was shown in Figure 11, $r = 0.99 \sim p < 0.001$. There was a very significant positive correlation between them.

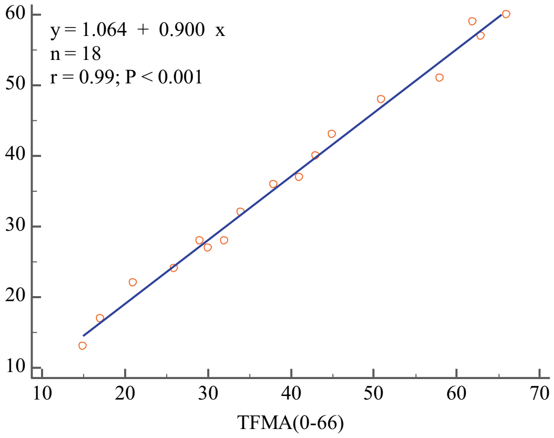

FIGURE 11
The correlation between SFMAM and TFMA.

5 Discussion

Rehabilitation assessment can evaluate the severity, development trend, and prognosis of patients with dysfunction. It provides an objective basis for formulating rehabilitation treatment plans. It also observes the development and changes of disability to evaluate the effect of rehabilitation treatment, and develops new and more effective means of rehabilitation treatment. Rehabilitation treatment often starts with a rehabilitation assessment and ends with another assessment. Therefore, the rehabilitation assessment of stroke patients is very important.

Rehabilitation physicians use protractors, grip dynamometers, and other equipment for manual measurement and evaluation. The measurement method is related to the doctor's preference, and the measurement results depend on the doctor's habits. The upper limb rehabilitation assessment time lasts more than 30 min. This longer time results in fewer clinical and scientific rehabilitation assessment methods. Most of the formalized rehabilitation assessments in hospitals are assessed only once at inpatient and once at discharge.

The lack of uniform evaluation standards among rehabilitation healthcare systems, the lack of reasonable evaluation indexes for rehabilitation physicians, and the lack of a way to compare patient treatment outcomes limit the development of rehabilitation therapy technology. Our proposed automated Fugl-Meyer system, including Azure Kinect and distributed pressure sensors need not be worn. The device uses automated measurements where the patient only interacts with the display without human intervention, improving standardization and accuracy of measurements. Each assessment takes less than 10 min, greatly improving the efficiency of rehabilitation assessment. Patient rehabilitation assessment time included the time for the patient to perform the assessment actions and the device switching time. The device switching times were all 3 min, and the time consumed by the patients varied, as shown in the Figure 12. At the same time, the addition of virtual rehabilitation assessment scenarios can greatly improve the enthusiasm of patients to participate in rehabilitation assessment.

Various technologies can be used to acquire human motion information, including data gloves, sEMG, IMUs, robots, and Kinect. Data gloves can accurately capture hand opening and closing information. However, they may be difficult to wear for patients with muscle contractures.

sEMG can measure the EMG signals of a limited number of muscles. Since human movement is the result of the joint action of upper limb muscles, sEMG cannot fully characterize the overall movement of the subject. Additionally, sEMG is susceptible to interference and requires close proximity to the muscle being measured. Measuring the sEMG signals of the active muscles in the shoulder joint necessitates the removal of clothing, making the measurement inconvenient (Merletti et al., 2021). The inertial measurement unit used to measure movement must be worn in multiple locations and is also prone to displacement, causing discomfort to the subject (Li and Yu, 2023). Robots for rehabilitation assessment can be expensive and limited to hospitals or large communities. However, the Kinect system offers a portable, cost-effective, and practical alternative that does not require markers and is convenient for patients to use. The Azure Kinect is even more optimized and accurate than the previous versions. It is important to prioritize patient comfort and universality when selecting an assessment device. This paper selects Azure Kinect for upper extremity joint acquisition. However, it should be noted that Azure Kinect has limited hand joint acquisition capabilities and can only track four joint information points: wrists, hand tip, palm center, and thumb. To enhance the accuracy of the automatic evaluation system, Azure Kinect is combined with MediaPipe to acquire hand posture.

Lee's device, which uses Kinect combined with FSR sensors for rehabilitation assessment, only measures the force exerted on the index finger and thumb fingertip. This limited measurement does not accurately reflect the force exertion in other parts of the hand. If a subject is unable to exert force on the index finger, the hand grip force information cannot be accurately measured.

To increase the generalizability of automated devices for rehabilitation assessment, this study proposes using a large-area distributed flexible pressure sensor to measure hand force during different gripping maneuvers. The flexible pressure sensor is distributed, thin, and easy to bend. It can be attached to various grasping tools to measure hand force information during different grasping modes, such as hook grasp., lateral pinch, pincer grasp., cylindrical grasp., and spherical grasp. The sensor is distributed and has a large area to test the force distribution of the entire palm. This allows for a more detailed and accurate measurement of the force exerted by the hand at each location. Figure 9 displays the force information of the entire palm on the healthy side. The five fingers' tips exert a more pronounced force, and a healthy individual's maximum fingertip force is approximately 12.2 N. Besides the fingertip's tip, force information is also present at the root of the index finger, the greater and lesser pisiform areas. Therefore, the distributed sensor proposed in this study covers a larger area and requires less interference without the need for the user to wear it. Users can grasp objects naturally, without the need for a demanding grip position.

The assessment criteria for patients may vary due to differences in joint strength and range of motion. This study extracted characteristic information, such as range of motion, speed, length ratio, angle, acceleration, and distribution force. The ratios of features or deviations between the affected and healthy sides were entered into a single/multigroup fuzzy logic assessment model for rehabilitation evaluation. This increases the standardization of the rehabilitation assessment system and reduces the impact of individual differences on the results.

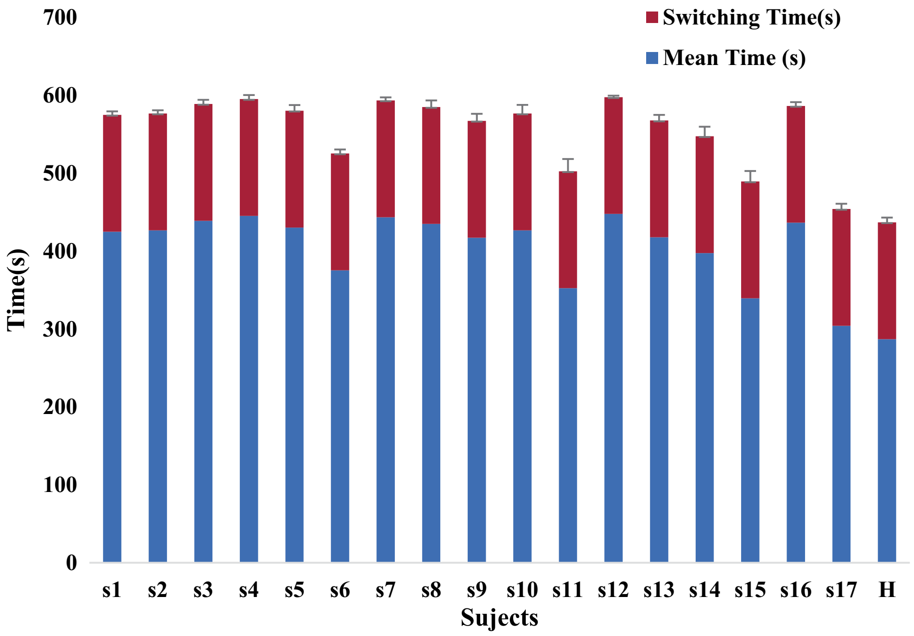

FIGURE 12
The rehabilitation assessment time.

The study proposes an automatic rehabilitation assessment system for upper limb motor function based on posture and distributed force measurement. The system only requires Azure Kinect and an array of DFPS to be connected to a computer and used in conjunction with the relevant software. It is simple to operate, easy to install, portable, and inexpensive, making it suitable for home rehabilitation assessment. Because rehabilitation training is a long-term process, it is not practical or cost-effective to conduct it exclusively in the hospital. During the recovery and after-effects period of a stroke, it is important to not only receive training in the hospital but also to pay attention to rehabilitation training at home. This training lacks the guidance of a doctor, so it is crucial to focus on rehabilitation assessment. An automated rehabilitation assessment device is essential. The automated assessment system proposed in this paper can realize safe and efficient home rehabilitation training and assessment, combined with the virtual rehabilitation training scenario previously proposed by the authors (Bai and Song, 2019).

The combination of Azure Kinect and MediaPipe can improve the accuracy of hand posture tracking by largely reducing occlusions and singularities. However, it cannot completely eliminate them. Occlusions can still occur if the shoulder, elbow, wrist, and Azure Kinect are in a straight line. Some scholars have proposed using Leap Motion for hand tracking. However, its hand tracking area is limited. Additionally, rehabilitation assessment is a dynamic process, and the tracking accuracy of Leap Motion decreases under high dynamic conditions. Therefore, dynamic high-precision tracking of hand joints remains a challenging problem to solve.

6 Conclusion

This research proposed an automatic assessment system for the motor function of hemiplegic upper limbs. The system can automatically assess the motor function of 30 movements on the FMA scale by measuring posture and distribution force. By comparing the posture and distribution force information between the affected and healthy sides, the influence of individual differences on the assessment results is reduced. The experiment on automated assessment with 17 participants demonstrated a significant correlation ($r = 0.99$, $p < 0.001$) between the results of the automated assessment system and those of the physician's assessment. This research lays the foundation for standardizing and unifying the automatic rehabilitation assessment system.

Data availability statement

The raw data supporting the conclusions of this article will be made available by the authors, without undue reservation.

Ethics statement

The studies involving humans were approved by Nanjing Tongren Hospital Science and Ethics Committee. The studies were conducted in accordance with the local legislation and institutional requirements. The participants provided their written informed consent to participate in this study. Written informed consent was obtained from the individual(s) for the publication of any potentially identifiable images or data included in this article.

Author contributions

JB: Conceptualization, Data curation, Formal analysis, Funding acquisition, Investigation, Methodology, Project administration, Resources, Software, Supervision, Validation, Visualization, Writing – original draft, Writing – review & editing. GL: Data curation, Software, Writing – original draft. XL: Writing – review & editing. XW: Conceptualization, Supervision, Writing – review & editing.

Funding

The author(s) declare financial support was received for the research, authorship, and/or publication of this article. This work was supported by the Natural Science Foundation of Jiangsu Province (Grant No. BK20210930), Natural Science Research of Jiangsu Higher Education Institutions of China (Grant No. 21KJB510039), and the Scientific Research Foundation of Nanjing Institute of Technology (Grant No. YKJ202045).

Conflict of interest

The authors declare that the research was conducted in the absence of any commercial or financial relationships that could be construed as a potential conflict of interest.

Publisher's note

References

Ambros-Antemate, J., Reyes-Flores, A., Argueta-Figueroa, L., Ramírez-Ramírez, R., Vargas- Treviño, M., Gutiérrez-Gutiérrez, J., et al. (2022). Accuracy of machine learning algorithms for the assessment of upper-limb motor impairments in patients with post-stroke hemiparesis: a systematic review and meta-analysis. *Adv. Clin. Exp. Med.* 31, 1309–1318. doi: 10.17219/acem/152596

Bai, J., and Song, A. (2019). Development of a novel home based multi-scene upper limb rehabilitation training and evaluation system for post-stroke patients. *IEEE Access* 7, 9667–9677. doi: 10.1109/ACCESS.2019.2891606

Chung, C., Su, M., Lee, S., Wu, E. H., Tang, L., and Yeh, S. (2022). An intelligent motor assessment method utilizing a bi-lateral virtual-reality task for stroke rehabilitation on upper extremity. *IEEE J. Transl. Eng. Health Med.* 10, 1–11. doi: 10.1109/JTEHM.2022.3213348

Da Gama, A. E. F., Chaves, T. M., Figueiredo, L. S., Baltar, A., Meng, M., Navab, N., et al. (2016). MirrARbilitation: a clinically-related gesture recognition interactive tool for an AR rehabilitation system. *Comput. Methods Prog. Biomed.* 135, 105–114. doi: 10.1016/j.cmpb.2016.07.014

Deb, S., Islam, M. F., Rahman, S., and Rahman, S. (2022). Graph convolutional networks for assessment of physical rehabilitation exercises. *IEEE Trans. Neural Syst. Rehabil. Eng.* 30, 410–419. doi: 10.1109/TNSRE.2022.3150392

Du, Y., Shi, Y., Ma, H., Li, D., Su, T., Meidege, O. Z., et al. (2022). Application of multi-dimensional intelligent visual quantitative assessment system to evaluate hand function rehabilitation in stroke patients. *Brain Sci.* 12:1698. doi: 10.3390/brainsci12121698

Dutta, D., Aruchamy, S., Mandal, S., and Sen, S. (2022). Poststroke grasp ability assessment using an intelligent data glove based on action research arm test: development, algorithms, and experiments. *IEEE Trans. Biomed. Eng.* 69, 945–954. doi: 10.1109/TBME.2021.3110432

Eichler, N., Hel-Or, H., Shmishoni, I., Itah, D., Gross, B., and Raz, S. Non-invasive motion analysis for stroke rehabilitation using off the shelf 3D sensors. (2018). Available at: https://go.exlibris.link/CVm1wb1J

Fang, Q., Mahmoud, S. S., Gu, X., and Fu, J. (2019). A novel multistandard compliant hand function assessment method using an infrared imaging device. *IEEE J. Biomed. Health Inform.* 23, 758–765. doi: 10.1109/JBHI.2018.2837380

Francisco-Martínez, C., Padilla-Medina, J. A., Prado-Olivarez, J., Pérez-Pinal, F. J., Barranco-Gutiérrez, A. I., and Martínez-Nolasco, J. J. (2022). Kinect v2-assisted semi-automated method to assess upper limb motor performance in children. *Sensors* 22:2258. doi: 10.3390/s22062258

Garro, F., Chiappalone, M., Buccelli, S., De Michieli, L., and Semprini, M. (2021). Neuromechanical biomarkers for robotic neurorehabilitation. *Front. Neurorobot.* 15:742163. doi: 10.3389/fnbot.2021.742163

Gladstone, D. J., Danells, C. J., and Black, S. E. (2002). The Fugl–Meyer assessment of motor recovery after stroke: a critical review of its measurement properties. *Neurorehabil. Neural Repair* 16, 232–240. doi: 10.1177/154596802401105171

Huo, W., Angeles, P., Tai, Y. F., Pavese, N., Wilson, S., Hu, M. T., et al. (2020). A heterogeneous sensing suite for multisymptom quantification of Parkinson's disease. *IEEE Trans. Neural Syst. Rehabil. Eng.* 28, 1397–1406. doi: 10.1109/TNSRE.2020.2978197

Kim, J., Park, G., Lee, S., and Nam, Y. (2020). Analysis of machine learning-based assessment for elbow spasticity using inertial sensors. *Sensors* 20:1622. doi: 10.3390/s20061622

Lee, S., Lee, Y., and Kim, J. (2018). Automated evaluation of upper-limb motor function impairment using Fugl–Meyer assessment. *IEEE Trans. Neural Syst. Rehabil. Eng.* 26, 125–134. doi: 10.1109/TNSRE.2017.2755667

Lee, S., Song, M., and Kim, J. (2016). Towards clinically relevant automatic assessment of upper-limb motor function impairment. 2016 IEEE-EMBS International Conference on Biomedical and Health Informatics (BHI). IEEE.

Li, Y., Li, C., Shu, X., Sheng, X., Jia, J., and Zhu, X. (2022). A novel automated RGB-D sensor-based measurement of voluntary items of the Fugl–Meyer assessment for upper extremity: a feasibility study. *Brain Sci.* 12:1380. doi: 10.3390/brainsci12101380

Li, C., Yang, H., Cheng, L., Huang, F., Zhao, S., Li, D., et al. (2022). Quantitative assessment of hand motor function for post-stroke rehabilitation based on HAGCN and multimodality fusion. *IEEE Trans. Neural Syst. Rehabil. Eng.* 30, 2032–2041. doi: 10.1109/TNSRE.2022.3192479

Li, T., and Yu, H. (2023). Upper body pose estimation using a visual-inertial sensor system with automatic sensor-to-segment calibration. *IEEE Sensors J.* 23, 6292–6302. doi: 10.1109/JSEN.2023.3241084

Meng, L., Zhang, T., Zhao, X., Wang, D., Xu, R., Yang, A., et al. (2023). A quantitative lower limb function assessment method based on fusion of surface EMG and inertial data in stroke patients during cycling task. *Biomed. Signal Process. Control* 85:104880. doi: 10.1016/j.bspc.2023.104880

Merletti, R., Campanini, I., Rymer, W. Z., and Disselhorst-Klug, C. (2021). Editorial: surface electromyography: barriers limiting widespread use of sEMG in clinical assessment and neurorehabilitation. *Front. Neurol.* 12:642257. doi: 10.3389/fneur.2021.642257

Miao, S., Dang, Y., Zhu, Q., Li, S., Shorfuzzaman, M., and Lv, H. (2021). A novel approach for upper limb functionality assessment based on deep learning and multimodal sensing data. *IEEE Access* 9, 77138–77148. doi: 10.1109/ACCESS.2021.3080592

Moon, J. H., Kim, J., Hwang, Y., Jang, S., and Kim, J. (2023). Novel evaluation of upper-limb motor performance after stroke based on normal reaching movement model. *J. Neuroeng. Rehabil.* 20:66. doi: 10.1186/s12984-023-01189-6

Ona Simbana, E. D., Sanchez-Herrera Baeza, P., Jardon Huete, A., and Balaguer, C. (2019). Review of automated systems for upper limbs functional assessment in neurorehabilitation. *IEEE Access* 7, 32352–32367. doi: 10.1109/ACCESS.2019.2901814

Oubre, B., Daneault, J., Jung, H., Whritenour, K., Miranda, J. G. V., Park, J., et al. (2020). Estimating upper-limb impairment level in stroke survivors using wearable inertial sensors and a minimally-burdensome motor task. *IEEE Trans. Neural Syst. Rehabil. Eng.* 28, 601–611. doi: 10.1109/TNSRE.2020.2966950

Pan, B., Huang, Z., Jin, T., Wu, J., Zhang, Z., and Shen, Y. (2021). Motor function assessment of upper limb in stroke patients. *J. Healthc. Eng.* 2021, 1–11. doi: 10.1155/2021/6621950

Ren, P., Bosch Bayard, J. F., Dong, L., Chen, J., Mao, L., Ma, D., et al. (2020). Multivariate analysis of joint motion data by Kinect: application to Parkinson's disease. *IEEE Trans. Neural Syst. Rehabil. Eng.* 28, 181–190. doi: 10.1109/TNSRE.2019.2953707

Sanford, J., Moreland, J., Swanson, L. R., Stratford, P. W., and Gowland, C. (1993). Reliability of the Fugl–Meyer assessment for testing motor performance in patients following stroke. *Phys. Ther.* 73, 447–454. doi: 10.1093/ptj/73.7.447

Sardari, S., Sharifzadeh, S., Daneshkhah, A., Nakisa, B., Loke, S. W., Palade, V., et al. (2023). Artificial intelligence for skeleton-based physical rehabilitation action evaluation: a systematic review. *Comput. Biol. Med.* 158:106835. doi: 10.1016/j.compbiomed.2023.106835

Turon, M., Fernández-Gonzalo, S., de Haro, C., Magrans, R., López-Aguilar, J., and Blanch, L. (2018). Mechanisms involved in brain dysfunction in mechanically ventilated critically ill patients: implications and therapeutics. *Ann. Transl. Med.* 6:30. doi: 10.21037/atm.2017.12.10

Ueyama, Y., Takebayashi, T., Takeuchi, K., Yamazaki, M., Hanada, K., Okita, Y., et al. (2023). Attempt to make the upper-limb item of objective Fugl–Meyer assessment using 9-axis motion. *Sensors* 23:5213. doi: 10.3390/s23115213

Van Crombrugge, I., Sels, S., Ribbens, B., Steenackers, G., Penne, R., and Vanlanduit, S. (2022). Accuracy assessment of joint angles estimated from 2D and 3D camera measurements. *Sensors* 22:1729. doi: 10.3390/s22051729

Wei, F., Xu, G., Wu, Q., Kuang, J., Tian, P., Qin, P., et al. (2022). Azure Kinect calibration and parameter recommendation in different scenarios. *IEEE Sensors J.* 22, 9733–9742. doi: 10.1109/JSEN.2022.3166540

Wolf, S. L., Lecraw, D. E., Barton, L. A., and Jann, B. B. (1989). Forced use of hemiplegic upper extremities to reverse the effect of learned nonuse among chronic stroke and head-injured patients. *Exp. Neurol.* 104, 125–132. doi: 10.1016/S0014-4886(89)80005-6

Wu, G., van der Helm, F. C. T., DirkJan Veeger, H. E. J., Makhsous, M., Van Roy, P., Anglin, C., et al. (2005). ISB recommendation on definitions of joint coordinate systems of various joints for the reporting of human joint motion—part II: shoulder, elbow, wrist and hand. *J. Biomech.* 38, 981–992. doi: 10.1016/j.jbiomech.2004.05.042

frontiers | Frontiers in Neuroscience

TYPE Original Research
PUBLISHED 21 February 2024
DOI 10.3389/fnins.2024.1355052

Design and motion control of exoskeleton robot for paralyzed lower limb rehabilitation

Zhiyong Zhu[1,2], Lingyan Liu[2], Wenbin Zhang[3], Cong Jiang[2], Xingsong Wang[2]* and Jie Li[1]*

[1]College of Automation, Nanjing University of Posts and Telecommunications, Nanjing, China, [2]School of Mechanical Engineering, Southeast University, Nanjing, China, [3]College of Computer Science and Software Engineering, Hohai University, Nanjing, Jiangsu, China

EDITED BY
Yuquan Leng,
Southern University of Science and Technology, China

REVIEWED BY
Yangkun Zhang,
Harbin Institute of Technology, Shenzhen, China
Zhenxing Sun,
Nanjing Tech University, China

*CORRESPONDENCE
Jie Li
✉ jieli@njupt.edu.cn
Xingsong Wang
✉ xswang@seu.edu.cn

RECEIVED 13 December 2023
ACCEPTED 05 February 2024
PUBLISHED 21 February 2024

CITATION
Zhu Z, Liu L, Zhang W, Jiang C, Wang X and Li J (2024) Design and motion control of exoskeleton robot for paralyzed lower limb rehabilitation. *Front. Neurosci.* 18:1355052. doi: 10.3389/fnins.2024.1355052

Introduction: Patients suffering from limb movement disorders require more complete rehabilitation treatment, and there is a huge demand for rehabilitation exoskeleton robots. Flexible and reliable motion control of exoskeleton robots is very important for patient rehabilitation.

Methods: This paper proposes a novel exoskeleton robotic system for lower limb rehabilitation. The designed lower limb rehabilitation exoskeleton robot mechanism is mainly composed of the hip joint mechanism, the knee joint mechanism and the ankle joint mechanism. The forces and motion of the exoskeleton robot were analyzed in detail to determine its design parameters. The robot control system was developed to implement closed-loop position control and trajectory planning control of each joint mechanism.

Results: Multiple experiments and tests were carried out to verify robot's performance and practicality. In the robot angular response experiments, the joint mechanism could quickly adjust to different desired angles, including 15°, 30°, 45°, and 60°. In the trajectory tracking experiments, the exoskeleton robot could complete tracking movements of typical actions such as walking, standing up, sitting down, go upstairs and go downstairs, with a maximum tracking error of ±5°. Robotic wearing tests on normal people were performed to verify the assistive effects of the lower limb rehabilitation exoskeleton at different stages.

Discussion: The experimental results indicated that the exoskeleton robot has excellent reliability and practicality. The application of this exoskeleton robotic system will help paralyzed patients perform some daily movements and sports.

KEYWORDS

exoskeleton robots, behavior-assistant robots, human-robot systems, motion control, rehabilitation application

1 Introduction

The research direction of lower limb rehabilitation exoskeletons is focused on the design of these devices for patients with paraplegia, an area that is grounded in bionics principles and informed by a multidisciplinary intersection of mechanical engineering, electrical engineering, biomedical sciences, human bionics, artificial intelligence, and sensing technologies (Plaza et al., 2023). Through the strategic integration of various sensors, a diverse array of technologies spanning sensing, signal acquisition, and microcomputing were harnessed to inform the design of these rehabilitation robotic systems (Sarajchi et al., 2021).

In the context of paraplegia patient care, traditional rehabilitation therapies typically involve one-on-one or multiple-therapist-to-one treatment modalities administered by rehabilitation therapists (Wang et al., 2022). However, these approaches are often characterized by inefficiencies, difficulties in movement control and effect assurance, challenges in rehabilitation assessment, and a shortage of qualified healthcare professionals (Manuli et al., 2021). Rehabilitation exoskeletons offer a compelling alternative in this scenario, as they can significantly reduce the workload burdening rehabilitation departments, effectively liberating these departments and enhancing treatment efficiencies. Moreover, these exoskeletons have the potential to promote patient engagement in rehabilitation training, while also enabling objective evaluations of training intensity, duration, and outcomes. Consequently, patients can benefit from more systematic, comprehensive, and standardized rehabilitation interventions (Pinto-Fernandez et al., 2020).

For individuals with lower limb injuries, the utilization of lower limb rehabilitation exoskeletons can play a pivotal role in facilitating normal daily activities. These exoskeletons not only address various challenges related to medical resource allocation and manual training in rehabilitation settings, but also allow for precise measurements of human kinematics and physiological data through sophisticated sensory systems. These measurements allow rehabilitation physicians to more accurately assess the patient's condition (de Miguel-Fernández et al., 2023) and provide an objective foundation for refining and optimizing rehabilitation programs tailored to individual patient needs (Plaza et al., 2021; Su et al., 2023).

With the enhancement of people's living standards, individuals afflicted with limb movement disorders will increasingly pursue more comprehensive rehabilitation therapies. Consequently, the demand for these rehabilitative treatments will continue to escalate. The lower limb rehabilitation exoskeleton, a specialized medical device designed for patients with lower limb paralysis or disabilities, will occupy a pivotal position in rehabilitation therapies (Huamanchahua et al., 2021). The rehabilitation exoskeleton robot is an industrialization research topic with significant market prospects. The development of rehabilitation robots also plays an important role in the technological development of medical rehabilitation.

Currently, exoskeletons for paraplegic patients are divided into two main categories: rehabilitation exoskeleton robots consisting of an exoskeleton, crutches or auxiliary support mechanisms, and a control handle, such as the ReWalk rehabilitation[1] (Zeilig et al., 2012) bionic robotic leg (Esquenazi et al., 2017); and exoskeletons that do not need crutches or other auxiliary support mechanisms[2] (Esquenazi et al., 2012). Trajectory tracking control (Aole et al., 2020) is the main control method in most of the current exoskeleton robots (Andrade et al., 2021) and plays an important role in the operation and implementation of exoskeleton robots (Shi et al., 2019; Li et al., 2021). Traditional robotic arm modeling and control theories have laid an important foundation for the modeling, analysis and control of lower limb exoskeleton robots (Caulcrick et al., 2021; Shi et al., 2021), such as the sensitivity amplification control (Zheng, 2021), identification of the dynamic model (Bryan et al., 2021) and real-time adjustment of torque.

Most current research predominantly concentrates on walking states, it doesn't adequately account for the diverse daily life scenarios encountered by paraplegic patients, such as activities like standing up, sitting down, navigating stairs, or managing slight inclines. Moreover, the trajectory tracking control methodologies commonly utilized often rely on trajectories derived from the movements of able-bodied individuals in their daily routines, overlooking the unique circumstances and needs of patients who use crutches (Embry and Gregg, 2020).

In this paper, a multi-scenario and full-process rehabilitation exoskeleton robot system for paraplegic patients is proposed, which can realize daily actions such as walking, standing and sitting. The designed exoskeleton robot contains active hip joint mechanism, active knee joint mechanism and passive ankle joint mechanism. Detailed mechanical analysis and design were performed for the exoskeleton joint mechanisms. The exoskeleton control system combined sensors and drive motors could achieve closed-loop control and tracking motion of each exoskeleton joint. Motion response experiments and robot trajectory tracking experiments were conducted to verify its response performance and reliability. Multiple groups of normal people wore exoskeletons to test the assistance effect of walking, standing up, sitting down and other movements. Series of experiments and tests verified the practicability and stability of the lower limb rehabilitation exoskeleton robot. This exoskeleton robot system can help paraplegic patients recover and greatly enhance their mobility.

2 Exoskeleton robot design and analysis

2.1 Robot principle

Human lower limb movement represents a sophisticated and systematic process, initiated by the brain's dissemination of intentional movement information (Leech et al., 2022). This information is conveyed through nerve conduction via the spinal cord, extending to the nerves innervating the lower limbs. Subsequently, these nerves exercise control over the contraction and extension of lower limb muscles, which ultimately impetus the rotational movement of skeletal joints. Although it is possible for exoskeleton robot active joints to generate greater torque than human joints, the number and degrees of freedom (DOF) of robot joints are typically much lower than the corresponding number in the human body. This disparity necessitates the orchestration of coordinated movement between the human body, characterized by an extensive range of DOF, and the exoskeleton, which operates with a more restricted range. The motion control algorithms employed in exoskeletons should be meticulously designed to accommodate the inherent joint motion characteristics of the human body, with the aim of minimizing the sense of discomfort and discomfiture during human-machine interaction.

The human lower limb comprises three primary joints, namely the hip, knee, and ankle joints, which collectively facilitate a wide range of locomotive functions. The main joint movement mechanisms of the human lower limbs are presented in Figure 1. Considering the particularity of the exoskeleton robot being applied to patients with lower limb paralysis, in order to

---

[1] [EB/OL] Rewalk. http://www.rewalk.com.

[2] [EB/OL] http://www.gaylord.org/Our-Programs/Spinal-Cord/Ekso-Bionic-Eksoskeleton.

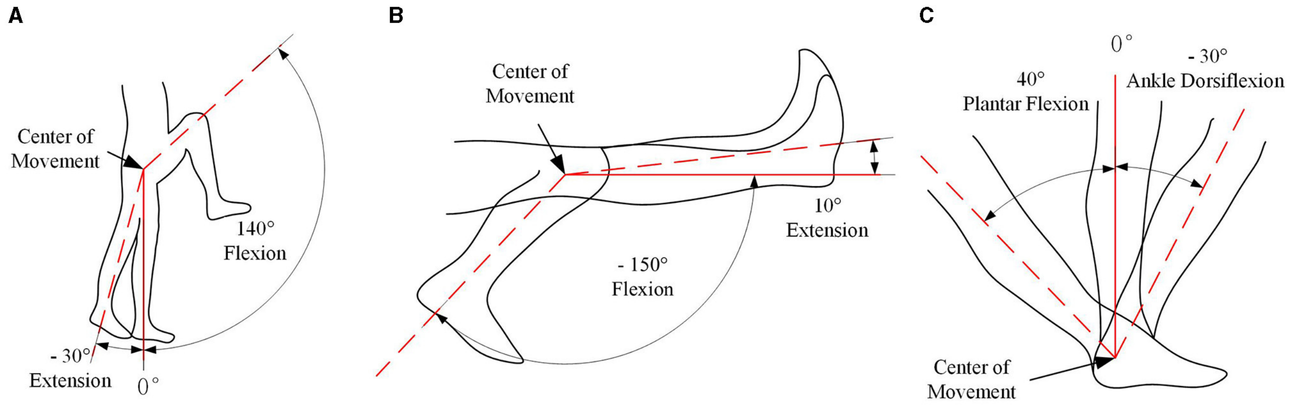

FIGURE 1
Movement mechanism diagram of the main joints of the human lower limbs. **(A)** Hip joint movement; **(B)** knee joint movement; **(C)** ankle joint movement.

TABLE 1 The lower limb DOF of the human and the developed exoskeleton robot.

DOF	Hip	Knee	Ankle
Human lower limb	3	1	3
Lower limb exoskeleton robot	1	1	3

TABLE 2 Joint motion range of human and exoskeleton on sagittal plane.

Joint	Human motion range	Exoskeleton motion range
Hip flexion/extension	−30° to 140°	−30° to 115°
Knee flexion/extension	−150° to 10°	−100° to 0°
Ankle dorsiflexion/plantar flexion	−30° to 40°	−20° to 20°

achieve walking purposes, the exoskeleton robot does not need to have the motion performance of all joints. Additionally, given the practical constraints posed by the need to optimize the size and weight of the exoskeleton, a judicious selection of joints is warranted. The designed lower limb exoskeleton robot has a total of 10 DOFs across both legs, with the hip and knee joints, each endowed with a single DOF, serving as active drivers of motion. Simultaneously, the ankle joint, endowed with three DOFs, operates as a passive joint. The DOF number of the lower lime exoskeleton robot is presented in Table 1.

In consideration of the operational context of wearable lower limb exoskeletons, each joint motion range should be consistent with the normal pedestrian walking. However, prioritizing the safety and wellbeing of the wearer, it is judicious to design the motion range of the exoskeleton system to be slightly restricted compared to that of human joints. The detail joint motion range on sagittal plane is presented in Table 2.

2.2 Robot mechanical design

The lower limb rehabilitation exoskeleton is a wearable mechanical system designed for patients with lower limb paralysis. This system integrates robotics technology, automation control theory, and clinical medical technology, culminating in an automated robotic device dedicated to facilitating a wide range of daily activities for these patients. When designing this robot system, the following critical factors should be considered:

(1) Rational allocation of DOF: given the exoskeleton's primary function of assisting paralyzed patients in accomplishing daily tasks—such as standing, sitting, climbing stairs, and walking—it is paramount to precisely determine joint positions and DOF. This ensures optimal support for these activities while mitigating the risk of secondary injuries to the patient;
(2) Adjustability of the mechanism: the application of the lower limb rehabilitation exoskeleton encompasses a vast age range, significant height disparities, and diverse body types. Consequently, the design process must accommodate patients with varying heights and weights by incorporating adjustable features such as leg bar length, waist width, and strap mechanisms;
(3) Reasonable allocation of joint movement range: while ensuring the basic range of motion of each joint, it is imperative to anticipate extreme scenarios, such as drive failures. To mitigate potential risks, safety limits must be designed to distribute joint movement ranges in a manner that guarantees wearer safety and prevents secondary injuries;
(4) Convenient wearability: as the lower limb rehabilitation exoskeleton is worn externally on the human body, it must prioritize wearability. Ideally, after a concise user training, individuals should be able to effortlessly don and doff the exoskeleton. This requires a thoughtful design approach that balances complexity with usability, ensuring maximum comfort and ease of use for the wearer.

According to the above design points, as shown in Figure 2, a complete set of lower limb rehabilitation exoskeleton robot is proposed. The overall weight of this exoskeleton robot is

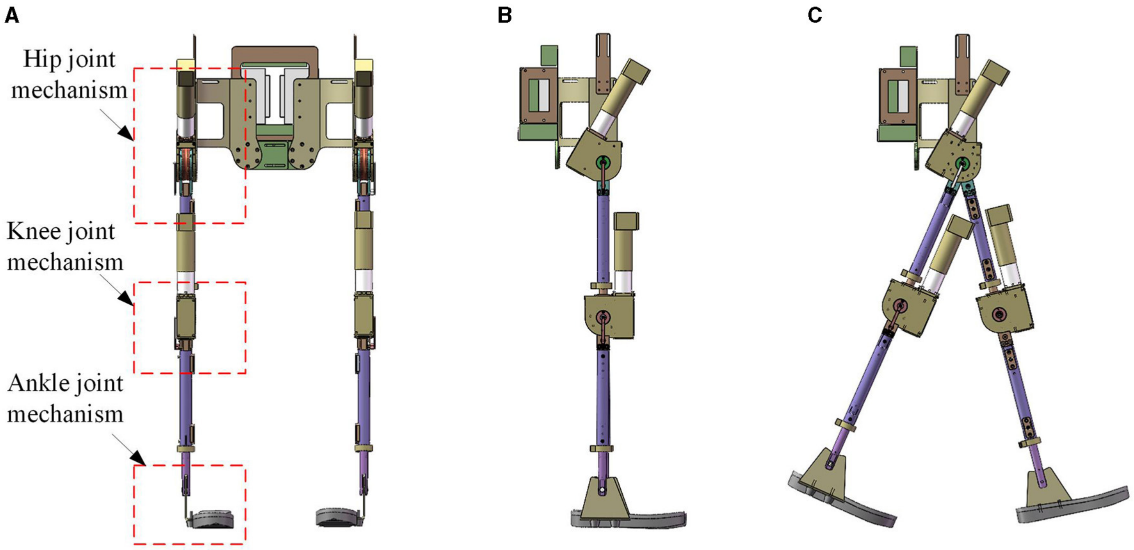

FIGURE 2
Design of lower limb rehabilitation exoskeleton. **(A)** Front view; **(B)** side view of upright state; **(C)** side view of stepping state.

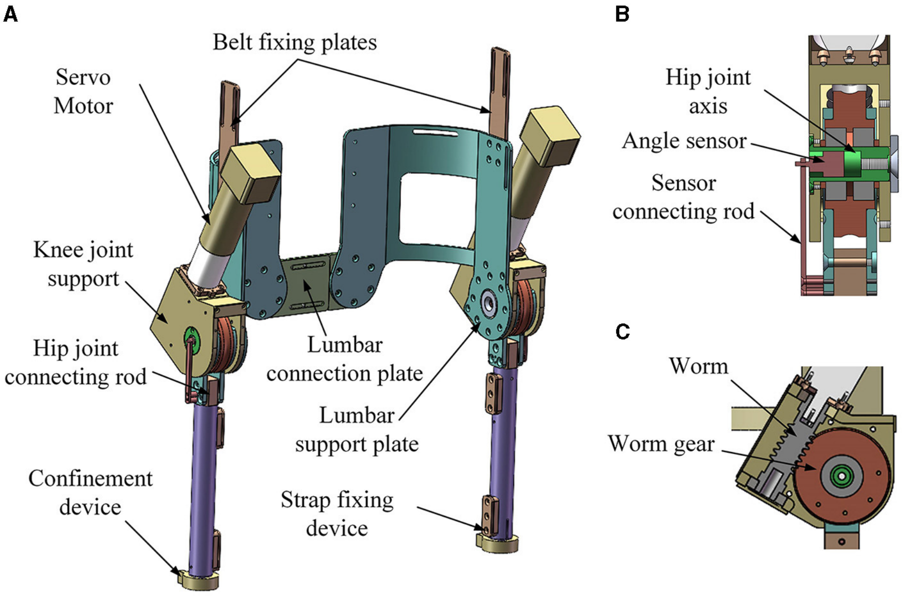

FIGURE 3
Hip joint mechanism of the lower limb rehabilitation exoskeleton. **(A)** Overall view; **(B)** front section view; **(C)** side section view.

<20 Kg.The designed exoskeleton robot mainly includes the backpack mechanism, the hip joint mechanism, the knee joint mechanism and the ankle joint mechanism.

The hip joint of the lower limb rehabilitation exoskeleton holds paramount importance, given its integral involvement in the majority of movements during daily exercises. Taking into account the prerequisites of safety, reliability, and practicality pertinent to patients with lower limb paralysis, the hip joint is designed as a driven joint. Figure 3 shows the hip joint mechanism of the lower limb rehabilitation exoskeleton.

Two hip joint mechanisms of the lower limb rehabilitation exoskeleton robot contain the following main components: servo motors, worms, worm gears, hip joint connecting rods, thigh poles, hip joint supports, hip joint axes, lumbar support plates, belt fixing plates, strap fixing devices, safety limit devices, confinement devices, sensor devices and a lumbar connecting plate. The sensor device contains sensor and sensor connecting rod.

The transmission process unfolds as follows: the servo motor initiates the motion by driving the reducer, which

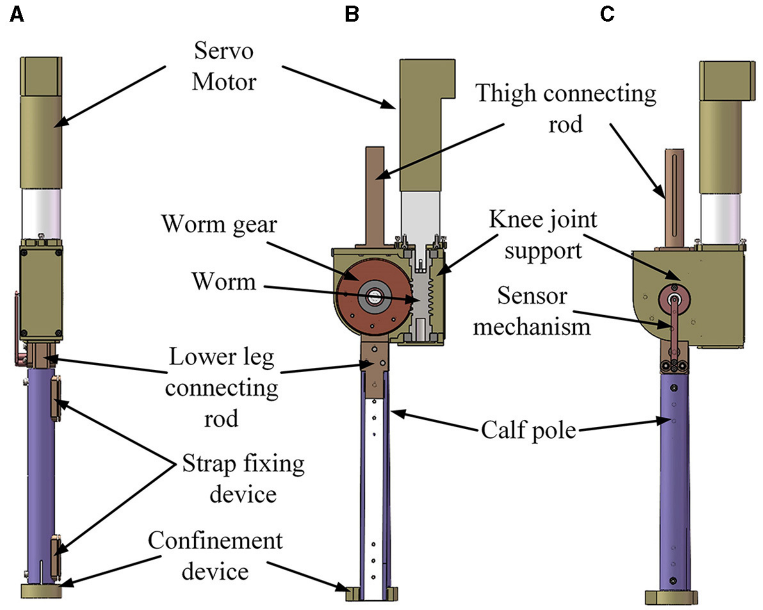

FIGURE 4
Knee joint mechanism of lower limb rehabilitation exoskeleton. **(A)** Front view; **(B)** section view; **(C)** side view.

subsequently propels the worm. The worm then engages the worm gear, leading to the rotation of the hip joint connecting rod. This rotation translates into the motion of the thigh pole, facilitating thigh movements in the human body. Concurrently, the sensor device plays a pivotal role by measuring the hip joint angle for purposes of real-time control and precision.

In the daily movements executed by the human body, the involvement of the knee joint is almost ubiquitous, underscoring its importance in the lower limb rehabilitation exoskeleton. The knee joint mechanism of the lower limb rehabilitation exoskeleton is designed as an active joint. It also uses the worm gear transmission method of the hip joint mechanism, and its core structure is similar to that of the hip joint mechanism. The knee joint mechanism of the lower limb rehabilitation exoskeleton is shown in Figure 4. Notwithstanding the similarities, several distinctions between the hip and knee joints are worth noting:

(1) Dissimilarities in joint angles during movement necessitate distinct safety limit and support frame structures for each joint;
(2) While the hip joint mechanism interfaces with the human waist, the upper segment of the knee joint mechanism interfaces with the thigh bar. The knee joint mechanism contains a thigh rod connecting rod and no waist link structure;
(3) In order to improve the overall appearance of the support frame, the end cover and support frame have been designed with certain improvements.

Based on the analysis of the ankle joint mechanism, the ankle joint mechanism of the lower limb rehabilitation exoskeleton has the following characteristics:

(1) The ankle joint mechanism has as the freedom of dorsiflexion and plantar flexion;
(2) The ankle joint mechanism is under-actuated and needs to have elastic elements to self-align;
(3) An elastic energy storage deformation and vibration damping mechanism is installed at the sole of the foot to increase the overall comfort of the mechanism.

The ankle joint mechanism of the lower limb rehabilitation exoskeleton is shown in Figure 5. The designed ankle joint mechanism encompasses several components: an end cap, a lower leg link rod, an upward push rod, a spring, a lower push rod, a pulley, a sole plate, an active axis, an upper sole, an elastic sole, and an auxiliary cushion block. Its movement principle is: when the sole of the wearer's foot is subjected to external force, the sole plate is driven by the sole to rotate around the axis, and the lower push rod is driven to move upward to compress the spring; when the external force disappears or decreases, the spring pushes the lower push rod downward, driving the sole plate to rotate around its axis, realizing that the ankle joint is in an under-driven form and has the function of autonomous dorsiflexion and plantar flexion freedom.

2.3 Motion and force analysis

The active drive of the ankle joint mechanism in the lower limb exoskeleton robot offers advantages in gait control and walking stability. However, it often necessitates additional drive sources, leading to increased complexity and bulkiness in the ankle joint structure. The focus of this study lies in catering to patients with lower limb paralysis. The ankle joint mechanism equipped

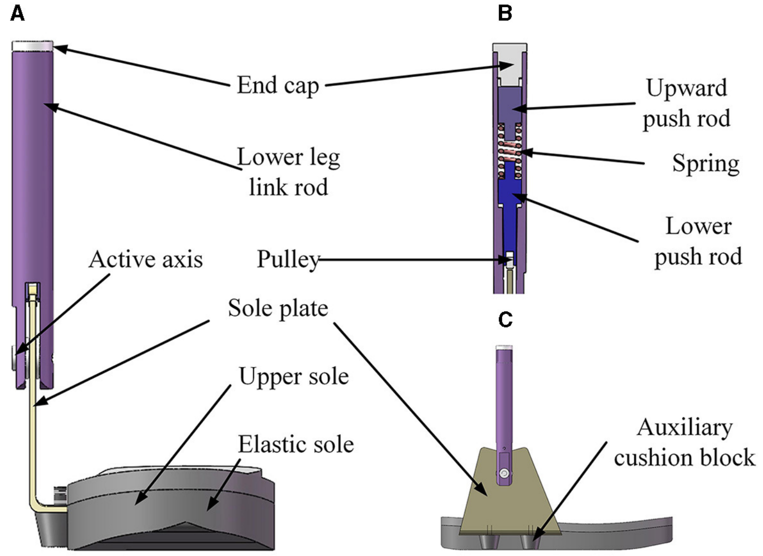

FIGURE 5
Ankle joint mechanism of lower limb rehabilitation exoskeleton. **(A)** Front view; **(B)** section view; **(C)** side view.

with functionalities of support, dorsiflexion, and plantarflexion can suffice for daily life activities, with the capacity for rotation that can autonomously return to a supporting position in an unstressed state. Based on the analysis of ankle joint motion mechanism, the sagittal plane of the ankle joint mechanism exhibits a dorsiflexion or plantarflexion range spanning from $+20^\circ$ to -20°, with the joint's torsional moment ranging between $+3$ to -3 Nm. Given these prerequisites, the ankle joint mechanism in this study is designed as an underdriven, elastic, and flexible structure.

The ankle joint mechanism of the lower limb rehabilitation exoskeleton robot has a motion range of dorsiflexion and plantar flexion in the sagittal plane of $+20^\circ$ to -20°. As the angle of rotation increases, a larger joint torsional moment becomes imperative. When the rotation angle reaches 20°, the joint torsional moment encompasses an approximate range of 3 Nm. The design process entails comprehensive calibration, precise determination of the distance change of the rotation center, appropriate spring selection, and pulley trajectory design. Figure 6 illustrates the posture change diagram of the ankle joint mechanism in the lower limb rehabilitation exoskeleton, depicting its movement from the support position to the maximum dorsiflexion, back to the support position, and subsequently to the maximum plantarflexion before returning to the support position.

In addressing the aforementioned requirements, modeling and analysis are performed, as illustrated in Figure 7. The diagram depicts the mechanism's motion, with the black solid line representing the initial state (equilibrium support position), and the black dashed line denoting an arbitrary state of the mechanism's movement. In the schematic, Point O represents the center of rotation, Point A represents the initial center of the pulley, Point B represents the center of the pulley in an arbitrary state, θ represents the angle of rotation, X represents the value corresponding to the change in height of actuator (from Point A to Point B), r represents the radius of the pulley, and l represents the distance from the lowest point on the upper part of the sole plate to the center of rotation. Other analysis parameters include: spring stiffness k, spring pressure F, joint moment of force M, torque effective distance d. X_1 represents the distance from an state trajectory point (intersection of trajectory diagonal and vertical central axis) to the center of rotation, X_2 represents the distance from the arbitrary state trajectory point to the center of the pulley, X_3 represents the distance from Point O to Point A, and β represents the angle between the initial position of the inclined plane and the horizontal line.

According to geometric relations, we can get:

$$\frac{l}{\sin(\pi/2 - \theta - \beta)} = X_1/\sin(\pi/2 + \beta) \tag{1}$$

$$X_2 = r/\cos(\beta + \theta) \tag{2}$$

$$X_3 = l + r/\cos\beta \tag{3}$$

$$\mathrm{X} = X_1 + X_2 - X_3 \tag{4}$$

According to Equations (1)–(4), X can be expressed as follows:

$$X = l \cdot \frac{\sin(\pi/2 + \beta)}{\cos(\beta + \theta)} + \frac{r}{\cos(\beta + \theta)} - l - \frac{r}{\cos\beta} \tag{5}$$

The torque effective distance d can be get:

$$d = (X_1 + X_2) \cdot \sin(\beta + \theta) \tag{6}$$

The spring force F and moment of force M are as follows:

$$F = K \cdot \mathrm{X} \tag{7}$$

$$M = F \cdot d \tag{8}$$

According to Equations (5)–(8), the effective joint moment M is calculated as:

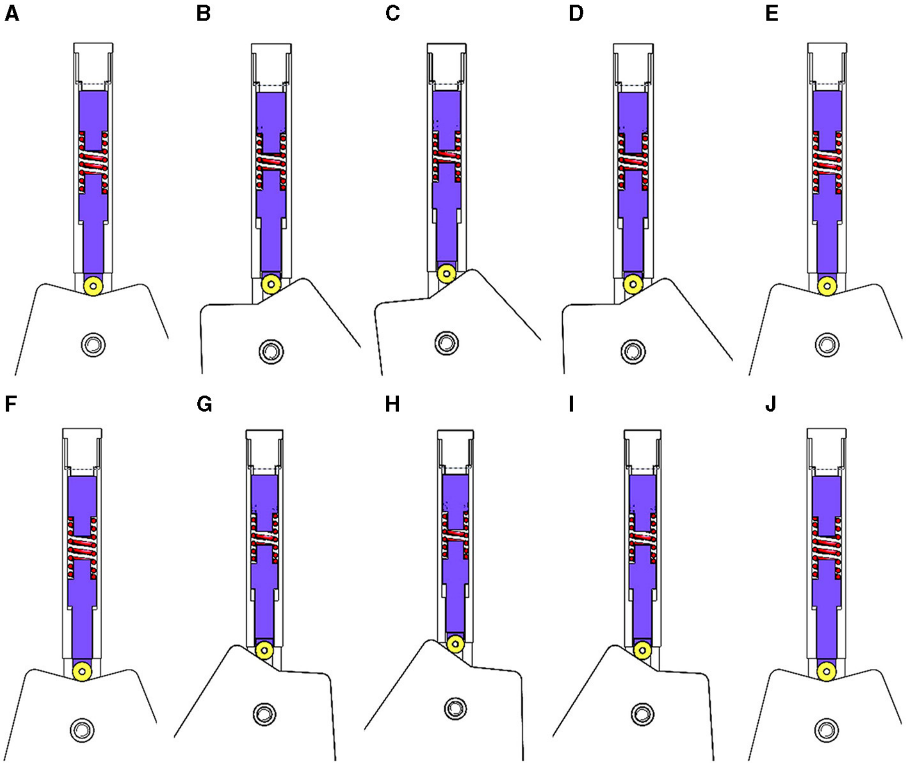

FIGURE 6
Posture changes of ankle joint mechanism. **(A–E)** Ankle dorsiflexion movement; **(F–J)** ankle plantar flexion movement.

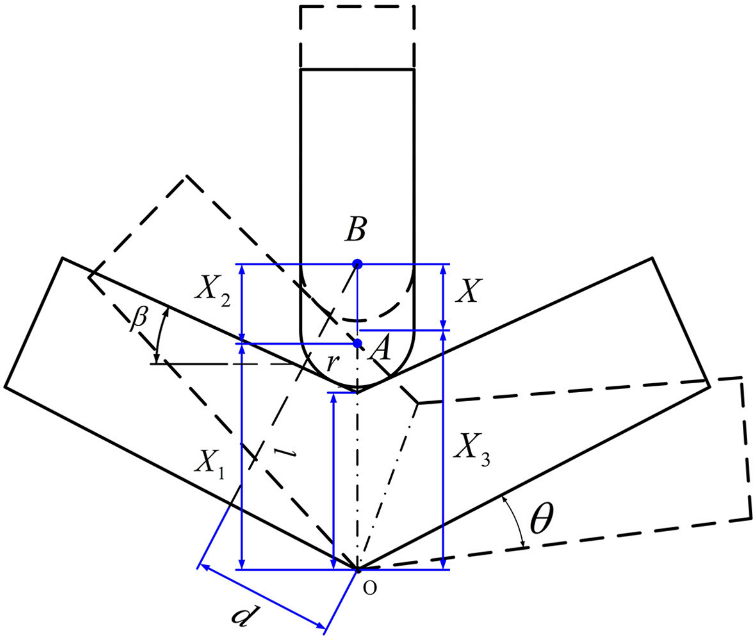

FIGURE 7
Ankle joint motion analysis of the lower limb rehabilitation exoskeleton.

TABLE 3 Performance parameters of compression springs.

Material	SWP-B(2.5)GB/T	Coiled way	Dextrorotation
Diameter	14.5 mm	Spin ratio	4.803
Free length	32 mm	Spring unit weight	12.13 g/pcs
Active coils	6.3	Pitch	4.28
Telomorphism	Rounded and smoothed	Rigidity	37 N/mm

$$M = k \cdot \left(l \cdot \frac{\sin(\pi/2 + \beta)}{\cos(\beta+\theta)} + \frac{r}{\cos(\beta+\theta)} - l - \frac{r}{\cos\beta} \right) \cdot (X_1 + X_2) \cdot \sin(\beta+\theta) \tag{9}$$

Calculated according to Equation (9), the moment M and angle θ that meet the design requirements can be obtained.

Due to the presence of friction in the mechanism, the minimum pressure angle is firstly verified to prevent the mechanism from self-locking phenomenon. Assume the following parameters: the pressure angle α, the minimum pressure angle $\alpha_{\min}$, and friction coefficient μ (value is 0.2), we can get:

$$F_f = F \cdot \cos\alpha \cdot \mu \tag{10}$$

$$F_t = F \cdot \sin\alpha \tag{11}$$

The force of friction and positive pressure can be calculated according to Equations (10) and (11). At the instance when force of friction F_f equals positive pressure F_t, it corresponds to the position where the minimum pressure angle, $\alpha_{\min}$ is 11°. According to the above calculation, the pressure angle of this structure is $\beta+\theta$. Since $0^\circ \leq \theta \leq 20^\circ$, $\beta \geq 11^\circ$ can ensure that the mechanism will not self-lock.

In the elastic component design stage, a compression spring with ends on both sides was chosen. In alignment with the ankle joint mechanism dimensions derived from the aforementioned calculations, an appropriate size and stiffness for the spring were determined. Additionally, considerations pertaining to installation dimensions and other related factors were also taken into account. After repeated verification and design, the specific performance parameters of the compression spring are presented in Table 3.

Upon analysis, the spring stiffness k is 37 N/mm. According to the design requirements, when θ is 20°, M approximates 3 Nm, it is concluded that β is 15° and l is 25 mm. Relationships between ankle angle θ and spring deformation X, as well as ankle angle θ and torque M are shown in Figure 8. It becomes evident that as the rotation angle θ escalates, the torque M also experiences an increase, reaching 3.1 N·m when θ is 20°.

3 Exoskeleton robot control system

3.1 Robot system composition

The lower limb exoskeleton primarily serves patients afflicted with lower limb motor dysfunction, essentially functioning as a mechatronic device that aids in rehabilitation training and facilitates the restoration of upright walking capabilities (Baud et al., 2021). The hardware design of the lower limb exoskeleton control system ought to adhere to fundamental principles:

(1) The primary controller must possess adequate peripheral interfaces capable of receiving diverse sensor signals integrated within the lower limb exoskeleton. Moreover, it is imperative for the human-machine interaction signals and underlying algorithms to exhibit expedited response times, enabling seamless adaptation to varying motion patterns and expeditious computation of control inputs for joint motors;

(2) Operating as a rehabilitation robot, the lower limb exoskeleton necessitates real-time, direct interaction with the patient, along with the capacity to document rehabilitation training data on storage devices or visualize it via monitors;

(3) Given its role as an assistive robot for patients with lower limb motor impairments undergoing gait training, ensuring safety, reliability, and stability is of paramount importance in the hardware design of the lower limb exoskeleton control system.

The control system hardware composition of the lower limb rehabilitation exoskeleton is shown in Figure 9. The hardware components of the lower limb rehabilitation exoskeleton consist of two subsystems: the wearable lower limb exoskeleton ontology control system and the remote monitoring system. The wearable lower limb exoskeleton ontology control system encompasses elements such as the central controller, motor drivers, servo motors, encoders, and photoelectric encoders. On the other hand, the remote monitoring system comprises a remote control unit and a remote computer. The wearer can operate the remote control unit to wirelessly transmit signals to the central controller, which subsequently issues corresponding control directives to the motor drivers. The motor drivers then activate the motors, initiating movement in the hip and knee joint mechanisms. The encoders are responsible for acquiring data and providing feedback to the central controller, facilitating closed-loop control. Concurrently, the central controller relays data in real-time to the remote computer, which is tasked with storing and exhibiting trajectory and joint information data.

3.2 Robot control method

The control framework of the lower limb rehabilitation exoskeleton consists of three layers: the perception layer, the decision-making layer, and the execution layer, which collectively control the perception, decision-making, and execution faculties of the exoskeleton robot. Figure 10 illustrates the logical architecture of the lower limb rehabilitation exoskeleton control framework. Patients manipulate the exoskeleton to operate in various modes, including standing up, sitting down, continuous walking, and climbing or descending stairs, through buttons positioned on the right crutch-mounted segment. Subsequently, the output from the perception layer conveys the designated trajectory for the exoskeleton to the decision-making layer. The decision-making layer utilizes an optimized typical joint trajectory as the foundational trajectory

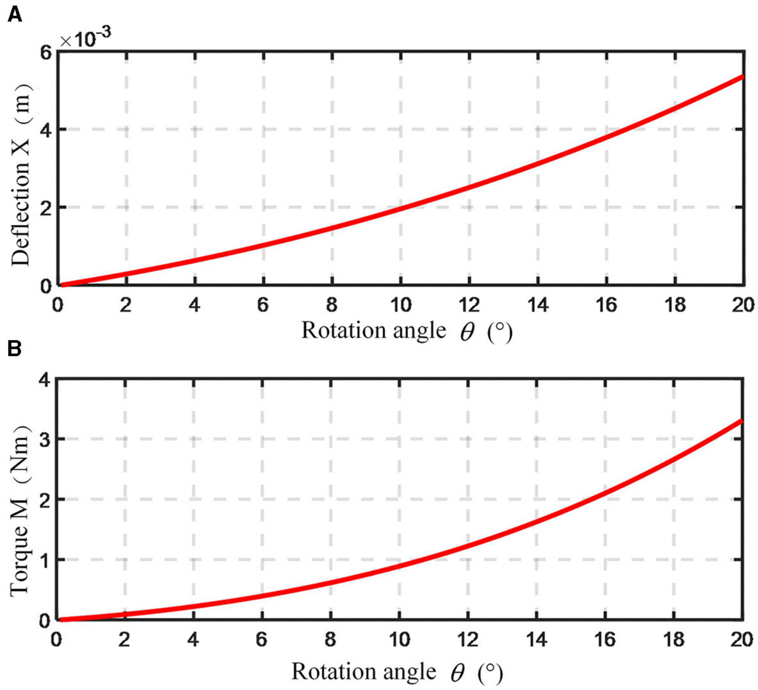

FIGURE 8
Variation curve of ankle spring deformation and moment. **(A)** Relationship between spring deformation and ankle joint angle; **(B)** relationship between moment and ankle joint angle.

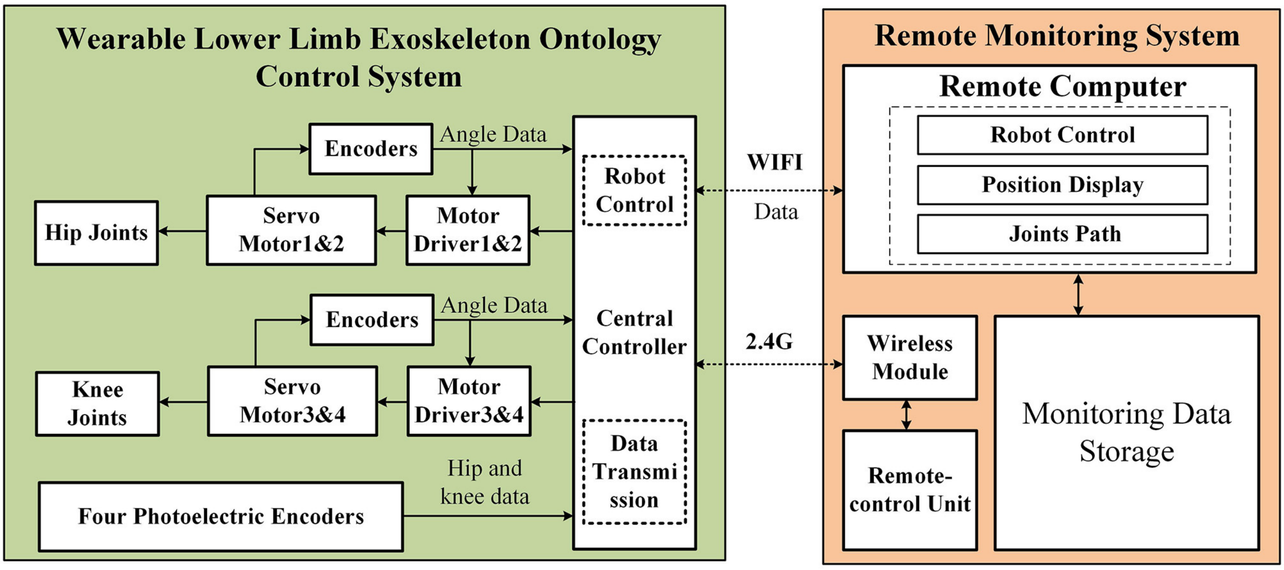

FIGURE 9
Control system hardware composition of the lower limb rehabilitation exoskeleton.

for trajectory tracking. Concurrently, this layer acquires human-computer interaction data via sensors, further refines and adjusts the trajectory being tracked by the exoskeleton, and ultimately relays the specific joint motion state information pertaining to the present moment to the execution layer. The execution layer processes the feedback signals from the sensors and the trajectory devised by the upper layer, achieving high-precision regulation of the joint motion state through a servo control driver.

A dual closed-loop PID control strategy tailored to joint motion is devised based on the prerequisites of early rehabilitation training. The detailed block diagram of this control strategy is depicted in Figure 11, facilitating the precise tracking of exoskeleton joints along the desired trajectory. Utilizing this

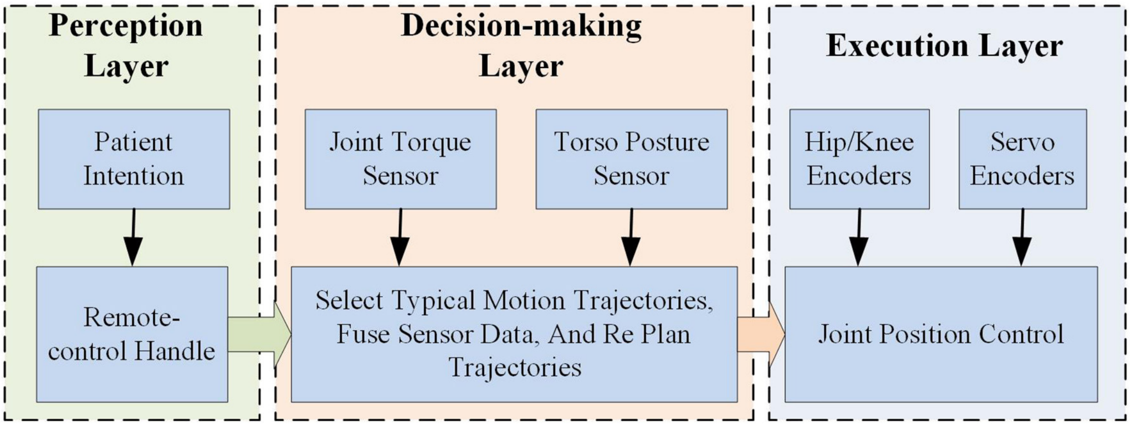

FIGURE 10
Control layer logic diagram of the lower limb rehabilitation exoskeleton.

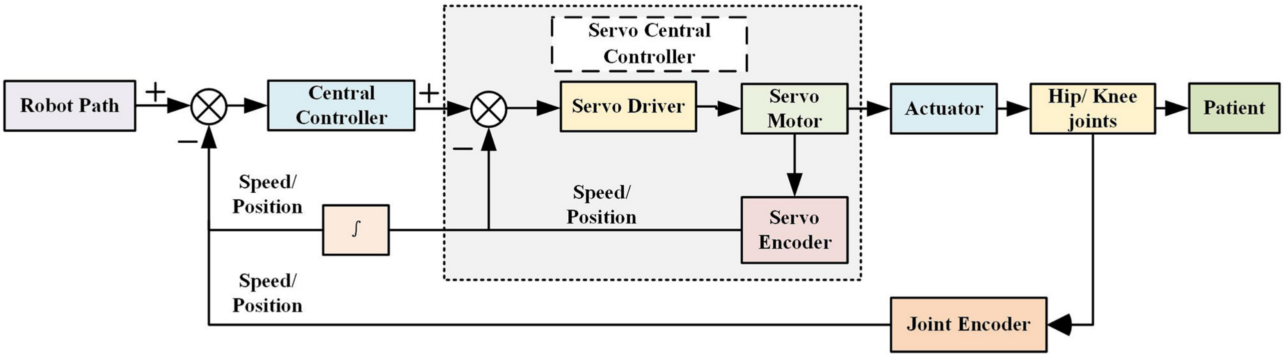

FIGURE 11
Control method of the lower extremity rehabilitation exoskeleton.

ideal trajectory as a foundation, a method for reproducible trajectory planning through the quantification of human-machine rejection was proposed. Additionally, an innovative human-machine gait joint moment cycle learning algorithm is adopted to compute the degree of human-machine rejection. To refine the ideal trajectory, a fuzzy controller is implemented, and its efficacy is substantiated through extensive human-computer experiments, enabling the attainment of trajectory reprogramming and tracking. To ensure the system's expedited response to perturbations, a fuzzy PID controller is integrated into the closed-loop joint position, thereby optimizing the system's overall performance.

4 Experiments and tests

Given the specificity that the lower limb exoskeleton will be directly applied to human lower limbs, the significance of its safety, stability, and reliability is particularly emphasized. To ensure the safety of the users, some fundamental experiments on the lower limb rehabilitation exoskeleton were performed: robotic motion response experiments and robotic trajectory tracking experiments. These experiments aim to assess the system's performance before progressing to experiments involving walking, standing up, and sitting down with able-bodied individuals.

4.1 Robot motion response experiments

The designed lower limb rehabilitation exoskeleton is mainly used to assist patients with lower limb paralysis to achieve basic daily movements. In practical control implementations, this exoskeleton is expected to exhibit swift responsiveness, attaining the desired angular positions as per control directives expeditiously. Consequently, conducting robotic motion response experiments for this lower limb rehabilitation exoskeleton becomes imperative.

Since the motion structures of the hip and knee joints are basically similar, the hip joint mechanism was selected for the robot motion response experiments. These response experiments were conducted at desired angles of 15°, 30°, 45°, and 60°. The specific experimental results are presented in Figure 12. At an angle of 15°,

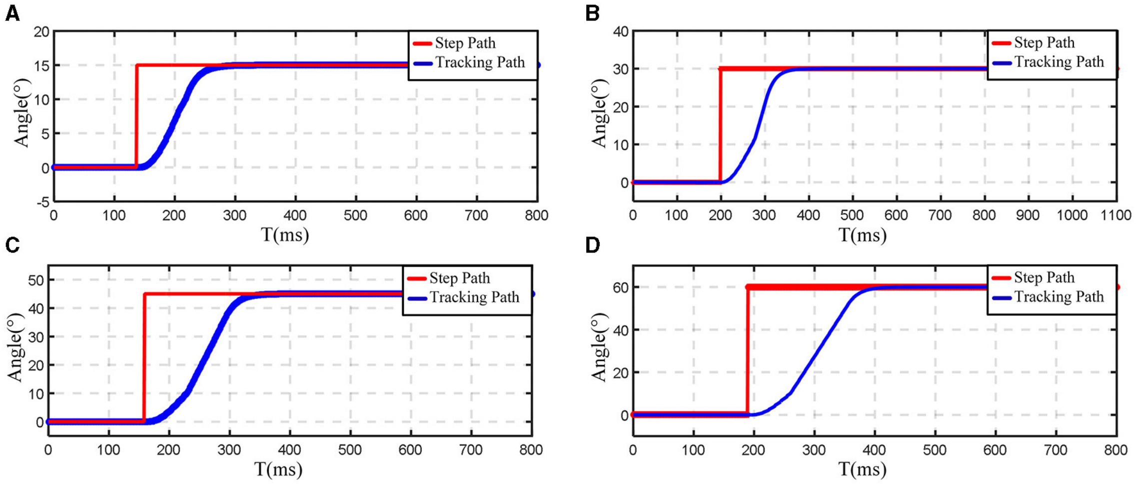

FIGURE 12
Experimental results of hip joint angular response. **(A)** 15°; **(B)** 30°; **(C)** 45°; **(D)** 60°.

the adjustment time is approximately 160 ms with a lag time of about 10 ms. Similarly, at angles of 30° and 45°, the adjustment times are around 180 and 200 ms, respectively, with a consistent lag time of about 10 ms. This lag can be primarily attributed to the use of a worm gear transmission. The backlash between the forward and reverse gears introduces return errors, leading to a delay in the rotation of the lower limb rehabilitation exoskeleton in the reverse direction.

Although the exoskeleton system's mechanical characteristics introduce a certain degree of lag in response, this lag time is practically negligible relative to the entire gait cycle. The experimental results demonstrated that the lower limb rehabilitation exoskeleton system's joint angle response speed could satisfy the practical control requirements for lower limb rehabilitation exoskeletons. The exoskeleton system performance meets the expectation for assisting patients with lower limb paralysis in executing daily movements.

4.2 Robot trajectory tracking experiments

The control strategy employed by the lower limb rehabilitation exoskeleton relies on passive control, which underscores the significance of the mechanism's trajectory tracking proficiency. The primary technical metric for the lower limb rehabilitation exoskeleton is its ability to precisely track the desired trajectory when operating in an unloaded state. In order to evaluate the trajectory tracking performance of the robot, during the experiment, the optimized motion curve was used as input, representing the expected gait trajectory. Meanwhile, the encoder captures the actual angular positions of the hip and knee joints of the exoskeleton, which are treated as the output or tracking trajectory. By analyzing the real-time discrepancies between the input and output trajectories, the trajectory tracking features of the exoskeleton were validated, thus ensuring its efficacy in assisting lower limb rehabilitation.

In the initial crutch walking trajectory tracking experiments, the optimized crutch walking joint curves were utilized as inputs and fed into the controller. The resulting output curves were collected. The trajectory tracking curves for both the hip and knee joints during crutch walking are presented in Figures 13A, B. The gait trajectory is represented by the blue line, the real-time tracking curve of the mechanism is shown in red, and the correction amount (or gap) is depicted by the black dotted line. It is evident that, within a gait cycle, the experimental results for crutch walking trajectory tracking are highly satisfactory. The tracking errors for both the hip and knee joints are consistently maintained within a range of ±3°, with the majority of the errors falling within ±1°. The tracking accuracy can meet the functional requirements of the exoskeleton.

Following the successful completion of the crutch walking trajectory tracking experiments, additional experiments were conducted to evaluate the exoskeleton's performance during activities such as standing up/sitting down with crutches and ascending/descending stairs with crutches. The results of these experiments are displayed in Figures 13C–H. The experimental results indicated that the actual tracking trajectory trended closely with the gait trajectories. The trajectory tracking errors are within a small range of ±5°, demonstrating excellent trajectory tracking capabilities for this unloaded lower limb rehabilitation exoskeleton.

From the figure, it can also be found that the tracking trajectory relative to the gait trajectory has a certain phase lag, which is mainly caused by two reasons: on the one hand, due to the worm gear has the return error characteristics; on the other hand, due to the motor needs a certain response time. In the experiments, the vast majority of the lag time is very small, basically in the range of 5 ms, and does not affect the overall performance of the mechanism.

The tracking curve and gait curve maximum error appeared in the trajectory tracking experiments on crutches standing up, and the instantaneous maximum error of 20°. By analyzing the gait trajectory, it can be found that the acceleration at the moment of standing up was too large, which was caused by the sudden change in speed (the curve was close to 90°). Although the error is large at this time, the tracking

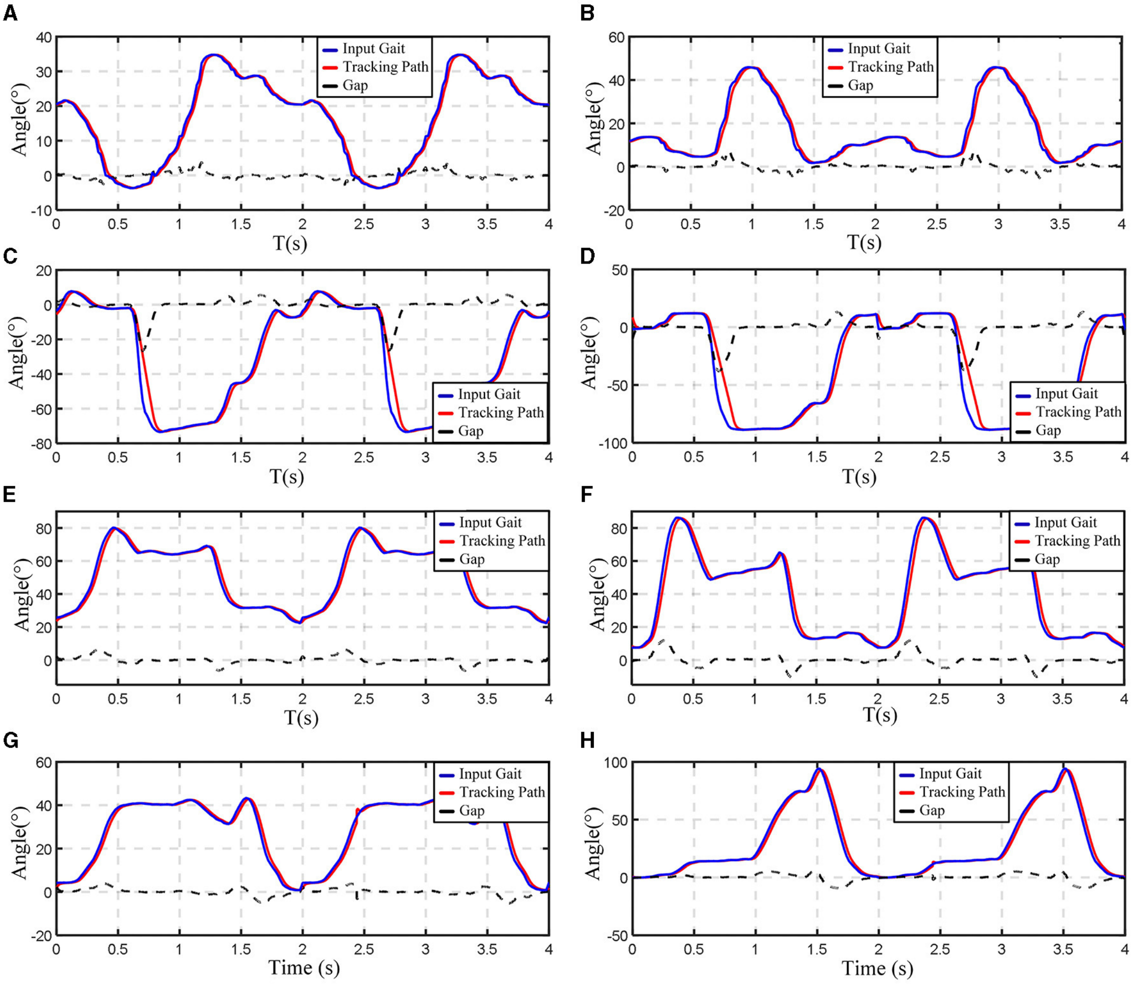

FIGURE 13
Experimental results of trajectory tracking. **(A)** Hip joint angle change while walking on crutches; **(B)** knee joint angle change while walking on crutches; **(C)** hip joint angle change while standing up and sitting down; **(D)** knee joint angle change while standing up and sitting down; **(E)** hip joint angle change while walking down the stairs; **(F)** knee joint angle change while walking down the stairs; **(G)** hip joint angle change while walking up the stairs; **(H)** knee joint angle change while walking up the stairs.

trajectory is always the same as the gait trajectory. There is a certain phase deviation and curvature difference, and the maximum deviation is <100 ms, which can meet the performance of the lower limb rehabilitation exoskeleton standing action.

There is a certain lag between the tracking trajectory and the gait trajectory, but its trend is always consistent and the error is within an acceptable range. The experimental results indicated that the lower limb rehabilitation exoskeleton had an excellent trajectory tracking performance under unloaded condition, and could meet the actual motion requirements.

4.3 Human-machine wearing tests

The safety, stability, and reliability of the developed lower limb rehabilitation exoskeleton mechanism have been verified through series of experiments. Tests involving normal humans wearing the exoskeleton were carried out, encompassing a range of activities such as walking, standing up, and sitting down.

In the preliminary experiments, gait curves and moment curves for the assisted walking, standing up, and sitting down processes of the lower limb exoskeleton were obtained. These curves were derived by measuring joint angle values and effective moment values in the sagittal plane of the active joints. The characteristics of these curves are used to verify the reliability and validity of the lower limb exoskeleton's assisted walking functionality. Additionally, subjective evaluations provided by the experimental subjects were utilized to assess the performance of the exoskeleton mechanism in assisting human movement.

During the test procedure, three healthy and normal experimental subjects were selected. The first subject was 24 years old, weighed 65 kg, and stood 174 cm tall. The second subject was 25 years old, weighed 62 kg, and measured 168 cm in height. The third subject was 50 years old, weighed 65 kg, and was 176 cm tall. The tests primarily consisted of standing up, walking, and sitting down activities. These subjects wore the lower limb

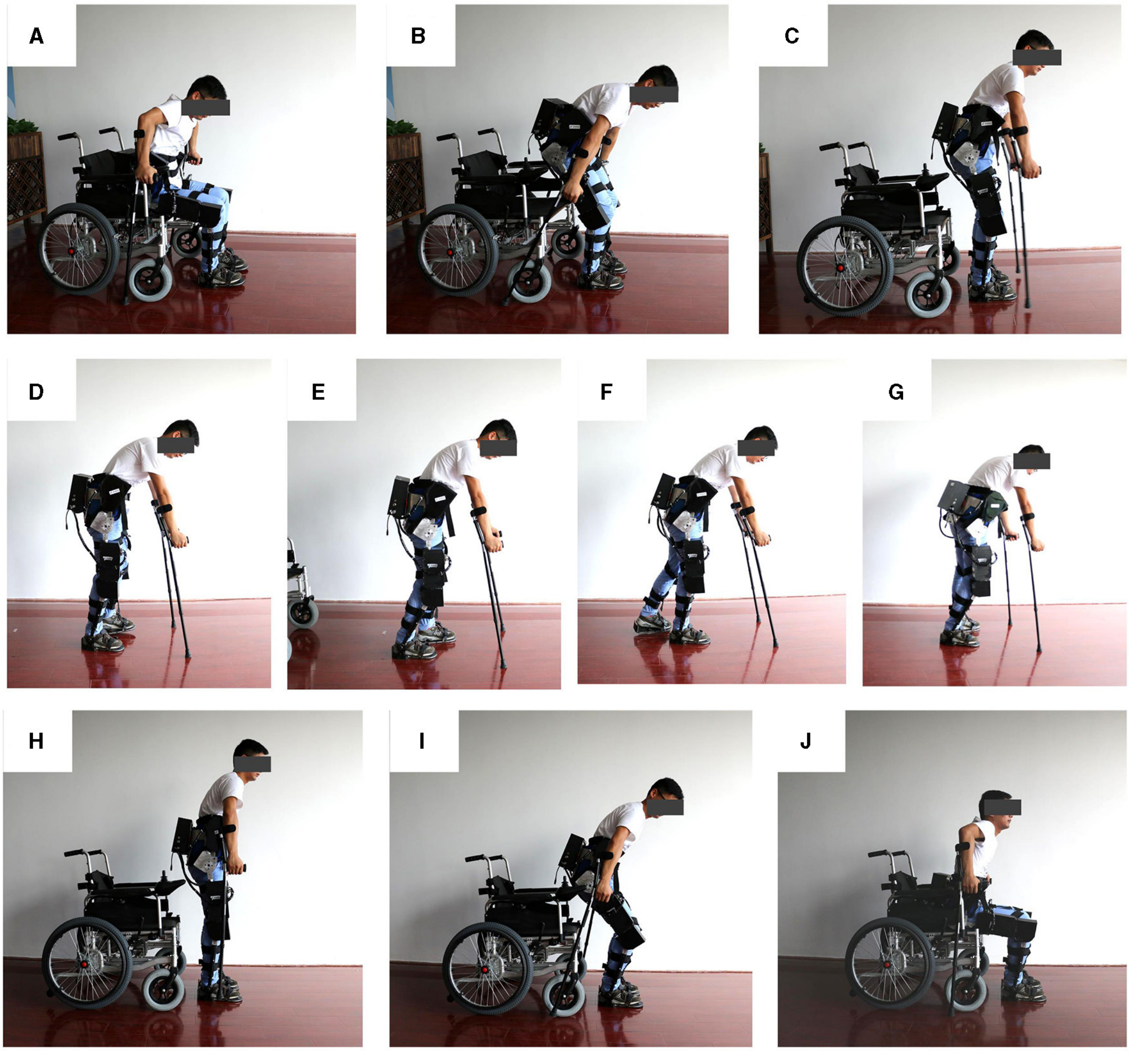

FIGURE 14
Test process of the lower limb rehabilitation exoskeleton robot worn by normal people. **(A–C)** Standing up test; **(D–G)** walking test; **(H–J)** sitting down test.

rehabilitation exoskeleton, which was placed in a wheelchair. They then performed the designated tasks while being supported by the exoskeleton and crutches. Specifically, the subjects stood up with assistance from the crutches and the exoskeleton, walked in a straight line for ∼10 meters while being supported by the crutches and exoskeleton, and finally sat down with the aid of the crutches and exoskeleton. Figure 14 shows the process of standing up, walking and sitting down in a normal human wearing the lower limb rehabilitation exoskeleton.

Through multiple tests, active joint angle and moment curves during motion were acquired. For analysis, a set of active joint angle and moment curves during the stand-up phase and another set within one gait cycle were selected as performance characteristic curves. Test curves of a normally-abled individual wearing an exoskeleton during stand-up are shown in Figures 15A, B, encompassing hip and knee joint angle and moment curves. The blue line represents actual joint moment curves, while the red line denotes actual joint angle curves, with the yellow-shaded area indicating the stand-up process. The joint angle curve trends align with the body's rising motion, with peak effective moments reaching 44 Nm for the hip and 68 Nm for the knee. The effective assistance can be provided by the lower limb rehabilitation exoskeleton during stand-up, enabling subjects to complete the action with support, thereby validating the exoskeleton's reliability and effectiveness in facilitating the stand-up process.

Test results of normal human walking wearing the lower limb rehabilitation exoskeleton are shown in Figures 15C, D. The exoskeleton gait aligns seamlessly with human walking patterns, exhibiting smooth, noise-free curves, thereby reinforcing the mechanism's reliability and stability. According the moment curves of both hip and knee joints, in a single gait cycle, the maximum effective moment for the hip joint reaches 65 and 34 Nm for the knee joint. These variations mirror typical gait patterns observed in healthy individuals. Synchronization between moment and angle curves, evident from their respective values

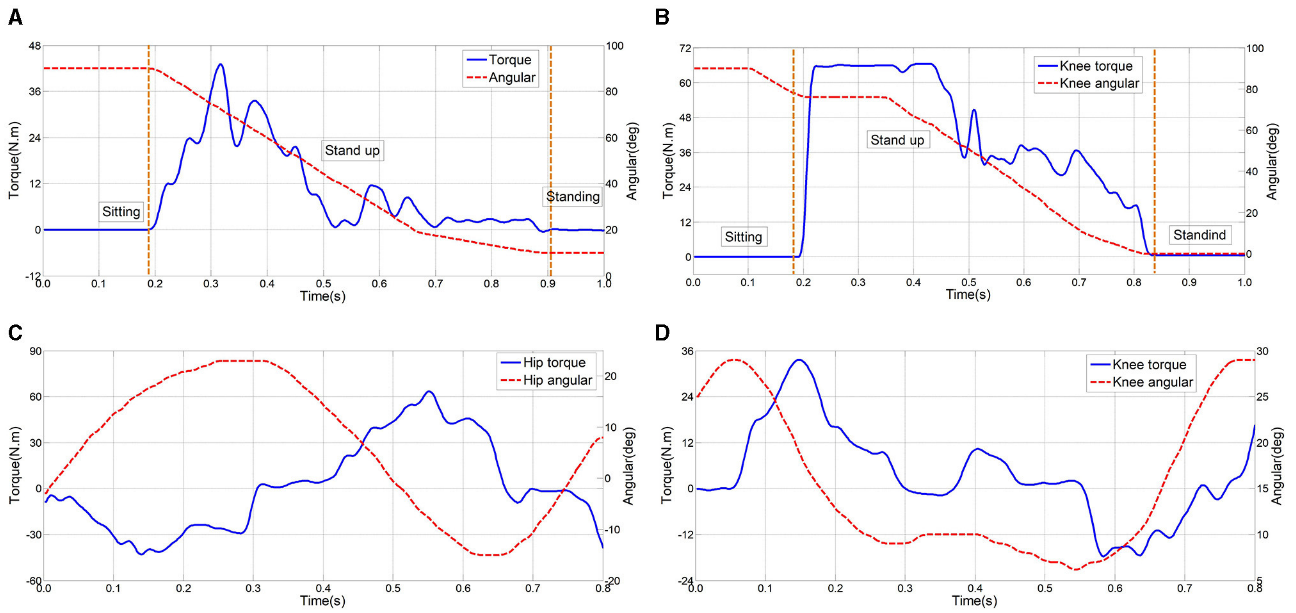

FIGURE 15
Test results of normal human wearing exoskeletons. **(A, B)** During stand-up stage; **(C, D)** during walking stage.

and trends, indicates the effective assistance provided by the lower limb rehabilitation exoskeleton to subjects during walking, thus verifying the exoskeleton's reliability and efficacy.

In the human-machine wearing tests, the peak torque value is smaller than the peak torque value when normal people walk. The main reasons include: (1) when the normal person wears the exoskeleton, the exoskeleton can provide gait torque, the human body may also provide some effective torque; (2) Using crutches to assist walking can appropriately reduce the joint torque required for actual walking.

Through interviews conducted with the three experimental subjects, users generally indicated that they could distinctly sense the assisted movement provided by the exoskeleton during walking, standing up, and sitting down. This was particularly evident in scenarios where, while walking, the experimental subjects consciously relinquished control of their lower limbs, allowing the exoskeleton to drive their lower limb movements. With the aiding effect of their upper limbs and crutches, they could adeptly execute the prescribed gait patterns. Moreover, during the processes of standing up and sitting down, even though it is challenging to assert that the human body did not contribute any assisting force, the experimental subjects could unmistakably perceive the assisted thrust generated by the exoskeleton.

Through the aforementioned experiments and subsequent analysis, it becomes evident that the lower limb rehabilitation exoskeleton offers substantial assistance to the experimental subjects in facilitating normal activities such as standing up and walking. The lower limb rehabilitation exoskeleton robot effectively aids the experimental subjects in accomplishing a wide range of movements, thereby validating the strong reliability, efficacy, and stability of the lower limb rehabilitation exoskeleton presented in this study.

5 Conclusion

In this paper, we propose a new exoskeleton robot system for lower limb rehabilitation. According to the design requirements, the mechanical structural design and force analysis of the lower limb rehabilitation exoskeleton are carried out. The structural components of the lower limb rehabilitation exoskeleton mainly include: the backpack mechanism, the hip joint mechanism, the knee joint mechanism and the ankle joint mechanism. The exoskeleton control system executes actions through a variety of hardware, such as sensors and drive motors, and can realize closed-loop position control and trajectory planning control of each exoskeleton joint mechanism. A series of performance experiments and wearing tests were conducted on the designed lower limb rehabilitation exoskeleton device. In the robot angle response experiment, four response angles were verified, including: 15°, 30°, 45°, and 60°. The experimental results indicated that the exoskeleton joints have fast response characteristics. Through testing typical movements such as walking, standing up, and going down and up and down stairs, the robot trajectory tracking experiments verified the excellent trajectory tracking characteristics of the lower limb rehabilitation exoskeleton, with a maximum tracking error of ±5°. In addition, multiple sets of wearing tests were performed to test the assistive effect of the lower limb rehabilitation exoskeleton during walking, standing up and sitting down to verify the reliability, safety, effectiveness and stability of the mechanism. This exoskeleton robotic system helps patients perform daily movements. The test results indicated that the exoskeleton robot has good reliability and safety. This exoskeleton robotic system is conducive to performing some daily movements and sports of paralyzed patients.

In future work, we will further verify the robot wearable application experiments in more complex daily life scenarios, the control methods will be optimized by combining electroencephalogram signals and other methods. Combined with clinical needs, the patient's status will be analyzed to enhance the effect of intelligent robots in the patient's rehabilitation process.

Data availability statement

The original contributions presented in the study are included in the article/supplementary material, further inquiries can be directed to the corresponding authors.

Ethics statement

Ethical approval was not required for the study involving humans in accordance with the local legislation and institutional requirements. Written informed consent to participate in this study was not required from the participants or the participants' legal guardians/next of kin in accordance with the national legislation and the institutional requirements. Written informed consent was obtained from the individual(s) for the publication of any potentially identifiable images or data included in this article.

Author contributions

ZZ: Investigation, Methodology, Writing – original draft. LL: Data curation, Methodology, Writing – review & editing. WZ: Formal analysis, Validation, Writing – review & editing. CJ: Formal analysis, Validation, Writing – review & editing. XW: Conceptualization, Funding acquisition, Supervision, Writing – review & editing. JL: Conceptualization, Project administration, Supervision, Writing – review & editing, Writing – original draft.

Funding

The author(s) declare financial support was received for the research, authorship, and/or publication of this article. This work was supported by National Natural Science Foundation of China (Grant No. 5217052119), Jiangsu Provincial Key Research and Development Program (Grant No.BE2021012-3), and Natural Science Research Start-up Foundation of Recruiting Talents of Nanjing University of Posts and Telecommunications (Grant No. NY223050).

Conflict of interest

The authors declare that the research was conducted in the absence of any commercial or financial relationships that could be construed as a potential conflict of interest.

Publisher's note

References

Andrade, R. M., Sapienza, S., Fabara, E. E., and Bonato, P. (2021). "Trajectory tracking impedance controller in 6-DoF lower-limb exoskeleton for over-ground walking training: preliminary results," in *2021 International Symposium on Medical Robotics (ISMR)* (Atlanta, GA: IEEE).

Aole, S., Elamvazuthi, I., Waghmare, L., Patre, B., and Meriaudeau, F. (2020). Improved active disturbance rejection control for trajectory tracking control of lower limb robotic rehabilitation exoskeleton. *Sensors* 20:3681. doi: 10.3390/s20133681

Baud, R., Manzoori, A. R., Ijspeert, A., and Bouri, M. (2021). Review of control strategies for lower-limb exoskeletons to assist gait. *J. Neuroeng. Rehabil.* 18, 1–34. doi: 10.1186/s12984-021-00906-3

Bryan, G. M., Franks, P. W., Collins, S. H., Klein, S. C., and Peuchen, R. J. (2021). A hip–knee–ankle exoskeleton emulator for studying gait assistance. *Int. J. Rob. Res.* 40, 722–746. doi: 10.1177/0278364920961452

Caulcrick, C., Huo, W., Franco, E., Mohammed, S., Hoult, W., Vaidyanatham, R., et al. (2021). Model predictive control for human-centred lower limb robotic assistance. *IEEE Transact. Med. Robot. Bionics* 3, 980–991. doi: 10.1109/TMRB.2021.3105141

de Miguel-Fernández, J., Lobo-Prat, J., Prinsen, E., Font-Llagunes, J. M., and Marchal-Crespo, L. (2023). Control strategies used in lower limb exoskeletons for gait rehabilitation after brain injury: a systematic review and analysis of clinical effectiveness. *J. Neuroeng. Rehabil.* 20:23. doi: 10.1186/s12984-023-01144-5

Embry, K. R., and Gregg, R. D. (2020). Analysis of continuously varying kinematics for prosthetic leg control applications. *IEEE Trans. Neural Syst. Rehabil. Eng.* 29, 262–272.

Esquenazi, A., Talaty, M., and Jayaraman, A. (2017). Powered exoskeletons for walking assistance in persons with central nervous system injuries: a narrative review. *PM&R* 9, 46–62. doi: 10.1016/j.pmrj.2016.07.534

Esquenazi, A., Talaty, M., Packel, A., and Saulino, M. (2012). The ReWalk powered exoskeleton to restore ambulatory function to individuals with thoracic-level motor-complete spinal cord injury. *Am. J. Phys. Med. Rehabil.* 91, 911–921. doi: 10.1097/PHM.0b013e318269d9a3

Huamanchahua, D., Taza-Aquino, Y., Figueroa-Bados, J., Alanya-Villanueva, J., Vargas-Martinez, A., Ramirez-Mendoza, R. A., et al. (2021). "Mechatronic exoskeletons for lower-limb rehabilitation: an innovative review," in *2021 IEEE International IOT, Electronics and Mechatronics Conference (IEMTRONICS)* (Toronto, ON: IEEE).

Leech, K. A., Roemmich, R. T., Gordon, J., Reisman, D. S., and Cherry-Allen, K. M. (2022). Updates in motor learning: implications for physical therapist practice and education. *Phys. Therapy* 102:pzab250. doi: 10.1093/ptj/pzab250

Li, W.-Z., Cao, G.-Z., and Zhu, A.-B. (2021). Review on control strategies for lower limb rehabilitation exoskeletons. *IEEE Access* 9, 123040–123060. doi: 10.1109/ACCESS.2021.3110595

Manuli, A., Maggio, M. G., Stagnitti, M. C., Aliberti, R., Cannavò, A., Casella, C., et al. (2021). Is intensive gait training feasible and effective at old age? A retrospective case-control study on the use of Lokomat Free-D in patients with chronic stroke. *J. Clin. Neurosci.* 92, 159–164. doi: 10.1016/j.jocn.2021.08.013

Pinto-Fernandez, D., Torricelli, D., Sanchez-Villamanan, M. C., Aller, F., Mombaur, K., Conti, R., et al. (2020). Performance evaluation of lower limb exoskeletons: a systematic review. *IEEE Transact. Neural Syst. Rehabil. Eng.* 28, 1573–1583. doi: 10.1109/TNSRE.2020.2989481

Plaza, A., Hernandez, M., Puyuelo, G., Garces, E., and Garcia, E. (2021). Lower-limb medical and rehabilitation exoskeletons: a review of the current designs. *IEEE Rev. Biomed. Eng.* 16, 278–291. doi: 10.1109/RBME.2021.3078001

Plaza, A., Hernandez, M., Puyuelo, G., Garces, E., and Garcia, E. (2023). Wearable rehabilitation exoskeletons of the lower limb: analysis of versatility and adaptability. *Disabil. Rehabil. Assist. Technol.* 18, 392–406. doi: 10.1080/17483107.2020.1858976

Sarajchi, M., Al-Hares, M. K., and Sirlantzi, M. (2021). Wearable lower-limb exoskeleton for children with cerebral palsy: a systematic review of mechanical design, actuation type, control strategy, and clinical evaluation. *IEEE Transact. Neural Syst. Rehabil. Eng.* 29, 2695–2720. doi: 10.1109/TNSRE.2021.3136088

Shi, D., Zhang, W., Zhang, W., and Ding, X. (2019). A review on lower limb rehabilitation exoskeleton robots. *Chin. J. Mech. Eng.* 32, 1–11. doi: 10.1186/s10033-019-0389-8

Shi, D., Zhang, W., Zhang, W., Ju, L., and Ding, X. (2021). Human-centred adaptive control of lower limb rehabilitation robot based on human–robot interaction dynamic model. *Mech. Mach. Theory* 162:104340. doi: 10.1016/j.mechmachtheory.2021.104340

Su, D., Hu, Z., Wu, J., Shang, P., and Luo, Z. (2023). Review of adaptive control for stroke lower limb exoskeleton rehabilitation robot based on motion intention recognition. *Front. Neurorobot.* 17, 1186175. doi: 10.3389/fnbot.2023.1186175

Wang, T., Zhang, B., Liu, C., Liu, T., Han, Y., Wamd, S., et al. (2022). A review on the rehabilitation exoskeletons for the lower limbs of the elderly and the disabled. *Electronics* 11:388. doi: 10.3390/electronics11030388

Zeilig, G., Weingarden, H., Zwecker, M., Dudkiewicz, I., Bloch, A., and Esquenazi, A. (2012). Safety and tolerance of the ReWalk^{TM} exoskeleton suit for ambulation by people with complete spinal cord injury: a pilot study. *J. Spinal Cord Med.* 35, 96–101. doi: 10.1179/2045772312Y.0000000003

Zheng, S. (2021). "Control strategy of lower-limb exoskeleton," in *Proceedings of the 2nd International Symposium on Artificial Intelligence for Medicine Sciences* (Beijing).

Frontiers in Neuroscience

TYPE Original Research
PUBLISHED 29 February 2024
DOI 10.3389/fnins.2024.1364338

EDITED BY
Ningbo Yu,
Nankai University, China

REVIEWED BY
Xufeng Yao,
University of Shanghai for Science and Technology, China
Changcheng Shi,
Ningbo Institute of Materials Technology and Engineering (CAS), China

*CORRESPONDENCE
Guoguang Fan
✉ fanguog@sina.com
Hua Lu
✉ luhua1969@hotmail.com

†These authors have contributed equally to this work and share first authorship

RECEIVED 02 January 2024
ACCEPTED 16 February 2024
PUBLISHED 29 February 2024

CITATION
Ying Y, Huang X, Song G, Zhao Y, Zhao X, Shi L, Gao Z, Li A, Gao T, Lu H and Fan G (2024) 3D-CAM: a novel context-aware feature extraction framework for neurological disease classification.
Front. Neurosci. 18:1364338.
doi: 10.3389/fnins.2024.1364338

3D-CAM: a novel context-aware feature extraction framework for neurological disease classification

Yuhan Ying[1,2,3†], Xin Huang[4†], Guoli Song[1,2], Yiwen Zhao[1,2], XinGang Zhao[1,2], Lin Shi[5], Ziqi Gao[1,2,3], Andi Li[1,2,3], Tian Gao[6], Hua Lu[7]* and Guoguang Fan[4]*

[1]State Key Laboratory of Robotics, Shenyang Institute of Automation, Chinese Academy of Sciences, Shenyang, China, [2]Institutes for Robotics and Intelligent Manufacturing, Chinese Academy of Sciences, Shenyang, China, [3]University of Chinese Academy of Sciences, Beiing, China, [4]Department of Radiology, The First Hospital of China Medical University, Shenyang, China, [5]Department of Neurosurgery, Beijing Tiantan Hospital, Capital Medical University, Beijing, China, [6]Shenyang Ligong University, Shenyang, China, [7]Department of Neurosurgery, Affiliated Hospital of Jiangnan University, Wuxi, China

In clinical practice and research, the classification and diagnosis of neurological diseases such as Parkinson's Disease (PD) and Multiple System Atrophy (MSA) have long posed a significant challenge. Currently, deep learning, as a cutting-edge technology, has demonstrated immense potential in computer-aided diagnosis of PD and MSA. However, existing methods rely heavily on manually selecting key feature slices and segmenting regions of interest. This not only increases subjectivity and complexity in the classification process but also limits the model's comprehensive analysis of global data features. To address this issue, this paper proposes a novel 3D context-aware modeling framework, named 3D-CAM. It considers 3D contextual information based on an attention mechanism. The framework, utilizing a 2D slicing-based strategy, innovatively integrates a Contextual Information Module and a Location Filtering Module. The Contextual Information Module can be applied to feature maps at any layer, effectively combining features from adjacent slices and utilizing an attention mechanism to focus on crucial features. The Location Filtering Module, on the other hand, is employed in the post-processing phase to filter significant slice segments of classification features. By employing this method in the fully automated classification of PD and MSA, an accuracy of 85.71%, a recall rate of 86.36%, and a precision of 90.48% were achieved. These results not only demonstrates potential for clinical applications, but also provides a novel perspective for medical image diagnosis, thereby offering robust support for accurate diagnosis of neurological diseases.

KEYWORDS

medical image analysis, computer-aided diagnosis, deep learning, Parkinson's disease, multiple system atrophy, regional Homogeneity, general feature extraction network

1 Introduction

In clinical practice, Parkinson's Disease (PD) and Multiple System Atrophy (MSA) are two neurodegenerative diseases. Despite their obvious differences in prognosis, treatment, and pathologic features, they are extremely similar in early symptoms (Palma et al., 2018). This poses a great challenge for doctors in their diagnosis (Song et al., 2007; Antonini, 2010).

Parkinson's disease has a high degree of heterogeneity, with different clinical subtypes, which makes diagnosis difficult (Wullner et al., 2023). According to statistics, the misdiagnosis rate of early-stage Parkinson's disease can be as high as 20–30% (Poewe and Wenning, 2002). Misdiagnosis can potentially lead to doctors providing patients with incorrect treatment plans, resulting in disease progression and even irreversible neurological damage. Therefore, it is evident that diagnostic methods that rely solely on the personal experience of physicians may not be sufficiently reliable. As a result, there is an urgent need for a scientifically validated auxiliary diagnostic approaches to assist doctors in making diagnoses.

In recent years, with the development of medical imaging technology, many studies have been conducted to differentiate PD and MSA using advanced medical imaging. Among them, machine learning-based methods for extracting medical image features have shown promising results. For example, Chen et al. (2017, 2023) explored the differences in brain functional connectivity patterns between patients with PD and MSA, provided a diagnostic tool for PD and MSA using machine learning methods. Pang et al. (2020) extracted radiomics features on Susceptibility-weighted-imaging using machine learning methods for differential diagnosis of PD and MSA. Kim et al. (2022) constructed a machine learning model to extract radiological features using medical images, successfully differentiating various types of Parkinsonian syndromes. Bu et al. (2023) utilized different kinds of medical images to build a radiological model based on machine learning to differentiate PD from MSA. Although the above methods have shown good results in the diagnosis of PD and MSA, they all rely on manually selecting key feature slices and segmenting regions of interest. In addition, the features extracted by machine learning methods are filtered from a fixed set, which also presents limitations.

Currently, deep learning, as a cutting-edge technology of machine learning, shows great potential in the field of computer-aided diagnosis (Greenspan et al., 2016) and has made remarkable achievements in many aspects such as medical image analysis, pathology diagnosis and clinical decision support (Litjens et al., 2017; Panayides et al., 2020; Rehman et al., 2021). Some scholars have started applying deep learning techniques to studies on PD or MSA (Zhao et al., 2019; Jyotiyana et al., 2022; Wu et al., 2022). Among them, for the specific task of PD and MSA classification, some scholars have achieved considerable results by applying deep learning methods based on medical images. For example, Huseyn (2020) utilized Magnetic Resonance Imaging (MRI) with an improved AlexNet network structure to diagnose Parkinson's disease, multiple system atrophy, and healthy individuals. Rau et al. (2023) proposed a deep learning algorithm capable of precisely segmenting the nucleus and shell, applying it to the diagnosis of PD and MSA. Compared to the aforementioned machine learning algorithms, although the features extracted by these methods are no longer limited to a fixed set of features, they still need to rely on manually selecting key feature slices and segmenting regions of interest, which does not allow for fully automated classification and diagnosis of diseases.

Therefore, we urgently need to develop a fully automatic classification model that can achieve classification diagnosis of PD and MSA without the need for manually selecting key feature slices and segmenting regions of interest. This approach would allow the model to comprehensively utilize data from the entire brain, enabling a comprehensive analysis of lesion features across various brain regions, thereby providing more reliable support for accurate diagnosis. In this study, we propose a novel 3D context-aware modeling framework called 3D-CAM. It allows a suitable convolutional neural network to be freely selected and embedded according to the dataset features in order to construct a classification model. The framework employs a 2D slicing-based strategy to process 3D Regional homogeneity (ReHo) data from brain Blood Oxygenation Level Dependent (BOLD) sequences (Zang et al., 2004). It segments the data into multiple 2D slices and uses them to train the classification model. The framework integrates two innovative modules: the Contextual Information Module and the Location Filtering Module. The Contextual Information Module is a feature enhancement module that can be inserted into any feature layer. It not only introduces features of adjacent slices, but also utilizes an attention mechanism to analyze the feature similarity between adjacent slices, enhancing focus on crucial features. This step effectively complements the inadequacy of 2D classification models in handling spatial information and contextual relationships. The Location Filtering Module is a post-processing module that not only leverages the 2D slice information to enable the model to concentrate on the slice segments with key features, but also analyzes and integrates the 2D slice information into the final 3D classification results. This step contributes to enhancing the model's classification performance and enables it to identify key features more accurately.

The main contributions of this paper are as follows:

- A feature extraction framework called 3D-CAM is proposed for neurological disease classification. The framework achieves automatic classification with significant results in the classification tasks of PD and MSA.
- We propose a Contextual Information Module that can fuse the features of adjacent slices in any feature layer, enabling the network to emphasize key features and capture the spatial correlation between slices.
- We propose a Location Filtering Module that accurately concentrates on slice segments with key features, effectively enhancing the model's classification performance by analyzing and integrating 2D slice information into 3D classification results.

2 Materials and methods

2.1 Dataset and preprocessing

The dataset for this study was obtained from the Neurology Outpatient Department of the First Hospital of China Medical University, covering patient data from July 2020 to August 2023.

For data acquisition, a 3.0 T MRI scanner outfitted with a 32-channel head coil was employed to acquire high-resolution T1 weighted MRI sequence and BOLD sequences in accordance with standardized scanning protocols. Subsequently, these sequences underwent processing to derive ReHo data. All processing procedures were executed using the Data Processing & Analysis of Brain Imaging (DPABI, RRID:SCR_010501), encompassing artifact removal, motion correction, temporal adjustments, and spatial normalization, as documented in pertinent literature (ChaoGan and YuFeng, 2010). Rigorous data quality assurance measures were undertaken, including meticulous data cleansing with manual exclusion of motion exceeding 3 mm, to ensure the integrity of the dataset.

Finally, we successfully obtained ReHo data from 189 patients, including 105 PD cases and 84 MSA cases. To ensure the effectiveness of model training, tuning, and evaluation, we divided these datasets into training set, validation set, and testing set according to the ratio of 7:1:2. Detailed sample information is shown in Figure 1.

2.2 Experimental setup and evaluation criteria

2.2.1 Implementation

The classification models in this paper are programmed using Python and Pytorch. We performed all experiments on a personal workstation with an Nvidia GeForce RTX 3080 GPU. For the optimizer, we chose a learning rate of 0.0001, a weight decay of 0.0001, and used a stochastic gradient descent algorithm with a momentum of 0.9. The batch size for training was set to 32. In addition, we chose the cross-entropy loss function during the training process. This loss function is widely used in classification problems and can effectively measure the difference between the model output and the real labels, which helps to optimize the network parameters to improve the classification accuracy.

2.2.2 Evaluation criteria

In evaluating the network's classification performance, various evaluation metrics were introduced, including accuracy, precision, and recall. These indices are defined by Equations (1)–(3). Where TP, FN, FP and TN represent correctly classified positive samples, misclassified positive samples, misclassified negative samples and correctly classified negative samples, respectively. In this paper, positive samples are PD patient data and negative samples are MSA patient data.

$$Accuracy = \frac{TN + TP}{TN + TP + FN + FP} \times 100\% \tag{1}$$

$$Recall = \frac{TP}{TP + FN} \times 100\% \tag{2}$$

$$Precision = \frac{TP}{TP + FP} \times 100\% \tag{3}$$

In addition, we introduce the Receiver Operating Characteristic (ROC) curve and the Area Under the Curve (AUC). The ROC curve is a curve plotted with the True Positive Rate (TPR) as the vertical coordinate and the False Positive Rate (FPR) as the horizontal coordinate at different thresholds. The AUC value is the area under the ROC curve, which is used as a measure of the quality of the classifier's prediction. The closer the AUC value is to 1, the better the performance of the classifier. In order to verify the robustness and generalization ability of the model, several experiments were conducted and the results were statistically analyzed and compared.

2.3 Methodology

2.3.1 Overall framework

In this work, we propose a novel deep learning-based framework for 3D medical image classification, named 3D-CAM. The framework of 3D-CAM is illustrated in Figure 2. 3D-CAM employs a 2D slicing-based strategy to slice the 3D ReHo data into multiple 2D slices for putting into the network. Unlike traditional training methods, we incorporate several adjacent slices surrounding the current slice as inputs to the network. 3D-CAM can be divided into two main stages as follows.

In the first stage, we freely choose a suitable convolutional network, such as ResNet (He et al., 2016), and embed it into the 3D-CAM framework. As the convolutional network extracts features from the current slice layer by layer, it also simultaneously extracts features from adjacent slices. During the feature extraction process, we introduce a Contextual Information Module at an optimal location. This module can simultaneously receive feature maps of the current

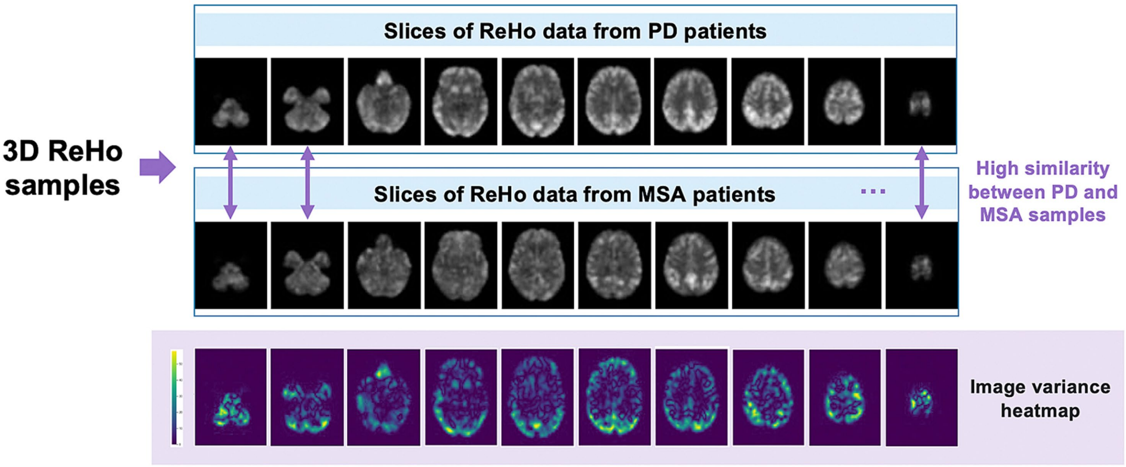

FIGURE 1
Example of ReHo data slices for PD patients and MSA patients.

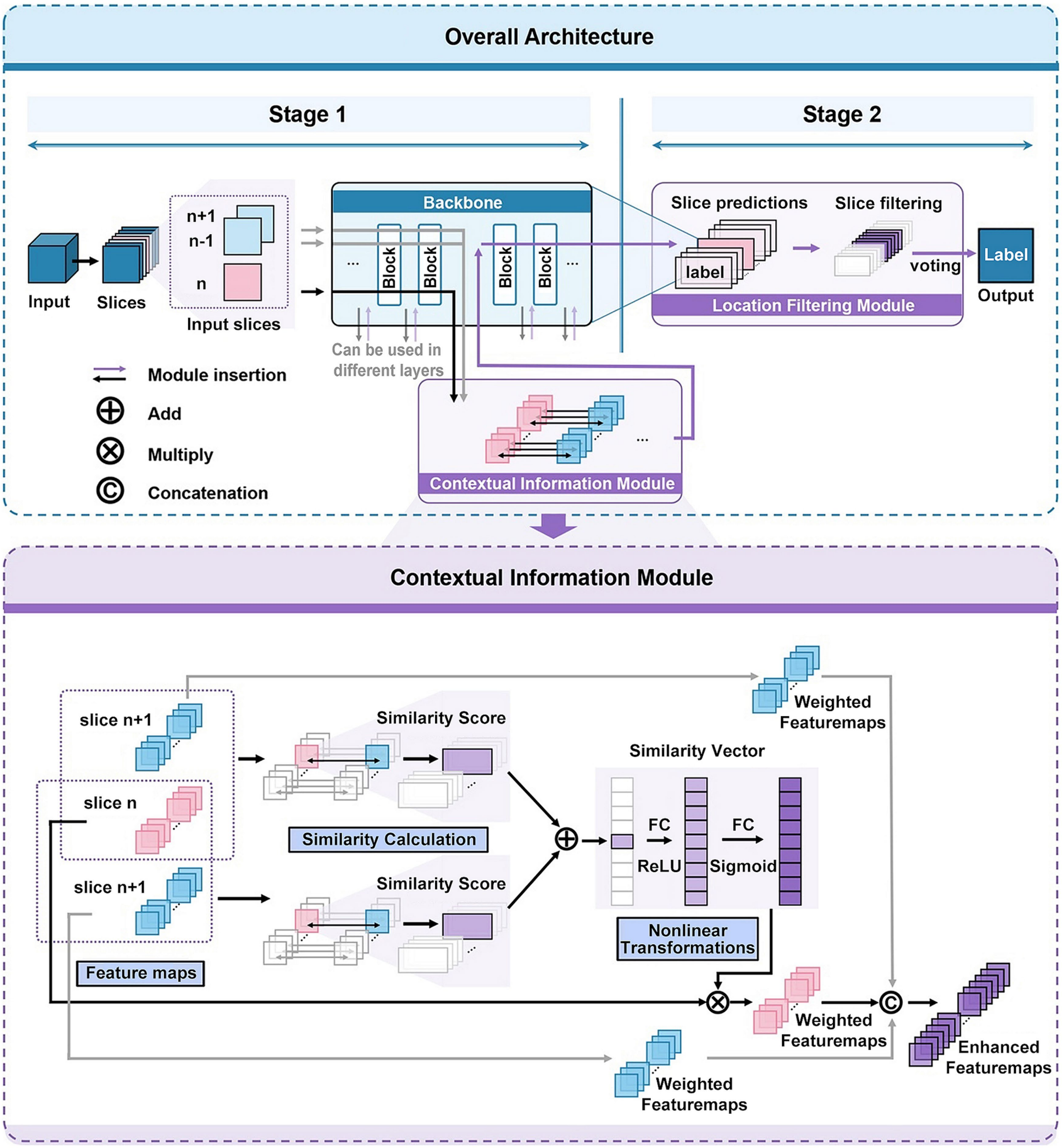

FIGURE 2
Network architecture of 3D-CAM. The upper part depicts the overall structure of 3D-CAM, including the specific configuration of the Location Filtering Module. The lower part depicts the detailed structure of the Contextual Information Module.

slice and its adjacent slices as inputs, thereby achieving the effect of introducing contextual information. In order to make the network focused on overall features and capture the spatial correlation between slices, we introduce attention mechanism in this module. By analyzing the similarity between the features of the current slice and its adjacent slices, we reassign weights to different features for feature enhancement. Afterwards, the enhanced features are further processed by convolutional networks to obtain the prediction results of 2D slices.

In the second stage, we introduce a Location Filtering Module to enhance the classification performance and integrate the 2D classification information into 3D classification results. This module is designed to filter the sliced segments with more significant classification features. In this step, we categorize all the 2D slice data used for training by location and compute the prediction accuracies of the slices with different locations in validation set. Based on this analysis, we filter out the consecutive slices with high prediction accuracy as the key prediction segments of the sample. Following this, we apply a voting mechanism to integrate the prediction results of each 2D slice within the segment to obtain 3D prediction results. This process aims to optimize and accurately extract segments with significant classification features serving as the basis for 3D classification.

2.3.2 Contextual information module

When a 2D slicing-based strategy is used to process 3D data, the connection between different 2D slices is usually ignored, which leads to the loss of some spatial information. Therefore, to comprehensively capture data features and conduct a holistic analysis, we propose a Contextual Information Module, depicted in specific structure as illustrated in Figure 2.

When inserting a Contextual Information Module at the lth layer of a neural network with a depth of L to extract features, each input slice, following the initial l layers of the neural network, generates a collection of feature maps denoted as (4). $F_i^{(l)}$ denotes the set of feature maps obtained by extracting the i th input slice in the lth layer of the neural network. N denotes the number of feature maps in the lth layer, and $f_{i,j}^{(l)}$ denotes the jth feature map extracted from the ith input slice after passing through l layers of the neural network.

$$F_i^{(l)} = \left\{ f_{i,1}^{(l)}, f_{i,2}^{(l)}, \dots, f_{i,N}^{(l)} \right\} \tag{4}$$

When the network acquires $F_i^{(l)}$, its adjacent slices features $F_{i-1}^{(l)}$ and $F_{i+1}^{(l)}$ are also acquired at the same time and stored in the contextual feature module.

Next, to enhance the neural network's attention to the overall features as well as to capture the spatial correlation between slices, we introduce attention mechanism. We compute the similarity between the feature map $f_{i,j}^{(l)}$ obtained from the current slice and the feature maps $f_{i-1,j}^{(l)}$ and $f_{i+1,j}^{(l)}$ of its adjacent slices. The Structural Similarity Index (SSIM) (Wang et al., 2004) is used here as a similarity measure. SSIM is an effective image similarity metric and its computation includes the consideration of statistics such as mean, variance and covariance. The SSIM formula (5) for calculating the similarity between two feature maps A and B is as follows:

$$\mathrm{SSIM}(A,B) = \frac{(2\mu_A\mu_B + c_1)(2\sigma_{AB} + c_2)}{\left(\mu_A^2 + \mu_B^2 + c_1\right)\left(\sigma_A^2 + \sigma_B^2 + c_2\right)} \tag{5}$$

In this formula, μ_A and μ_B denote the pixel mean values of feature maps A and B, μ_A^2 and μ_B^2 denote their respective pixel variances, σ_{AB} is their pixel covariance, and c_1 and c_2 are constants introduced for stability.

Based on the aforementioned SSIM formula, we define the weight (6) as the average value of the similarity between the feature map $f_{i,j}^{(l)}$ and its adjacent slices of the feature maps $f_{i-1,j}^{(l)}$, $f_{i+1,j}^{(l)}$. The formula for this weight is as follows:

$$\omega_{i,j}^{(l)} = \frac{\mathrm{SSIM}\left(f_{i-1,j}^{(l)}, f_{i,j}^{(l)}\right) + \mathrm{SSIM}\left(f_{i,j}^{(l)}, f_{i+1,j}^{(l)}\right)}{2} \tag{6}$$

In this formula, $\mathrm{SSIM}\left(f_{i-1,j}^{(l)}, f_{i,j}^{(l)}\right)$ denotes the similarity between feature maps $f_{i,j}^{(l)}$ and $f_{i-1,j}^{(l)}$, while $\mathrm{SSIM}\left(f_{i,j}^{(l)}, f_{i+1,j}^{(l)}\right)$ denotes the similarity between feature maps $f_{i,j}^{(l)}$ and $f_{i+1,j}^{(l)}$. The introduction of such weights aims to make the network paying more attention to the consistency of overall features while capturing spatial correlations between slices.

In order to better capture the correlation between feature maps, we specially design a neural network (7, 8) structure to dynamically adjust the original weight $\omega_{i,j}^{(l)}$. This structure comprises two linear layers and two activation functions. Here, W_1 and b_1 denote the weight matrix and bias terms of the first linear layer, and ReLU denotes the activation function of the first layer. W_2 and b_2 denote the weight matrix and bias terms of the second linear layer, and Sigmoid denotes the activation function of the second layer. The formulas are as follows:

$$h_{i,j}^{(l)} = \mathrm{ReLU}\left(W_1 . \omega_{i,j}^{(l)} + b_1\right) \tag{7}$$

$$\omega_{i,j}^{(l)\prime} = \mathrm{Sigmoid}\left(W_2 \cdot h_{i,j}^{(l)} + b_2\right) \tag{8}$$

Then, applying the adjusted weight $\omega_{i,j}^{(l)\prime}$ to the original feature map, the weighted feature map (9) can be obtained.

$$\hat{f}_{i,j}^{(l)} = \omega_{i,j}^{(l)\prime} \cdot f_{i,j}^{(l)} \tag{9}$$

After that, each feature map in $F_i^{(l)}$ is weighted based on the previously mentioned steps to form a new set (10) of feature maps:

$$\hat{F}_i^{(l)} = \left\{ \hat{f}_{i,1}^{(l)}, \hat{f}_{i,2}^{(l)}, \dots, \hat{f}_{i,N_l}^{(l)} \right\} \tag{10}$$

By introducing the attention mechanism, we adjust the weight of each feature map. The new set of feature maps $\hat{F}_i^{(l)}$ contains more spatially relevant and globally consistent features. It is conducive to better integrating spatial information into the feature extraction process, improving the perceptual ability and performance of the network.

In order to better incorporate the spatial information into the feature extraction network, we embed the feature maps $f_{i-1,1}^{(l)}$ and $f_{i+1,j}^{(l)}$ of adjacent slices together into the network, so as to comprehensively considering the contribution of adjacent slices features to the current features. We use weights α, β to perform weighted summation on the feature map sets $F_{i-1}^{(l)}$, $F_i^{(l)}$ and $F_{i+1}^{(l)}$ to obtain the final feature (11) after enhancement, where α is a smaller weight than β to emphasize the importance of the current slice. The formula of $W_i^{(l)}$ is:

$$W_i^{(l)} = \alpha \cdot F_{i-1}^{(l)} + \beta \cdot F_i^{(l)} + \alpha \cdot F_{i+1}^{(l)} \tag{11}$$

This approach efficiently integrates the features of adjacent slices into the current feature maps, enhancing the capacity for global information representation of features.

After processing in the Contextual Information Module, we obtain a set of enhanced feature maps. These feature maps contain more spatial information and help the network to focus more on overall feature consistency while taking into account the importance of different features. Using similarity information to enhance the perception of spatial correlation can improve the feature representation capability of the network.

2.3.3 Location filtering module

In order to improve the classification performance and integrate the 2D classification information into 3D classification results, this paper introduces a Location Filtering Module. In many 3D medical datasets, such as the dataset used in this paper, the slices at both ends usually contain less image information. Therefore, we want to filter the slice segments with more significant classification features located in the center location and vote them as key slice segments to obtain more accurate classification results.

First, we calculated the prediction accuracies of slices at different locations in the validation set. Let the number of 2D slices for each sample be N and the location number be i (from 1 to N). The accuracy of each location i is Acc_i (12). Here, $Correct_i$ denotes the number of correctly predicted samples at location i, and $Total_i$ denotes the total number of samples at location i.

$$Acc_i = \frac{Correct_i}{Total_i} \times 100\% \tag{12}$$

Next, we aim to find a contiguous segment among all possible slice segments where the average accuracy within that segment exceeds the threshold T. Additionally, this segment should be the longest among all possible segments, in order to retain as much information as possible while maintaining a high level of accuracy. This selected segment can be considered as the key slice segment and will be involved in subsequent voting and analyses. The formula to find this segment (13) is shown below:

$$(S,L) = \mathrm{argmax}_{j,k}\left(k \cdot 1\left(\sum_{l=j}^{j+k-1} Acc_l > k \cdot T\right)\right) \tag{13}$$

In this equation, j and k are parameters used to search for the longest segment. j represents the starting position, while k represents the length of the segment. $1(\cdot)$ is an indicator function that returns 1 if $\sum_{l=j}^{j+k-1} Acc_l > k \cdot T$ and 0 otherwise. Through this step, we finally identify the region of interest with a starting position S and length L with high prediction accuracy and use it as the key prediction segment.

Next, we adopt a voting mechanism to integrate the prediction results of each 2D slice located at the key slice segment aforementioned (14). The specific formula is as follows:

$$P(c) = \frac{1}{N'} \sum_{i=1}^{N'} 1(c_i = c) \tag{14}$$

In this equation, $P(c)$ denotes the probability that the final weighted voting prediction result is class c. N' denotes the total number of filtered slices in the key slice segment. $1(\cdot)$ is an indicator function, which indicates 1 when $c_i = c$, and 0 otherwise. c_i denotes the prediction category of the ith slice. Finally, 3D prediction results can be obtained based on the prediction probability $P(c)$.

3 Results

In order to verify the reliability of the proposed method in this paper and to propose new methods for automatic diagnosis of PD and MSA, we conducted the following experiments.

3.1 Model selection and performance comparison

We applied our proposed innovative framework, 3D-CAM, to the classification tasks of PD and MSA. Specifically, we applied the two innovative modules, the Contextual Information Module and the Location Filtering Module, to specific layers of the classical model in order to enhance its performance. To ensure consistency, we inserted the Contextual Information Module in the layers corresponding to the 32×32 feature maps of each model. Additionally, we have investigated several families of classical convolutional neural network models, including EfficientNet (Tan and Le, 2020), DenseNet (Huang et al., 2018), ResNet (He et al., 2016), and Inception (Szegedy et al., 2015) as backbones. In order to identify the model with the best performance in our task, we compared multiple versions in each model family. Finally, we selected the best-performing model from each family for further analysis. The experimental results are detailed in Table 1.

In our experiments, we observe that different feature extraction networks can be embedded into 3D-CAM, while all of them show different degrees of improvement in classification accuracy. We also find that for our task, ResNet34-based 3D-CAM shows the best performance with 85.71% accuracy on the test set.

TABLE 1 Comparative experimental results of different models.

Model	Accuracy	Recall	Precision
Inception	65.71%	68.18%	75.00%
Inception +3D-CAM	77.14%	77.27%	85.00%
DenseNet	68.57%	72.73%	76.19%
DenseNet +3D-CAM	80.00%	81.82%	85.71%
EfficientNet	71.72%	68.18%	83.33%
EfficientNet +3D-CAM	82.86%	86.36%	86.36%
ResNet	71.42%	72.73%	80.00%
ResNet + 3D-CAM	**85.71%**	**86.36%**	**90.48%**

The best-performing results are highlighted in bold.

3.2 Ablation experiments

To verify the effect of our proposed two modules on the model performance, we conducted ablation experiments. On the currently best-performing model, we gradually removed these two modules and obtained two sets of ablation experimental results, as detailed in Table 2. Here, Module 1 represents the Contextual Information Module, and Module 2 represents the Location Filtering Module.

The results of the ablation experiments showed that the removal of either module resulted in a significant decrease in model performance. This validates the importance of both modules to the model performance. These results strongly support the validity of our proposed modules and confirm their positive impact on the overall model performance.

3.3 Optimal insertion location analysis of the contextual information module

In order to determine the optimal insertion location of the Contextual Information Module, we conducted additional experiments. On the base of the currently best-performing model, we adjusted the insertion location of the Contextual Information Module and observed its effect on the model performance. We attempted to insert the modules at locations with different feature map sizes and recorded the optimal performance of the model performance in each case, as shown in Table 3.

The results above show that inserting the Contextual Information Module after a feature map of 32×32 size can bring the maximum performance improvement to the model with an accuracy of 85.71%. The ROC curve of the best-performing model is shown in Figure 3, with an AUC value of 0.85. This result also demonstrates the impact of different insertion locations of the Contextual Information Module on the model performance. These results strongly support the necessity of exploring the optimal insertion location for the Contextual Information Module and provide important ideas for improving the model performance.

TABLE 2 Ablation experiments.

Model	Accuracy	Recall	Precision
ResNet	71.42%	72.73%	80.00%
ResNet + Module 1	74.29%	72.73%	84.21%
ResNet + Module 1 + Module 2	**85.71%**	**86.36%**	**90.48%**

The best-performing results are highlighted in bold.

TABLE 3 Experimental results inserted by the Module 1 at different locations on the optimal model.

Feature map size at the Module 1 insertion point	Accuracy	Recall	Precision
64 × 64	80.00%	81.82%	85.71%
32 × 32	**85.71%**	**86.36%**	**90.48%**
16 × 16	82.86%	81.82%	90.00%
8 × 8	74.29%	77.27%	80.95%

The best-performing results are highlighted in bold.

In summary, through all the aforementioned experiments, we have successfully determined the optimal model for this task. This process not only validates the effectiveness of the proposed innovative modules, but also provides an effective method for the automatic classification of PD and MSA.

4 Discussion

Our experimental results demonstrate that the deep learning framework 3D-CAM can effectively classify PD and MSA based on medical images, achieving a classification accuracy of 85.71% and an AUC value of 0.85. This outcome shows the capability of our research method to learn disease-related image features from medical imaging data in an effective manner.

We speculate that the reason why the 3D-CAM framework performs well in experiments and outperforms other classical deep learning models is because it is specifically designed for PD and MSA classification tasks. It not only learns features from the current slice but also integrates key features from adjacent slices. At the same time, by utilizing attention mechanisms, it allows the network to focus more on overall features and the segment of slices that contain crucial features.

Recently, several studies have shown promising results in the diagnosis of PD and MSA using machine learning methods, such as Chen et al. (2017), Pang et al. (2020), Bu et al. (2023), and Chen et al. (2023). Among them, the dataset volume used by Pang et al. (2020) is comparable to our research, making it highly relevant. They obtained an AUC value of 0.862 in the classification task of PD and MSA on the test set, slightly higher than our result of 0.85. Although their results slightly outperforms the one we proposed, the approach by Pang et al. (2020) relies on manually selecting key feature slices and segmenting regions of interest, which greatly increases the subjectivity and complexity of the classification process. Moreover, the features extracted by machine learning methods are selected from a fixed set, which

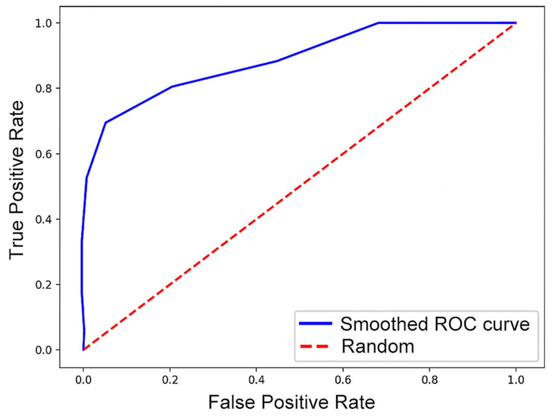

FIGURE 3
ROC curve.

also presents limitations. The other studies based on machine learning methods mentioned above also suffer from these issues.

Some researchers have attempted to diagnose PD and MSA through deep learning methods, such as Huseyn (2020) and Rau et al. (2023). Among them, Huseyn (2020) proposed an innovative deep learning model, achieving an accuracy of about 88% in the classification task of PD and MSA, slightly higher than our proposed model's accuracy of 85.71%. However, the aforementioned deep learning methods still rely on manually selecting key feature slices and segmenting regions of interest, which does not allow for fully automated classification and diagnosis of diseases. In addition, neurodegenerative diseases affect the entire brain of patients, and relying solely on local brain information within the regions of interest limits exploration of lesion features in other brain regions.

Compared to previous studies, 3D-CAM framework has achieved significant progress in the classification of PD and MSA. It no longer rely on manual selection of slices and regions of interest, successfully achieving fully automated classification. This method significantly reduces the investment of manpower and time. Additionally, by conducting direct analysis of global brain data instead of restricting to specific regions of interest, it enables the capture of more comprehensive feature information from the entire brain, leading to a significant enhancement in diagnostic accuracy and efficiency.

However, despite the promising results achieved by our approach, it is important to note some potential limitations. Firstly, although we have conducted our research using a large amount of data, the outcomes are still constrained by the current dataset. In the future, with the increase of data volume, we are expected to further optimize the model to obtain more reliable and comprehensive diagnostic results. Secondly, our study has focused solely on the classification tasks of PD and MSA, and applications to other neurological disorders have not been explored. Therefore, future research can further investigate the applicability of this framework in classifying other diseases.

In conclusion, our research has proposed an effective deep learning framework that offers a reliable solution for the classification of PD and MSA based on medical imaging, achieving satisfactory classification accuracy. This study offers strong support for early detection of neurodegenerative diseases and has broad prospect for clinical application. Additionally, our research provides new ideas and tools for the diagnosis and treatment of neurodegenerative diseases, and is expected to provide solid support for the future advancement of related fields.

Data availability statement

The raw data supporting the conclusions of this article will be made available by the authors, without undue reservation.

Ethics statement

The studies involving humans were approved by the Medical Research Ethics Committee of the First Affiliated Hospital of China Medical University. The studies were conducted in accordance with the local legislation and institutional requirements. The participants provided their written informed consent to participate in this study. Written informed consent was obtained from the individual(s) for the publication of any potentially identifiable images or data included in this article.

Author contributions

YY: Writing – original draft, Writing – review & editing, Methodology, Project administration. XH: Writing – original draft, Writing – review & editing, Project administration. GS: Funding acquisition, Resources, Writing – review & editing. YZ: Funding acquisition, Resources, Writing – review & editing. XZ: Funding acquisition, Resources, Writing – review & editing. LS: Funding acquisition, Resources, Writing – review & editing. ZG: Funding acquisition, Resources, Writing – review & editing. AL: Funding acquisition, Resources, Writing – review & editing. TG: Funding acquisition, Resources, Writing – review & editing. HL: Funding acquisition, Resources, Writing – review & editing. GF: Supervision, Writing – review & editing.

Funding

The author(s) declare financial support was received for the research, authorship, and/or publication of this article. This work was supported by the National Natural Science Foundation of China (62073314 and 92048203), Liaoning Provincial Natural Science Foundation of China (2022-YQ-06), Beijing Hospitals Authority Clinical Medicine Development of special funding support (YGLX202321), Beijing Natural Science Foundation (JQ23038), and Wuxi Science and Technology Bureau's Research Project Plan (Y20222022).

Acknowledgments

We are grateful to all the patients who provided data for this study.

Conflict of interest

The authors declare that the research was conducted in the absence of any commercial or financial relationships that could be construed as a potential conflict of interest.

Publisher's note

References

Antonini, A. (2010). Imaging for early differential diagnosis of parkinsonism. *Lancet Neurol.* 9, 130–131. doi: 10.1016/S1474-4422(09)70360-6

Bu, S., Pang, H., Li, X., Zhao, M., Wang, J., Liu, Y., et al. (2023). Multi-parametric radiomics of conventional T1 weighted and susceptibility-weighted imaging for differential diagnosis of idiopathic Parkinson's disease and multiple system atrophy. *BMC Med. Imaging* 23:204. doi: 10.1186/s12880-023-01169-1

ChaoGan, Y., and YuFeng, Z. (2010). DPARSF: a MATLAB toolbox for "pipeline" data analysis of resting-state fMRI. *Front. Syst. Neurosci.* 4:13. doi: 10.3389/fnsys.2010.00013

Chen, B., Cui, W., Wang, S., Sun, A., Yu, H., Liu, Y., et al. (2023). Functional connectome automatically differentiates multiple system atrophy (parkinsonian type) from idiopathic Parkinson's disease at early stages. *Hum. Brain Mapp.* 44, 2176–2190. doi: 10.1002/hbm.26201

Chen, B., Fan, G., Sun, W., Shang, X., Shi, S., Wang, S., et al. (2017). Usefulness of diffusion-tensor MRI in the diagnosis of Parkinson variant of multiple system atrophy and Parkinson's disease: a valuable tool to differentiate between them? *Clin. Radiol.* 72, 610.e9–610.e15. doi: 10.1016/j.crad.2017.02.005

Greenspan, H., Ginneken, B. V., and Summers, R. M. (2016). Guest editorial deep learning in medical imaging: overview and future promise of an exciting new technique. *IEEE Trans. Med. Imaging* 35, 1153–1159. doi: 10.1109/TMI.2016.2553401

He, K., Zhang, X., Ren, S., and Sun, J. (2016). Deep residual learning for image recognition. in Proceedings of the IEEE Conference on Computer Vision and Pattern Recognition, 770–778.

Huang, G., Liu, Z., Van Der Maaten, L., and Weinberger, K. Q. (2018). Densely connected convolutional networks. in Proceedings of the IEEE Conference on Computer Vision and Pattern Recognition, 2261–2269.

Huseyn, E. (2020). Deep learning based early diagnostics of Parkinsons disease. *arXiv* arXiv:2008.01792

Jyotiyana, M., Kesswani, N., and Kumar, M. (2022). A deep learning approach for classification and diagnosis of Parkinson's disease. *Soft. Comput.* 26, 9155–9165. doi: 10.1007/s00500-022-07275-6

Kim, Y. S., Lee, J. H., and Gahm, J. K. (2022). Automated differentiation of atypical parkinsonian syndromes using brain Iron patterns in susceptibility weighted imaging. *Diagnostics* 12:637. doi: 10.3390/diagnostics12030637

Litjens, G., Kooi, T., Bejnordi, B. E., Setio, A. A. A., Ciompi, F., Ghafoorian, M., et al. (2017). A survey on deep learning in medical image analysis. *Med. Image Anal.* 42, 60–88. doi: 10.1016/j.media.2017.07.005

Palma, J. A., Norcliffe-Kaufmann, L., and Kaufmann, H. (2018). Diagnosis of multiple system atrophy. *Auton. Neurosci.* 211, 15–25. doi: 10.1016/j.autneu.2017.10.007

Panayides, A. S., Amini, A., Filipovic, N. D., Sharma, A., Tsaftaris, S. A., Young, A., et al. (2020). AI in medical imaging informatics: current challenges and future directions. *IEEE J. Biomed. Health Inform.* 24, 1837–1857. doi: 10.1109/JBHI.2020.2991043

Pang, H., Yu, Z., Li, R., Yang, H., and Fan, G. (2020). MRI-based Radiomics of basal nuclei in differentiating idiopathic Parkinson's disease from parkinsonian variants of multiple system atrophy: a susceptibility-weighted imaging study. *Front. Aging Neurosci.* 12:587250. doi: 10.3389/fnagi.2020.587250

Poewe, W., and Wenning, G. (2002). The differential diagnosis of Parkinson's disease. *Eur. J. Neurol.* 9, 23–30. doi: 10.1046/j.1468-1331.9.s3.3.x

Rau, A., Schroter, N., Rijntjes, M., Bamberg, F., Jost, W. H., Zaitsev, M., et al. (2023). Deep learning segmentation results in precise delineation of the putamen in multiple system atrophy. *Eur. Radiol.* 33, 7160–7167. doi: 10.1007/s00330-023-09665-2

Rehman, A., Ahmed Butt, M., and Zaman, M. (2021). A survey of medical image analysis using deep learning approaches. in Proceedings of 5th International Conference on Computing Methodologies and Communication (ICCMC), 1334–1342.

Song, Y. J., Lundvig, D. M., Huang, Y., Gai, W. P., Blumbergs, P. C., Hojrup, P., et al. (2007). p25alpha relocalizes in oligodendroglia from myelin to cytoplasmic inclusions in multiple system atrophy. *Am. J. Pathol.* 171, 1291–1303. doi: 10.2353/ajpath.2007.070201

Szegedy, C., Liu, W., Jia, Y., Sermanet, P., Reed, S., Anguelov, D., et al. (2015). Going deeper with convolutions. in Proceedings of the IEEE Conference on Computer Vision and Pattern Recognition, 2818–2826.

Tan, M., and Le, Q. (2020). EfficientNet: rethinking model scaling for convolutional neural networks. in Proceedings of the International Conference on Machine Learning. PMLR, 6105–6114.

Wang, Z., Bovik, A. C., Sheikh, H. R., and Simoncelli, E. P. (2004). Image quality assessment: from error visibility to structural similarity. *IEEE Trans. Image Process.* 13, 600–612. doi: 10.1109/tip.2003.819861

Wu, P., Zhao, Y., Wu, J., Brendel, M., Lu, J., Ge, J., et al. (2022). Differential diagnosis of parkinsonism based on deep metabolic imaging indices. *J. Nucl. Med.* 63, 1741–1747. doi: 10.2967/jnumed.121.263029

Wullner, U., Borghammer, P., Choe, C. U., Csoti, I., Falkenburger, B., Gasser, T., et al. (2023). The heterogeneity of Parkinson's disease. *J. Neural Transm. (Vienna)* 130, 827–838. doi: 10.1007/s00702-023-02635-4

Zang, Y., Jiang, T., Lu, Y., He, Y., and Tian, L. (2004). Regional homogeneity approach to fMRI data analysis. *NeuroImage* 22, 394–400. doi: 10.1016/j.neuroimage.2003.12.030

Zhao, Y., Wu, P., Wang, J., Li, H., Navab, N., Yakushev, I., et al. (2019). A 3D deep residual convolutional neural network for differential diagnosis of parkinsonian syndromes on 18F-FDG PET images. in 2019 41st Annual International Conference of the IEEE Engineering in Medicine and Biology Society (EMBC), 3531–3534.

frontiers | Frontiers in Neuroscience

TYPE Original Research
PUBLISHED 15 March 2024
DOI 10.3389/fnins.2024.1380150

EDITED BY
Yuquan Leng,
Southern University of Science and Technology, China

REVIEWED BY
Guozheng Xu,
Nanjing University of Posts and Telecommunications, China
Pengwen Xiong,
Nanchang University, China

*CORRESPONDENCE
Jianwei Cui
✉ cjw@seu.edu.cn

RECEIVED 01 February 2024
ACCEPTED 04 March 2024
PUBLISHED 15 March 2024

CITATION
Huang Z, Cui J, Wang Y and Yu S (2024) Improving wheelchair user sitting posture to alleviate lumbar fatigue: a study utilizing sEMG and pressure sensors.
Front. Neurosci. 18:1380150.
doi: 10.3389/fnins.2024.1380150

Improving wheelchair user sitting posture to alleviate lumbar fatigue: a study utilizing sEMG and pressure sensors

Zizheng Huang, Jianwei Cui*, Yuanbo Wang and Siji Yu

Jiangsu Key Lab of Remote Measurement and Control, School of Instrument Science and Engineering, Southeast University, Nanjing, China

Background: The wheelchair is a widely used rehabilitation device, which is indispensable for people with limited mobility. In the process of using a wheelchair, they often face the situation of sitting for a long time, which is easy to cause fatigue of the waist muscles of the user. Therefore, this paper hopes to provide more scientific guidance and suggestions for the daily use of wheelchairs by studying the relationship between the development of muscle fatigue and sitting posture.

Methods: First, we collected surface Electromyography (sEMG) of human vertical spine muscle and analyzed it in the frequency domain. The obtained Mean Power Frequency (MPF) was used as the dependent variable. Then, the pose information of the human body, including the percentage of pressure points, span, and center of mass as independent variables, was collected by the array of thin film pressure sensors, and analyzed by a multivariate nonlinear regression model.

Results: When the centroid row coordinate of the cushion pressure point is about 16(range, 7.7-16.9), the cushion pressure area percentage is about 80%(range, 70.8%-89.7%), and the cushion pressure span range is about 27(range, 25-31), the backrest pressure point centroid row coordinate is about 15(range, 9.1-18.2), the backrest pressure area percentage is about 35%(range, 11.8%-38.7%), and the backrest pressure span range is about 16(range, 9-22). At this time, the MPF value of the subjects decreased by a small percentage, and the fatigue development of the muscles was slower. In addition, the pressure area percentage at the seat cushion is a more sensitive independent variable, too large or too small pressure area percentage will easily cause lumbar muscle fatigue.

Conclusion: The results show that people should sit in the middle and back of the seat cushion when riding the wheelchair, so that the Angle of the hip joint can be in a natural state, and the thigh should fully contact the seat cushion to avoid the weight of the body concentrated on the buttocks; The back should be fully in contact with the back of the wheelchair to reduce the burden on the waist, and the spine posture can be adjusted appropriately according to personal habits, but it is necessary to avoid maintaining a chest sitting position for a long time, which will cause the lumbar spine to be in an unnatural physiological Angle and easily lead to fatigue of the waist muscles.

KEYWORDS

sEMG, muscle fatigue, MPF, sitting posture detection, multiple nonlinear regression

1 Introduction

With the spread of electronic communication devices and changes in office practices, sedentary lifestyles are spreading around the world, with approximately one-third of the global population aged 15 years and older experiencing inactivity (Park et al., 2020). Unlike the sedentary daily office population, wheelchair users are forced to sit in wheelchairs for long periods due to their lack of autonomous mobility.

In modern society, wheelchairs, as an important rehabilitation aid, are widely used in individuals with limited mobility, especially those suffering from spinal cord injury, motor nervous system diseases, elderly people, or other lower limb mobility disorders (Mikołajewska and Mikołajewski, 2013; Leaman and La, 2017). Although wheelchairs play an important role in improving the quality of life and social participation of these people, the health problems caused by prolonged use of wheelchairs also require attention. When people are in a sitting posture, the lumbar muscle group plays a key role in supporting the spine and maintaining posture stability (Callaghan and McGill, 2001; O'Sullivan et al., 2002; Nowakowska et al., 2017), and is an important part of the core muscle group of the human body. However, sitting in a wheelchair for a long time may lead to persistent tension and fatigue of the waist muscles, which may cause discomfort in the waist, which greatly affects the comfort of wheelchair users.

Previous studies have pointed out that different sitting positions have a direct impact on waist comfort (Vergara and Page, 2002). One study (Black et al., 1996) classified sitting positions as comfortable (taking a comfortable, relaxed position), hunched, upright, and forward-leaning (leaning forward by hip flexion), and evaluated the effect of lumbar and pelvic tilt changes (achieved by hip flexion) on cervical vertebrae while maintaining lumbar lordosis. Another study (Claus et al., 2009) classified the Slump, Flat, Long lordosis, and Short lordosis types of sitting based on their thoracolumbar and lumbar angles, and discussed which spinal formations were beneficial. The methods adopted in these studies need to verbally describe or show pictures to the subjects to make them imitate each posture. The postures presented vary greatly under the influence of people's subjective factors, so the detection and classification of sitting posture require more objective features or indicators.

There are also differences in people's sitting posture in different scenarios. Current studies on sitting comfort in different scenarios include: Literature (Schmidt et al., 2014) analyzed several papers suggesting the optimal driving posture of cars, and discussed several factors affecting the optimal posture such as gender, seat design, body shape, and age; Literature (Mörl and Bradl, 2013) studied the waist posture and muscle activity of the human body in the office. However, most people who use wheelchairs lack self-care ability and often face a situation in which they are in a relatively fixed posture for dozens of minutes or even longer, so a reasonable sitting posture will be very effective in delaying the generation of lumbar muscle fatigue of wheelchair users. At the muscle level, fatigue means that muscle fibers have a reduced ability to produce force (Marco et al., 2017). The measurement of fatigue in the state of exercise is generally to measure the change of muscle power or power, which is achieved by the maximum autonomous contraction test (MVCs) (Yousif et al., 2019). For wheelchair users, most of the time the body is in a static state, so the use of non-invasive technology such as sEMG can better assess the state of muscle fatigue (Barsotti et al., 2020). For example, literature (Liu et al., 2019) studies an EMG patch device that can be transmitted wirelessly and uses the EMD method to decompose the sEMG signal to obtain MF value to evaluate muscle fatigue state. In another paper (Cahyadi et al., 2019), DELSYS Bagnoli EMG 8 channel and surface EMG sensor-based single difference system were used to collect sEMG data, and the average power frequency (MNF) in frequency domain analysis was used as an index to study the progress of muscle fatigue during arm movement.

At present, there are relatively few studies on the influence of different sitting positions on lumbar fatigue during wheelchair use. Therefore, the objective of this paper is to obtain the lumbar muscle fatigue status of wheelchair users by studying the detection method of human sitting position and sMEG collection and analysis method and to combine the characteristics of human sitting position with frequency domain analysis. The effects of different sitting conditions on the fatigue progress of lumbar muscles were analyzed. Ultimately, we hope to provide more scientific recommendations for wheelchair users by comparing the effects of different sitting positions on lumbar muscle fatigue.

The remainder of this article is organized as follows. In Section 2, we describe the materials and methods used in the study. In Section 3, we describe the steps of the experiment and the multivariate nonlinear regression model. In Section 4, we present the results and discuss them. Finally, we give a conclusion about the whole article.

2 Materials and methods

2.1 sEMG data acquisition methods

The sEMG signals collection process for muscle fatigue analysis in this study is as follows: Initially, sEMG signals raw signals were obtained from the erector spinae muscles using Ag/AgCI electrodes with adhesive properties and wires (as shown in Figure 1, where white represents positive, black represents negative, and green represents the reference electrode). The wires were connected to an sEMG signals acquisition board for signal collection and storage, and finally, the data were imported to a PC for further analysis.

The sEMG signals acquisition board, designed and manufactured by our team, is depicted in Figure 2. According to the Nyquist sampling theorem, the sampling frequency must be twice the maximum signal frequency. As the frequency range of sEMG signals is 0 ~ 500 Hz, the sampling rate of our designed sEMG signals acquisition board is set at 1000 Hz.Since the original sEMG signal is a weak electrical signal with a small amplitude that is challenging to directly collect, we initially used an amplifier circuit with a gain of 500 (AD620, Analog Devices) to amplify it. Subsequently, the signal

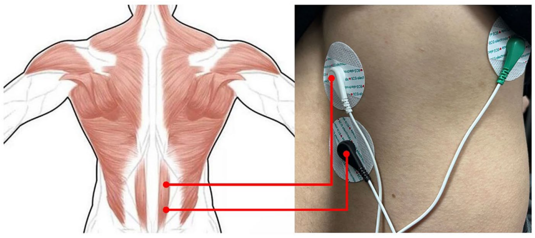

FIGURE 1
Schematic diagram of Ag/AgCl electrode placement.

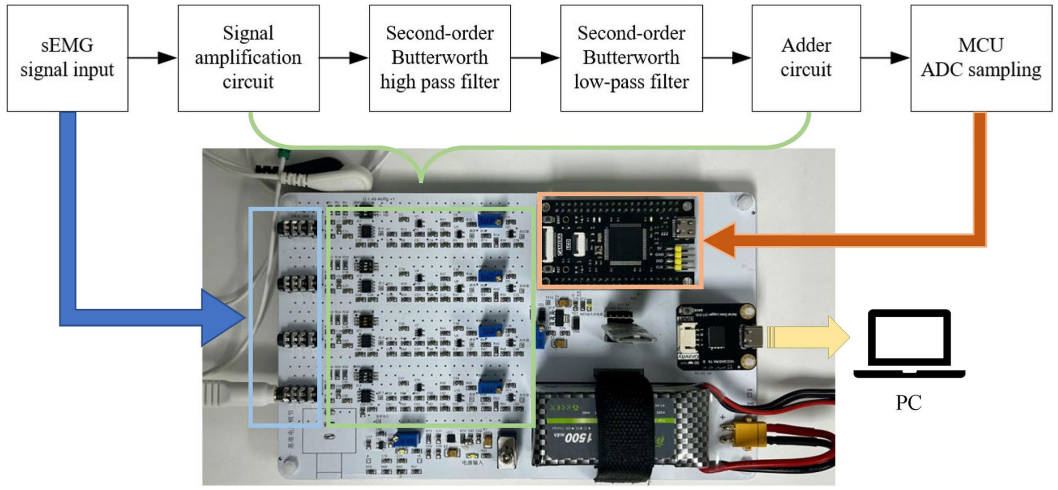

FIGURE 2
sEMG acquisition board structure diagram.

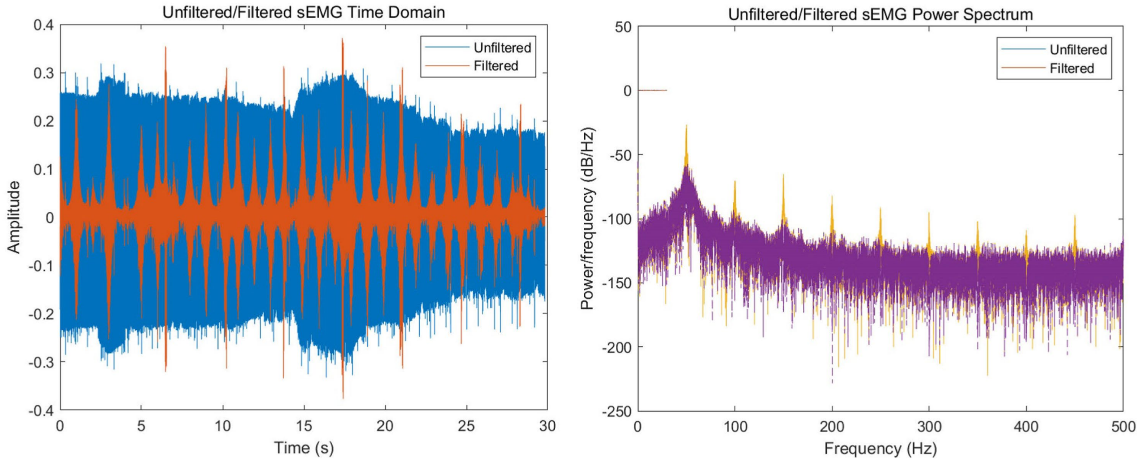

FIGURE 3
Time-domain and power spectral density comparison of sEMG signals before and after notch filtering.

underwent filtering processing through a second-order Butterworth high-pass filter with a cutoff frequency of 10 Hz and a second-order Butterworth low-pass filter with a cutoff frequency of 500 Hz. This filtering aimed to avoid interference from DC components, baseline drift, and high-frequency signals. Since the ADC (Analog-to-Digital Converter) of the microcontroller can only accept non-negative inputs, and the amplitude of the electromyographic signal is negative, the signal also needs to be elevated through an adder circuit (LM321, Texas Instruments). Finally, we collected the sEMG signal through the ADC pins of the microcontroller and stored it in memory for retrieval by the PC.

2.2 Data preprocessing

The raw sEMG data collected after acquisition is in the form of digital output from the ADC. Therefore, we need to perform a calculation to restore the amplitude of the signal. The calculation formula is shown in Equation 1.

$$sEMG\ Amplitude = \frac{Digital\ value \cdot V_{ref}}{2^n - 1} - V_{add} \tag{1}$$

In the formula, *Digital value* is the digital value output by the ADC, V_{ref} is the reference voltage of the ADC, n is the number of bits of the ADC, and V_{add} is the elevated voltage value of the adder circuit. The raw sEMG data is already in a relatively suitable frequency range through the filter in the circuit, but we also need to filter it to eliminate power frequency interference. In Figure 3, we can see from the power density diagram of the original signal that there are relatively obvious power frequency interference of 50 Hz and its harmonics, so we use a 45 dB attenuated Butterworth trap filter in Matlab to eliminate these noises.

2.3 Muscle fatigue analysis methods

After the collection of sEMG data is completed, frequency domain analysis of sEMG data is required to obtain characteristic parameters related to the development of muscle fatigue. Among them, MF median frequency and MPF average power frequency are commonly used to judge muscle fatigue (Cao et al., 2018). The average power frequency is the weighted average of the spectrum, obtained by multiplying each frequency component of the spectrum by its corresponding power, then summing all frequencies, and finally dividing by the total power. The basic formula is shown in Equation 2.

$$MPF = \frac{\int_{f_a}^{f_b} f \cdot P(f)\,df}{\int_{f_a}^{f_b} P(f)\,df} \tag{2}$$

In the formula, f represents frequency, f_a and f_b are the upper and lower limits of the spectrum, and $P(f)$ is the power at the frequency f.

2.4 Sitting posture detection methods

As for the detection methods of human posture, scholars from various countries have proposed a variety of feasible schemes. For example, van Nassau et al. (2015) and Rowlands et al. (2014) chose the scheme of activPAL activity monitor, which detected human posture by wearing an accelerometer on the wrist and thigh of the subjects. However, this method can only roughly determine whether the human body is in a standing or sitting position, and cannot obtain more detailed information about the human posture. Estrada and Vea (2016) used a customized belt to fix three gyroscopes on the subjects' thoracic vertebrae, thoracolumbar vertebrae, and lumbar vertebrae to detect the human sitting position. Although this scheme could better restore the shape of the human spine, due to the need for additional wearing devices on the back during the detection process, it could not fully restore the natural sitting position. Similar to the scheme adopted by Huang and Ouyang (2012) and Matuska et al. (2020), multiple pressure sensors were installed on the back and cushion of the seat to detect the human sitting position. However, due to the small number of sensor points, this scheme could only detect several preset sitting types.

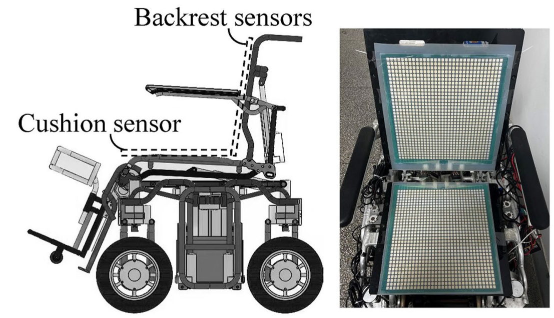

FIGURE 4
Schematic diagram of thin film pressure sensor installation locations.

In the actual sitting state, due to the differences in people's sitting habits and body types, it is not completely accurate to distinguish the sitting position of the human body simply by the Angle of the seat. Therefore, to better obtain the force distribution of the wheelchair without affecting the seated position of the passenger, a 32*32 array thin film pressure sensor was selected to be installed on the cushion and back of the wheelchair, as shown in Figure 4. This array pressure sensor has 1,024 independent sampling points. It can better restore the force of the back of the wheelchair and the cushion, and use it to distinguish the sitting situation of the human body. According to the actual sampling requirements, our team independently designed a collection card system (Cui et al., 2023), which can collect and report data for each point.

2.5 Sitting posture feature extraction methods

Seating posture data is obtained from the array-type thin-film pressure sensor mentioned in Section 2.4. Each force unit of this sensor acts as a variable resistor. Based on this characteristic, we designed a data acquisition card with a voltage series negative feedback amplifier circuit, capable of collecting the resistance values at each point on the sensor. Additionally, the acquisition card features a row-column scanning circuit, which, under MCU control, connects the specified force unit to the feedback amplifier circuit, followed by voltage value collection through ADC. According to the characteristics of the series negative feedback amplifier circuit, the output voltage of the ADC can be derived from Equation 3.

$$V_{out} = \left(1 + \frac{R_f}{R}\right) \times V_{in} \tag{3}$$

In the formula, R_f represents the resistance value of the force unit, R is a fixed resistor, V_{in} is the input voltage at the inverting terminal of the operational amplifier. Therefore, through the ADC-collected voltage value V_{out}, we can obtain the value of R_f. Then, using the characteristic curve of R_f with pressure, the pressure received by each force unit can be calculated. For the collected pressure data, we will save it through the upper computer of the PC. The pressure data of several different sitting states are shown in Figure 5. Part A shows a sitting position with a relatively backward seating position and a large backrest contact area; Part B demonstrates a sitting position with a relatively forward seating position and a small backrest contact area; Part C demonstrates a sitting posture in which the seating position and backrest contact area are moderate.

For the collected pressure data, we extract three features to reflect the body posture: pressure percentage, span, and centroid, as shown in Figure 6. The percentage refers to the percentage of pressure points exceeding a certain threshold in the entire sitting posture area compared to the total number of sensor force units. A higher percentage indicates a larger contact area between the body and the wheelchair, reflecting a more even pressure distribution, while a lower percentage indicates a smaller contact area. The span represents the distribution range of pressure points in the row direction, i.e., the difference between the top and bottom rows of pressure points, reflecting the variation range of the sitting posture in the row direction. The centroid represents the average position

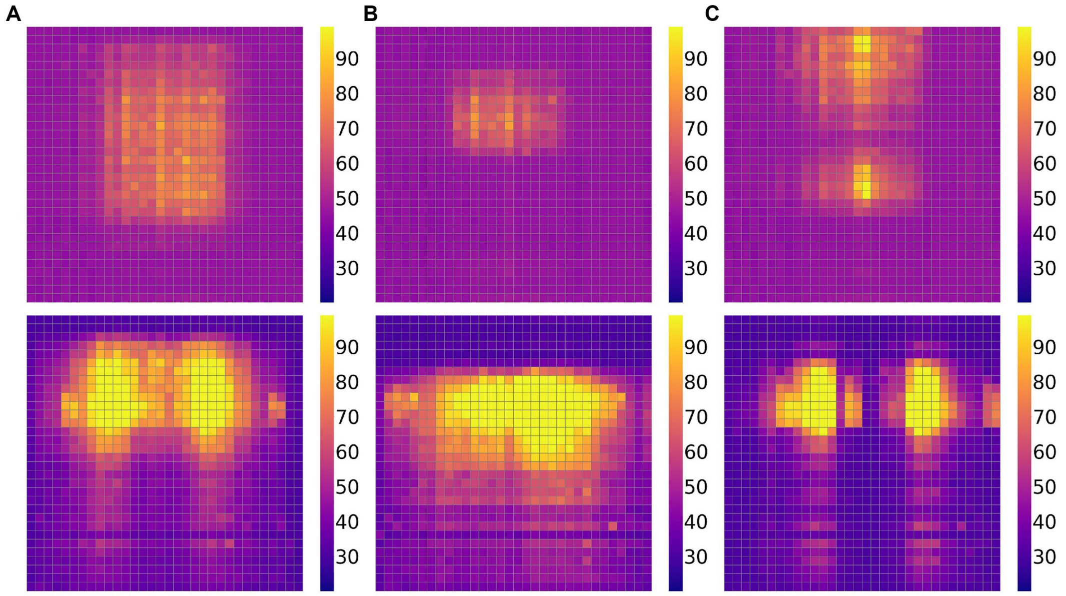

FIGURE 5
Three sets of pressure data graphs for different situations, with the upper part being the backrest and the lower part being the seat cushion: Part **(A)** represents the seating position being rear; Part **(B)** indicates that the seating position is in the front; Part **(C)** indicates a moderate seating position.

of pressure points in the entire sitting posture. It is the center position calculated based on weights (i.e., pressure values). Here, we only calculate the row coordinate of the centroid (the column coordinate is more correlated with the occupant's position relative to the sensor and less relevant to the sitting posture), and its calculation formula is shown in Equation 4.

$$Centroid\_row = \frac{\sum_i y_i p_i}{\sum_i y_i} \tag{4}$$

In the formula, y_i represents the vertical coordinate of the pressure point, and p_i represents the pressure value of that point. The above three characteristic quantities provide information about the distribution, balance, and range of variation of sitting posture respectively, and also include body shape factors to a certain extent. Compared with the human posture features such as lumbar spine and pelvic Angle commonly used in previous studies (Ma et al., 2016; Wan et al., 2021), the features derived from pressure data can more truly reflect the load distribution and posture changes of the human body on the wheelchair, rather than the information of some specific joints or parts. Moreover, there is no need to wear additional equipment in the collection process. The error caused by flexible materials such as clothing and straps can be eliminated, and the sitting position of the human body can be better restored and presented.

3 Experiment and analysis

3.1 Experiment procedures

The experiment invited 20 male volunteers, aged between 21 and 34, whose daily work and life were mainly office environment. All volunteers had no diseases related to the waist or spine. We informed

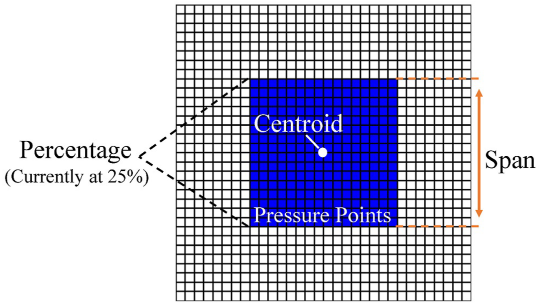

FIGURE 6
Schematic diagram of three seating posture features.

the subjects about the types and uses of data to be collected and obtained their consent. Before the experiment, we will inform each subject of the specific process of the experiment, including the placement of electrode strips and the process of data collection. To minimize the impact on the subject's wheelchair usage habits, the sitting posture in the wheelchair is not specified, and personal usage habits shall be subject to.

To ensure that people's physical state is relatively consistent, the experiment is chosen to be carried out at 9 o 'clock every day, and only one experiment is carried out every day. Before the formal start of each experiment, we first disinfected and cleaned the waist skin of the subjects, and then placed the electrode patch at the position of the vertical spinal muscle and started the collection of sEMG. When the subject sits in the wheelchair, we will properly adjust the leg support Angle of the wheelchair so that the knee joint is in a state of 90°, and the foot height will be adjusted so that each subject's feet can be naturally placed on the foot without hanging. The backrest Angle and foot Angle of the wheelchair remain unchanged, and the volunteers can freely adjust their sitting position

FIGURE 7
Schematic Diagram of muscle fatigue and seating posture detection experiment.

within 1 min after the start of the experiment until the most comfortable state, as shown in Figure 7. The whole experiment will last for 1 h. During the experiment, the fit degree between the back of the subject and the back of the wheelchair should be kept unchanged as far as possible. The buttocks and legs should not have large movements, while the upper limbs can move freely. We will check the current sitting position through the upper computer every 5 min to ensure that there is no major change in sitting position.

We will collect the sitting position data and the sEMG data of the vertical spine muscle for the first time 1 min after the start of the experiment. When the experiment time reaches 60 min, we will collect the sEMG data of the vertical spine muscle for the second time, and the duration of each sEMG data collection is 30 s.

3.2 Multiple nonlinear regression

In all the experimental data, the dependent variable was the percentage decrease in the average power frequency of the EMG signal, and the independent variable was six sitting features from the human body. Due to the non-simple linear relationship between the dependent variable and independent variables in this study, the data exhibits different curvatures in certain regions. Therefore, a multivariate nonlinear regression analysis is employed to analyze the relationship between fatigue values and sitting posture features. In multivariate nonlinear regression, it is commonly assumed that there is a complex nonlinear relationship between the dependent and independent variables, and nonlinear functions are used to fit the data. This model can more accurately describe the relationship between actual data and variables, capturing nonlinear effects.

We used MATLAB software for data analysis and multivariate binomial regression toolbox for regression analysis. The basic formula of the pure quadratic model invoked is shown in Equation 5.

$$y = \left(\beta_0 + \beta_1 x_1 + \ldots + \beta_m x_m + \sum_{i=1}^{m} \beta_{ii} x_i^2 \right) \tag{5}$$

In the equation, y is the dependent variable, $\boldsymbol{x_1 - x_m}$ are independent variables, β_0 is the intercept, $\beta_0 - \beta_m$ are coefficients of independent variables, and $\beta_{11} - \beta_{mm}$ are coefficients of quadratic terms. The experimental data are shown in Table 1. The leftmost part is the dependent variable, that is, the percentage decline of MPF value, and the rest is the independent variable. From left to right, they are respectively: line coordinates of the centroid of the pressure point at the cushion, percentage of the pressure area at the cushion, row span of the pressure area at the cushion, line coordinates of the centroid of the pressure point at the backrest, percentage of the pressure area at the backrest and row span of the pressure at the backrest.

Firstly, import the data of 6 independent variables into a 20×6 matrix as input variables, denoted as $X = [x_1, x_2, x_3, x_4, x_5, x_6]$, and import the dependent variable into a 20×1 matrix as output, denoted as Y. Secondly, invoke the rstool command to import the input, output, and the model, as shown in Figure 8. The images from left to right represent the centroid coordinates of pressure points at the cushion, the percentage of pressure area at the cushion, the range of pressure span at the cushion, the centroid coordinates of pressure points at the backrest, the percentage of pressure area at the backrest and the range of pressure span at the backrest and the regression relationship between the percentage decline of MPF. The red dotted line represents the independent variable, the green represents the dependent variable, and the purple line represents the change interval of the actual data.

4 Result and discussion

By moving the data label in Figure 8, it can be seen that when the centroid row coordinate of the cushion pressure point is about 16, the cushion pressure area percentage is about 80%, and the cushion pressure span range is about 27, the backrest pressure point centroid row coordinate is about 15, the backrest pressure area percentage is about 35%, and the backrest pressure span range is about 16. At this time, the MPF value of the subjects decreased by a small percentage, and the fatigue development of the muscles was slower. In addition, we can see that the pressure area percentage at the seat cushion is a more sensitive independent variable, too large or too small pressure area percentage will easily cause lumbar muscle fatigue, and too small pressure area percentage is caused by the seat position too far forward or the big legs do not touch the seat cushion. The excessive pressure area percentage is caused by the seating position too far back, which is also confirmed by the changing trend of the pressure point centroid coordinates at the cushion and the pressure span range at the cushion. In addition, the data analysis results of the backrest can show that maintaining a large percentage of pressure area is conducive to delaying the generation of muscle fatigue, that is, people should contact the back of the wheelchair as much as possible to reduce the burden on the waist, whether it is the back or the waist to contact the back of the wheelchair can play a certain effect, depending on the individual's sitting habits. However, try to avoid the sitting posture with the chest, maintaining such a sitting posture for a long time is easy to leads to fatigue of the waist muscles, which can be seen from the centroid coordinates of the pressure point at the back.

Due to the limitations of the site and experimental conditions, the experimental subjects in this paper are all men. Considering the differences in body structure between different genders, the experimental results of women may be somewhat deviated from the current results. Therefore, we plan to recruit female volunteers to further supplement the experimental samples in the future to improve the universality of the conclusions.

TABLE 1 Experimental data.

MPF	Seat			Backrest		
	Centroid	Percentage	Span	Centroid	Percentage	Span
−6.2894	15.30519	82.48828	28	13.2854	38.76953	22
−6.9056	12.77845	76.95313	30	11.51089	30.56641	21
−6.4382	13.82326	83.88672	28	12.81855	31.93359	16
−7.2153	10.03658	70.85938	28	9.18744	37.20703	22
−6.9228	11.05657	75.76953	26	10.90965	18.75	14
−6.321	16.49812	80.53906	26	14.48153	29.88281	20
−6.5555	13.20405	78.61328	28	14.27513	31.54297	20
−7.1298	7.769629	89.78906	29	16.97433	32.03125	14
−6.8112	9.52833	77.27344	26	16.53466	11.81641	9
−6.7243	14.36115	77.12891	23	18.23038	22.16797	17
−6.5408	9.067584	81.05469	28	14.7101	27.05078	21
−7.0093	10.89296	86.64063	28	16.17976	33.39844	22
−6.7687	12.06241	80.85938	30	15.37197	32.51953	21
−6.5976	14.04636	79.48828	28	12.22669	22.94922	17
−6.4891	16.96319	80.61328	25	10.25274	31.64063	15
−7.0564	11.3105	72.36328	26	15.07457	15.82031	14
−6.6645	14.0427	78.61328	29	9.301891	26.75781	21
−6.8461	10.63302	85.21484	31	15.36672	19.33594	13
−6.3887	12.87032	83.46875	25	12.11112	33.39844	17
−7.0313	11.8302	86.13281	28	15.442	17.77344	21

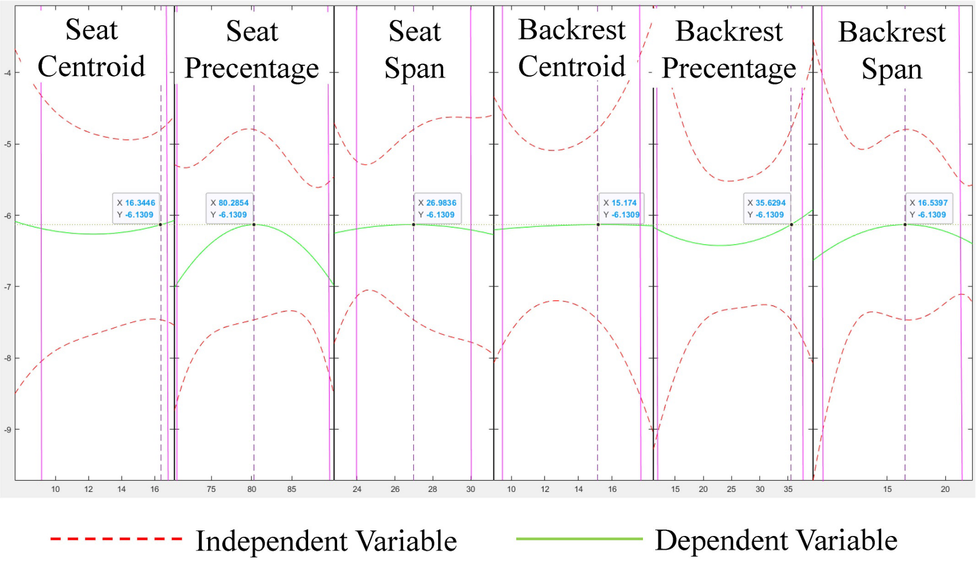

FIGURE 8
Multivariate nonlinear regression curve plot.

5 Conclusion

Because of the situation that wheelchair users are prone to lumbar muscle fatigue when they keep sitting for a long time, this paper hopes to study the relationship between different sitting positions and the development of lumbar muscle fatigue in the process of using wheelchairs, to provide more scientific guidance and suggestions for the use of wheelchairs. First, sEMG signal data from the upright spine muscle of the human body were collected, and the MPF decline percentage of the sEMG signal was obtained as the dependent variable through frequency domain analysis. Then, an array of thin film pressure sensors was used to obtain information on human sitting posture, and six features of pressure point centroid, area percentage, and span from the seat cushion and backrest were extracted as independent variables. Multivariate nonlinear regression is used to capture the relationship between independent variables and dependent variables. Through the analysis of the experimental data, we give the following suggestions for the use of wheelchairs: When riding a wheelchair, people should sit in the middle and back of the seat cushion, so that the Angle of the hip joint can be in a natural state, and the thigh part should fully contact the seat cushion to avoid the weight of the body concentrated on the hip; The back should also be fully in contact with the back of the wheelchair to reduce the burden on the waist, and the spine posture can be adjusted appropriately according to personal habits, but to avoid maintaining a chest for a long time, which will lead to the lumbar spine in an unnatural physiological Angle and easily lead to fatigue of the waist muscles.

Data availability statement

The original contributions presented in the study are included in the article/supplementary material, further inquiries can be directed to the corresponding author.

Author contributions

ZH: Methodology, Writing – original draft, Writing – review & editing. JC: Conceptualization, Funding acquisition, Methodology, Resources, Supervision, Writing – review & editing. YW: Conceptualization, Data curation, Formal analysis, Methodology, Writing – review & editing. SY: Validation, Visualization, Writing – review & editing.

Funding

The author(s) declare financial support was received for the research, authorship, and/or publication of this article. This research was funded by China's National Key R&D Program (2020YFC2007401): Multimodal intelligent sensing, human-machine interaction, and active safety technology.

Conflict of interest

The authors declare that the research was conducted in the absence of any commercial or financial relationships that could be construed as a potential conflict of interest.

Publisher's note

References

Barsotti, A., Khalaf, K., and Gan, D. (2020). Muscle fatigue evaluation with Emg and acceleration data: A case study. *Annu. Int. Conf. IEEE Eng. Med. Biol. Soc.* 20, 3138–3141. doi: 10.1109/EMBC44109.2020.9175315

Black, K. M., Mcclure, P., and Polansky, M. (1996). The influence of different sitting positions on cervical and lumbar posture. *Spine* 21, 65–70. doi: 10.1097/00007632-199601010-00015

Cahyadi, B. N., Khairunizam, W., Zunaidi, I., Hui Ling, L., Shahriman, A. B., Zuradzman, M. R., et al. (2019). Muscle fatigue detections during arm movement using Emg signal. *IOP Conf. Ser.: Mater. Sci. Eng.* 557:012004. doi: 10.1088/1757-899x/557/1/012004

Callaghan, J. P., and Mcgill, S. M. (2001). Low Back joint loading and kinematics during standing and unsupported sitting. *Ergonomics* 44, 280–294. doi: 10.1080/00140130118276

Cao, A., Zhang, S., Liu, R., Zou, L., and Fan, C. E. (2018). Muscle fatigue state classification system based on surface electromyography signal. *J. Comput. Appl.* 38, 1801–1808. doi: 10.11772/j.issn.1001-9081.2017102549

Claus, A. P., Hides, J. A., Moseley, G. L., and Hodges, P. W. (2009). Is 'ideal' sitting posture real?: measurement of spinal curves in four sitting postures. *Man. Ther.* 14, 404–408. doi: 10.1016/J.Math.2008.06.001

Cui, J., Huang, Z., Li, X., Cui, L., Shang, Y., and Tong, L. (2023). Research On Intelligent Wheelchair Attitude-Based Adjustment Method Based On Action Intention Recognition. *Micromachines* 14:1265. doi: 10.3390/mi14061265

Estrada, J. E., and Vea, L. A. Real-Time Human Sitting Posture Detection Using Mobile Devices. (2016) *IEEE Region 10 Symp.*, 9. 140–144. doi: 10.1109/TENCONSpring.2016.7519393

Huang, Y. R., and Ouyang, X. F. Sitting posture detection and recognition using force sensor. (2012) 5th International Conference On Biomedical Engineering And Informatics, Chongqing, China.

Leaman, J., and La, H. M. (2017). A comprehensive review of smart wheelchairs: past, present, and future. *IEEE Trans. Hum. Mach. Syst.* 47, 486–499. doi: 10.1109/Thms.2017.2706727

Liu, S.-H., Lin, C.-B., Chen, Y., Chen, W., Huang, T.-S., and Hsu, C.-Y. (2019). An Emg patch for the real-time monitoring of muscle-fatigue conditions during exercise. *Sensors* 19:3108. doi: 10.3390/s19143108

Ma, S., Cho, W. H., Quan, C. H., and Lee, S. *A sitting posture recognition system based on 3 Axis accelerometer*. (2016) IEEE Conference On Computational Intelligence In Bioinformatics And Computational Biology (Cibcb), Chiang Mai, Thailand.

Marco, G., Alberto, B., and Taian, V. (2017). Surface Emg and muscle fatigue: Multi-Channel approaches to the study of myoelectric manifestations of muscle fatigue. *Physiol. Meas.* 38, R27–R60. doi: 10.1088/1361-6579/Aa60b9

Matuska, S., Paralic, M., and Hudec, R. (2020). A smart system for sitting posture detection based on force sensors and Mobile application. *Mob. Inf. Syst.* 2020, 1–13. doi: 10.1155/2020/6625797

Mikołajewska, E., and Mikołajewski, D. (2013). Wheelchair development from the perspective of physical therapists and biomedical engineers. *Adv. Clin. Exp. Med.* 19, 771–776.

Mörl, F., and Bradl, I. (2013). Lumbar posture and muscular activity while sitting during office work. *J. Electromyogr. Kinesiol.* 23, 362–368. doi: 10.1016/J.Jelekin.2012.10.002

Nowakowska, K., Gzik, M., Michnik, R., Myśliwiec, A., Jurkojć, J., Suchoń, S., et al. (2017). "The loads acting on lumbar spine during sitting down and standing up" in *Innovations in biomedical engineering*. eds. M. Gzik, E. Tkacz, Z. Paszenda and E. Piętka (Cham: Springer International Publishing), 169–176.

O'sullivan, P. B., Grahamslaw, K. M., Kendell, M., Lapenskie, S. C., Möller, N. E., and Richards, K. V. (2002). The effect of different standing and sitting postures on trunk muscle activity in a pain-free population. *Spine* 27, 1238–1244. doi: 10.1097/00007632-200206010-00019

Park, J. H., Moon, J. H., Kim, H. J., Kong, M. H., and Oh, Y. H. (2020). Sedentary lifestyle: overview of updated evidence of potential health risks. *Korean J. Fam. Med.* 41, 365–373. doi: 10.4082/Kjfm.20.0165

Rowlands, A. V., Olds, T. S., Hillsdon, M., Pulsford, R., Hurst, T. L., Eston, R. G., et al. (2014). Assessing sedentary behavior with the Geneactiv: introducing the sedentary sphere. *Med. Sci. Sports Exerc.* 46, 1235–1247. doi: 10.1249/MSS.0000000000000224

Schmidt, S., Amereller, M., Franz, M., Kaiser, R., and Schwirtz, A. (2014). A literature review on optimum and preferred joint angles in automotive sitting posture. *Appl. Ergon.* 45, 247–260. doi: 10.1016/J.Apergo.2013.04.009

Van Nassau, F., Chau, J. Y., Lakerveld, J., Bauman, A. E., and Van Der Ploeg, H. P. (2015). Validity and responsiveness of four measures of occupational sitting and standing. *Int. J. Behav. Nutr. Phys. Act.* 12:144. doi: 10.1186/S12966-015-0306-1

Vergara, M., and Page, Á. (2002). Relationship between comfort and Back posture and mobility in sitting-posture. *Appl. Ergon.* 33, 1–8. doi: 10.1016/S0003-6870(01)00056-4

Wan, Q., Zhao, H., Li, J., and Xu, P. (2021). Hip positioning and sitting posture recognition based on human sitting pressure image. *Sensors* 21:426. doi: 10.3390/s21020426

Yousif, H. A., Zakaria, A., Rahim, N. A., Salleh, A. F. B., Mahmood, M., Alfarhan, K. A., et al. (2019). Assessment of muscles fatigue based on surface Emg signals using machine learning and statistical approaches: a review. *IOP Conf. Ser.: Mater. Sci. Eng.* 705:012010. doi: 10.1088/1757-899x/705/1/012010

frontiers | Frontiers in Neuroscience

TYPE Original Research
PUBLISHED 26 March 2024
DOI 10.3389/fnins.2024.1330634

EDITED BY
Yingbai Hu,
The Chinese University of Hong Kong, China

REVIEWED BY
Rong Song,
Sun Yat-sen University, China
Yisen Huang,
The Chinese University of Hong Kong, China

*CORRESPONDENCE
Xiangyu Wang
✉ wangxyu@nankai.edu.cn

RECEIVED 31 October 2023
ACCEPTED 11 March 2024
PUBLISHED 26 March 2024

CITATION
Ren F, Wang X, Yu N and Han J (2024) Adaptive fuzzy control for tendon-sheath actuated bending-tip system with unknown friction for robotic flexible endoscope. *Front. Neurosci.* 18:1330634. doi: 10.3389/fnins.2024.1330634

Adaptive fuzzy control for tendon-sheath actuated bending-tip system with unknown friction for robotic flexible endoscope

Fan Ren[1], Xiangyu Wang[1,2]*, Ningbo Yu[1,2] and Jianda Han[1,2]

[1]The Tianjin Key Laboratory of Intelligent Robotics, College of Artificial Intelligence, Institute of Robotics and Automatic Information Systems, Nankai University, Tianjin, China, [2]The Institute of Intelligence Technology and Robotic Systems, Shenzhen Research Institute of Nankai University, Shenzhen, China

Introduction: The tendon-sheath actuated bending-tip system (TAB) has been widely applied to long-distance transmission scenes due to its high maneuverability, safety, and compliance, such as in exoskeleton robots, rescue robots, and surgical robots design. Due to the suitability of operation in a narrow or tortuous environment, TAB has demonstrated great application potential in the area of minimally invasive surgery. However, TAB involves highly non-linear behavior due to hysteresis, creepage, and non-linear friction existing on the tendon routing, which is an enormous challenge for accurate control.

Methods: Considering the difficulties in the precise modeling of non-linearity friction, this paper proposes a novel fuzzy control scheme for the Euler-Lagrange dynamics model of TAB for achieving tracking performance and providing accurate friction compensation. Finally, the asymptotic stability of the closed-loop system is proved theoretically and the effectiveness of the controller is verified by numerical simulation carried out in MATLAB/Simulink.

Results: The desired angle can be reached quickly within 3 s by adopting the proposed controller without overshoot or oscillation in Tracking Experiment, demonstrating the regulation performance of the proposed control scheme. The proposed method still achieves the desired trajectory rapidly and accurately without steady-state errors in Varying-friction Experiment. The angle errors generated by external disturbances are <1 deg under the proposed controller, which returns to zero in 2 s in Anti-disturbance Experiment. In contrast, comparative controllers take more time to be steady and are accompanied by oscillating and residual errors in all experiments.

Discussion: The proposed method is model-free control and has no strict requirement for the dynamics model and friction model. It is proved that advanced tracking performance and real-time response can be guaranteed under the presence of unknown bounded non-linear friction and time-varying non-linear dynamics.

KEYWORDS

tendon-sheath mechanism, fuzzy control, friction compensation, robust control, robotic flexible endoscope

1 Introduction

The tendon-sheath mechanisms (TSM) have attracted widespread interest in the field of surgery, pipeline inspection, and rehabilitation due to their flexibility, safety, and dexterity, such as applied in the neurosurgery surgical robot, the otolaryngology robot, the cardiac surgical robot, etc. (Burgner-Kahrs et al., 2015; Do et al., 2015a, 2016; Kang et al., 2020; Yin et al., 2020; Wang et al., 2023). The flexible characteristics of

TSM make it highly versatile and applicable in narrow scenarios (Berthet-Rayne et al., 2018; Wang et al., 2020, 2021; Rho et al., 2021). Consequentially, numerous studies have focused on the application of TSM in the field of tendon-sheath actuated bending-tip (TAB) systems for natural orifice transluminal endoscopic surgeries (NOTES) as shown in Figure 1 in which bronchi is provided by Servier Medical Art (https://smart.servier.com) under CC BY 3.0 license. Due to the fact that the TAB can be deformed to fit the shape of the channel to avoid damaging the inner organ. However, the unknown friction existing in the tendon routing introduces motion backlash and persistent residual errors, which in turn increases the difficulties in the accurate tracking task of TAB systems. Therefore, it still requires extra effort to address the control issues of TAB systems.

The hysteresis effect is a crucial issue for the precise control of TAB systems. Most previous studies focused on improving the model accuracy of the hysteresis phenomenon in the TSM. For example, Do et al. (2015a,c, 2016) modified the Coleman-Hodgdon model for the hysteresis phenomenon of TSM and proposed a series of control methods, where no exact value of model parameters are required. Moreover, Thai et al. (2021) developed a simplified hysteresis model based on the generalized Bouc-Wen hysteresis model, while providing higher accuracy than previous Bouc-Wen models. Legrand et al. (2018) and Zhang et al. (2014) built piecewise models for the TAB systems. Similarly, Lee et al. (2021) proposed a simplified piecewise linear model to construct both backlash hysteresis and dead zone compensators together. Their research suggested that the errors from backlash hysteresis and dead zone are considerably reduced and therefore the accuracy of robotic control is improved.

Friction in the tendon-sheath actuator brings significant effects on the control performance of the objective system, such as additional chattering and input backlash. Previous research has focused on developing specific friction models for TSM to improve the modeling precision of the TAB. For example, inspired by the static Coulomb friction model and Hill muscle model, Zhang et al. (2017) presented a high-accuracy transmission model for the TSM. Moreover, Do et al. (2015b) developed a dynamic friction model to predict friction force for small displacement by using the LuGre model, which can capture the asymmetric loops and dead zone accurately. With consideration of the interaction continuity, Norouzi-Ghazbi and Janabi-Sharifi (2020) successfully proposed an equivalent model to estimate forces and moments applied to the sheath of the TSM. Furthermore, Jung and Bae (2016) proposed a feedforward scheme based on the force transmission model to compensate for the friction in a double-tendon-sheath actuated system. However, the TAB system has unknown dynamics and time-varying parameters, and it is very difficult to compensate for friction in real time precisely. In addition, whenever there is a change in working conditions caused by variations in TSM/TAB configurations, the friction model needs to be reidentified to achieve optimal results, which is challenging to apply in dynamic environments. Hence, there still remain open issues with design controllers that can overcome these model uncertainties for TAB systems.

Various control schemes have been proposed for TAB systems based on the concept of hysteresis compensation for TSM (Wu et al., 2014). Considerable works have focused on the perfect cancellation of backlash-like hysteresis using nonlinear adaptive algorithms and machine learning. Nguyen et al. (2014) developed an adaptive control scheme without requiring prior information of TAB systems to eliminate the hysteresis effects. To realize the position control of the TAB system Without sensory feedback, Wang et al. (2018) proposed a non-collocated position control method based on the inverse model of the TSM and 3-D reconstruction algorithm. Besides, Jiang et al. (2015) provided an adaptive PID controller with friction compensation for accurate position control of the dynamic model of TSM. Machine learning has also demonstrated its effectiveness in position control of the TAB system in recent years. For example, based on the kinematic model, Porto et al. (2019) proposed a learning-based hysteresis compensation technique, which directly employed the off-line parameters. Furthermore, Wu et al. (2019) proposed a neural-network-based sliding-mode control scheme by applying the radial basis function network to improve the position-control accuracy of the TAB system with modeling uncertainties and external disturbances. It is noteworthy that the integration of visual servoing with neural networks has recently become a research hotspot (Huang et al., 2022; Li et al., 2023; Cui et al., 2024). To ensure the tip of an instrument remains consistently centered in the camera, Huang et al. (2024) proposed an error learning-based sliding mode control, realizing the 4-DOF visual servo control in the robotic flexible endoscope system. The aforementioned research is impressive and offers a novel research perspective. However, these control schemes rely on an accurate reference model, and the updated process may be time-consuming in training. Therefore, developing a model-free adaptive controller to handle unknown friction for the TAB system is a worthwhile study.

In this paper, to achieve robust control of the TAB system with time-varying dynamics model parameters, a novel adaptive fuzzy controller is proposed. In particular, the complex frictional force between the tendon and sheath may be affected by the sheath deformation and lumina pressure, which brings difficulties to the accurate modeling of the TAB system. To handle this issue, the fuzzy logic system is utilized to compensate for the time-varying dynamics associated with unknown friction. The stability of the closed-loop system is guaranteed by Lyapunov-based analysis. Then, numerical simulations are implemented to further validate the tracking performance of the proposed control scheme. The main contributions of this manuscript can be summarized as follows:

1) By lumping the unknown friction, a novel dynamics model of TAB is established. It's worth mentioning that the proposed model diminishes its reliance on a priori information regarding friction and obviates the necessity for model-based linearization or supplementary linear parameterization conditions for global dynamics, thus rendering it more versatile.
2) To the best of our knowledge, this paper *first* applies fuzzy logic in the estimation of nonlinear dynamics due to unknown friction in TAB. By combining robust control with fuzzy logic regulated by an adaptive method, satisfactory performance can still be achieved under unknown time-varying friction and external perturbations.

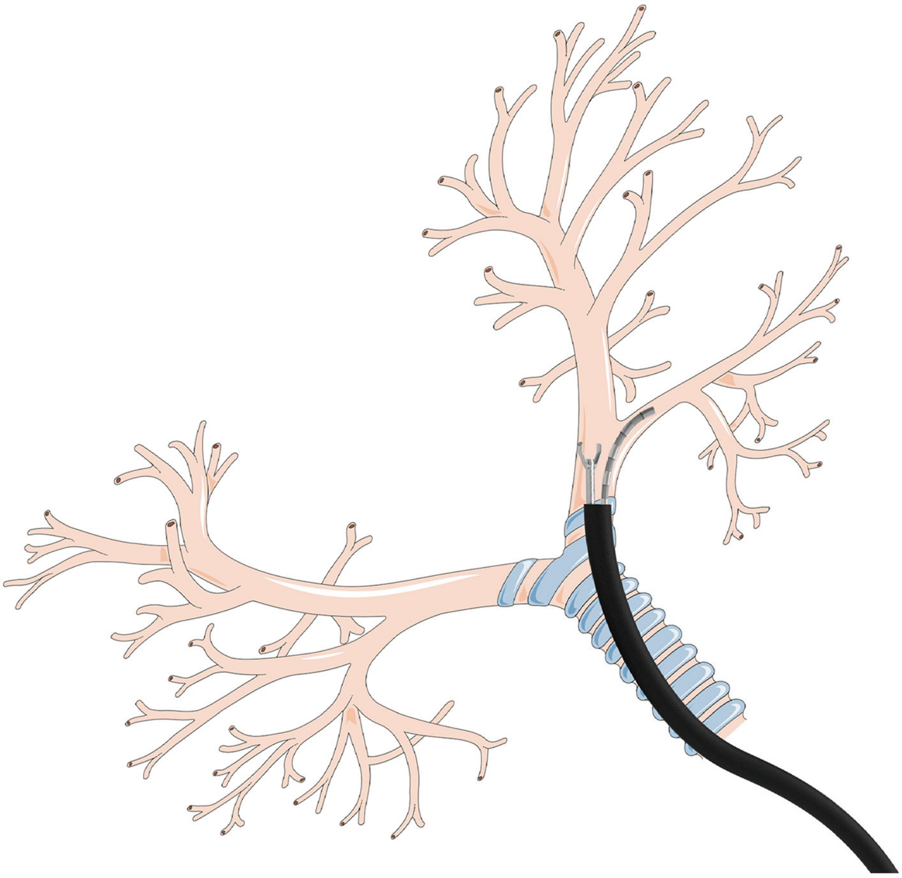

FIGURE 1
Illustration of TAB utilized in flexible bronchoscopy.

3) The asymptotic stability of the closed-loop system is rigorously proven stable using the Lyapunov method, and the effectiveness and robustness of the controller under perturbations are verified through simulation experiments.

The rest of this paper is arranged as follows: Section 2 introduces the problem formulation including the dynamics model of the TAB system and control objective. Next, A robust fuzzy-based controller is given in Section 3 with the Lyapunov stability analysis in Section 4. Then, Section 5 describes the simulation results and analysis of the proposed method. Finally, Section 6 provides the conclusion of this research.

2 Problem formulation

In this paper, the control problem for the bending motion of the TAB system was focused on. As shown in Figure 2, TAB consists of two sections of soft materials with different elastic modulus, and two symmetrically distributed actuators are built in as tendons. To facilitate the analysis of the dynamics, the bending tip is assumed to be a part of a constant curvature arc. Then, based on the Lagrangian theory, the dynamics model of the TAB system can be depicted as the following form as studied in Wang et al. (2023):

$$M(\alpha)\ddot{\alpha} + C(\alpha,\dot{\alpha})\dot{\alpha} + G(\alpha) = \mu - F_f \tag{1}$$

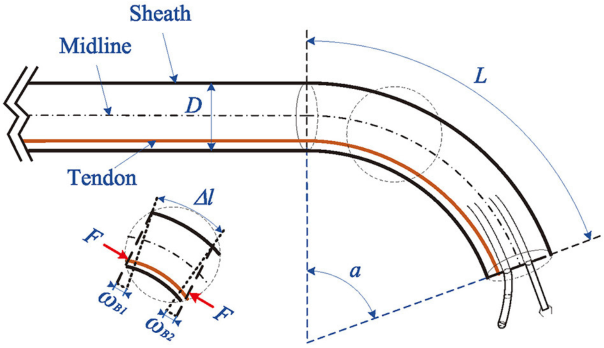

FIGURE 2
The driving principle of TAB system.

where $M(\alpha)$, $C(\alpha,\dot{\alpha})$, $G(\alpha)$ represent the inertia matrix, centripetal and Coriolis force, and the gravitational force, respectively. The detailed physical meaning of parameters in Equation (2) are given in Table 1. μ represents the input control, F_f denotes the unknown friction. $M(\alpha)$, $C(\alpha,\dot{\alpha})$, $G(\alpha)$ in Equation (1) are depicted, respectively, as follows:

$$M(\alpha) = \frac{mL_f^2}{3\alpha^2},\ C(\alpha,\dot{\alpha}) = -\frac{mL_f^2\dot{\alpha}}{3\alpha^3},\ G(\alpha) = \frac{5\pi ED^4\alpha}{64L_f} \tag{2}$$

TABLE 1 Nomenclature and symbols in nominal dynamics model.

Symbols	Physical meaning	Unit
α	Bending angle of TAB's bending part	deg
α_d	Desired angle	deg
m	Mass of TAB's bending part	kg
L_f	Length of TAB's bending part	m
E	Young's modulus of bending part's epidermis of TAB	Pa
D	Diameter of TAB's bending part	m

where α, $\dot{\alpha}$, L_f, D, m, and E represent the bending angle, the bending angular velocity, the length, the diameter, the mass of the bending part, and Young's modulus of the scope's epidermis, respectively. For simplicity, the term $M(\alpha)$, $C(\alpha, \dot{\alpha})$, and $G(\alpha)$ will be abbreviated as M, C and G respectively. According to Equation 2, it can be found that they satisfy the following properties.

Property 1. In this paper, α is the system output, and $M(\alpha)$ is positive and bounded, which can be described as follows:

$$\exists x_1 > 0, x_2 > 0, x_1 \leq M(\alpha) \leq x_2 \tag{3}$$

Property 2. In Equation 2, $M(\alpha)$ and $C(\alpha, \dot{\alpha})$ are associated and satisfy

$$\forall \alpha \in R^n, \frac{1}{2}\dot{M}(\alpha) - C(\alpha, \dot{\alpha}) = 0 \tag{4}$$

It is generally accepted that certain models take major friction effects into account, notably encompassing Coulomb friction and Stribeck effects in tandem, with the aim of achieving a more precise representation of friction. Regrettably, owing to the material creepage and the time-varying contact force between the tendon and the sheath, attaining a precise description of friction distribution in TAB solely reliant on existing models is a formidable challenge (Zhang et al., 2017; Norouzi-Ghazbi and Janabi-Sharifi, 2020; Yin et al., 2022). Moreover, the static controller struggles to effectively handle dynamic uncertainties caused by the bending of soft material. In practical application, the time-varying friction between the tendon and sheath is typically assumed to change slowly and without abrupt variations. Nevertheless, the friction F_f and model parameters $M(\alpha)$, $C(\alpha, \dot{\alpha})$, $G(\alpha)$ are also unknown but bounded (UBB). The basic control task is to estimate dynamic parameters in real-time to achieve the tracking control of the bending part under the disturbances of unknown friction. Specifically, the control task can be quantified as follows:

$$\lim_{t\to\infty} e(t) = \lim_{t\to\infty} \alpha(t) - \alpha_d = 0 \tag{5}$$

where α_d represents the desired angle.

3 Controller design

An angle control algorithm based on fuzzy adaptive sliding mode control is presented in this paper. In order to facilitate the subsequent procedure, from Equation 5, the angle tracking errors, angular velocity tracking errors, and angular acceleration tracking errors of the bending part are defined respectively as follows:

$$\begin{aligned} e &= \alpha_d - \alpha \\ \dot{e} &= \dot{\alpha}_d - \dot{\alpha} \\ \ddot{e} &= \ddot{\alpha}_d - \ddot{\alpha} \end{aligned} \tag{6}$$

where $\ddot{\alpha}$, α_d, $\dot{\alpha}_d$ and $\ddot{\alpha}_d$ represent the angular acceleration, desired angle, angular velocity, and angular acceleration, respectively. An intermediate variable $\dot{\alpha}_a$ is defined as follows:

$$\dot{\alpha}_a = \dot{\alpha}_d + c(\alpha_d - \alpha) \tag{7}$$

where c is a known positive constant. From Equations 6 and 7, the sliding surface is defined as follows:

$$s = \dot{e} + ce = \dot{\alpha}_a - \dot{\alpha} \tag{8}$$

Then, the derivative of the sliding mode variable is derived as follows:

$$\dot{s} = \ddot{e} + c\dot{e} = \ddot{\alpha}_a - \ddot{\alpha} \tag{9}$$

From Equation 1, the dynamics model can be written as follows:

$$\ddot{\alpha} = M^{-1}(\mu - C\dot{\alpha} - G - F_f) \tag{10}$$

From Equations 8–10, it can be presented as follows:

$$\begin{aligned} M\dot{s} &= M\ddot{\alpha}_a - M\ddot{\alpha} \\ &= M\ddot{\alpha}_a - \mu + C\dot{\alpha} + G + F_f \\ &= -Cs - \mu + F_f + M\ddot{\alpha}_a + C\dot{\alpha}_a + G \end{aligned} \tag{11}$$

The unknown dynamics in Equation 11 is defined as a nonlinear function $P = M\ddot{\alpha}_a + C\dot{\alpha}_a + G$. Then, it can be simplified that

$$\ddot{\alpha}_a = M^{-1}(P - C\dot{\alpha}_a - G) \tag{12}$$

The fuzzy approximation is widely recognized as an effective technique to estimate the nonlinear and uncertainty of the system in robot control, owing to its strong capability for approximations and fault tolerance (Zhao et al., 2023). In this article, the problem of time-varying dynamics and unknown friction in TAB can be effectively solved by constructing a fuzzy system to approximate the intricate nonlinear dynamics and utilizing a model-free sliding mode control scheme.

Lemma 1. The nonlinear dynamics P can be approximated by the constructed fuzzy system with reasonable errors, it is expressed as the following continuous equation (Wang, 1994).

$$P = {\theta^*}^{\mathrm{T}}\phi(\xi) + \varepsilon \tag{13}$$

$$|\varepsilon| \leq \varepsilon_U \tag{14}$$

where θ^* represents adaptive weight vector, $\phi(\xi)$ is the fuzzy basic function, ε is the approximation error, ε_U represents the upper boundary of fuzzy approximation errors. Define input states of fuzzy system as $x = [\alpha; \dot{\alpha}]^{\mathrm{T}}$, then fuzzy basic function $\phi(\xi)$ is constructed as follow:

$$\phi\left(\xi\right) = \phi_{l_1 l_2}\left(x\right) = \frac{\prod_{i=1}^{2} \mu_{A_i^{l_i}}\left(x_i\right)}{\sum_{l_1=1}^{l_M} \sum_{l_2=1}^{l_N} \left(\prod_{i=1}^{2} \mu_{A_i^{l_i}}\left(x_i\right)\right)} \tag{15}$$

where $l_i (i = 1, 2)$ represents the number of membership, l_M and l_N represent the maximum number and the minimum number of membership, respectively, $A_i^{l_i}$ is Fuzzy set of input variables x_i, $\mu_{A_i^{l_i}}\left(x_i\right)$ represents the membership function of input variables $x_i (i = 1, 2)$.

According to the former description of the friction between tendon and sheath, the sampling time can be selected small enough to reduce the estimation errors to ensure the validity of the method (Elmali and Olgac, 1996; Wu et al., 2019). The unknown friction is estimated by the following equation:

$$\hat{F}_f = \mu_{t-T} - M\ddot{\alpha} - C\dot{\alpha} - G \tag{16}$$

where $\hat{F}_f$ represents the estimated friction, μ_{t-T} is control input in the previous time step. The estimation errors $\tilde{F}_f$ are described as $\tilde{F}_f = F_f - \hat{F}_f$. As a result, it is reasonable to assume that the estimated errors are bounded, and the boundary can be given as follows:

$$\left|\tilde{F}_f\right| < \rho \tag{17}$$

where ρ is a positive constant representing the upper boundary. In order to solve the chattering problem, the saturated function sat(s) and the control law are elaborately designed as follows respectively:

$$\mathrm{sat(s)} = \begin{cases} 1 & s > \Delta \\ s/\Delta & |s| \le \Delta \\ -1 & s < -\Delta \end{cases} \tag{18}$$

$$\mu = \hat{\theta}^{\mathrm{T}}\phi(\xi) + \hat{F}_f + a \cdot s + b \cdot \mathrm{sat}(s) \tag{19}$$

where $\hat{\theta}$ is the approximation value of θ^*, a and b are two positive constants. And the approximation value $\hat{\theta}$ will be estimated by the following update law:

$$\dot{\hat{\theta}} = L\phi(\xi)s \tag{20}$$

where L is a known positive constant. By utilizing the designed controller 19 with update law 20, time-varying dynamics and unknown friction will be compensated in real-time. The overall block diagram of the proposed strategy is shown in Figure 3.

4 Closed-loop stability analysis

TAB system with the proposed control law is asymptotic stable in the Lyapunov sense. The Lyapunov stability criteria was used to verify the closed-loop stability of the TAB system under the proposed adaptive fuzzy robust control strategy.

Proof. A Lyapunov candidate function is adopted as follows:

$$V = \frac{1}{2}(Ms^2 + L^{-1}\tilde{\theta}^{\mathrm{T}}\tilde{\theta}) \tag{21}$$

where the errors between the ideal value and approximation are represented as $\tilde{\theta} = \theta^* - \hat{\theta}$. Differentiating Equation 21 and substituting Equations 10 and 11, for the ease of derivation, the auxiliary terms are added to the last two terms, $\dot{V}$ can be arranged as:

$$\begin{aligned} \dot{V} &= Ms\dot{s} + \frac{1}{2}\dot{M}s^2 - L^{-1}\tilde{\theta}^{\mathrm{T}}\dot{\hat{\theta}} \\ &= Ms\{\ddot{\alpha}_a - M^{-1}(\mu - C\dot{\alpha} - G - F_f)\} \\ &\quad - L^{-1}\tilde{\theta}^{\mathrm{T}}\dot{\hat{\theta}} + \frac{1}{2}\dot{M}s^2 - Cs^2 + Cs^2 \end{aligned} \tag{22}$$

According to the designed controller, based on Equation 16, by inserting Equations 19 into 22 it can be indicated as follows:

$$\begin{aligned} \dot{V} = Ms\{&\ddot{\alpha}_a - M^{-1}[\hat{\theta}^{\mathrm{T}}\phi(\xi) + a \cdot s + b \cdot \mathrm{sat}(s) - C\dot{\alpha} - G \\ &+ \hat{F}_f - F_f]\} - L^{-1}\tilde{\theta}^{\mathrm{T}}\dot{\hat{\theta}} + \frac{1}{2}\dot{M}s^2 - Cs^2 + Cs^2 \end{aligned} \tag{23}$$

Then, for eliminating time-varying model parameters M and G, according to Equations 13–15, substitute Equations 12 and 13 for $\ddot{\alpha}$ and P respectively, Equation 23 can be re-expressed as:

$$\begin{aligned} \dot{V} &= Ms\{M^{-1}(P - C\dot{\alpha}_a - G) - M^{-1}[\hat{\theta}^{\mathrm{T}}\phi(\xi) + a \cdot s + b \cdot \mathrm{sat}(s) \\ &\quad - C\dot{\alpha} - G - \tilde{F}_f]\} - L^{-1}\tilde{\theta}^{\mathrm{T}}\dot{\hat{\theta}} + \frac{1}{2}\dot{M}s^2 - Cs^2 + Cs^2 \\ &= Ms\{M^{-1}[\theta^{*\mathrm{T}}\phi(\xi) + \varepsilon - C\dot{\alpha}_a - G] - M^{-1}[\hat{\theta}^{\mathrm{T}}\phi(\xi) + a \cdot s \\ &\quad + b \cdot \mathrm{sat}(s) - C\dot{\alpha} - G - \tilde{F}_f]\} - L^{-1}\tilde{\theta}^{\mathrm{T}}\dot{\hat{\theta}} + \frac{1}{2}\dot{M}s^2 - Cs^2 + Cs^2 \\ &= s[\theta^{*\mathrm{T}}\phi(\xi) - \hat{\theta}^{\mathrm{T}}\phi(\xi) + \varepsilon - C(\dot{\alpha}_a - \dot{\alpha}) - a \cdot s \\ &\quad - b \cdot \mathrm{sat}(s) + \tilde{F}_f] - L^{-1}\tilde{\theta}^{\mathrm{T}}\dot{\hat{\theta}} + \frac{1}{2}\dot{M}s^2 - Cs^2 + Cs^2 \end{aligned} \tag{24}$$

Further simplification, by combining Equations 8 and the definition of $\tilde{\theta}$ to Equation 24, the added positive auxiliary term Cs^2 is offset, $\dot{V}$ can be derived as:

$$\begin{aligned} \dot{V} &= s[\tilde{\theta}^{\mathrm{T}}\phi(\xi) + \varepsilon - Cs - a \cdot s - b \cdot \mathrm{sat}(s) + \tilde{F}_f] - L^{-1}\tilde{\theta}^{\mathrm{T}}\dot{\hat{\theta}} \\ &\quad + \tfrac{1}{2}\dot{M}s^2 - Cs^2 + Cs^2 \\ &= s[\varepsilon - Cs - a \cdot s - b \cdot \mathrm{sat}(s) + \tilde{F}_f] + s\tilde{\theta}^{\mathrm{T}}\phi(\xi) - L^{-1}\tilde{\theta}^{\mathrm{T}}\dot{\hat{\theta}} \\ &\quad + \tfrac{1}{2}\dot{M}s^2 - Cs^2 + Cs^2 \\ &= s[\varepsilon - b \cdot \mathrm{sat}(s) + \tilde{F}_f] - (C + a)s^2 + s\tilde{\theta}^{\mathrm{T}}\phi(\xi) - L^{-1}\tilde{\theta}^{\mathrm{T}}\dot{\hat{\theta}} \\ &\quad + \tfrac{1}{2}\dot{M}s^2 - Cs^2 + Cs^2 \\ &= s[\varepsilon - b \cdot \mathrm{sat}(s) + \tilde{F}_f] - a \cdot s^2 + s\tilde{\theta}^{\mathrm{T}}\phi(\xi) - L^{-1}\tilde{\theta}^{\mathrm{T}}\dot{\hat{\theta}} \\ &\quad + \tfrac{1}{2}\dot{M}s^2 - Cs^2 \end{aligned} \tag{25}$$

After that, by substituting update law Equation 20, and according to *Property 1 and Property 2*, i.e. Equations 3 and 4 the last four terms will be eliminated, and Equation (25) is deduced as:

$$\dot{V} = s\left[\varepsilon - b \cdot \mathrm{sat}(s) + \tilde{F}_f\right] - a \cdot s^2 \tag{26}$$

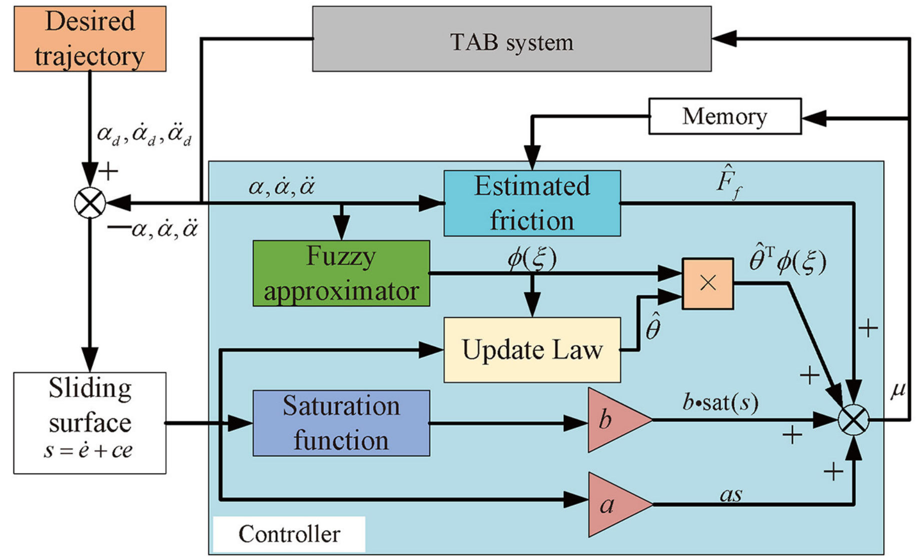

FIGURE 3
The block diagram of proposed controller.

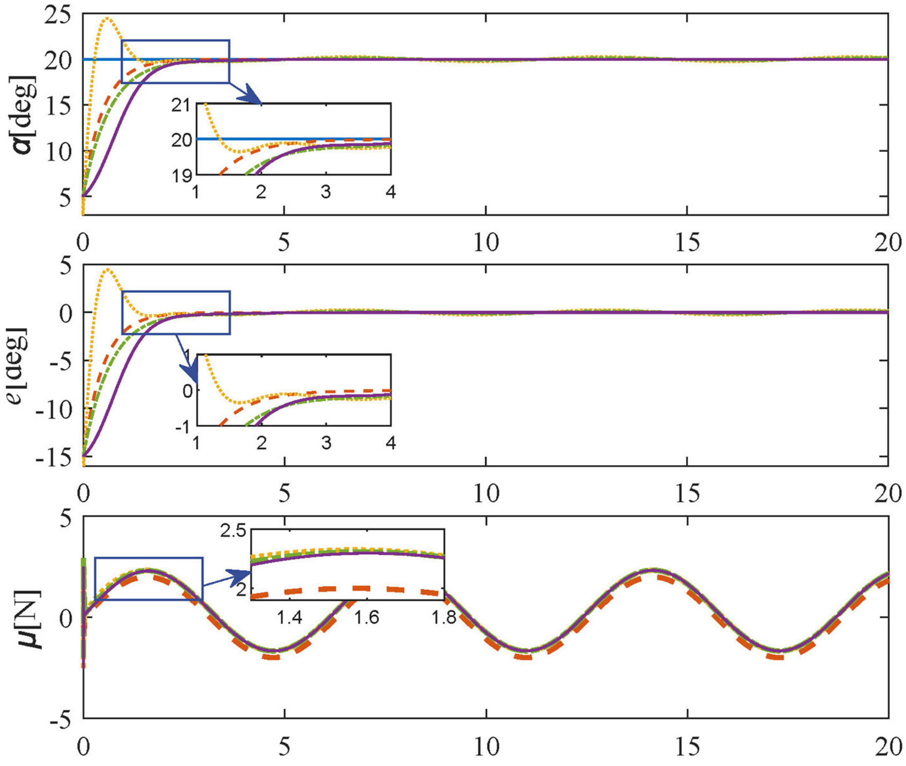

FIGURE 4
Simulation results in **Tracking experiment:** Case 1 (reference values-blue solid line; proposed controller-orange dashed line; PID controller-yellow dotted line; SMPI controller-green dash-dot line; LQR controller-purple solid line).

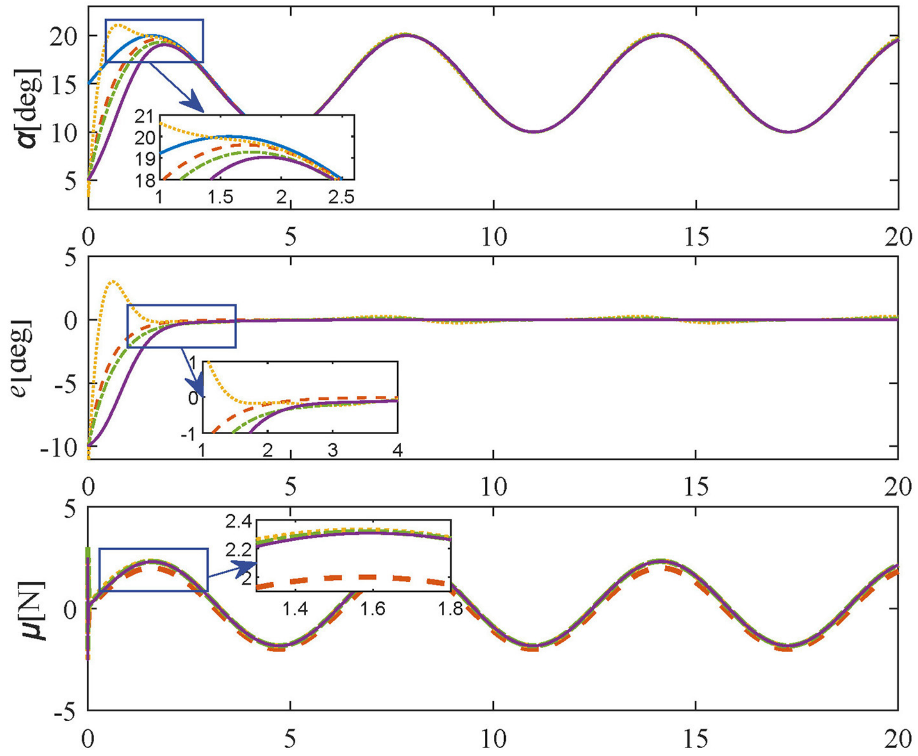

FIGURE 5
Simulation results in **Tracking experiment:** Case 2 (reference values-blue solid line; proposed controller-orange dashed line; PID controller-yellow dotted line; SMPI controller-green dash-dot line; LQR controller-purple solid line).

Finally, a is a positive constant, and according to Equations 17, 18, Equation 26 can be expressed as follows:

$$\begin{aligned}\dot{V} &\leq s[\varepsilon - b \cdot \mathrm{sat}(s) + \tilde{F}_f] \\ &\leq |s| \left[|\varepsilon| + \left|\tilde{F}_f\right| - b \cdot \mathrm{sat}(|s|)\right] \\ &\leq |s| \left(|\varepsilon| + \rho - b\right)\end{aligned} \tag{27}$$

If the positive gain b satisfies

$$b \geq |\varepsilon| + \rho \tag{28}$$

By inserting Equations 28 into 27, $\dot{V}$ is obtained as

$$\dot{V} \leq 0 \tag{29}$$

Equations 21 and 29 indicate that the chosen Lyapunov candidate V is positive definite, and $\dot{V}$ is negative definite. As a result, the asymptotic stability of the TAB system under the proposed control law has been proved. The angle-tracking errors gradually converge to 0 and approach the sliding surface (i.e., s = 0) in finite time. □

5 Simulation and analysis

In this section, simulation experiments and results are provided to validate the performance of the proposed control scheme. Firstly, three different tracking trajectories are designed to evaluate the tracking performance of the control scheme. Then, experiments on varying-friction with and anti-disturbance experiments are conducted to compare the performance and robustness of the proposed scheme with the standard PID controller, sliding mode-PI (SMPI) controller, and linear quadratic regulator (LQR) controller. The reason for choosing PID-based methods and LQR as the controllers for comparison is because they have been widely applied and demonstrated good performance in the field of robotic flexible endoscope (Jiang et al., 2020; Kong et al., 2023). It should be pointed out that the three comparative control methods have been modified according to the dynamics model of this paper, and the control gains have been correspondingly adjusted by trial and error to guarantee tracking accuracy. The three controllers and their elaborately tuned control gains are adopted as follows respectively:

1. Standard PID controller

$$\mu = K_p e + K_i \int e dt + K_d \dot{e} \tag{30}$$

where K_p, K_i, K_d are positive gains. After appropriate optimization adjustments, they are selected as $K_p = 1000$, $K_i = 3000$, $K_d = 200$.

2. SMPI controller

$$\begin{aligned} s &= \dot{e} + ce \\ \mu &= K_{sp} s + K_{si} \int s dt \end{aligned} \tag{31}$$

where $e = \alpha_d - \alpha$, c, K_{sp} and K_{si} are positive gains. They are chosen as $c = 1.5$, $K_{sp} = 3$, $K_{si} = 3000$.

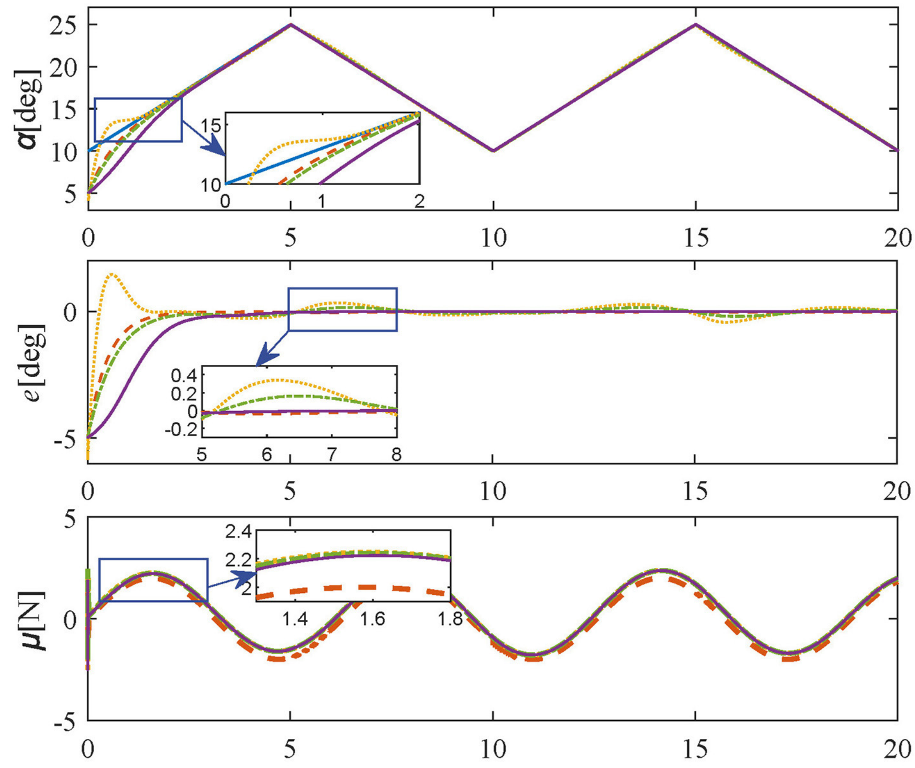

FIGURE 6
Simulation results in **Tracking experiment:** Case 3 (reference values-blue solid line; proposed controller-orange dashed line; PID controller-yellow dotted line; SMPI controller-green dash-dot line; LQR controller-purple solid line).

3. LQR controller

$$\begin{aligned} J &= \int_0^\infty \boldsymbol{e}^{\mathrm{T}}\boldsymbol{Q}\boldsymbol{e} + \boldsymbol{\mu}^{\mathrm{T}}\boldsymbol{R}\boldsymbol{\mu}\,\mathrm{d}t \\ \boldsymbol{\mu} &= -\boldsymbol{K}\boldsymbol{e} \end{aligned} \tag{32}$$

where $\boldsymbol{e} = [e, \dot{e}]^{\mathrm{T}}$, $\boldsymbol{Q}$ and $\boldsymbol{R}$ are weighting matrix. They are selected as $\boldsymbol{Q} = \mathrm{diag}\{1, 20\}$, $\boldsymbol{R} = \mathrm{diag}\{0.01\}$.

5.1 Tracking experiments in different cases

To validate the effectiveness of the proposed control algorithm, a series of numerical simulations were carried out in a MATLAB/Simulink environment. To ensure the fidelity of the simulation, parameters in the dynamics model were selected to align with the actual material parameters of the real TAB system, as presented in previous work (Wang et al., 2023).

$$\begin{aligned} &m = 0.01\mathrm{kg},\ E = 500\mathrm{Pa},\ D = 0.003\mathrm{m} \\ &L_f = 0.15\mathrm{m},\ \alpha(0) = 5\,\mathrm{deg} \end{aligned} \tag{33}$$

Then, to achieve satisfactory tracking performance, the control gains in Equations 19 and 20 are elaborately tuned as:

$$a = 5, b = 2, c = 2, L = 2 \tag{34}$$

Considering both computational accuracy and computational cost, the membership function of each state is set to 5 fuzzy subsets corresponding to its value range. Then, the fuzzy logic system with 2 input states α and $\dot{\alpha}$ can produce 25 fuzzy rules. Based on the operational constraints of α and $\dot{\alpha}$ applied in real robotic flexible endoscope, the Gaussian membership functions are selected as follows respectively by trial and error.

$$\begin{cases} f(\alpha, \sigma_1, v_i) = e^{-\frac{(\alpha - v_i)^2}{2\sigma_1{}^2}} \\ f(\dot{\alpha}, \sigma_2, w_i) = e^{-\frac{(\dot{\alpha} - w_i)^2}{2\sigma_2{}^2}} \end{cases} \tag{35}$$

where σ_1, σ_2, v_i and w_i $(i = 1, 2, 3, 4, 5)$ are prechosen coefficients. The values of them are selected as $\sigma_1 = 1.39, \sigma_2 = 0.93, v_i = [\frac{5(9-\pi)}{2}, \frac{5(18-\pi)}{4}, 22.5, \frac{5(18+\pi)}{4}, \frac{5(9+\pi)}{2}], w_i = [\frac{5\pi}{3}, \frac{5\pi}{6}, 0, -\frac{5\pi}{6}, -\frac{5\pi}{3}]$.

Remark 1. In this article, the parameters in the control law are tuned by trial and error to guarantee optimal performance. Fine-tuning a and c will reduce response time, L is closely associated with the steady-state error of the system, and proper b can effectively prevent system oscillations or overshoot. Parameters in fuzzy logic are empirically tuned by trial and error to ensure the accuracy of approximation. σ_1 and σ_2 influence the shape of the membership functions, thereby affecting the results of fuzzy inference. v_i and w_i are empirically partitioned into equal intervals based on the operational range.

To verify the tracking performance of the proposed controller, three different tracking cases are chosen as follows:

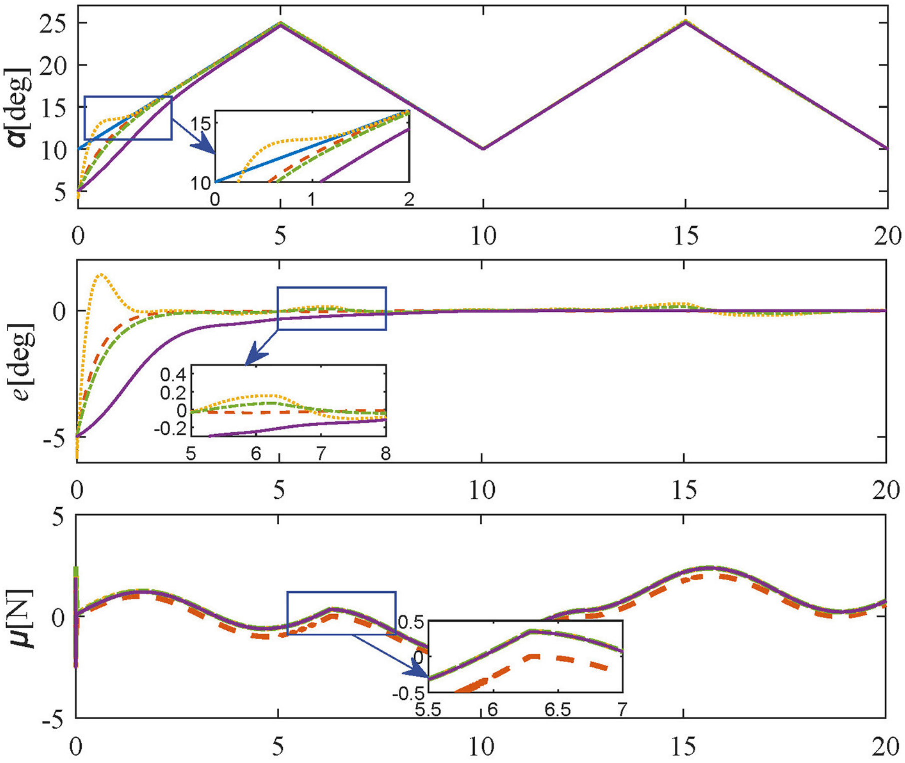

FIGURE 7
Simulation results in **Varying-friction experiment** (reference values-blue solid line; proposed controller-orange dashed line; PID controller-yellow dotted line; SMPI controller-green dash-dot line; LQR controller-purple solid line).

1) Case 1: (step trajectory) The amplitude of the step trajectory is set as 20 deg.

2) Case 2: (sine trajectory) The frequency, the initial phase, the amplitude, and the offset of the desired sine trajectory are set as π rad/sec, 0 deg, 5 deg, and 15 deg, respectively.

$$y_d(t) = 5\sin(t) + 15 \tag{36}$$

3) Case 3: (triangular-wave trajectory) The frequency, amplitude, and offset of the desired triangular-wave trajectory are set as 0.1 Hz, 7.5 deg, and 17.5 deg, respectively.

In **Tracking experiments: Case 1**, the parameters of the proposed method are set as in Equations 33 and 34. Also, the initial and target angles are set to 5 deg and 20 deg respectively. The simulation results of Tracking experiments: Case 1 are shown in Figure 4, the desired angle can be reached quickly within 3 s by adopting the proposed controller without overshoot or oscillation, demonstrating the regulation performance of the proposed control scheme. In contrast, comparative methods, i.e. Equations 30–32 take more time to be steady and are accompanied by oscillating and residual errors.

In **Tracking experiments: Case 2**, to further confirm the tracking performance of the proposed method, the same parameters are set as Case 1. The initial angle and desired trajectory are set to 5 deg and Equation 36, respectively. The results of Tracking experiments: Case 2 are given in Figure 5, the angle errors can be quickly converged to 0 within 3 s without overshoot or oscillation by adopting the proposed control method. In contrast, as shown in Figure 5, comparative methods take a longer time to achieve the desired trajectory, and there are obvious overshooting and oscillations. Therefore, the simulation results show that the proposed method has a faster response and smaller steady-state errors than comparative controllers.

The simulation results of **Tracking experiments: Case 3** are shown in Figure 6, the bending-tip can reach the desired trajectory within 3 s by using the proposed control method. For comparative methods, the response time is longer. Besides, oscillations still exist for comparative methods at 5, 10, and 15 s. In contrast, the proposed method guarantees regulation stability without any residual errors. Therefore, the simulation results of three different cases in tracking experiments show that the proposed method has satisfactory tracking performance and acceptable steady response.

5.2 Varying-friction experiment

In order to test the dynamic adaptability of the proposed controller, in this experiment, the friction force is set as a time-varying signal with constant amplitude and varying offset for simulating the switching of working conditions. Three bounded sets of unidentified friction, each representing different working conditions due to different ranges were employed. It is worth mentioning that the form of friction in this experiment is just selected as an example, the controller proposed in this paper only requires the friction force to be bounded without a specific model,

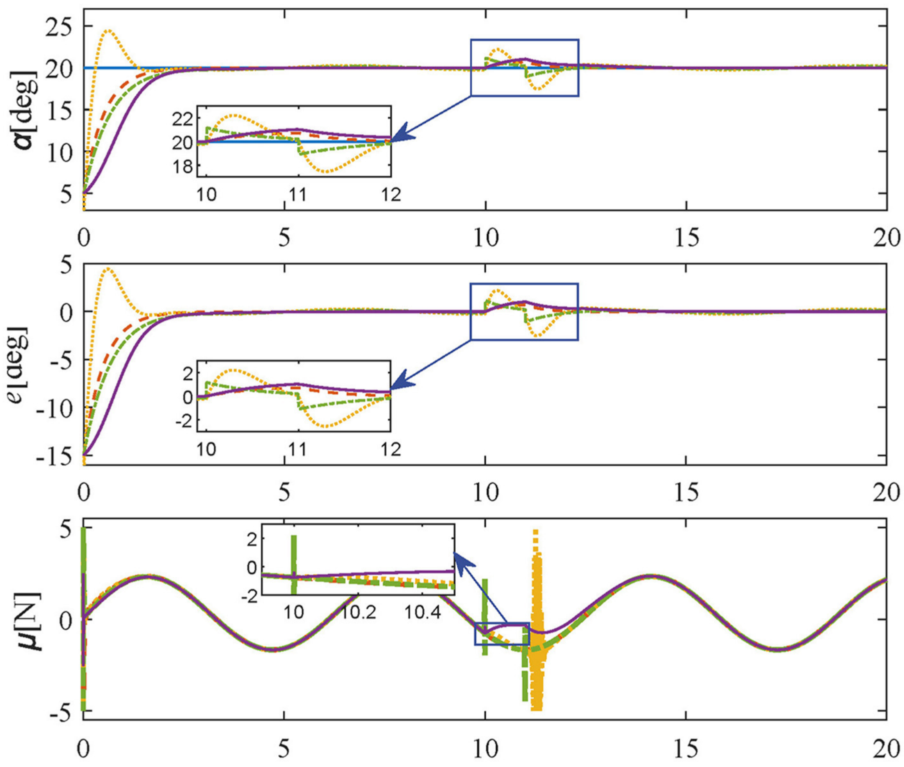

FIGURE 8
Simulation results in **Anti-disturbance experiment** (reference values-blue solid line; proposed controller-orange dashed line; PID controller-yellow dotted line; SMPI controller-green dash-dot line; LQR controller-purple solid line).

which is a contribution of this paper. The specific form of friction force is as follows:

$$F_f = \begin{cases} \sin t & 0 \le t < 6.28 \\ \sin(t + \pi/2) - 1 & 6.28 \le t < 12.56 \\ \sin(t - \pi/2) + 1 & 12.56 \le t \le 20 \end{cases} \quad (37)$$

The simulation results of **Varying-friction experiment** are shown in Figure 7, the same parameters are set as in Tracking experiments: Case 3. As shown in Figure 7, the proposed method still achieves the desired trajectory rapidly and accurately without steady-state errors. In contrast, the PID controller and SMPI controller have obvious oscillations near 6.28 s and 12.56 s, and the LQR controller has a much slower transient response. In consequence, the proposed method can effectively cope with varying friction Equation 37 under different working conditions.

5.3 Anti-disturbance experiment

To verify the robustness of the controller suffering episodic disturbances in the unstructured environment, a constant external force of 1N lasting 1 second is added at the 10th second on the basis of Tracking experiments: Case 1, and the simulation results of **Anti-disturbance experiment** are shown in Figure 8. The angle errors generated by external disturbances are less than 1 deg under the proposed controller, which returns to zero in 2 s. In contrast, the same disturbances under comparative methods excite larger amplitudes (LQR) and sharper force fluctuations (PID, SMPI). In summary, the proposed method is non-sensitive to disturbances and fast-tracking of the desired trajectory without steady-state errors. As a result, it is possible to conclude with certainty that the proposed controller has both excellent tracking performance and satisfactory robustness.

Remark 2. Although the method proposed in this paper achieves effective tracking and compensation of unknown bounded friction, there are still some limitations. One concern about the proposed controller is that the setting of fuzzy logic membership functions and fuzzy rules relies on empirical knowledge and requires considerable effort to tune for satisfactory performance. It is worth mentioning that reinforcement learning has demonstrated significant performance in finding optimal control policy in recent years (Goharimanesh et al., 2020). As a consequence, fuzzy control based on reinforcement learning is poised to become a further improvement for our method in the future.

6 Conclusions

Based on the Lagrangian dynamics model for the TAB systems, this paper proposed a robust controller for tracking tasks. Specifically, the nonlinear friction with consideration of its boundary is described according to the dynamics model of TAB. Then, the fuzzy logic system is used to achieve the estimation of nonlinear time-varying dynamics. At last, a sliding mode control method was designed, which achieved effective tracking performance and compensation of the unknown boundary friction. Lyapunov stability criteria was also utilized to prove the asymptotic stability of the proposed controller. Simulations are also carried out to validate the efficiency of the proposed method. The proposed method is model-free control and has no strict requirement for the dynamics model and friction model. It is proved that advanced tracking performance and real-time response can be guaranteed under the presence of unknown bounded nonlinear friction and time-varying nonlinear dynamics. In future research, we will further investigate the universal applicability of the proposed method in addressing unknown friction and its practical utilization in experiments involving flexible endoscope robots.

Data availability statement

The raw data supporting the conclusions of this article will be made available by the authors, without undue reservation.

Author contributions

FR: Data curation, Methodology, Software, Writing – original draft, Conceptualization. XW: Funding acquisition, Project administration, Supervision, Writing – review & editing. NY: Funding acquisition, Writing – review & editing. JH: Funding acquisition, Writing – review & editing.

Funding

The author(s) declare that financial support was received for the research, authorship, and/or publication of this article. This work was supported by National Key R&D Program of China (Grant No. 2022YFB4702800), National Natural Science Foundation of China (Grant No. 62303248), Guanddong Basic and Applied Basic Research Foundation (Grant Nos. 2024A1515010102 and 2023A1515110678), and China Postdoctoral Science Foundation Funded Project (Grant No. 2023M731804).

Conflict of interest

The authors declare that the research was conducted in the absence of any commercial or financial relationships that could be construed as a potential conflict of interest.

Publisher's note

References

Berthet-Rayne, P., Leibrandt, K., Kim, K., Seneci, C. A., Shang, J., and Yang, G.-Z. (2018). "Rolling-joint design optimization for tendon driven snake-like surgical robots," in *2018 IEEE/RSJ International Conference on Intelligent Robots and Systems (IROS)* (Madrid: IEEE), 4964–4971.

Burgner-Kahrs, J., Rucker, D. C., and Choset, H. (2015). Continuum robots for medical applications: a survey. *IEEE Trans. Robot.* 31, 1261–1280. doi: 10.1109/TRO.2015.2489500

Cui, Z., Huang, Y., Li, W., Chiu, P. W. Y., and Li, Z. (2024). Noise-resistant adaptive gain recurrent neural network for visual tracking of redundant flexible endoscope robot with time-varying state variable constraints. *IEEE Trans Ind Electron.* 71, 2694–2704. doi: 10.1109/TIE.2023.3270533

Do, T., Tjahjowidodo, T., Lau, M., and Phee, S. (2015a). Adaptive control for enhancing tracking performances of flexible tendon-sheath mechanism in natural orifice transluminal endoscopic surgery. *Mechatronics* 28, 67–78. doi: 10.1016/j.mechatronics.2015.04.002

Do, T., Tjahjowidodo, T., Lau, M. W. S., and Phee, S. J. (2015b). A new approach of friction model for tendon-sheath actuated surgical systems: nonlinear modelling and parameter identification. *Mechan. Mach. Theory* 85, 14–24. doi: 10.1016/j.mechmachtheory.2014.11.003

Do, T. N., Tjahjowidodo, T., Lau, M. W. S., and Phee, S. J. (2015c). "Enhanced performances for cable-driven flexible robotic systems with asymmetric backlash profile," in *2015 IEEE International Conference on Technologies for Practical Robot Applications (TePRA)* (Woburn, MA: IEEE), 1–6.

Do, T. N., Tjahjowidodo, T., Lau, M. W. S., and Phee, S. J. (2016). "Adaptive tracking approach of flexible cable conduit-actuated notes systems for early gastric cancer treatments," in *Informatics in Control, Automation and Robotics: 11th International Conference, ICINCO 2014.* (Vienna: Springer), 79–97.

Elmali, H., and Olgac, N. (1996). Implementation of sliding mode control with perturbation estimation (smcpe). *IEEE Trans. Control Syst. Technol.* 4, 79–85. doi: 10.1109/87.481770

Goharimanesh, M., Mehrkish, A., and Janabi-Sharifi, F. (2020). A fuzzy reinforcement learning approach for continuum robot control. *J. Intellig, Robot, Syst,* 100, 809–826. doi: 10.1007/s10846-020-01237-6

Huang, Y., Li, J., Zhang, X., Xie, K., Li, J., Liu, Y., et al. (2022). A surgeon preference-guided autonomous instrument tracking method with a robotic flexible endoscope based on dvrk platform. *IEEE Robot. Autom. Lett.* 7, 2250–2257. doi: 10.1109/LRA.2022.3143305

Huang, Y., Li, W., Zhang, X., Li, J., Li, Y., Sun, Y., et al. (2024). 4-dof visual servoing of a robotic flexible endoscope with a predefined-time convergent and noise-immune adaptive neural network. *IEEE/ASME Trans. Mechatron.* 29, 576–587. doi: 10.1109/TMECH.2023.3286850

Jiang, S., Lou, J., Yang, Z., Dai, J., and Yu, Y. (2015). Design, analysis and control of a novel tendon-driven magnetic resonance-guided robotic system for minimally invasive breast surgery. *Proc. Institut. Mech. Eng. Part H.* 229, 652–669. doi: 10.1177/0954411915599018

Jiang, W., Zhou, Y., Wang, C., Peng, L., Yang, Y., and Liu, H. (2020). Navigation strategy for robotic soft endoscope intervention. *Int. J. Med. Robot. Comput. Assist. Surg.* 16, e2056. doi: 10.1002/rcs.2056

Jung, Y., and Bae, J. (2016). "Simulation analysis on friction compensation of a double tendon-sheath actuation system," in *2016 13th International Conference on Ubiquitous Robots and Ambient Intelligence (URAI)* (Xi'an: IEEE), 510–514.

Kang, B. B., Kim, D., Choi, H., Jeong, U., Kim, K. B., Jo, S., et al. (2020). Learning-based fingertip force estimation for soft wearable hand robot with tendon-sheath mechanism. *IEEE Robot. Autom. Lett.* 5, 946–953. doi: 10.1109/LRA.2020.2966391

Kong, X., Mo, H., Dong, E., Liu, Y., and Sun, D. (2023). Automatic tracking of surgical instruments with a continuum laparoscope using data-driven control in robotic surgery. *Adv. Intellig. Syst.* 5, 2200188. doi: 10.1002/aisy.202200188

Lee, D.-H., Kim, Y.-H., Collins, J., Kapoor, A., Kwon, D.-S., and Mansi, T. (2021). Non-linear hysteresis compensation of a tendon-sheath-driven robotic manipulator using motor current. *IEEE Robot. Autom. Lett.* 6, 1224–1231. doi: 10.1109/LRA.2021.3057043

Legrand, J., Ourak, M., Javaux, A., Gruijthuijsen, C., Ahmad, M. A., Van Cleynenbreugel, B., et al. (2018). From a disposable ureteroscope to an active lightweight fetoscope characterization and usability evaluation. *IEEE Robot. Autom. Lett.* 3, 4359–4366. doi: 10.1109/LRA.2018.2866204

Li, J., Huang, Y., Zhang, X., Xie, K., Xian, Y., Luo, X., et al. (2023). An autonomous surgical instrument tracking framework with a binocular camera for a robotic flexible laparoscope. *IEEE Robot. Autom. Lett.* 8, 4291–4298. doi: 10.1109/LRA.2023.3281934

Nguyen, T., Do, T., Lau, M., and Phee, S. (2014). "Modelling, design, and control of a robotic running foot for footwear testing with flexible actuator," in *Proceedings of the the 1th International Conference in Sports Science Technology (ICSST)* (Singapore: ICSST), 11–12.

Norouzi-Ghazbi, S., and Janabi-Sharifi, F. (2020). Dynamic modeling and system identification of internally actuated, small-sized continuum robots. *Mech. Mach. Theory* 154, 104043. doi: 10.1016/j.mechmachtheory.2020.104043

Porto, R. A., Nageotte, F., Zanne, P., and Mathelin, M. (2019). "Position control of medical cable-driven flexible instruments by combining machine learning and kinematic analysis," in *2019 International Conference on Robotics and Automation (ICRA)* (Montreal, QC: IEEE), 7913–7919. doi: 10.1109/ICRA.2019.8793692

Rho, E., Kim, D., Lee, H., and Jo, S. (2021). Learning fingertip force to grasp deformable objects for soft wearable robotic glove with tsm. *IEEE Robot. Autom. Lett.* 6, 8126–8133. doi: 10.1109/LRA.2021.3102968

Thai, M. T., Phan, P. T., Hoang, T. T., Low, H., Lovell, N. H., and Do, T. N. (2021). Design, fabrication, and hysteresis modeling of soft microtubule artificial muscle (smam) for medical applications. *IEEE Robot. Autom. Lett.* 6, 5089–5096. doi: 10.1109/LRA.2021.3072599

Wang, L.-X. (1994). *Adaptive fuzzy Systems and Control: Design and Stability Analysis*. Hoboken: Prentice-Hall Inc.

Wang, X., Bie, D., Han, J., and Fang, Y. (2020). Active modeling and compensation for the hysteresis of a robotic flexible ureteroscopy. *IEEE Access* 8, 100620–100630. doi: 10.1109/ACCESS.2020.2984424

Wang, X., Yu, N., Bie, D., Han, J., and Fang, Y. (2021). A novel esmf-based observer and control scheme for a type of tendon-sheath hysteresis system. *Automatica* 131, 109800. doi: 10.1016/j.automatica.2021.109800

Wang, X., Yu, N., Han, J., and Fang, Y. (2023). Modeling and adaptive control for tendon sheath artificial muscle actuated bending-tip systems with unknown parameters and input hysteresis: An experimental research. *IEEE Trans Ind Electron.* 70, 10588–10597. doi: 10.1109/TIE.2022.3219105

Wang, X., Zhang, Q., Shen, X., and Li, J. (2018). Noncollocated position control of tendon-sheath actuated slender manipulator. *IEEE Trans. Control Syst. Technol.* 28, 688–696. doi: 10.1109/TCST.2018.2884222

Wu, Q., Wang, X., Chen, B., and Wu, H. (2019). Neural network-based sliding-mode control of a tendon sheath-actuated compliant rescue manipulator. *Proc. Instit. Mech. Eng.* 233, 1055–1066. doi: 10.1177/0959651819825984

Wu, Q., Wang, X., Chen, L., and Du, F. (2014). Transmission model and compensation control of double-tendon-sheath actuation system. *IEEE Trans Ind Electron* 62, 1599–1609. doi: 10.1109/TIE.2014.2360062

Yin, M., Huang, B., Yi, Z., and Cai, S. (2022). Rbf network-based adaptive sliding mode control strategy for the tendon-sheath driven joint of a prosthetic hand. *Technol. Health Care* 30, 1155–1165. doi: 10.3233/THC-213242

Yin, M., Xu, Z., Zhao, Z., and Wu, H. (2020). Mechanism and position tracking control of a robotic manipulator actuated by the tendon-sheath. *J. Intellig. Robot. Syst.* 100, 849–862. doi: 10.1007/s10846-020-01245-6

Zhang, L. A., Khare, R., Wilson, E., Wang, S. X., Peters, C. A., and Cleary, K. (2014). "Robotic assistance for manipulating a flexible endoscope," in *2014 IEEE International Conference on Robotics and Automation (ICRA)I* (Hong Kong: IEEE), 5380–5385.

Zhang, Q., Wang, X., Tian, M., Shen, X., and Wu, Q. (2017). Modeling of novel compound tendon-sheath artificial muscle inspired by hill muscle model. *IEEE Trans Ind Electron* 65, 6372–6381. doi: 10.1109/TIE.2017.2784377

Zhao, W., Liu, Y., and Yao, X. (2023). Adaptive fuzzy containment and vibration control for multiple flexible manipulators with model uncertainties. *IEEE Trans. Fuzzy Syst.* 31, 1315–1326. doi: 10.1109/TFUZZ.2022.3199573

frontiers | Frontiers in Neuroscience

TYPE Original Research
PUBLISHED 02 April 2024
DOI 10.3389/fnins.2024.1377702

EDITED BY
Bi Zhang,
Chinese Academy of Sciences (CAS), China

REVIEWED BY
Jing Guo,
Stanford University, United States
Tuantuan Zhao,
Mayo Clinic, United States

*CORRESPONDENCE
Zhiqiang Zhang
✉ zhangzq@sj-hospital.org
Xiangnan Yuan
✉ yuanxn@sj-hospital.org

RECEIVED 28 January 2024
ACCEPTED 22 March 2024
PUBLISHED 02 April 2024

CITATION
Li X, Li H, Liu Y, Liang W, Zhang L, Zhou F, Zhang Z and Yuan X (2024) The effect of electromyographic feedback functional electrical stimulation on the plantar pressure in stroke patients with foot drop.
Front. Neurosci. 18:1377702.
doi: 10.3389/fnins.2024.1377702

The effect of electromyographic feedback functional electrical stimulation on the plantar pressure in stroke patients with foot drop

Xiaoting Li, Hanting Li, Yu Liu, Weidi Liang, Lixin Zhang, Fenghua Zhou, Zhiqiang Zhang* and Xiangnan Yuan*

Department of Rehabilitation, Shengjing Hospital of China Medical University, Shenyang, China

Purpose: The purpose of this study was to observe, using Footscan analysis, the effect of electromyographic feedback functional electrical stimulation (FES) on the changes in the plantar pressure of drop foot patients.

Methods: This case–control study enrolled 34 stroke patients with foot drop. There were 17 cases received FES for 20 min per day, 5 days per week for 4 weeks (the FES group) and the other 17 cases only received basic rehabilitations (the control group). Before and after 4 weeks, the walking speed, spatiotemporal parameters and plantar pressure were measured.

Results: After 4weeks treatments, Both the FES and control groups had increased walking speed and single stance phase percentage, decreased step length symmetry index (SI), double stance phase percentage and start time of the heel after 4weeks ($p<0.05$). The increase in walking speed and decrease in step length SI in the FES group were more significant than the control group after 4weeks ($p<0.05$). The FES group had an increased initial contact phase, decreased SI of the maximal force (Max F) and impulse in the medial heel after 4weeks ($p<0.05$).

Conclusion: The advantages of FES were: the improvement of gait speed, step length SI, and the enhancement of propulsion force were more significant. The initial contact phase was closer to the normal range, which implies that the control of ankle dorsiflexion was improved. The plantar dynamic parameters between the two sides of the foot were more balanced than the control group. FES is more effective than basic rehabilitations for stroke patients with foot drop based on current spatiotemporal parameters and plantar pressure results.

KEYWORDS

stroke, foot drop, gait analysis, electrical stimulation therapy, electromyography feedback, rehabilitation

1 Introduction

Stroke is one of the most serious diseases affecting humans, and it can cause chronic motor dysfunction (Johnston et al., 2009). An epidemiological survey showed that there are more than 7 million stroke survivors in China, and about 70% of them have dysfunction (Liu et al., 2007), which affects their quality of life and imposes a huge burden on their families and society (Patel et al., 2019). Foot drop is a common abnormal gait after stroke, and is caused by the decrease in the motor control of the tibialis anterior muscle, high tension of the plantar flexor muscle, or the contracture of the ankle joint (Kottink et al., 2012). This abnormal gait can disturb the foot contact pattern with ground, increase asymmetry of both legs and case high risk of falls. So it is an urgent to find an effective and convenient treatment method to correct foot drop.

Common treatments for foot drop include ankle foot orthosis (AFO), transcutaneous electrical nerve stimulation and FES (Bosch et al., 2014; Gil-Castillo et al., 2020). The conventional therapy for foot drop is the application of AFO. AFO passively immobilizes the ankle in a neutral position during walking. Although AFO can alleviate some walking difficulty, it is not conducive to providing or maintaining dynamic functions (Nolan et al., 2015). An alternative method to promote active movement is functional electrical stimulation (FES) of the common peroneal nerve. In contrast to AFO, no mechanical constraints are imposed by FES, enabling normal ankle range of motion and facilitating optimal residual plantarflexor activity (Liberson et al., 1961). Although a meta-analysis showed that gait speed and functional capacity were not significantly different between AFO and FES (Prenton et al., 2016). Walking in daily life demands continual adaptations to environmental challenges, such as inclines, uneven terrain, or traffic. Compared to AFO, FES is better in dealing with complex environmental conditions and overcoming obstacles because of its unrestricted ankle motion (Berenpas et al., 2019). FES is a practical, long-term, and cost-effective treatment for the correction of drop foot (Taylor et al., 2013). These advantages may explain why patient satisfaction is higher for FES than AFO (Bosch et al., 2014). Transcutaneous electrical nerve stimulation is an effective treatment in improving muscle strength and preventing muscle atropy (Thomaz et al., 2019), but this passive electrical stimulation has not report beneficial to improve foot drop gait (Park and Wang, 2017). While the advantages of FES are that it actively increases muscle recruitment and corrects abnormal gait (Reisman et al., 2013; Melo et al., 2015).

Collaborative efforts of stroke rehabilitation and neural engineering demonstrated how neuroprosthetics can control devices and ultimately facilitate body functional recovery (Moritz et al., 2008; Bouton et al., 2016; Biasiucci et al., 2018). In this study, we used a type of electromyographic feedback FES, which translated myoelectric signals into meaningful electrical impulsions that may drive activity-dependent neuroplasticity and functional motor recovery (Daly and Wolpaw, 2008; Ethier et al., 2015; Bao et al., 2020). Compared to some passive treatments such as acupuncture and low frequency electrotherapy, FES requires more active participation, and gives patients more positive feedback. The neuronal activity might be modified through this individualized practice with feedback and reward (Milosevic et al., 2020).

However, how to evaluate the effect of FES on foot drop? Most previous studies focused on lower limb function scales and ankle joint range of motion (Laufer et al., 2009; Bidabadi et al., 2019). In fact, the most direct and important process during walking is the interaction between feet and the ground. The plantar pressure system focuses on the interaction between feet and the contact surface (Low and Dixon, 2010). The system can obtain quantitative data related to walking, including spatiotemporal parameters and pressure distributions (Leunkeu et al., 2014; Lim et al., 2016). Plantar pressure-related studies have investigated patients with flat and cavus feet, diabetes mellitus, pressure ulcers, strokes, obesity, rheumatoid arthritis, Parkinson's disease, and spinal cord injury (Janisse, 1993; Kimmeskamp and Hennig, 2001; Morrison et al., 2010; Manor and Chen, 2014; Skopljak et al., 2014; Yuan et al., 2019; Li et al., 2023).

Recent studies have reported the immediate effect of FES to plantar pressure (Yuan et al., 2015) and outcomes of implantable FES to velocity and life quality (Buentjen et al., 2019). However, such studies have rarely assessed the effect of non-invasive FES to the spatiotemporal and plantar pressure variables in foot drop patients. Therefore, in the current study, we intended to verify the potential benefits of FES over control patients during walking in one treatment cycle. We proposed the hypotheses that both the FES and control groups would improve the spatiotemporal parameters and plantar pressure results. The FES group had better ankle dorsiflexion control than the control group. This study perhaps the first one to link FES with ankle dorsiflexion control of foot drop after stroke, demonstrating the improvement of neuromuscular control by myoelectric signals feedback FES and providing another optimal clinical decision for the treatment of foot drop after stroke.

2 Participants and methods

2.1 Design

This was a retrospective, case–control study. Because one treatment course for FES was about 3–4 weeks. So the FES group received FES and basic rehabilitation for 4 weeks and the control group only received basic rehabilitation for 4 weeks (17 cases in each group). Basic rehabilitation mainly refers to gait correction training by a same physical therapist. Patients walked on the treadmill with FES at self comfortable speed. The treatment timeline was 20 min per day, 5 days per week for 4 weeks. Footscan plantar pressure and walking speed tests were finished not more than 1 week before treatment, and within 1 week of completing the training (testing was performed without the FES machine). The flowchart of the experiment was shown in Figure 1.

2.2 Participants

Between June 2017 and June 2019, a total of 34 subjects were collected from the Rehabilitation Department at Shengjing Hospital of China Medical University, China. All subjects provided signed informed consent. The protocols were approved by the Clinical Research Ethics Committee at Shengjing Hospital of China Medical University (approval No. 2015PS438KJ). The inclusion/exclusion criteria were as follows.

Inclusion criteria of stroke patients:

1. The diagnosis of stroke was established by magnetic resonance imaging or computed tomography scan.
2. First-ever unilateral stroke (hemorrhagic or ischemic) and all subjects were able to understand and follow the experimental instructions.
3. Ability to walk independently, without assisting devices for more than 10 m.
4. The mortified Ashworth score of spasticity of the lower extremities was less than level II.

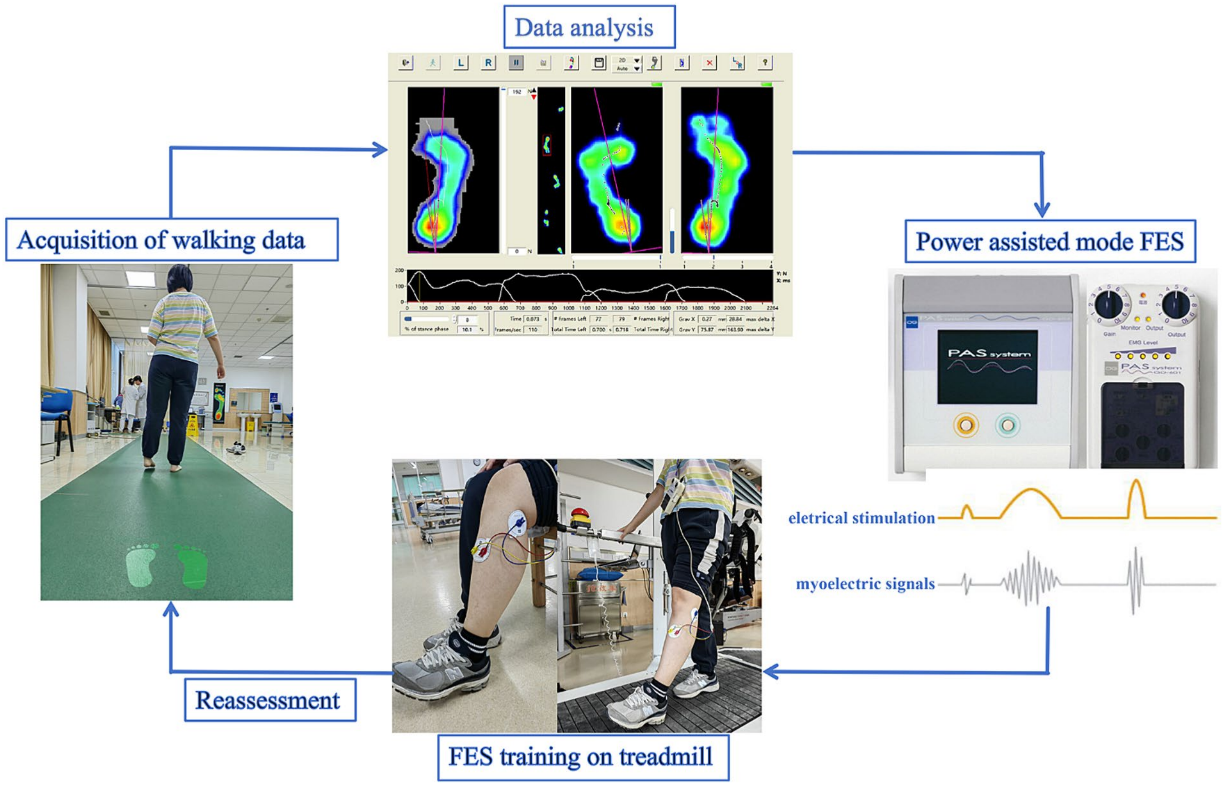

FIGURE 1
Flowchart of the experiment. FES, Functional electrical stimulation.

5 Foot drop during walking, but the Brunnstrom stage was phase III or higher (patients could perform ankle dorsiflexion voluntarily).

Exclusion criteria of stroke patients:

Bilateral paralysis, subarachnoid hemorrhage, sequelae of previous neurologic or orthopedic disorders that could impair locomotion, limited range of motion or severe spasticity of the lower extremities, skin lesions or rashes, severe cognitive or visuospatial dysfunction, and/or severe medical illness.

2.3 Intervention (treatment methods)

Foot drop individuals who still retained voluntary residual myoelectric signals, which means patients could perform ankle dorsiflexion voluntarily allow the use of FES. The FES (PAS system, Japan KR-7) consisted of a mainframe, a controller, and electrodes. The controller was a single-channel stimulator powered by 4AA batteries with output current of 0–27 mA at a frequency of 1–100 Hz to produce a bi-phasic rectangular pulse at 150 µm. The application mode was power assisted. Before treatment, the subjects were informed that the purpose of the FES was to assist with lifting their toes while their foot is elevated. The patient then assumed a sitting position. Two surface electrodes were placed near the peroneal head (directly over the motor nerve) and tibialis anterior muscle. Firstly, we asked patients to perform dorsiflexion of their ankle and we regulated the sensitivity according to the myoelectric signals that the computer received. Then, we established the minimal and maximal output current and synchronized the host data with the controller, removed the host, and instructed the patient to wear the controller while walking on the treadmill at the patient's comfortable speed. The treatment timeline was 20 min per day, 5 days per week for 4 weeks. Each machine was individually programmed (stimulation intensity and duration) by an experienced clinician. Rarely occurring adverse events include skin rashes and pain at the site of electrical stimulation.

2.4 Acquisition of walking data

Walking data were collected using the Footscan plantar pressure system (RSscan International, Olen, Belgium) with 8,192 resistive sensors within a 1 m long force plate. The force plate was mounted on the center of a 10 m long rubber flat surface. The pressure range was 1–127 N/cm^2. The frequency of data acquisition (up to 500 Hz) was adjusted according to the walking speed from 10 meters walk test (10MWT), the faster the walking speed, the higher the acquisition frequency. In order to adapt themselves to the experimental process, each subject practiced walking along the flat surface at their comfortable and self-selected speed in their bare feet at least two times. Then, each subject was asked to walk on the Footscan plantar pressure system for at least three successful trials. In one successful trial, 2–4 footprints can be collected on each side of the foot. Then the mean spatiotemporal parameters were calculated from all the footprints. Because the calculation of pressure parameters needs a complete footprint. Whereas the footprints at the edge of the force plate were incomplete, so each foot had one complete footprint in one gait cycle for the calculation of pressure parameters. Subjects were permitted to rest for at least 2 min between trials, if expressing fatigue. Because the force plate was only 1 m long, so patients completed 10MWT (Beata et al., 2018) for walking speed (Figure 2). Data collection for each subject was performed by a same experimenter who was not involved in the treatment.

2.5 Data analysis

Patients completed 10MWT for walking speed analysis (m/s).

The Footscan plantar pressure system divided the foot into the 10 anatomical regions (Figure 3), including (1) toe 1 (T1), (2) toes 2 to 5 (T2–5), (3) metatarsal 1 (Meta 1, M1), (4) metatarsal 2 (Meta 2, M2), (5) metatarsal 3 (Meta 3, M3), (6) metatarsal 4 (Meta 4, M4), (7) metatarsal 5 (Meta 5, M5), (8) midfoot (MF), (9) heel medial (HM), and (10) heel lateral (HL).

Subjects' spatiotemporal parameters included gait cycle time, double/single stance time, stride length, start time of the heel, initial contact phase, and step length. The pressure parameters included maximum force (Max F), impulse, contact area, and symmetry index (SI).

Calculations of the average gait parameters. To ensure that the parameters were comparable between different subjects, some of the parameters were standardized. The specific formula is as follows:

The stance phase percentage was calculated as the percentage of stance time to gait cycle time:

$$\left(\begin{matrix}\text{single /}\\ \text{double}\end{matrix}\right)\text{stance phase percentage} = \frac{\left(\begin{matrix}\text{single /}\\ \text{double}\end{matrix}\right)\text{stance time}}{\text{gait cycle time}} \times 100\%$$

The initial contact phase percentage was calculated as the percentage of initial contact phase to stance time:

$$\text{initial contact phase percentage} = \frac{\text{initial contact phase}}{\text{stance time}} \times 100\%$$

The regional Max F percentage was calculated as the percentage of the Max F value of the 10-anatomical regions to the sum of Max F value in the whole foot:

$$\text{regional max F percentage} = \frac{\text{max F value of each region}}{\text{max F value of the whole foot}} \times 100\%$$

The regional impulse percentage was calculated as the percentage of impulse value of the 10-anatomical regions to the sum of impulse value in the whole foot:

$$\text{regional impulse percentage} = \frac{\begin{matrix}\text{impulse value of}\\ \text{each region}\end{matrix}}{\begin{matrix}\text{impulse value of}\\ \text{the whole foot}\end{matrix}} \times 100\%$$

The regional contact area percentage was calculated as the percentage of contact area value of the 10-anatomical regions to the sum of contact area value in the whole foot:

$$\text{regional contact area percentage} = \frac{\begin{matrix}\text{contact area of}\\ \text{each region}\end{matrix}}{\begin{matrix}\text{contact area of}\\ \text{the whole foot}\end{matrix}} \times 100\%$$

The calculation formula of the SI of the gait variables was as follows. The Step length SI, Max F SI, impulse SI and contact area SI values were calculated separately. The closer an SI value was to 0, the better the symmetry was.

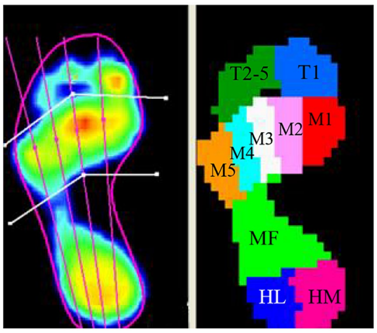

FIGURE 3
The foot pressure was divided into 10 anatomical regions in the Footscan plantar pressure system (T1, toe 1; T2–5, toes 2 to 5; M1, metatarsal 1; M2, metatarsal 2; M3, metatarsal 3; M4, metatarsal 4; M5, metatarsal 5; MF, midfoot; HM, heel medial; HL, heel lateral).

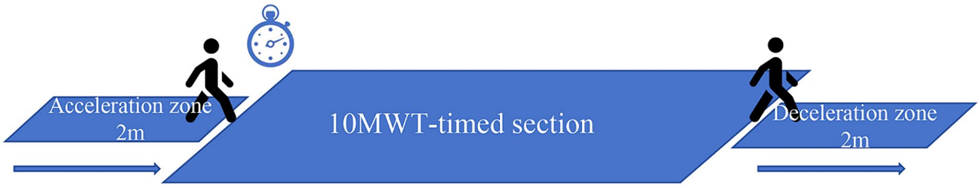

FIGURE 2
10MWT.

$$\text{symmetry index} = \left| \frac{\text{variables of unparalysed side}}{\text{variables of paralysed side}} - 1 \right|$$

2.6 Statistical analysis

SPSS 20.0 software (SPSS, Chicago, IL, United States) was used for data analysis. The data were expressed as the mean ± SD. Normal distribution was tested first. The paired *t*-test was used for intragroup analyses and the independent-samples *t*-test was used for intergroup comparisons of the gait parameters of the FES-group and the control-group (the Wilcoxon test was used if the data were not normally distributed). Values with $p < 0.05$ were considered statistically significant. Intergroup comparisons were performed when intragroup comparisons of both groups were statistically significant.

3 Results

The study did not detect any significant differences in the baseline demographics between the FES-group and control-group ($p > 0.05$; Table 1).

3.1 Spatiotemporal variables in the FES group and the control group

After treatment, the walking speed increased in both groups ($p < 0.05$), with the FES group improving more than the control group ($p < 0.05$). The FES group exhibited increased step lengths in the affected side ($p < 0.05$), while the control group had increased step length in the unaffected side and decreased step length in the affected side ($p < 0.05$). Both of the groups exhibited improved step length SIs ($p < 0.05$), and the FES group improved more than the control group ($p < 0.05$). Stance time percentage, and double support time percentage decreased, and single support time percentage increased in both groups after treatment ($p < 0.05$), but there was no significant difference between the two groups ($p > 0.05$). The gait cycle time of both groups decreased after 3 weeks of treatment, but there was no significant difference between the two groups ($p > 0.05$) (Table 2).

3.2 Start time of the heel and initial contact phase percentage

Both groups had earlier heel medial and heel lateral start times after 4 weeks ($p < 0.05$), and there was no significant difference between the two groups ($p > 0.05$). Only the FES group had a

TABLE 1 Baseline demographics.

Group	Sex		Age (years)	Body mass (kg)	Body mass index (kg/m^2)	Lesions		Affected side		Mean time since stroke (weeks)
	Male	Female				Infarct	Hemorrhage	Left	Right	
FES	13	4	43.5 (13.64)	66.69 (8.64)	24.16 (2.1)	12	5	10	7	10.25 (4.59)
Control	11	6	49.42 (12.03)	67.53 (10.4)	25.09 (2.74)	13	4	9	8	8.97 (5.18)

FES, Functional electrical stimulation. Values are presented as mean (standard deviation).

TABLE 2 Spatiotemporal variables in the FES group and control group.

Parameters		FES group ($n = 17$)		Control group ($n = 17$)		Intragroup *P*		Intergroup *P*	
		Baseline	Week 4	Baseline	Week 4	FES group	Control group	Baseline	Week 4
Walking speed (m/s)		0.46 (0.18)	0.63 (0.3)	0.43 (0.1)	0.49 (0.09)	0.01	0.04	0.54	0.04
Stride length (cm)		60.31 (13.03)	71.02 (21.38)	57.49 (13.17)	59.62 (14.43)	0.13	0.57	0.32	0.54
Step length (cm)	Unaffected side	30.44 (8.17)	34.54 (11.24)	27.62 (13.33)	33.15 (10.22)	0.12	0.02	0.15	0.36
	Affected side	32.02 (7.39)	40.26 (13.94)	34.57 (4.78)	29.58 (8.14)	0.01	0.01	0.24	0.01
Step length SI		0.3 (0.3)	0.15 (0.11)	0.39 (0.19)	0.23 (0.18)	0.04	0.001	0.14	0.03
Gait cycle time (ms)		1822.52 (378.331)	1685.26 (451.69)	1691.26 (235.62)	1619.93 (364.76)	0.11	0.05	0.09	0.06
Stance phase percentage (%)		70.65 (10.02)	63.88 (9.99)	70.47 (3.13)	66.28 (6.96)	0.03	0.03	0.95	0.42
Single stance phase percentage (%)		19.96 (5.47)	23.16 (6.66)	16.06 (6.06)	22.18 (3.71)	0.03	0.001	0.06	0.60
Double stance phase percentage (%)		26.41 (8.32)	22.03 (5.79)	25.41 (5.59)	21.72 (2.97)	0.04	0.001	0.68	0.84

SI: Symmetry index; values are presented as the mean (standard deviation). Intragroup P: baseline vs. after 4 weeks (the paired *t*-test). Intergroup P: FES group vs. control group (the independent-samples *t*-test).

significantly longer initial contact phase percentage after 4 weeks ($p < 0.05$) (Table 3). Before treatment, the lateral metatarsal bones (Figure 4A) or flat foot (Figure 5A) of the affected side (right) contacted to the ground first. After treatment, the heel contacted the ground first (Figures 4B, 5B). The abnormal initial contact points were corrected after FES treatment (Figures 4, 5).

3.3 Regional Max F, impulse, contact area percentage and symmetry index of the FES group and control group

Result of regional Max F/impulse/contact area percentage: The regional Max F percentage of toe 1 increased in both groups ($p < 0.05$), and the FES group increased more than the control group ($p < 0.05$). The regional Max F and contact area percentage of the midfoot both increased in the FES group ($p < 0.05$) (Figures 6A–C; Table 4).

Results of regional Max F/impulse/contact area percentage SI (Figures 7A–C; Table 4): The regional Max F and impulse percentage SI of the medial heel both decreased ($p < 0.05$) (Figures 7A,B; Table 4). The regional impulse percentage SI of the meta5 and midfoot decreased in the FES group after 4 weeks ($p < 0.05$) (Figure 7B; Table 4).

4 Discussion

Drop foot may be caused by decrease of ankle dorsiflexion control, increase of plantar flexor tension, or both. We mainly

TABLE 3 Start times of the heel and initial contact phase percentage.

Parameters	FES group ($n = 17$)		Control group ($n = 17$)		Intragroup *P*		Intergroup *P*	
	Baseline	Week 4	Baseline	Week 4	FES group	Control group	Baseline	Week 4
Heelmedial start time (ms)	10.85 (19.03)	2.36 (6.67)	23.32 (26.90)	3.45 (6.90)	0.02	0.03	0.13	0.64
Heellateral start time (ms)	16.82 (24.86)	2.38 (6.73)	12.02 (11.52)	3.42 (6.98)	0.02	0.04	0.24	0.66
Initial contact phase percentage (%)	1.50 (2.71)	4.16 (3.23)	2.89 (1.58)	3.54 (4.00)	0.01	0.94	0.06	0.77

Values are presented as the mean (standard deviation). Intragroup P: baseline vs. after 4 weeks (the paired *t*-test). Intergroup P: FES group vs. control group (the independent-samples *t*-test).

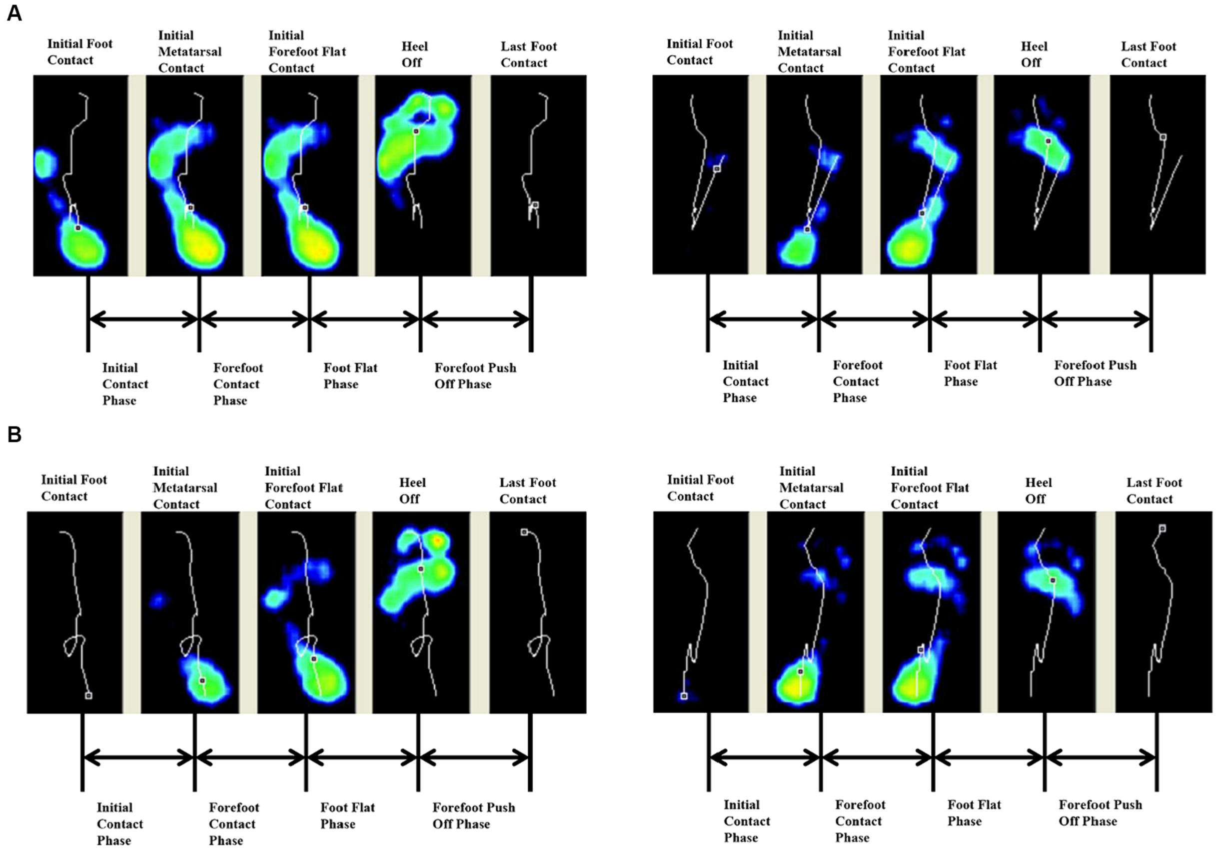

FIGURE 4
Abnormal lateral metatarsal bones as the initial contact points and the correction from a patient before and after FES treatment. **(A)** Before treatment, the lateral metatarsal bones of the affected side (right) contacted the ground first. **(B)** After treatment, the heel of the affected side (right) contacted the ground first.

focused on the control of the tibialis anterior muscle in this study. The tibialis anterior muscle does eccentric contraction during the initial contact phase to control the fall of the foot and does concentric contraction during the initial swing phase to promote the propulsion. So if the tibialis anterior muscle is not activated properly, the motion control caused by eccentric contraction and motion generation caused by concentric contraction are both badly affected (Sheng, 2009). Therefore, no matter what kind of problem causes foot drop, improving the control of dorsiflexion is conducive for propulsion (motion generation) and maintaining support stability (motion control) (Tenniglo et al., 2018). In this study, we focused on the gait parameters including spatiotemporal variables, initial contact phase and plantar pressure after FES. We found that the most meaningful result was the longer initial contact phase, which means better motion control of dorsiflexion after FES than the control group.

4.1 Spatiotemporal variables

Insufficient ankle dorsiflexion in the late swing phase would affect the initial loading site, and then decreased the walking speed (Sheng, 2009). Previous studies indicated that FES can increase walking speed (Embrey et al., 2010; Hakansson et al., 2011; Sabut et al., 2011; Taylor et al., 2013; Buentjen et al., 2019). However, gait speed lacks the sensitivity to differentiate the true restitution of gait impairments. If increases in walking speed are because of the compensations of the non-paretic leg, it will aggravate the asymmetry (Allen et al., 2018). Thus, the assessment of other spatiotemporal parameters will help assess walking quality. Decreases in the double stance phase and increases in the single stance phase percentage of the affected limb were considered a better weight bearing (Mâaref et al., 2010). The stance and swing phase percentages are usually unbalanced in stroke patients (Hollman et al., 2011; Kilby et al., 2014). The stance phase percentage of healthy individuals is about 60%. In this study, both groups had less stance phase percentages after treatment, and returned to close to normal (60%). Therefore, FES and basic rehabilitation can improve weight bearing capacity (Kim and Hwangbo, 2015). We found the step length of the paretic limb was longer than the nonparetic limb before treatment, which was similar to the results of Xu et al. (2016), Kottink et al. (2012), and Meijer et al. (2011). The gait patterns of healthy individuals are symmetrical (Plotnik et al., 2013). The main reason for asymmetrical gait is that with shorter stance phase and poor weight bearing of the paretic limb, the center of gravity will move to the nonparetic side, which will results in dysfunction in the swing phase (Kamibayashi et al., 2010; Rusu et al., 2014) and cause

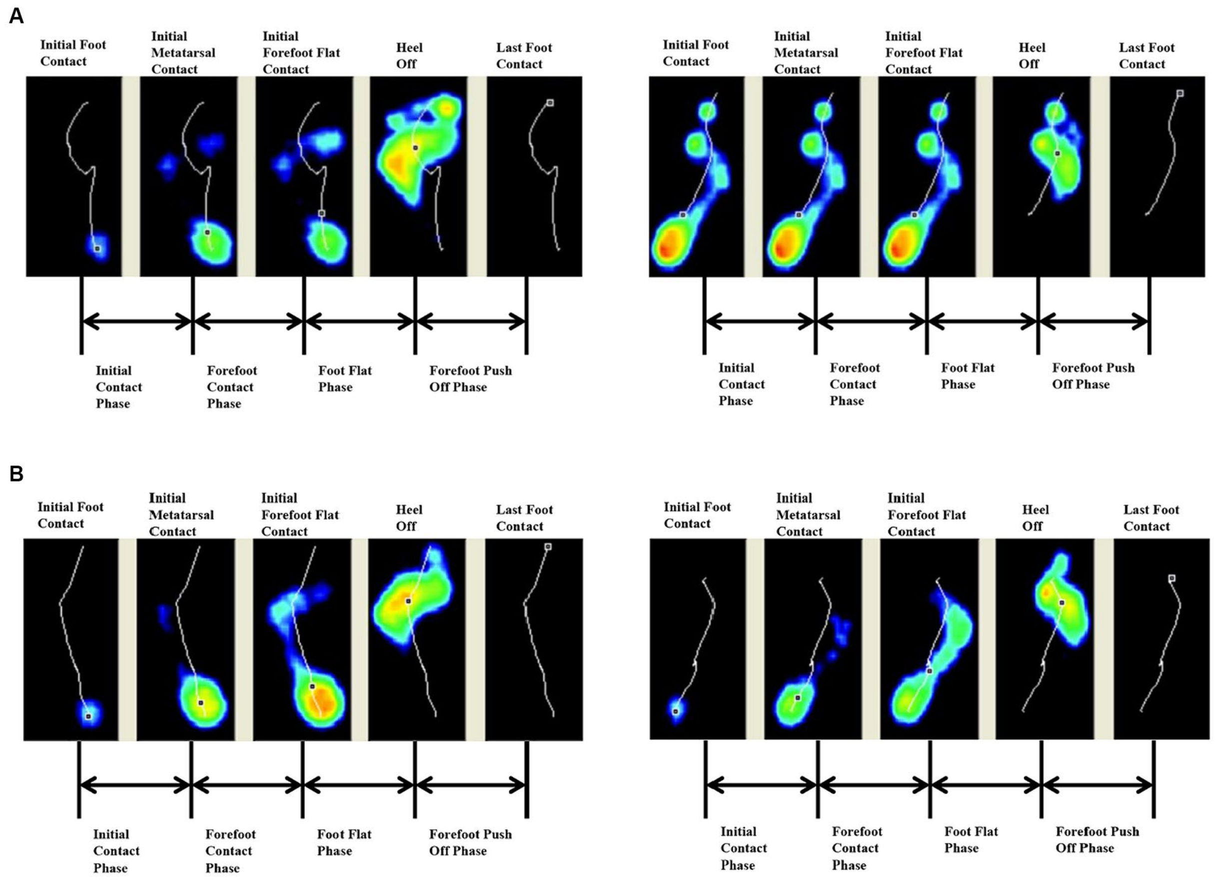

FIGURE 5
Abnormal flat foot as the initial contact point and the correction from a patient before and after FES treatment. **(A)** Before treatment, the affected side (right) exhibited flat foot at the initial contact phase. **(B)** After treatment, the heel of the affected side (right) contacted the ground first.

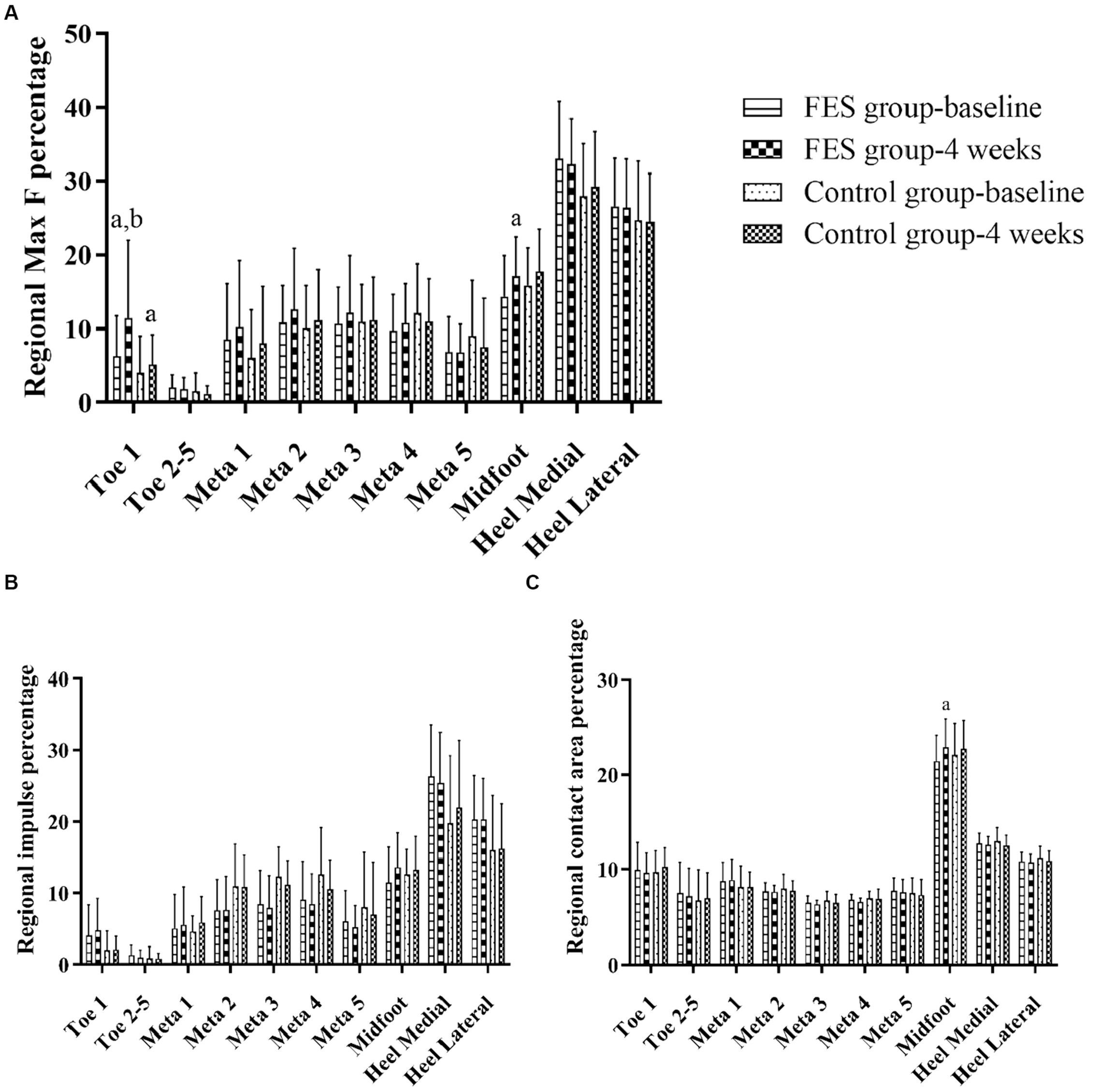

FIGURE 6
Result of Max F, impulse and contact area percentage in the 10 anatomical regions of the affected side. **(A)** Regional Max F percentage. **(B)** Regional impulse percentage. **(C)** Regional contact area percentage. "a" $p < 0.05$, significant difference between baseline to 4 weeks (the paired *t*-test). "b" $p < 0.05$, significant difference between FES and control group after 4 weeks (the independent-samples *t*-test). Max F, Maximum force; Meta, Metatarsal.

shorter step length in the nonparetic leg (Patterson et al., 2010). Compared to changes in step length, the improvement of symmetry is more important in decreasing the risk of falling (Meijer et al., 2011).

4.2 Initial contact points and initial contact phase

A gait cycle starts from the initial contact of the heel. If the ankle dorsiflexion is insufficient, the initial contact is at the forefoot, the outer edge of the foot, or the whole foot palm, which affects the stability of the supporting phase. If the ground reaction force falls in front of the knee, overextension of the knee will occur, affecting the forward movement of the tibia and leading to insufficient propulsion, a compensatory reduction of the stride length, and a deceleration of speed (Perry et al., 2010). Such actions are called "well begun, half done." Thus, the correction of the abnormal initial contact mode is an important part of the normalization of the whole walking cycle.

During normal gait, the heel touches the ground first. Thus, the start time of the heel is 0 ms. However, in patients with drop foot, the lateral metatarsal bones contacted to the ground first (Figure 4A). Under those conditions, the stability of the stance phase was destroyed and the risk of falls increases. After 4 weeks, the start time of the medial and lateral heel were decreased, and thus, both FES and basic rehabilitation can effectively correct the abnormal initial contact mode. Thus, the heel contacted the ground first (Figure 4B), which was the most basic and key step for the onset of the gait cycle.

TABLE 4 Some absolute values of regional Max F, impulse, contact area percentage and symmetry index of the FES group and control group.

Parameters	FES group ($n = 17$)		Control group ($n = 17$)		Intragroup *P*		Intergroup *P*	
	Baseline	Week 4	Baseline	Week 4	FES group	Control group	Baseline	Week 4
Regional Max F percentage of Toe 1	6.28 (5.45)	11.44 (10.49)	4.01 (4.94)	5.13 (4.05)	0.03	0.02	0.41	0.01
Regional Max F percentage of Midfoot	14.35 (5.58)	17.10 (5.29)	15.86 (5.03)	17.76 (5.67)	0.04	0.19	0.65	0.87
Regional contact area percentage of Midfoot	21.45 (2.69)	22.89 (2.96)	22.05 (3.34)	22.72 (3.01)	0.02	0.48	0.07	0.79
Regional Max F percentage SI of Heel Medial	0.25 (0.26)	0.14 (0.16)	0.44 (0.44)	0.25 (0.3)	0.01	0.09	0.08	0.03
Regional impulse percentage SI of Meta 5	1.45 (1.69)	0.64 (0.89)	0.92 (1.02)	0.62 (0.67)	0.04	0.28	0.11	0.87
Regional impulse percentage SI of Midfoot	1.03 (1.53)	0.41 (0.24)	0.36 (0.33)	0.57 (0.51)	0.04	0.11	0.05	0.16
Regional impulse percentage SI of Heel Medial	0.31 (0.21)	0.17 (0.10)	0.62 (0.45)	0.45 (0.3)	0.02	0.09	0.07	0.03

Values are presented as the mean (standard deviation). Intragroup P: baseline vs. after 4 weeks (the paired *t*-test). Intergroup P: FES group vs. control group (the independent-samples *t*-test).

The start time of the heel is a time point. This is different from the initial contact phase, which is the range in time from heel strike to when the complete heel contacts the ground. In healthy individuals, the increasing pre-tibial activity at the end of the swing phase can ensure the ankle and foot are prepared for the following heel strike (Perry et al., 2010). Other research showed that foot and ankle motor control at the initial contact phase can significantly improve the stability and posture (Lee et al., 2013). Stroke patients had an inadequacy in eccentric contraction or loss of the control of the tibialis anterior at the end of the swing phase, which caused flat foot or drop foot following heel strike (Figure 5A). Recently, most studies have focused on the ankle angle following heel strike using 3D gait analysis (Bae et al., 2019; d'Andrea et al., 2023), but few studies focus on the control of ankle dorsiflexion at the initial contact phase. The time of the initial contact phase can reflect the motor control of tibialis anterior eccentric contraction. The heel strike process was gentle and the foot slap was decreased, thus, improving shock absorption (Figure 5B). In this study, the normal range of the initial contact phase percentage was 5–15% (according to Footscan software). The FES group was close to the normal range after 4 weeks (4.16%). This may be because FES needs to detect patients' active contraction signal first, and then release the corresponding electrical stimulation, which is a positive feedback. Thus, those patients were more likely to focus on ankle dorsiflexion during the training process, and had a stronger sense of active participation, improving their active control. This was also the most significant and irreplaceable result of FES in this study, which was difficult for conventional rehabilitation (control group) to achieve it.

4.3 Plantar pressure parameters

The peak pressure in the toe 1 region occurred at the end of the stance phase, i.e., the propulsive phase (Booth et al., 2018). In this study, the Max F percentage in the toe 1 area of the affected side increased more significantly in the FES group, which indicated that FES was more beneficial than basic rehabilitation to enhance the propulsive force at the end of the stance phase (Sabut et al., 2011; Lee et al., 2014; Melo et al., 2015; Schiemanck et al., 2015). The medial heel was the area with the largest proportion of Max F and impulse in the sole. Therefore, the improvement of Max F and impulse SI in the medial heel and the SI decrease in other regions indicated that the forces on both sides were symmetrical during the supporting period, which was conducive to the maintenance of posture stability and the reduction in the risk of falls. Because the longer initial contact phase can lead to a more stable ankle joint (Sheng, 2009), so the forces on the bilateral sole were more balanced in the FES group. The reasons why there were some baseline differences between the two groups and most of the pressure parameters were not statistically significant. To analyze the possible causes, this study observed the effect of FES after 4 weeks of treatment. There was no FES effect during the data collection process, which was different from the previous experiment to observe the immediate effect of FES on plantar pressure (Yuan et al., 2015). Secondly, the diversity of plantar pressure distribution patterns was affected to a moderate degree (<50%) by various factors, such as walking speed, step length, weight, gender, foot structure, range of motion, peripheral sensation (Menz and Morris, 2006; Yan et al., 2013). Previous studies found that changes in gait speed have an impact on the forces in all areas of the foot (Burnfield et al., 2004). Booth et al. (2018) found that with increases in walking speed, the heel pressure increased in the early stage and decreased in the middle stage of the support phase. The pressure in most areas decreased in the middle and end of the support phase. In this study, the changes in spatiotemporal parameters such as velocity and step length had an impact on the plantar pressure. There were also various foot contact and force patterns in post-stroke patients (Hillier and Lai, 2009; Jasiewicz et al., 2019). Thus, the changes in the symmetry index before and after 4 weeks on both feet would be more significant.

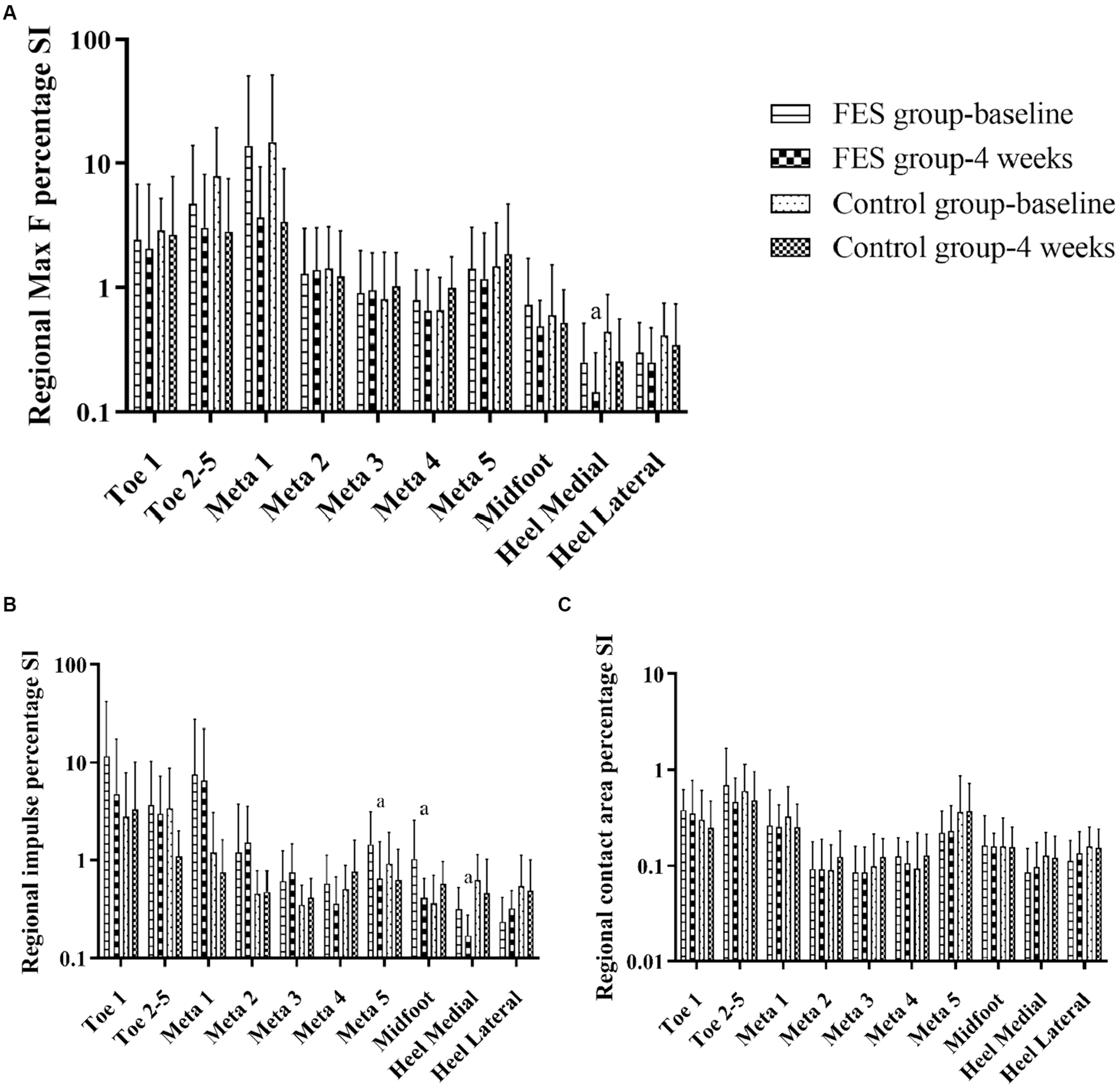

FIGURE 7
Results of Max F, impulse and contact area percentage SI in the 10 anatomical regions. **(A)** Regional Max F percentage SI. **(B)** Regional impulse percentage SI. **(C)** Regional contact area percentage SI. "a" $p < 0.05$, significant difference between baseline to 4 weeks (the paired *t*-test). Max F, Maximum force; SI, Symmetry index; Meta, Metatarsal.

4.4 Limitations

A limited number of subjects meeting inclusion criteria were collected over a 2-year period. So the limitation of this study was that the sample size was small. This was an observational study, and we intended to summarize possible advantages of FES from the existing cases. To further clarify the specific differences between FES and basic rehabilitation, the sample size should be further increased. Additionally, there were many factors that affect gait abnormalities in hemiplegic patients, and thus, the individual differences were large. The plantar pressure data represented the results of the entire support phase, and there was no distinction between the initial contact phase, the loading-response phase, and the propulsive phase. In this study, we only collected and analyzed the spatiotemporal parameters and dynamic plantar data, while the specific muscle activation and strength evaluation in the walking state needed to be combined with electromyography data.

5 Conclusion

The aim of this study was to observe the effect of FES on the changes in the plantar pressure of drop foot patients. The results showed that the therapeutic effect of FES include a more balanced plantar dynamic parameters, and the improvement of gait speed, step length SI, initial contact phase and propulsion force than the control group. Therefore, under the conditions used in this study, the therapeutic effect of FES in drop foot patients, and in particular, in the improvement of ankle joint control during the heel strike process was better than that observed following simple basic rehabilitation.

Data availability statement

The original contributions presented in the study are included in the article/supplementary material, further inquiries can be directed to the corresponding authors.

Ethics statement

The studies involving humans were approved by Clinical Research Ethics Committee at Shengjing Hospital of China Medical University (approval no. 2015PS438KJ). The studies were conducted in accordance with the local legislation and institutional requirements. The participants provided their written informed consent to participate in this study.

Author contributions

XL: Conceptualization, Data curation, Methodology, Validation, Writing – original draft, Writing – review & editing. HL: Data curation, Investigation, Software, Writing – original draft. YL: Data curation, Software, Writing – original draft. WL: Resources, Visualization, Writing – original draft. LZ: Conceptualization, Methodology, Writing – review & editing. FZ: Methodology, Resources, Supervision, Writing – review & editing. ZZ: Methodology, Resources, Writing – review & editing. XY: Funding acquisition, Methodology, Resources, Software, Writing – review & editing.

Funding

The author(s) declare that financial support was received for the research, authorship, and/or publication of this article. The research was supported by the Natural Science Foundation of China (81902297) and the Foundation of Department of Science and Technology of Liaoning province (2021-KF-12-04).

Acknowledgments

We are thankful for the support from colleagues in the department of rehabilitation.

Conflict of interest

The authors declare that the research was conducted in the absence of any commercial or financial relationships that could be construed as a potential conflict of interest.

Publisher's note

References

Allen, J. L., Ting, L. H., and Kesar, T. M. (2018). Gait rehabilitation using functional electrical stimulation induces changes in ankle muscle coordination in stroke survivors: a preliminary study. *Front. Neurol.* 9:1127. doi: 10.3389/fneur.2018.01127

Bae, D. Y., Shin, J. H., and Kim, J. S. (2019). Effects of dorsiflexor functional electrical stimulation compared to an ankle/foot orthosis on stroke-related genu recurvatum gait. *J. Phys. Ther. Sci.* 31, 865–868. doi: 10.1589/jpts.31.865

Bao, S. C., Khan, A., Song, R., and Tong, K. Y. (2020). Rewiring the lesioned brain: electrical stimulation for post-stroke motor restoration. *J. Stroke* 22, 47–63. doi: 10.5853/jos.2019.03027

Beata, L., Nilsson, M. H., Oskar, H., and Peter, H. (2018). The clinical significance of 10-m walk test standardizations in Parkinson's disease. *J. Neurol.* 265, 1829–1835. doi: 10.1007/s00415-018-8921-9

Berenpas, F., Geurts, A., Den, B., and Van, S. (2019). Surplus value of implanted peroneal functional electrical stimulation over ankle-foot orthosis for gait adaptability in people with foot drop after stroke. *Gait Posture* 71, 157–162. doi: 10.1016/j.gaitpost.2019.04.020

Biasiucci, A., Leeb, R., Iturrate, I., Perdikis, S., Al-Khodairy, A., Corbet, T., et al. (2018). Brain-actuated functional electrical stimulation elicits lasting arm motor recovery after stroke. *Nat. Commun.* 9:2421. doi: 10.1038/s41467-018-04673-z

Bidabadi, S. S., Iain, M., Lee, G. Y. F., Morris, S., and Tan, T. (2019). Classification of foot drop gait characteristic due to lumbar radiculopathy using machine learning algorithms. *Gait Posture* 71, 234–240. doi: 10.1016/j.gaitpost.2019.05.010

Booth, B. G., Keijsers, N. L. W., Sijbers, J., and Huysmans, T. (2018). STAPP: spatiotemporal analysis of plantar pressure measurements using statistical parametric mapping. *Gait Posture* 63, 268–275. doi: 10.1016/j.gaitpost.2018.04.029

Bosch, P. R., Harris, J. E., and Wing, K. (2014). Review of therapeutic electrical stimulation for dorsiflexion assist and orthotic substitution from the American congress of rehabilitation medicine stroke movement interventions subcommittee. *Arch. Phys. Med. Rehabil.* 95, 390–396. doi: 10.1016/j.apmr.2013.10.017

Bouton, C. E., Shaikhouni, A., Annetta, N. V., Bockbrader, M. A., Friedenberg, D. A., Nielson, D. M., et al. (2016). Restoring cortical control of functional movement in a human with quadriplegia. *Nature* 533, 247–250. doi: 10.1038/nature17435

Buentjen, L., Kupsch, A., Galazky, I., Frantsev, R., Heinze, H. J., Voges, J., et al. (2019). Long-term outcomes of semi-implantable functional electrical stimulation for central drop foot. *J. Neuroeng. Rehabil.* 16:72. doi: 10.1186/s12984-019-0542-8

Burnfield, J. M., Few, C. D., and Mohamed, O. S. (2004). The influence of walking speed and footwear on plantar pressures in older adults. *Clin. Biomech.* 19, 78–84. doi: 10.1016/j.clinbiomech.2003.09.007

Daly, J. J., and Wolpaw, J. R. (2008). Brain–computer interfaces in neurological rehabilitation. *Lancet Neurol.* 7, 1032–1043. doi: 10.1016/S1474-4422(08)70223-0

d'Andrea, F., Taylor, P., Yang, K., and Heller, B. (2023). Can inertial measurement unit sensors evaluate foot kinematics in drop foot patients using functional electrical stimulation? *Front. Hum. Neurosci.* 17:1225086. doi: 10.3389/fnhum.2023.1225086

Embrey, D. G., Holtz, S. L., Alon, G., Brandsma, B. A., and Mccoy, S. W. (2010). Functional electrical stimulation to dorsiflexors and plantar flexors during gait to improve walking in adults with chronic hemiplegia. *Arch. Phys. Med. Rehabil.* 91, 687–696. doi: 10.1016/j.apmr.2009.12.024

Ethier, C., Gallego, J., and Miller, L. E. (2015). Brain-controlled neuromuscular stimulation to drive neural plasticity and functional recovery. *Curr. Opin. Neurobiol.* 33, 95–102. doi: 10.1016/j.conb.2015.03.007

Gil-Castillo, J., Alnajjar, F., Koutsou, A., Torricelli, D., and Moreno, J. C. (2020). Advances in neuroprosthetic management of foot drop: a review. *J. Neuroeng. Rehabil.* 17:46. doi: 10.1186/s12984-020-00668-4

Hakansson, N. A., Kesar, T., Reisman, D., Binder-Macleod, S., and Higginson, J. S. (2011). Effects of fast functional electrical stimulation gait training on mechanical recovery in Poststroke gait. *Artif. Organs* 35, 217–220. doi: 10.1111/j.1525-1594.2011.01215.x

Hillier, S., and Lai, M. S. (2009). Insole plantar pressure measurement during quiet stance post stroke. *Top. Stroke Rehabil.* 16, 189–195. doi: 10.1310/tsr1603-189

Hollman, J. H., McDade, E. M., and Petersen, R. C. (2011). Normative spatiotemporal gait parameters in older adults. *Gait Posture* 34, 111–118. doi: 10.1016/j.gaitpost.2011.03.024

Janisse, D. J. (1993). A scientific approach to insole design for the diabetic foot. *Foot* 3, 105–108. doi: 10.1016/0958-2592(93)90075-E

Jasiewicz, B., Klimiec, E., Młotek, M., Guzdek, P., Duda, S., Adamczyk, J., et al. (2019). Quantitative analysis of foot plantar pressure during walking. *Med. Sci. Monit.* 25, 4916–4922. doi: 10.12659/MSM.914915

Johnston, S. C., Mendis, S., and Mathers, C. D. (2009). Global variation in stroke burden and mortality: estimates from monitoring, surveillance, and modelling. *Lancet Neurol.* 8, 345–354. doi: 10.1016/S1474-4422(09)70023-7

Kamibayashi, K., Nakajima, T., Fujita, M., Takahashi, M., Ogawa, T., Akai, M., et al. (2010). Effect of sensory inputs on the soleus H-reflex amplitude during robotic passive stepping in humans. *Exp. Brain Res.* 202, 385–395. doi: 10.1007/s00221-009-2145-2

Kilby, M. C., Slobounov, S. M., and Newell, K. M. (2014). Aging and the recovery of postural stability from taking a step. *Gait Posture* 40, 701–706. doi: 10.1016/j.gaitpost.2014.08.002

Kim, S. G., and Hwangbo, G. (2015). The effect of obstacle gait training on the plantar pressure and contact time of elderly women. *Arch. Gerontol. Geriatr.* 60, 401–404. doi: 10.1016/j.archger.2015.02.007

Kimmeskamp, S., and Hennig, E. M. (2001). Heel to toe motion characteristics in Parkinson patients during free walking. *Clin. Biomech.* 16, 806–812. doi: 10.1016/S0268-0033(01)00069-9

Kottink, A., Tenniglo, M., Vries, W., Hermens, H., and Buurke, J. (2012). Effects of an implantable two-channel peroneal nerve stimulator versus conventional walking device on spatiotemporal parameters and kinematics of hemiparetic gait. *J. Rehabil. Med.* 44, 51–57. doi: 10.2340/16501977-0909

Laufer, Y., Hausdorff, J. M., and Ring, H. (2009). Effects of a foot drop neuroprosthesis on functional abilities, social participation, and gait velocity. *Am. J. Phys. Med. Rehabil.* 88, 14–20. doi: 10.1097/PHM.0b013e3181911246

Lee, N. K., Kwon, J. W., Son, S. M., Nam, S. H., Choi, Y. W., and Kim, C. S. (2013). Changes of plantar pressure distributions following open and closed kinetic chain exercise in patients with stroke. *NeuroRehabilitation* 32, 385–390. doi: 10.3233/NRE-130859

Lee, Y. H., Yong, S. Y., Kim, S. H., Kim, J. H., and Hwang, S. (2014). Functional electrical stimulation to ankle Dorsiflexor and Plantarflexor using single foot switch in patients with hemiplegia from hemorrhagic stroke. *Ann. Rehabil. Med.* 38, 310–316. doi: 10.5535/arm.2014.38.3.310

Leunkeu, A. N., Lelard, T., Shephard, R. J., Doutrellot, P. L., and Ahmaidi, S. (2014). Gait cycle and plantar pressure distribution in children with cerebral palsy: clinically useful outcome measures for a management and rehabilitation. *NeuroRehabilitation* 35, 657–663. doi: 10.3233/NRE-141163

Li, K., Sun, F. L., Guo, H. B., Shi, Z. J., Yao, R., and Zhang, H. (2023). Comparison of the plantar pressure distribution and mechanical alignmentin patients with varus knee osteoarthritis following high tibial osteotomy. *BMC Musculoskelet. Disord.* 24:479. doi: 10.1186/s12891-023-06603-7

Liberson, W. T., Holmquest, H. J., Scot, D., and Dow, M. (1961). Functional electrotherapy: stimulation of the peroneal nerve synchronized with the swing phase of the gait of hemiplegic patients. *Arch. Phys. Med. Rehabil.* 42, 101–105.

Lim, B. O., O'Sullivan, D., Choi, B. G., and Kim, M. Y. (2016). Comparative gait analysis between children with autism and age-matched controls: analysis with temporal-spatial and foot pressure variables. *J. Phys. Ther. Sci.* 28, 286–292. doi: 10.1589/jpts.28.286

Liu, M., Wu, B., Wang, W. Z., Lee, L. M., Zhang, S. H., and Kong, L. Z. (2007). Stroke in China: epidemiology, prevention, and management strategies. *Lancet Neurol.* 6, 456–464. doi: 10.1016/S1474-4422(07)70004-2

Low, D. C., and Dixon, S. J. (2010). Footscan pressure insoles: accuracy and reliability of force and pressure measurements in running. *Gait Posture* 32, 664–666. doi: 10.1016/j.gaitpost.2010.08.002

Mâaref, K., Martinet, N., Grumillier, C., Ghannouchi, S., André, J. M., and Paysant, J. (2010). Kinematics in the terminal swing phase of unilateral transfemoral amputees: microprocessor-controlled versus swing-phase control prosthetic knees. *Arch. Phys. Med. Rehabil.* 91, 919–925. doi: 10.1016/j.apmr.2010.01.025

Manor, N., and Chen, I. H. (2014). Infarct hemisphere and noninfarcted brain volumes affect locomotor performance following stroke. Neurology: official journal of the American Academy of. *Neurology* 82, 828–834. doi: 10.1212/WNL.0000000000000186

Meijer, R., Plotnik, M., Zwaaftink, E. G., van Lummel, R. C., Ainsworth, E., Martina, J. D., et al. (2011). Markedly impaired bilateral coordination of gait in post-stroke patients: is this deficit distinct from asymmetry? A cohort study. *J. Neuroeng. Rehabil.* 8:23. doi: 10.1186/1743-0003-8-23

Melo, P. L., Silva, M. T., Martins, J. M., and Newman, D. J. (2015). Technical developments of functional electrical stimulation to correct drop foot: sensing, actuation and control strategies. *Clin. Biomech. (Bristol, Avon)* 30, 101–113. doi: 10.1016/j.clinbiomech.2014.11.007

Menz, H. B., and Morris, M. E. (2006). Clinical determinants of plantar forces and pressures during walking in older people. *Gait Posture* 24, 229–236. doi: 10.1016/j.gaitpost.2005.09.002

Milosevic, M., Marquez-Chin, C., Masani, K., Hirata, M., Nomura, T., Popovic, M. R., et al. (2020). Why brain-controlled neuroprosthetics matter: mechanisms underlying electrical stimulation of muscles and nerves in rehabilitation. *Biomed. Eng. Online* 19, 1–30. doi: 10.1186/s12938-020-00824-w

Moritz, C. T., Perlmutter, S. I., and Fetz, E. E. (2008). Direct control of paralysed muscles by cortical neurons. *Nature* 456, 639–642. doi: 10.1038/nature07418

Morrison, K. E., Hudson, D. J., Davis, I. S., Richards, J. G., Royer, T. D., Dierks, T. A., et al. (2010). Plantar pressure during running in subjects with chronic ankle instability. *Foot Ankle Int.* 31, 994–1000. doi: 10.3113/FAI.2010.0994

Nolan, K. J., Yarossi, M., and Mclaughlin, P. (2015). Changes in center of pressure displacement with the use of a foot drop stimulator in individuals with stroke. *Clin. Biomech.* 30, 755–761. doi: 10.1016/j.clinbiomech.2015.03.016

Park, S. J., and Wang, J. S. (2017). The immediate effect of FES and TENS on gait parameters in patients after stroke. *J. Phys. Ther. Sci.* 29, 2212–2214. doi: 10.1589/jpts.29.2212

Patel, A. P., Fisher, J. L., Nichols, E., Abd-Allah, F., and Samy, A. (2019). Global, regional, and national burden of brain and other CNS cancer, 1990–2016: a systematic analysis for the global burden of disease study 2016. *Lancet Neurol.* 18, 376–393. doi: 10.1016/S1474-4422(18)30468-X

Patterson, K. K., Gage, W. H., Brooks, D., Black, S. E., and Mcilroy, W. E. (2010). Evaluation of gait symmetry after stroke: a comparison of current methods and recommendations for standardization. *Gait Posture* 31, 241–246. doi: 10.1016/j.gaitpost.2009.10.014

Perry, J., Burnfield, J. M., and Inc, S. (2010). *Gait analysis: Normal and pathological function*. New Jersey: SLACK Incorporated, 576.

Plotnik, M., Bartsch, R. P., Zeev, A., Giladi, N., and Hausdorff, J. M. (2013). Effects of walking speed on asymmetry and bilateral coordination of gait. *Gait Posture* 38, 864–869. doi: 10.1016/j.gaitpost.2013.04.011

Prenton, S., Hollands, K. L., and Kenney, L. P. (2016). Functional electrical stimulation versus ankle foot orthoses for foot-drop: a meta-analysis of orthotic effects. *J. Rehabil. Med.* 48, 646–656. doi: 10.2340/16501977-2136

Reisman, D., Kesar, T., Perumal, R., Roos, M., Rudolph, K., Higginson, J., et al. (2013). Time course of functional and biomechanical improvements during a gait training intervention in persons with chronic stroke. *J. Neurol. Phys. Ther.* 37, 159–165. doi: 10.1097/NPT.0000000000000020

Rusu, L., Neamtu, M. C., Rosulescu, E., Cosma, G., Dragomir, M., and Marin, M. I. (2014). Analysis of foot and ankle disorders and prediction of gait in multiple sclerosis rehabilitation. *Eur. J. Med. Res.* 19:73. doi: 10.1186/s40001-014-0073-5

Sabut, S. K., Sikdar, C., Kumar, R., and Mahadevappa, M. (2011). Functional electrical stimulation of dorsiflexor muscle: effects on dorsiflexor strength, plantarflexor spasticity, and motor recovery in stroke patients. *NeuroRehabilitation* 29, 393–400. doi: 10.3233/NRE-2011-0717

Schiemanck, S., Berenpas, F., Van Swigchem, R., Pepijn, V. D. M., De Vries, J., Beelen, A., et al. (2015). Effects of implantable peroneal nerve stimulation on gait quality, energy expenditure, participation and user satisfaction in patients with post-stroke drop foot using an ankle-foot orthosis. *Restor. Neurol. Neurosci.* 33, 795–807. doi: 10.3233/RNN-150501

Sheng, B. (2009). *Motor control training research into clinical practice*. Beijing: People's Medical Publishing House.

Skopljak, A., Sukalo, A., Batic-Mujanovic, O., Becirevic, M., and Zunic, L. (2014). Assessment of diabetic polyneuropathy and plantar pressure in patients with diabetes mellitus in prevention of diabetic foot. *Med. Arch.* 68, 389–393. doi: 10.5455/medarh.2014.68.389-393

Taylor, P., Humphreys, L., and Swain, I. (2013). The long-term cost-effectiveness of the use of functional electrical stimulation for the correction of dropped foot due to upper motor neuron lesion. *J. Rehabil. Med.* 45, 154–160. doi: 10.2340/16501977-1090

Tenniglo, M. J., Buurke, J. H., Prinsen, E. C., Kottink, A. I., Nene, A. V., and Rietman, J. S. (2018). Influence of functional electrical stimulation of the hamstrings on knee kinematics in stroke survivors walking with stiff knee gait. *J. Rehabil. Med.* 50, 719–724. doi: 10.2340/16501977-2367

Thomaz, S. R., Cipriano, G. Jr., Formiga, M. F., Fachin-Martins, E., Cipriano, G. F. B., Martins, W. R., et al. (2019). Effect of electrical stimulation on muscle atrophy and spasticity in patients with spinal cord injury – a systematic review with meta-analysis. *Spinal Cord* 57, 258–266. doi: 10.1038/s41393-019-0250-z

Xu, B. L., Yan, T. B., Yang, Y. L., Ou, R. Q., and Huang, S. P. (2016). Effect of normal-walking-pattern-based functional electrical stimulation on gait of the lower extremity in subjects with ischemic stroke: a self controlled study. *NeuroRehabilitation* 38, 163–169. doi: 10.3233/NRE-161306

Yan, S. H., Zhang, K., Tan, G. Q., Yang, J., and Liu, Z. C. (2013). Effects of obesity on dynamic plantar pressure distribution in Chinese prepubescent children during walking. *Gait Posture* 37, 37–42. doi: 10.1016/j.gaitpost.2012.05.018

Yuan, X. N., Li, X. T., Li, H. T., Liu, Y., Sun, S., Wan, Y. C., et al. (2015). Immediate effect of biofeedback functional electrical stimulation on plantar pressure under walking mode in patients with stroke. *Chinese J. Rehabil. Theory Pract.* 21, 1191–1196. doi: 10.3969/j.issn.1006-9771.2015.10.015

Yuan, X. N., Liang, W. D., Zhou, F. H., Li, H. T., Zhang, L. X., Zhang, Z. Q., et al. (2019). Comparison of walking quality variables between incomplete spinal cord injury patients and healthy subjects by using a footscan plantar pressure system. *Neural Regen. Res.* 14, 354–360. doi: 10.4103/1673-5374.244798

frontiers | Frontiers in Neuroscience

TYPE Original Research
PUBLISHED 04 April 2024
DOI 10.3389/fnins.2024.1379495

EDITED BY
Benyan Huo,
Zhengzhou University, China

REVIEWED BY
Xiaolong Chen,
Chongqing University, China
Weihong Ren,
Harbin Institute of Technology, China

*CORRESPONDENCE
Jiwei Li
✉ lijiwei@sia.cn
Jun Feng
✉ junfeng2336@gmail.com

RECEIVED 31 January 2024
ACCEPTED 19 March 2024
PUBLISHED 04 April 2024

CITATION
Liu L, Feng J, Li J, Chen W, Mao Z and Tan X (2024) Multi-layer CNN-LSTM network with self-attention mechanism for robust estimation of nonlinear uncertain systems. *Front. Neurosci.* 18:1379495. doi: 10.3389/fnins.2024.1379495

Multi-layer CNN-LSTM network with self-attention mechanism for robust estimation of nonlinear uncertain systems

Lin Liu[1], Jun Feng[1,2]*, Jiwei Li[2,3,4]*, Wanxin Chen[2,3,4], Zhizhong Mao[1] and Xiaowei Tan[2,3]

[1]College of Information Science and Engineering, Northeastern University, Shenyang, Liaoning, China, [2]State Key Laboratory of Robotics, Shenyang Institute of Automation, Chinese Academy of Sciences, Shenyang, Liaoning, China, [3]Institutes for Robotics and Intelligent Manufacturing, Chinese Academy of Sciences, Shenyang, Liaoning, China, [4]University of Chinese Academy of Sciences, Beijing, China

Introduction: With the help of robot technology, intelligent rehabilitation of patients with lower limb motor dysfunction caused by stroke can be realized. A key factor constraining the clinical application of rehabilitation robots is how to realize pattern recognition of human movement intentions by using the surface electromyography (sEMG) sensors to ensure unhindered human-robot interaction.

Methods: A multilayer CNN-LSTM prediction network incorporating the self-attention mechanism (SAM) is proposed, in this paper, which can extract and learn the periodic and trend characteristics of the sEMG signals, and realize the accurate autoregressive prediction of the human motion information. Firstly, the multilayer CNN-LSTM network utilizes the CNN layer for initial feature extraction of data, and the LSTM network is used to improve the enhancement of the historical time-series features. Then, the SAM is used to improve the global feature extraction performance and parallel computation speed of the network.

Results: In comparison with existing test is carried out using actual data from five healthy subjects as well as a clinical hemiplegic patient to verify the superiority and practicality of the proposed algorithm. The results show that most of the model's prediction $R > 0.9$ for different motion states of healthy subjects; in the experiments oriented to the motion characteristics of patient subjects, the angle prediction results of $R > 0.99$ for the untrained data on the affected side, which proves that our proposed model also has a better effect on the angle prediction of the affected side.

Discussion: The main contribution of this paper is to realize continuous motion estimation of ankle joint for healthy and hemiplegic individuals under non-ideal conditions (weak sEMG signals, muscle fatigue, high muscle tension, etc.), which improves the pattern recognition accuracy and robustness of the sEMG sensor-based system.

KEYWORDS

nonlinear systems, surface electromyography signal, machine learning network, uncertainties, robust estimation

1 Introduction

Stroke and other diseases may lead to lower limb motor dysfunction in patients. With the assistance of robotic technology, intelligent rehabilitation therapy can be realized to reduce the workload of clinical medical staff and improve the efficiency of patients' rehabilitation training (Kapelner et al., 2020). In the human–machine interaction between rehabilitation robots and patients, traditional human–machine interaction techniques often involve the robot passively receiving instructions, which may not be convenient for patients with motor function impairments (Zhai et al., 2017; Zhang et al., 2022). In recent years, human–machine interaction technology needs to evolve toward allowing robots to actively understand human behavioral intentions, resulting in a new type of interaction based on human biological signals.

Human bioelectric signal is the potential difference activated when the nerve signal containing human behavioral information is transmitted to the relevant organs or tissues, which is a direct reflection of human behavioral intentions (Ma et al., 2021). It is of great significance to break the human–machine barrier and realize natural human–machine interaction by decoding human bioelectric signals to recognize human behaviors, and empowering robots to understand the human body's intentions as an information medium for interaction between human beings and the outside world (Qi et al., 2020). Currently, widely studied bioelectric signals include electromyogram (EMG), electroencephalogram (EEG), electrocardiogram (ECG), and electrooculography (EOG). We focus on the surface electromyography (sEMG), which originates from the bioelectrical activity of spinal motor neurons under the control of the motor cortex of the brain, and are the temporal and spatial sum of sequences of action units produced by peripherally active motor units. Since sEMG has the advantages of being non-invasive, and simple to use, it is more suitable to be applied to the design of human–machine interaction control systems for rehabilitation robots (Xiong et al., 2021). The core technology to build the EMG human–machine interaction system is to decode the human body's motion intention through EMG signals, and the usually discussed motion intention decoding includes two categories, one is to recognize the discrete limb movements based on sEMG, such as the movements of the hand's clenched fist, extended palm, etc., and the other is to estimate the continuous joint motions based on sEMG, such as the continuous quantities of the joint moments and the joint angles, etc. In this study, we focus on healthy people and hemiplegic patients, and carry out research on sEMG-based continuous motion estimation methods for the foot and ankle area of the lower limb, which lays the foundation for future natural human–machine interaction control.

Human walking characteristics are crucial in studies targeting the continuous movement of the lower limb. Many features of the musculoskeletal system of the lower limbs implied in the human walking information. Human walking information can be used as a basis for the recognition of human movement intentions and the estimation and prediction of the human body's movements, which in turn improves the stability and accuracy of human–computer interactions with external devices, such as exoskeletons. It is also possible to compare the gait characteristics of different walking bodies, especially between healthy and patients. This enables an intelligent online evaluation of patient rehabilitation effects, such as stroke rehabilitation. Lower limb walking in healthy people is cyclic, and the inherent states of its musculoskeletal system, such as human limb properties and muscle activation states, are also relatively stable and have good model interpretability, so mechanistic models have been used to describe them in many studies (Zhang L. et al., 2021). There are also some research works that describe machine learning models such as neural networks with straightforward modeling process and unrestricted utilization of sEMG.

However, in research focused on hemiplegic patients, there are large differences in the nature of the bilateral cyclic reciprocity, with the healthy side usually experiencing weak functional decline and the affected side experiencing more severe fluctuations in cyclic information (Aymard et al., 2000; Zhao et al., 2023). The alternation of useful and useless information can lead to problems such as gradient disappearance or gradient explosion, causing loss of information (Meng et al., 2023). In addition, these weakly abled people are also prone to problems such as muscle fatigue or even spasticity, and in some cases excessive muscle tone (Zhang et al., 2019; Moniri et al., 2021), all of which will lead to a high degree of difficulty in estimating the continuity of a patient's lower extremities based on EMG signals (Sarasola-Sanz et al., 2018; Fleming et al., 2021; Zhu et al., 2022).

In machine learning network architectures for the study of continuous lower limb motion, auto-regression is a widely used method for time series prediction. It can capture the correlation and dependency of input and output sequences well, and has the advantages of simple structure, flexible order selection and easy application (Lehtokangas et al., 1996). The observations at the current time of the time series data are correlated with the historical observations. Autoregressive technologies can make use of cyclical, trend and seasonal characteristics of historical data to predict future data (Yin et al., 2023). The combination of autoregressive techniques and neural networks can effectively improve the ability of learning, understanding and forecasting of time series data (Taskaya-Temizel and Casey, 2005). A nonlinear autoregressive neural network with exogenous inputs has been proposed to model the dynamic behavior of an automotive air conditioning system (Ng et al., 2014). Combing autoregressive integrated moving average (ARIMA) and probabilistic neural network (PNN), a hybrid network model has been proposed in order to improve the prediction accuracy of ARIMA models (Khashei et al., 2012). Therefore, this article will process the sampled motion data by autoregressive technology, so that the network can fully learn the hidden features and improve the learning efficiency of the network.

In order to improve the robustness of time series signal prediction, a convolutional neural network (CNN) can be used to extract initial features from the data (Shao et al., 2024). The CNN is a specific type of feedforward neural network with a grid topology (Li Z. et al., 2021). CNN uses sparse interaction, parameter sharing and variant representation techniques to improve the feature extraction performance of convolutional operations (Li et al., 2016). Each convolution layer of CNN contains multiple convolution kernels, and each convolution checks data for sliding convolution to achieve feature extraction of time series data to obtain local features and short-term dependencies. The pooling layer performs summary statistics on the output obtained by the convolution layer (Gu et al., 2018). The local perception and weight sharing of CNN can also effectively reduce the number of weight parameters for model learning, thus improving the efficiency of model learning.

Based on deep CNN, a joint multi-task learning algorithm has been developed to predict effectively attributes in images (Abdulnabi et al., 2015). A joint classification-and-prediction framework has been proposed based on CNN for automatic sleep staging (Phan et al., 2018). Combing CNN architecture with depth wise separable convolutions with kernels (CNN-DSCK) has developed for prediction rating exploiting product review (Khan and Niu, 2021). The prediction applications of these complex systems show the advantages of CNN networks in time series feature extraction. For complex and long-term dynamic systems, whose data series have long-term correlation, LSTM network with better long-term feature capture ability can be considered for feature extraction (Bi et al., 2021; Zhang N. et al., 2021; Zha et al., 2022). LSTM network is an improvement of recurrent neural network (RNN) network, which can effectively improve the gradient disappearance and gradient explosion of RNN network in time series prediction (Kim and Cho, 2019). Complex system prediction based on LSTM network has achieved a series of innovative results (Rathore and Harsha, 2022). Based on multi-layer LSTM networks, a forecasting method with a strong capability has been proposed for predicting highly fluctuating demand (Abbasimehr et al., 2020). According to the characteristics of chemical process data, a key alarm variables prediction model has been developed in chemical process based on dynamic-inner principal component analysis (DiPCA) and LSTM network (Bai et al., 2023). Adding self-attention mechanism after LSTM network can further capture the correlation between features directly from a global perspective (Zhang et al., 2020). Increasing attention mechanisms can also compensate for gradient disappearance or gradient explosion problems that LSTM networks face, which can lead to loss of information in time series data (Li J. et al., 2021). By integrating CNN, attention mechanism and LSTM, it is expected to build a network with better predictive performance.

Therefore, this article proposes a robust multi-layer network with excellent performance by integrating LSTM network with CNN network and adding self-attention mechanism technology. In order to extract and learn the period and trend characteristics of EMG signals, autoregressive processing is performed on the collected data. The CNN layer is used to extract the features from the EMG signal. The LSTM network is used to consolidate and enhance the historical temporal features. self-attention mechanism (SAM) is utilized to improve the global feature extraction performance and the parallel computing speed of the network. Finally, compared with the existing algorithm, the superiority and practicability of the proposed network are verified by using the data of healthy laboratory subjects and clinical patients with hemiplegia.

The main contributions of this article are as follows: (1) To address the periodicity of human lower limb gait walking, a multi-layer machine learning network architecture has been designed. It improves the interpretability and prediction accuracy of the auto-regression model, and reduces the problems of gradient disappearance or explosion caused by redundant sensor information. (2) The practicality of the algorithm has been validated, undergoing testing not only on healthy individuals but also utilizing data from hemiplegic patients. It has successfully achieved continuous lower limb motion estimation under non-ideal conditions (weak sEMG signals, muscle fatigue, high muscle tension, etc.). This ensures both accuracy and robustness in identification, laying a foundation for the design of human–machine interaction methods for future rehabilitation robots.

In order to facilitate understanding, the chapter part of this article is summarized as: a novel artificial intelligence algorithm is proposed in section "2 Materials and methods," the experiments and results are presented in section "3 Experiments and results," and finally main key conclusions of this article are given in section "4 Discussion and conclusion."

2 Materials and methods

2.1 Data acquisition and processing

Five subjects (age: 26.6 ± 2.6 years, height: 1.74 ± 0.08 m, weight: 69 ± 10.9 kg) and one patient tester (male, 67 years old, Brunnstrom stage IV) participated in the data collection of this experiment. The sEMG signal acquisition equipment is a Noraxon Ultium EMG system and AgCl electrodes, as shown in **Figure 1**. Alcohol wipes are used to wipe the surface skin of the tested muscles to remove impurities such as dead skin and sweat adhering to the skin surface. Two electrodes for each channel are spaced 20 mm apart and affixed to the muscle belly along the muscle fiber direction of the target muscles of both legs of the subjects (Hermens et al., 2000). Subjects walk on a treadmill at 2.0 km/h, 3 km/h, and 5.0 km/h and EMG signals are collected. Subjects walk for 3 min at a time with a 1-min rest between each trial to avoid the effects of muscle fatigue. The sEMG sampling frequency is 1,200 Hz, as shown in **Figure 2**, three muscles of the ankle joint, tibialis anterior, peroneus longus, and gastrocnemius are collected. Meanwhile, the kinematic parameters are collected using a Noraxon myoMOTION Inertial Measurement Unit (IMU), which collects the angular changes in the sagittal plane of the ankle joint of the lower limb, with a sampling frequency of 200 Hz. Written informed consent was signed by all subjects before inclusion in this study. The experimental procedures follow the Declaration of Helsinki and were approved by the Ethics Committee of Liaoning Provincial People's Hospital (Grant No. 2022HS007).

In this experiment, the ankle EMG input and output signals of five healthy individuals and one stroke patient are used as test and validation signals for the network model. Four sets of test data with a length of 120,000 are obtained from the left foot of the healthy tester under four states: 2 km/h speed, 3 km/h speed, 5 km/h speed, and plantarflexion dorsiflexion maneuver. Two tests are conducted on the left foot of the stroke patient and the length of the sampled data is taken as 70,000. Due to the large amount of noise signals in the original acquired sEMG signals, and the frequency range of sEMG signals are in the range of 0–500 Hz. In this article, the original sEMG signals are filtered and denoised, and then the irrelevant noises are removed from the original sEMG signals in order to retain the valuable information as much as possible. The sEMG signals are first band-pass filtered with a fourth-order 10–500 Hz Butterworth band-pass filter. Then, a 50 Hz trap filter is used to eliminate the industrial frequency interference. After that, the data used will be normalized.

FIGURE 1
Noraxon sEMG and inertial sensor acquisition system.

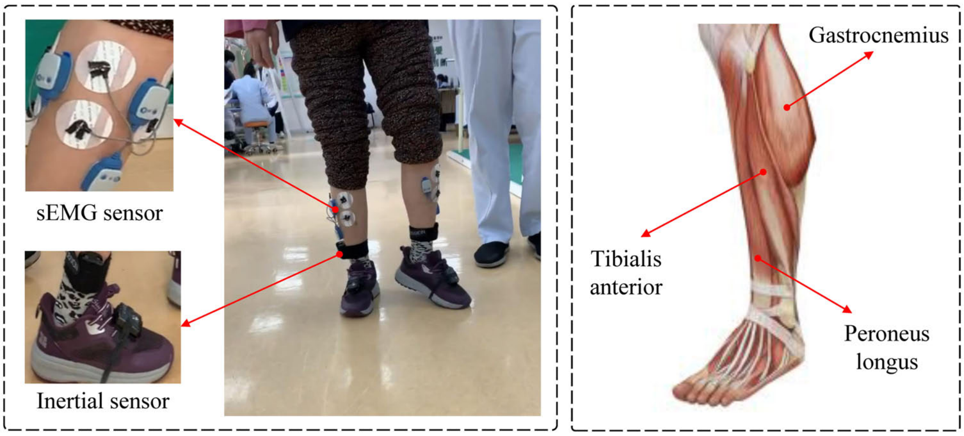

FIGURE 2
Setup of the EMG signal acquisition experiment.

2.2 CNN-LSTM networks with self-attention

2.2.1 Convolutional neural network

For the collected data, CNN uses convolution layer to convolve the input vector matrix to extract the local features of the time series data. The feature sequence generation equation is shown in Equation 1.

$$C_{hi} = f(W_h X_{i:i+h-1} + b) \tag{1}$$

where W_h is the weight matrix of the convolution kernel; b is biased unit; $X_{i:i+h-1}$ is the sequence matrix from i to $i+h-1$ in a time series; h is the size of the convolution kernel; f is the activation function.

The calculated feature set C_n can be expressed as Equation 2.

$$C_n = \{C_1, C_2, ..., C_{i+h-1}\} \tag{2}$$

The pooling layer extracts the features of the time series obtained by the convolution layer, outputs a matrix of fixed size, reduces the dimension of the output result and retains the features. In this article, the maximum pooling method is used to calculate the pooling layer. The computational equation of the eigenvector after the pooling of convolution nuclei is represented by Equation 3.

$$C_{pool} = Max(C_1, C_2, ..., C_{n-h+1}) \tag{3}$$

2.2.2 LSTM neural network

LSTM network is a variant of RNN. The key point of LSTM is to control the flow and forgetting of information through the use of structures called gates. The function of these gates is to selectively allow information to pass through or prevent the flow of information, and the core unit is the cell state, which can be regarded as the network's memory. The LSTM network consists of several key components.

1. Cell state: it is the main storage unit of LSTM and is responsible for storing and transmitting information.
2. Input gate: the input gate determines whether new information is added to the status unit at the current time step.
3. Forget gate: the forget gate determines what information is deleted from the state unit.

4. Output gate: the output gate determines which information in the state unit is output to the next time step. The relevant calculation formulas are shown as Equations 4–9.

$$I_t = \sigma(X_t W_{xi} + H_{t-1} W_{hi} + b_i) \tag{4}$$

$$F_t = \sigma(X_t W_{xf} + H_{t-1} W_{hf} + b_f) \tag{5}$$

$$O_t = \sigma(X_t W_{xo} + H_{t-1} W_{ho} + b_o) \tag{6}$$

$$\tilde{C}_t = tanh(X_t W_{xc} + H_{t-1} W_{hc} + b_c) \tag{7}$$

$$C_t = F_t \odot C_{t-1} + I_t \odot \tilde{C}_t \tag{8}$$

$$H_t = O_t \odot tanh(C_t) \tag{9}$$

The principle is to combine the current input X_t and the hidden state H_{t-1} of the previous time step, which are activated by sigmoid function respectively. Calculate the activation value I_t of the input gate; calculate the activation value F_t of the forgetting gate and O_t of the output gate; X_t and H_{t-1} are combined, and then activated by tanh function to selectively retain the current memory, which is recorded as $\tilde{C}_t$; the state C_{t-1} of the previous time step is selectively forgotten by using the forgetting gate F_t. The input gate I_t is used to selectively retain the current state $\tilde{C}_t$ of the time step, and the two are added together to update the state unit C_t. Multiply the new state unit C_t with the output gate O_t to get the hidden state H_t of the current time step.

2.2.3 Self-attention mechanism

Compared with conventional networks such as RNN and LSTM, which process the features of time series data with equal weight, self-attention can calculate the correlation degree between each time series data from a global perspective, and allocate different attention to different locations at the end to enhance the main features of time series data. The self-attention mechanism can flexibly adapt to different input sequences and task requirements. For time series $A = [a_1, a_2, ...a_n]$, the attention $B = [b_1, b_2, ...b_n]$ of each position is obtained by obtaining the correlation degree between the sequence data. The specific calculation process is as follows.

Each value of the sequence A maps to three different spaces. For each input a_i, multiply by three trainable weights w_q, w_k, and w_v, respectively, to obtain three values of q_i, k_i, and v_i, namely query, key, and value as shown in Equations 10–12.

$$q_i = w_q \cdot a_i \tag{10}$$

$$k_i = w_k \cdot a_i \tag{11}$$

$$v_i = w_v \cdot a_i \tag{12}$$

Using the weight matrices, W_q, W_k, and W_v, they can be further expressed in the following matrix form, as shown in Equations 13–15.

$$Q = W_q \cdot A \tag{13}$$

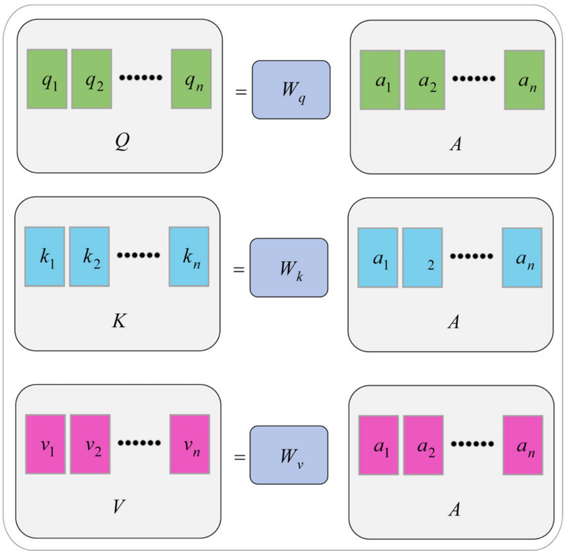

FIGURE 3
Generation of Q, K and V matrices.

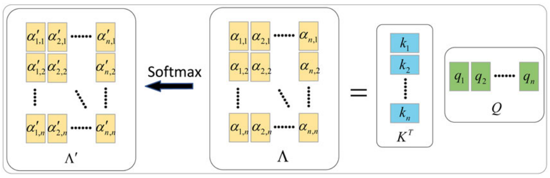

FIGURE 4
Generation of Λ and Λ'.

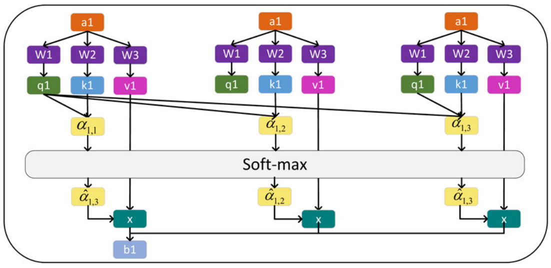

FIGURE 5
Generation of output matrix O.

$$K = W_K \cdot A \tag{14}$$

$$V = W_V \cdot A \tag{15}$$

The generation diagram of matrix Q, K, and V is shown in Figure 3.

With each input value $a_i (i = 1, ...n)$ corresponding to q_i, and all input values a_j corresponding to k_j, calculate the degree of correlation between a_i and a_j by dot product, as shown in Equation 16.

$$\delta_{i,j} = (k_i)^{\tau} \cdot q_j \tag{16}$$

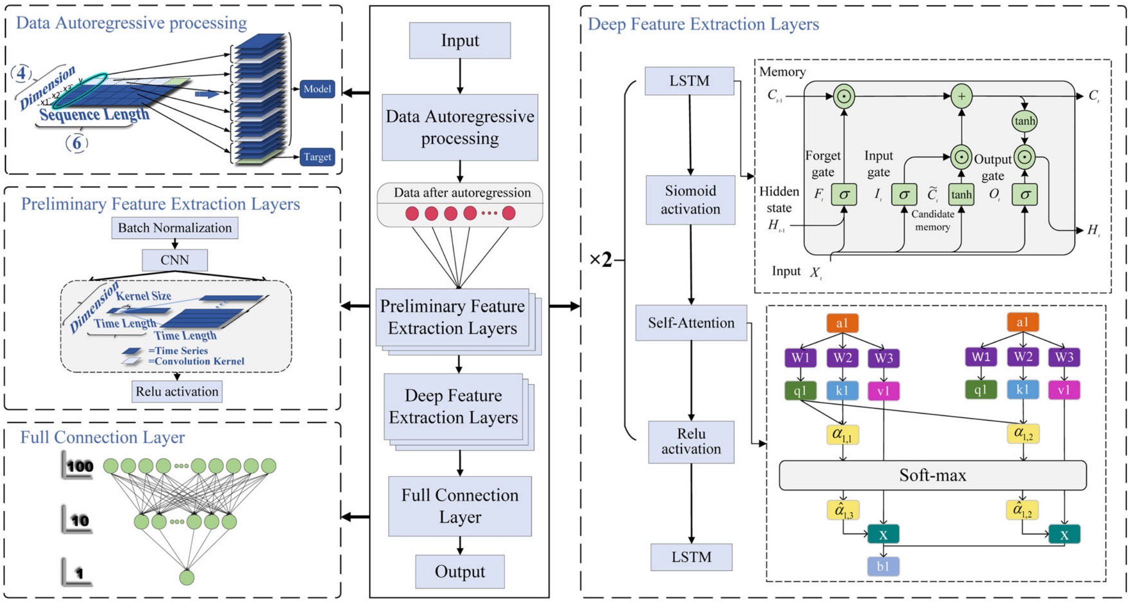

FIGURE 6
Proposed CNN-LSTM network model with self-attention mechanism.

Its matrix form is shown in Equation 17.

$$\Delta = K^T \cdot Q \tag{17}$$

Dividing $\delta_{i,j}$ by the dimension $\sqrt{d_k}$ of q_i or k_i can control the size of the dot product result to prevent situations where the gradient is too large or too small and leads to poor training results, as shown in Equation 18.

$$\alpha_{i,j} = \frac{\delta_{i,j}}{\sqrt{d_k}} \tag{18}$$

Its matrix form is shown in Equation 19.

$$\Lambda = \frac{\Delta}{\sqrt{d_k}} \tag{19}$$

The activated correlation matrix Λ' can be obtained by softmax operation on the correlation matrix Λ.

The calculation process is shown in Figure 4.

Use the resulting Λ' and V to calculate the attention corresponding to each input vector a_i as shown in Equation 20.

$$b_i = \sum\nolimits_{j=1}^{n} v_j \cdot \alpha'_{i,j} \tag{20}$$

Its matrix form can be expressed as Equation 21.

$$B = V \cdot \Lambda' \tag{21}$$

where B is the matrix of attention b_i.

The computational equation of the self-attention mechanism can be summarized as Equation 22.

$$Output = softmax(\frac{K^T Q}{\sqrt{d_k}})V \tag{22}$$

The calculation process of attention b_1 for the first input value a_1 is shown in Figure 5.

2.2.4 CNN-LSTM network

The proposed CNN-LSTM prediction model integrated with self-attention mechanism in this article is shown in Figure 6. The predictive network model mainly includes data autoregressive processing, preliminary feature extraction layer based on CNN network, depth feature extraction layer based on LSTM network, and full connection layer. Note that in practical engineering applications, the collected data should be cleaned reasonably, including removing singular values, averaging and noise elimination which can effectively improve the training and testing effect of the network. The time step of autoregression cannot be taken too long or too short. If the time step is taken too long, the less relevant time series information in the past may be added to the current information prediction, which may reduce the prediction accuracy. If the time step is taken too short, it may reduce the correlation extraction between continuous data. Therefore, in the practical application process, the regression time step should be selected according to the specific research object and sequence characteristics. When the network is used for online prediction or control, too many network layers may improve the prediction accuracy of the algorithm, but it may also increase the computing burden of the network.

2.2.4.1 Autoregressive processing

Surface electromyography has typical nonlinear and fast time-varying characteristics, and it is difficult to capture and extract the trend of sEMG by conventional fitting methods. In order to improve the periodicity, trend and seasonality of the output data, autoregressive processing should be carried out on the pre-training data.

2.2.4.2 Preliminary feature extraction layer

In order to make the input data after autoregressive processing easier to train, the batch normalization layer (BN layer) is used to

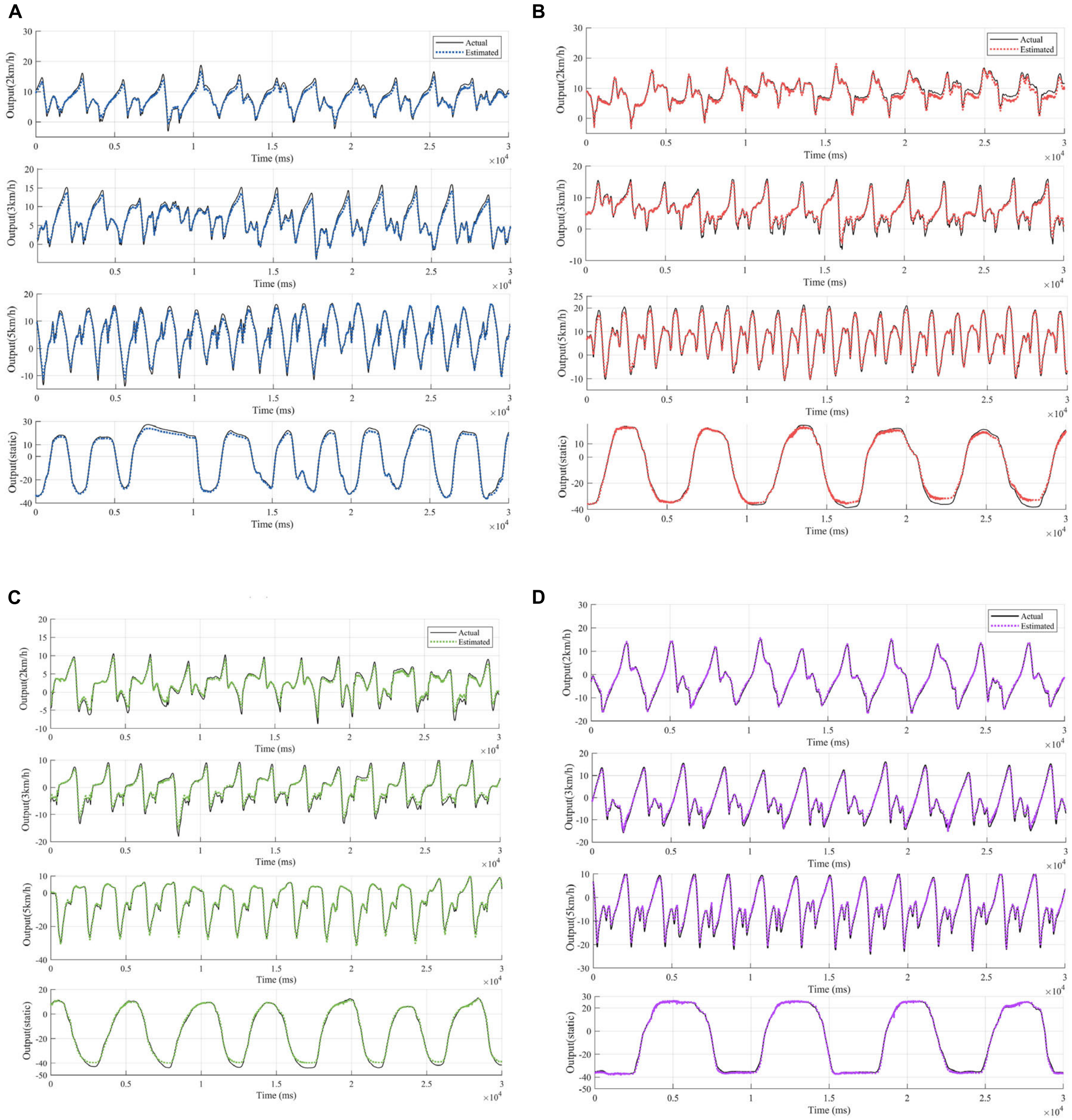

FIGURE 7
Fitted curves of ankle EMG signals at four exercise speeds in four healthy subjects. **(A)** Fitting results for subject 1. **(B)** Fitting results for subject 2. **(C)** Fitting results for subject 3. **(D)** Fitting results for subject 4.

normalize each batch. The normalized operation of the BN layer can not only improve the convergence speed of the network model, but also enhance the correlation degree between the data in the batch, and prevent the model from overtraining some data and resulting in overfitting. Then, the features of the time series are initially extracted by using CNN. The CNN can not only extract features through the convolution operation of multiple convolution kernels, but also obtain local dependencies of sequence data by convolution operation with sliding window. For the obtained features, the ReLU activation layer can be activated to enhance the expression ability of the features.

2.2.4.3 Depth feature extraction layer

The extracted features can be used to further extract the long-term dependencies in the time series data through the LSTM network. The data processed by the LSTM layer enters the Sigmoid layer for activation. Then, the self-attention mechanism is added to calculate the correlation between all features and the weight matrix, and the weight matrix is constantly trained, so that the model can allocate attention independently according to the data characteristics, and improve the role of features in prediction. Finally, the ReLU activation layer is used to activate the features. After the above two deep feature extraction, the obtained deep features are fed into the LSTM layer for comprehensive strengthening and consolidation.

2.2.4.4 Fully connected layer

The features obtained from the depth feature extraction layer are mapped to the fully connected layer to obtain the prediction results. In order to make the model have stronger generalization

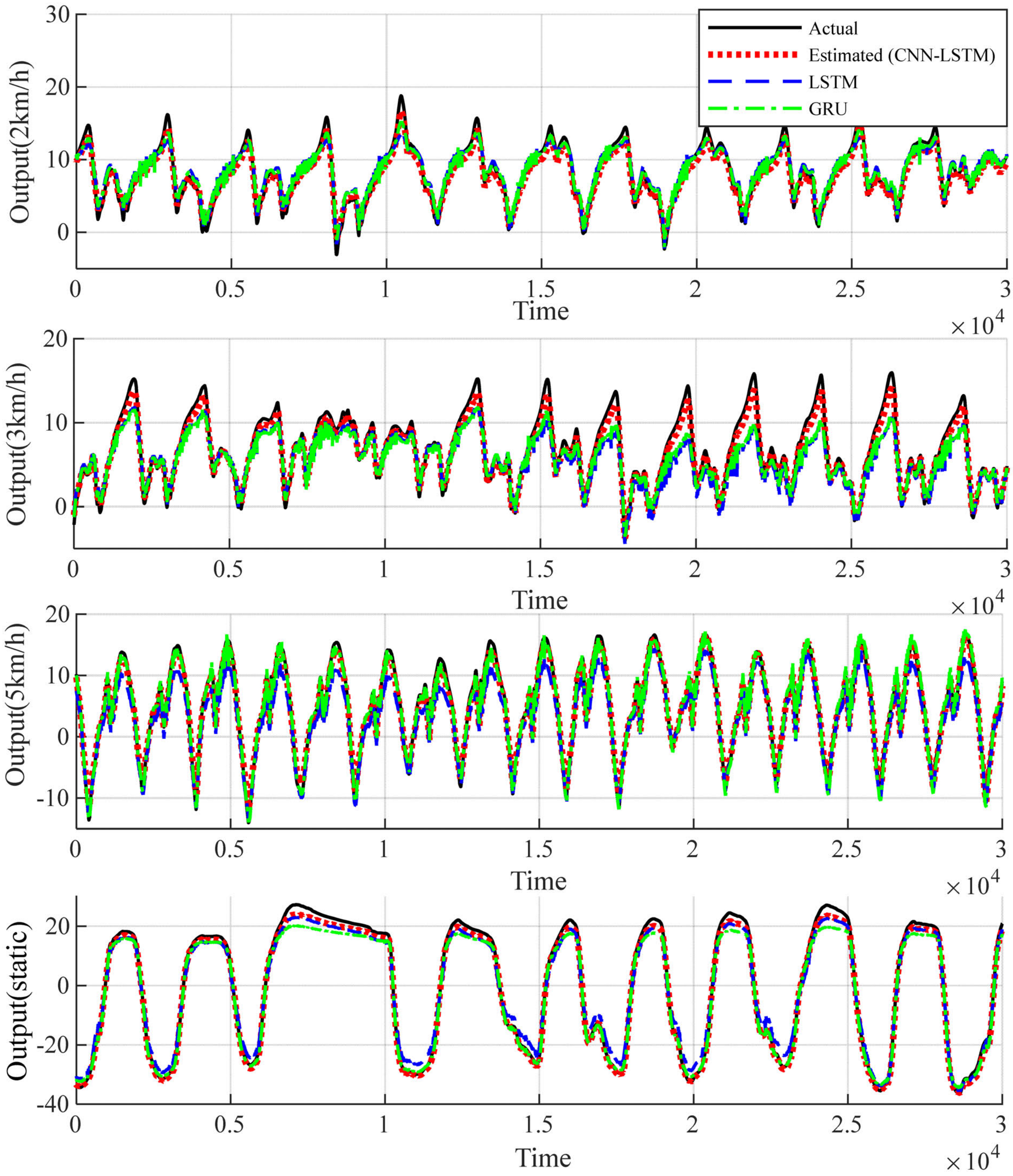

FIGURE 8
Comparison of the fitting results of the proposed algorithm for healthy subject 1 with the experimental results of the existing algorithm.

ability and avoid the problem of gradient vanishing or gradient explosion, the network proposed in this article adopts the strategy of gradually decreasing the number of neurons, and uses two linear mapping layers in the fully connected layer to continuously reduce the number of neurons, and obtains the single-valued prediction result. In addition, adding the intermediate mapping layer can also enable the model to learn more feature combinations and representations.

3 Experiments and results

3.1 Performance evaluation

The R^2 score and Root Mean Square Error (*RMSE*) are commonly used as evaluation metrics of regression performance for continuous estimation of joint angles (Zhong et al., 2022). In order to obtain more accurate continuous estimation results

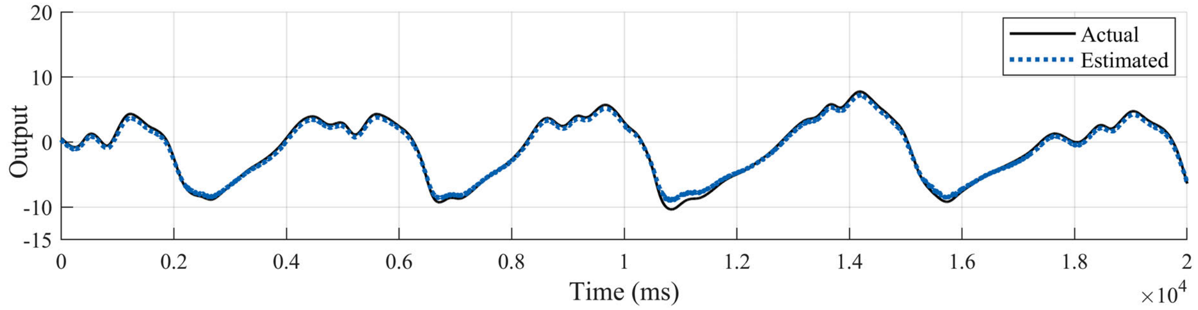

FIGURE 9
Fitted curves of EMG signals of the healthy ankle from the first set of data of the diseased test subjects.

TABLE 1 Comparison of MSE based on training data.

	Healthy (group 1)	Healthy (group 2)	Healthy (group 3)	Healthy (group 4)	Patient (group 1)
2 km/h	0.7412	0.6723	0.5221	0.2811	0.2362
3 km/h	0.5030	0.6530	0.9210	0.6909	\
5 km/h	0.6857	0.6110	0.6741	0.6267	\
Static	2.4677	3.7219	3.1074	1.0042	\

for the lower extremity joints, the regression performance of the lower extremity hip, knee, and ankle joints is evaluated using the following R^2 performance metrics. R^2 and *RMSE* are defined as shown in **Equations 23**, **24**, respectively:

$$R^2 = 1 - \frac{\sum_{i=1}^{n} (\theta_i - \widehat{\theta}_i)^2}{\sum_{i=1}^{n} (\theta_i - \overline{\theta})^2} \in [0, 1] \tag{23}$$

$$RMSE = \sqrt{\frac{\sum_{i=1}^{n} \left(\theta_i - \widehat{\theta}_i\right)^2}{n}} \tag{24}$$

where θ_i is the actual value of the angle of the target joint, $\widehat{\theta}_i$ is the angle of the joint predicted by the model, $\overline{\theta}$ is the average value of the actual angle θ_i, and n is the length of the sampling sequence. In addition, we perform a statistical analysis using one-way analysis of variance (ANOVA) under the 0.05 level of significance.

3.2 Result and discussion

Since each healthy person has 4 test states, 5 healthy people contain 20 sets of test data. The patients contain 2 sets of test data. Considering that the output signals are characterized by obvious periodicity, trend and seasonality, autoregressive processing is performed on the test data in order to highlight the characteristics of the output data for the training of the proposed network model. According to the length of the data sequence, the data of the first 4 healthy subjects, which is the first 90,000 points of the 16 sets of data with the first 50,000 points of the first set of data of the patients are taken respectively. The time step of autoregression is chosen as 5, which is the input and output data at the moment of t−1, t−2,......t−5 and the input data at the moment of t are used simultaneously for the prediction of the output data at the moment of t. In the experimental process, for the proposed network, one layer CNN is set for initial feature extraction. A two-layer LSTM network with SAM followed by one-layer LSTM is used for depth feature extraction. Three full connection layers is applied to obtain the predicted output. Adam is used as an optimizer to determine the optimal solution of the loss function. The parameter setting strategy of the network not only ensures that the network captures data characteristics efficiently, but also does not have too much computational burden. Since the data input dimension is 3 and the output dimension is 1, the data before combination is a vector of 6 rows and 4 columns. The data after regression combination is transformed into a vector of 1 row and 24 columns, where the data in the first 23 columns are treated as input data to the model, and the data in the last 1 column is the output data corresponding to the current t moment. Combined with the time dimension, the length of the time series is 1,490,000. The first 23 columns of data are input into the model to obtain the predicted value y of the model, and the loss value is calculated for the predicted value and the 24th column of output data in order to update the parameters of the network model and complete the learning and training of the model. Using the trained model, predictions are made for the posterior 30,000 points of data for the first 4 health testers, and for the posterior 20,000 points of data for patient group 1. The test results for the four groups of health testers are shown in **Figure 7**. In order to highlight the superiority, the existing prediction LSTM algorithm in Dong et al. (2023) and the algorithm in Zhou et al. (2022) are also tested for prediction healthy subject 1 in **Figure 8**. Comparison and verification results show that the proposed prediction algorithm has better prediction accuracy and robustness. The results for patient group 1 are shown in **Figure 9**. The results show that the proposed method has good tracking performance for lower limb motion angle prediction.

The results of the MSE comparison between the predicted data and the real data for the different exercise modes are shown in **Table 1**. It can be seen from the table that the MSE errors in the

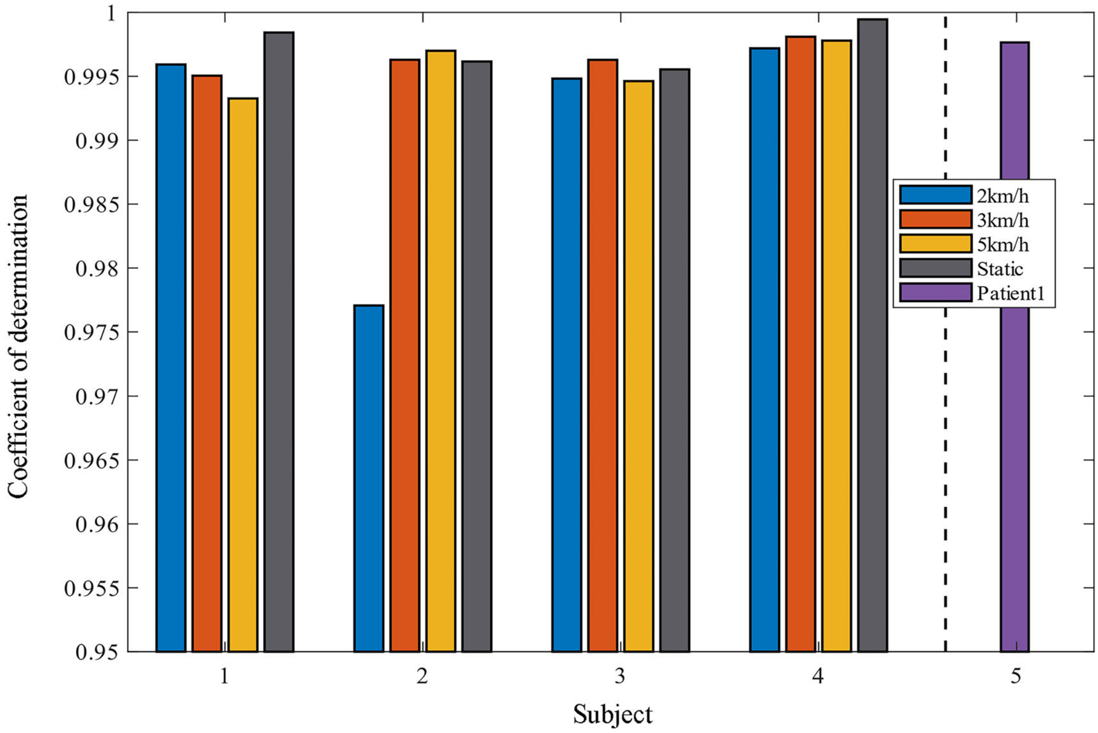

FIGURE 10
Histogram of the coefficient of determination of projected versus real data.

walking condition are small and within 1° for both healthy and diseased subjects. The static metatarsal dorsiflexion exercise had an MSE within 5° due to the wider angular range of the exercise. R^2 can be used as a better criterion for use in this study as the error range of MSE fluctuates due to the different angular ranges of motion of different subjects in different modes of motion.

3.2.1 Effects of different exercise modes

The ankle angle prediction curves for the four movement speeds of the testers are shown in Figures 7, 9. Not only the tracking deviation between the estimated angle and the target angle of healthy subjects is small in the CNN-LSTM model, but the model also shows good regression performance for the ankle motion of diseased testers. It can be seen that our proposed multilayer CNN-LSTM network model incorporating the self-attention mechanism has good tracking performance and high prediction accuracy.

Two indicators, *RMSE* and R^2 are used to evaluate the quality of the method in predicting the ankle joint angle. Comparison of the coefficient of determination between the predicted data and the real data under different motion modes is shown in Figures 10, 11, and it can be seen that most of the coefficients of determination are above 0.99, which means that the predicted data of the model have a better correlation with the real data, and they can reflect the dynamic characteristics of the system very well. It should be noted that the movement of the tester at 2 km/h belong to slow movement. Due to the difference in height and weight, in this case, the lower limbs of the test subjects cannot be fully moved, resulting in different EMG signals for each test subject. The test results in Figure 7 also show that the prediction error is larger under the motion state of 2 km/h. Therefore, the error band for 2 km/h is larger in Figure 11. When the walking speed is increased to 3 km/h, it is closer to the natural walking speed of the human body, the human gait is more natural, the muscle coordination is stable and flexible, and the prediction performance will be improved. However, when the walking speed increases to 5 km/h, which is faster than the human walking speed, the accuracy starts to decrease. This indicates that the closer the walking speed is to the normal walking speed of human body, the better the muscle

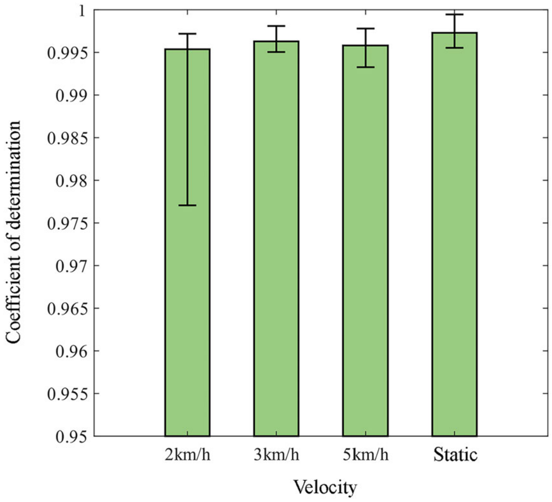

FIGURE 11
Comparison of the coefficient of determination between predicted and real data for different exercise modes.

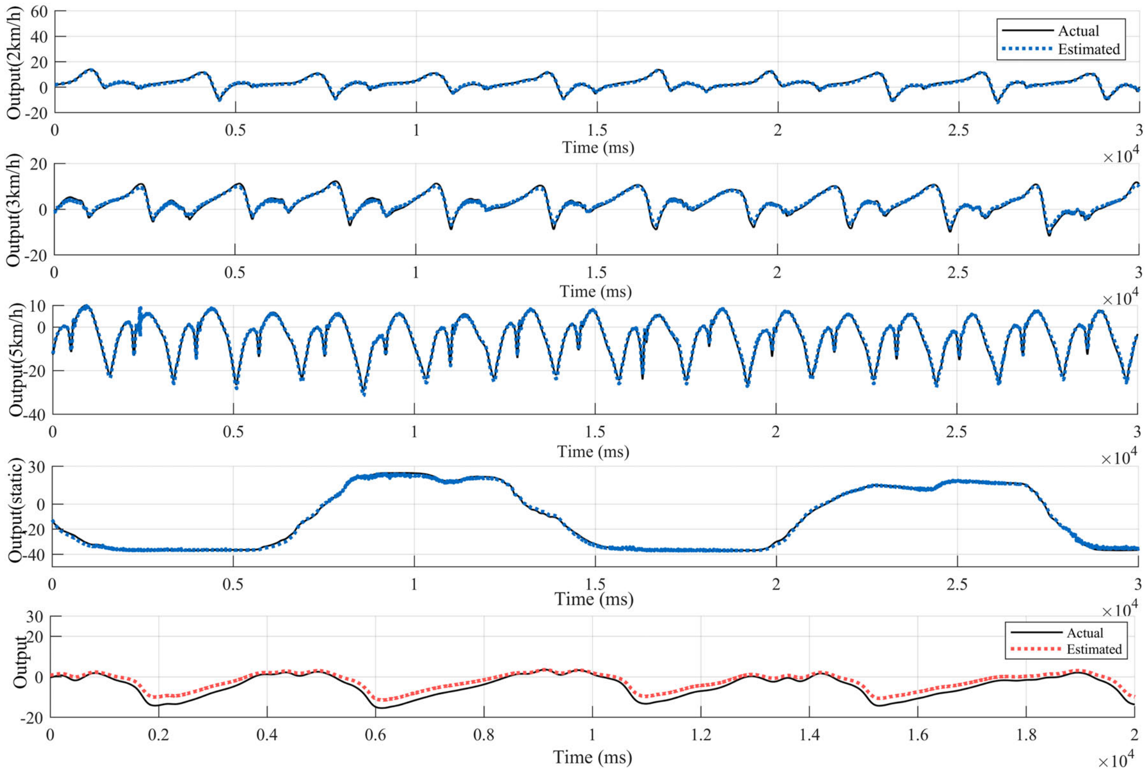

FIGURE 12
Cross-validation of ankle EMG signal fitting curves for the fifth healthy tester and the second set of data from the diseased tester.

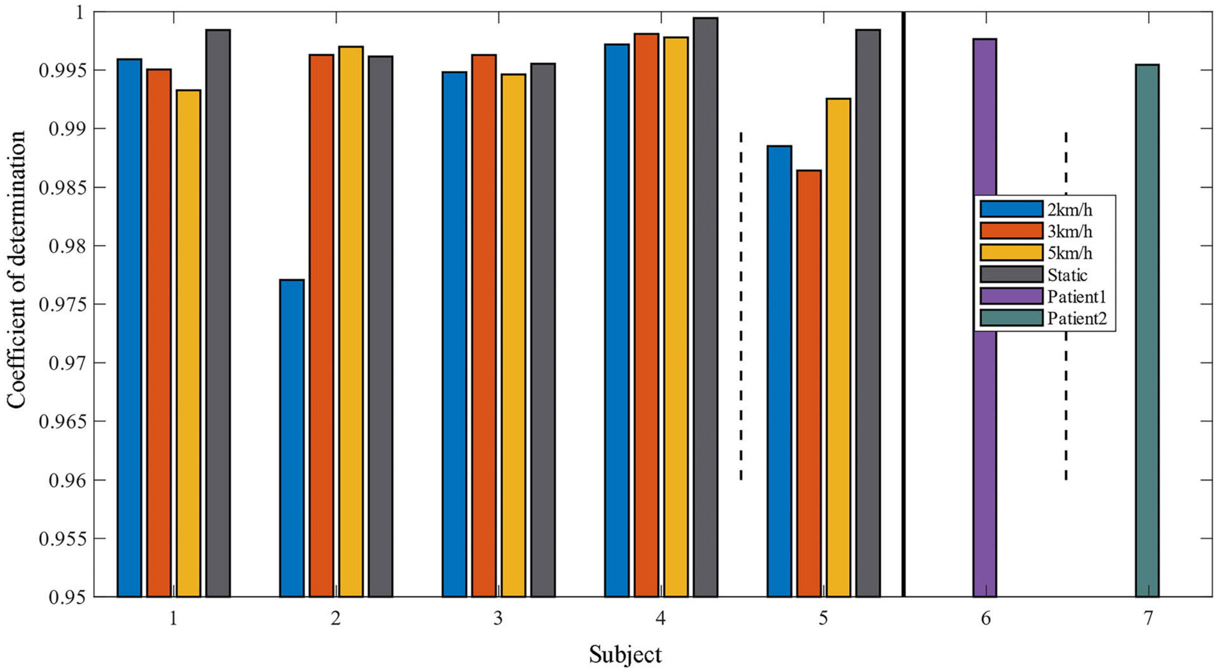

FIGURE 13
Comparison of determination coefficients between prediction and cross-validation data.

coordination of the lower limbs is; when it is faster or slower than the normal walking speed of human body, the muscles of the lower limbs are in a situation of insufficient coordination or fatigue, which is contrary to the normal pattern, and the prediction results of the model will decline more and more, which is in line with the normal walking law. For the static plantarflexion

TABLE 2 Comparison of MSE based on test data.

2 km/h (healthy group 5)	3 km/h (healthy group 5)	5 km/h (healthy group 5)	Static (healthy group 5)	Left foot (patient group 2)
0.2728	0.6909	0.6267	1.0042	6.0589

state, the model predicted the best results, which may be due to the fact that there is no floor force contact with the ankle plantar dorsiflexion in the static state, which reduces the complex interactions between the foot and the ground or the influence of shoes.

3.2.2 Effects between healthy and patient subjects

The MSE values of healthy subjects and patients under walking exercise showed significant differences. Since people with weak abilities are also prone to problems such as muscle fatigue or even cramps, and in some cases there are factors such as high muscle tone, this study can further explore the reasons for these differences, such as physical fitness differences, testing conditions, and health status. It helps to understand the differences in physiological responses between healthy and sick subjects at different exercise intensities. As shown in Table 1 the MSE values of sick subjects are generally lower than those of healthy subjects, which suggests that there are some differences between the results of sick testers and the expected values in these particular exercises.

3.2.3 Effects of model-oriented motor characteristics of healthy and patient subjects

For patients with lower limb motor dysfunction, there is usually a more severe motor deficit on the affected side, whereas the functional decline is usually weaker on the healthy side. As a result, the sEMG signals we acquire often alternate between useful and useless information, which can lead to problems such as gradient vanishing or gradient explosion, causing loss of information. In addition, these dysfunctional people are prone to problems such as muscle fatigue and even spasticity. The angles of their lower limb movements are more complicated and abnormal. Therefore, extracting the relationship between sEMG signals and movement trajectories under the above more complicated and non-ideal factors is a challenging problem.

In order to verify the generalization performance of our proposed model and the motion estimation performance for subjects with lower limb motor dysfunction, we input the second set of untrained data from the fifth healthy and diseased participants into the model for ankle joint angle prediction. The results are shown in Figure 12. For healthy subject 5, who is not included in the trained dataset, sEMG and corresponding movement angles are measured at different movement speeds (2 km/h, 3 km/h, 5 km/h) and static plantarflexion and dorsiflexion movement states. The results in Figure 13 indicate that, in comparison with subjects 1–4, the predicted R for the walking angle of healthy subject 5 without model training is slightly lower but still greater than 0.985. However, with $p > 0.05$, the difference is not statistically significant. This confirms that the model exhibits good prediction performance for data from subjects not included in the training set. For patient subject 2, the $R > 0.99$ for the untrained data on the affected side demonstrates the effectiveness of our proposed model in predicting angles on the affected side. However, as indicated in Table 2, the MSE value is higher compared to the training data, reaching 6.0589. This may be attributed to the extensive angle fluctuation in the late stages of exercise due to muscle spasm or fatigue in diseased subjects. Consequently, the MSE value of the prediction exhibits a substantial error compared to that of the training data.

By estimating the lower limb motion for subjects other than the training data, it can be seen that our proposed method not only has better model generalization ability, but also can predict the lower limb motion angle of the patient in a more ideal way. This helps to identify the physiological differences between healthy individuals and patients in specific movement states or static states. Further analysis can try to identify the physiological or medical factors that lead to these differences, which has potential applications for disease diagnosis, treatment, or health status assessment.

4 Discussion and conclusion

In this article, a multilayer CNN-LSTM prediction network model incorporating a self-attention mechanism is proposed. In order to validate the performance of the model in predictive tracking of ankle joint mobility for different populations. The remaining data of both healthy and patient subjects are treated as test data and inputted into the model, and the prediction results of different motion states for the fused model are compared. The results show that most of the model's prediction $R > 0.9$ for different motion states of healthy subjects; in the experiments oriented to the motion characteristics of patient subjects, the angle prediction results of $R > 0.99$ for the untrained data on the affected side, which proves that our proposed model also has a better effect on the angle prediction of the affected side. Therefore, the model we propose in this article not only has a good exercise estimation ability for healthy subjects, but also can be used for exercise estimation of lower limb dysfunction, which helps to understand the differences in physiological responses between healthy and patients under different exercise modalities, and further analysis can try to find out the physiological or medical factors that lead to these differences, which can then be used for the evaluation of rehabilitation efficacy oriented to clinical patients. The main merits of the proposed method include that the design network architecture has been designed and improves the interpretability and prediction accuracy of the auto-regression model, and reduces the problems of gradient disappearance or explosion caused by redundant sensor information.

Electromyogram neural information collected from the human body provides a new idea for human–robot interaction, and this study provides a feasible solution for accurately estimating the ankle angle of the lower extremity in both health and patients. Future work can be applied to the control of exoskeleton robots, clinical rehabilitation training and evaluation. However, this study also has some limitations. Since patients with post-stroke hemiparesis are virtually unable to perform lower limb walking movements in Brunnstrom stage I and II, our experiment was only able to estimate movements for patients in stage III and above. Subsequently, we will expand the number and range of subjects and explore multi-sensor fusion methods to enhance the reliability of the model.

Data availability statement

The raw data supporting the conclusions of this article will be made available by the authors, without undue reservation.

Ethics statement

The studies involving humans were approved by the Ethics Committee of Liaoning Provincial People's Hospital. The studies were conducted in accordance with the local legislation and institutional requirements. The participants provided their written informed consent to participate in this study. Written informed consent was obtained from the individual(s) for the publication of any potentially identifiable images or data included in this article.

Author contributions

LL: Conceptualization, Investigation, Methodology, Validation, Writing – original draft. JF: Data curation, Formal analysis, Software, Writing – original draft. JL: Conceptualization, Methodology, Validation, Writing – review & editing. WC: Data curation, Formal analysis, Software, Writing – original draft. ZM: Funding acquisition, Project administration, Resources, Writing – review & editing. XT: Funding acquisition, Project administration, Resources, Writing – review & editing.

Funding

The author(s) declare financial support was received for the research, authorship, and/or publication of this article. This work was partly supported by the National Natural Science Foundation of China under grant numbers 62333007, 62103406, and U22A2067, and supported by the Applied Basic Research Program Project of Liaoning Province under grant number 2022JH2/101300102.

Conflict of interest

The authors declare that the research was conducted in the absence of any commercial or financial relationships that could be construed as a potential conflict of interest.

Publisher's note

References

Abbasimehr, H., Shabani, M., and Yousefi, M. (2020). An optimized model using LSTM network for demand forecasting. *Comput. Indust. Eng.* 143:106435.

Abdulnabi, A. H., Wang, G., Lu, J., and Jia, K. (2015). Multi-task CNN model for attribute prediction. *IEEE Trans. Multimedia* 17, 1949–1959.

Aymard, C., Katz, R., Lafitte, C., Lo, E., Pénicaud, A., Pradat-Diehl, P., et al. (2000). Presynaptic inhibition and homosynaptic depression: A comparison between lower and upper limbs in normal human subjects and patients with hemiplegia. *Brain* 123(Pt 8), 1688–1702. doi: 10.1093/brain/123.8.1688

Bai, Y., Xiang, S., Cheng, F., and Zhao, J. (2023). A dynamic-inner LSTM prediction method for key alarm variables forecasting in chemical process. *Chin. J. Chem. Eng.* 55, 266–276.

Bi, J., Zhang, X., Yuan, H., Zhang, J., and Zhou, M. A. (2021). Hybrid prediction method for realistic network traffic with temporal convolutional network and LSTM. *IEEE Trans. Autom. Sci. Eng.* 19, 1869–1879.

Dong, S., Zhang, Y., and Zhou, X. (2023). Intelligent hybrid modeling of complex leaching system based on LSTM neural network. *Systems* 11:78.

Fleming, A., Stafford, N., Huang, S., Hu, X., Ferris, D., and Huang, H. (2021). Myoelectric control of robotic lower limb prostheses: A review of electromyography interfaces, control paradigms, challenges and future directions. *J. Neural Eng.* 18:10.1088/1741-2552/ac1176. doi: 10.1088/1741-2552/ac1176.

Gu, J., Wang, Z., Kuen, J., Ma, L., Shahroudy, A., Shuai, B., et al. (2018). Recent advances in convolutional neural networks. *Pattern Recogn.* 77, 354–377.

Hermens, H., Freriks, B., Disselhorst-Klug, C., and Rau, G. (2000). Development of recommendations for SEMG sensors and sensor placement procedures. *J. Electromyogr. Kinesiol.* 10, 361–374. doi: 10.1016/s1050-6411(00)00027-4

Kapelner, T., Sartori, M., Negro, F., and Farina, D. (2020). Neuro-musculoskeletal mapping for man-machine interfacing. *Sci. Rep.* 10:5834. doi: 10.1038/s41598-020-62773-7

Khan, Z. Y., and Niu, Z. (2021). CNN with depthwise separable convolutions and combined kernels for rating prediction. *Expert Syst. Appl.* 170: 114528.

Khashei, M., Bijari, M., and Ardali, G. A. R. (2012). Hybridization of autoregressive integrated moving average (ARIMA) with probabilistic neural networks (PNNs). *Comput. Indust. Eng.* 63, 37–45.

Kim, T. Y., and Cho, S. B. (2019). Predicting residential energy consumption using CNN-LSTM neural networks. *Energy* 182, 72–81.

Lehtokangas, M., Saarinen, J., Huuhtanen, P., and Kaski, K. (1996). Predictive minimum description length criterion for time series modeling with neural networks. *Neural Comput.* 8, 583–593. doi: 10.1162/neco.1996.8.3.583

Li, J., Wang, X., Tu, Z., and Lyu, M. R. (2021). On the diversity of multi-head attention. *Neurocomputing* 454, 14–24.

Li, Y., Hao, Z., and Lei, H. (2016). Survey of convolutional neural network. *J. Comput. Appl.* 36:2508.

Li, Z., Liu, F., Yang, W., Peng, S., and Zhou, J. (2021). A survey of convolutional neural networks: Analysis, applications, and prospects. *IEEE Trans. Neural Netw. Learn. Syst.* 33, 6999–7019.

Ma, C., Guo, W., Zhang, H., Williams Samuel, O., Xiaopeng, J., Xu, L., et al. (2021). A novel and efficient feature extraction method for deep learning based continuous estimation. *IEEE Robot. Autom. Lett.* 6, 7341–7348. doi: 10.1109/TUFFC.2024.3350033

Meng, L., Zhang, T., Zhao, X., Wang, D., Xu, R., Yang, A., et al. (2023). A quantitative lower limb function assessment method based on fusion of surface EMG and inertial data in stroke patients during cycling task. *Biomed. Signal Process. Control* 85: 104880.

Moniri, A., Terracina, D., Rodriguez-Manzano, J., Strutton, P., and Georgiou, P. (2021). Real-time forecasting of sEMG features for trunk muscle fatigue using machine learning. *IEEE Trans. Biomed. Eng.* 68, 718–727. doi: 10.1109/TBME.2020.3012783

Ng, B. C., Darus, I. Z. M., Jamaluddin, H., and Kamar, H. M. (2014). Dynamic modelling of an automotive variable speed air conditioning system using nonlinear autoregressive exogenous neural networks. *Appl. Thermal Eng.* 73, 1255–1269.

Phan, H., Andreotti, F., Cooray, N., Chén, O. Y., and De Vos, M. (2018). Joint classification and prediction CNN framework for automatic sleep stage classification. *IEEE Trans. Biomed. Eng.* 66, 1285–1296. doi: 10.1109/TBME.2018.2872652

Qi, S., Wu, X., Chen, W. H., Liu, J., Zhang, J., and Wang, J. (2020). sEMG-based recognition of composite motion with convolutional neural network. *Sens. Actuators A Phys.* 311:112046. doi: 10.1109/JBHI.2022.3179630

Rathore, M. S., and Harsha, S. P. (2022). An attention-based stacked BiLSTM framework for predicting remaining useful life of rolling bearings. *Appl. Soft Comput.* 131:109765.

Sarasola-Sanz, A., Irastorza-Landa, N., López-Larraz, E., Shiman, F., Spüler, M., Birbaumer, N., et al. (2018). Design and effectiveness evaluation of mirror myoelectric interfaces: A novel method to restore movement in hemiplegic patients. *Sci. Rep.* 8:16688. doi: 10.1038/s41598-018-34785-x

Shao, Q. Y., Zhang, Y., Liu, J., Sun, Z., and Dong, S. (2024). Investigation of flexible graphene hybrid knitted sensor for joint motion recognition based on convolutional neural network fusion long short-term memory network. *J. Indust. Textiles* 54:15280837231225827.

Taskaya-Temizel, T., and Casey, M. C. (2005). A comparative study of autoregressive neural network hybrids. *Neural Netw.* 18, 781–789.

Xiong, D., Zhang, D., Zhao, X., Chu, Y., and Zhao, Y. (2021). Synergy-based neural interface for human gait tracking with deep learning. *IEEE Trans. Neural Syst. Rehabil. Eng.* 29, 2271–2280. doi: 10.1109/TNSRE.2021.3123630

Yin, H., Safikhani, A., and Michailidis, G. (2023). A general modeling framework for network autoregressive processes. *Technometrics* 65, 579–589.

Zha, W., Liu, Y., Wan, Y., Luo, R., Li, D., Yang, S., et al. (2022). Forecasting monthly gas field production based on the CNN-LSTM model. *Energy* 260:124889.

Zhai, X., Jelfs, B., Chan, R., and Tin, C. (2017). Self-recalibrating surface EMG pattern recognition for neuroprosthesis control based on convolutional neural network. *Front. Neurosci.* 11:379. doi: 10.3389/fnins.2017.00379

Zhang, L., Li, Z., Hu, Y., Smith, C., Gutierrez-Farewik, E., and Wang, R. (2021). Ankle joint torque estimation using an EMG-driven neuromusculoskeletal model and an artificial neural network model. *IEEE Trans. Autom. Sci. Eng.* 18, 564–573.

Zhang, N., Shen, S. L., Zhou, A., and Jin, Y. F. (2021). Application of LSTM approach for modelling stress–strain behaviour of soil. *Appl. Soft Comput.* 100:106959.

Zhang, X., Li, H., Dong, R., Lu, Z., and Li, C. (2022). Electroencephalogram and surface electromyogram fusion-based precise detection of lower limb voluntary movement using convolution neural network-long short-term memory model. *Front. Neurosci.* 16:954387. doi: 10.3389/fnins.2022.954387

Zhang, X., Tang, X., Zhu, X., Gao, X., Chen, X., and Chen, X. (2019). A regression-based framework for quantitative assessment of muscle spasticity using combined EMG and inertial data from wearable sensors. *Front. Neurosci.* 13:398. doi: 10.3389/fnins.2019.00398

Zhang, Y., Xu, B., and Zhao, T. (2020). Convolutional multi-head self-attention on memory for aspect sentiment classification. *IEEE/CAA J. Autom. Sin.* 7, 1038–1044.

Zhao, H., Xu, H., Wang, Z., Wang, L., Qiu, S., Peng, D., et al. (2023). Analysis and evaluation of hemiplegic gait based on wearable sensor network. *Inform. Fusion* 90, 382–391.

Zhong, W., Fu, X., and Zhang, M. (2022). A muscle synergy-driven ANFIS approach to predict continuous knee joint movement. *IEEE Trans. Fuzzy Syst.* 30, 1553–1563.

Zhou, J., Qin, Y., Chen, D., Liu, F., and Qian, Q. (2022). Remaining useful life prediction of bearings by a new reinforced memory GRU network. *Adv. Eng. Inform.* 53:101682.

Zhu, B., Zhang, D., Chu, Y., Gu, Y., and Zhao, X. (2022). SeNic: An open source dataset for sEMG-based gesture recognition in non-ideal conditions. *IEEE Trans. Neural Syst. Rehabil. Eng.* 30, 1252–1260. doi: 10.1109/TNSRE.2022.3173708

frontiers | Frontiers in Neuroscience

TYPE Original Research
PUBLISHED 12 April 2024
DOI 10.3389/fnins.2024.1364409

MF-Net: multi-scale feature extraction-integration network for unsupervised deformable registration

Andi Li[1,2,3], Yuhan Ying[1,2,3], Tian Gao[1,2,4], Lei Zhang[5], Xingang Zhao[1,2], Yiwen Zhao[1,2], Guoli Song[1,2] and He Zhang[6]*

[1]State Key Laboratory of Robotics, Shenyang Institute of Automation, Chinese Academy of Sciences, Shenyang, China, [2]Institutes for Robotics and Intelligent Manufacturing, Chinese Academy of Sciences, Shenyang, China, [3]University of Chinese Academy of Sciences, Beijing, China, [4]School of Automation and Electrical Engineering, Shenyang Ligong University, Shenyang, China, [5]Spine Surgery Unit, Shengjing Hospital of China Medical University, Shenyang, China, [6]Orthopedic Department, The Second Affiliated Hospital of Chongqing Medical University, Chongqing, China

OPEN ACCESS

EDITED BY
Benyan Huo,
Zhengzhou University, China

REVIEWED BY
Yanding Qin,
Nankai University, China
Weihong Ren,
Harbin Institute of Technology, China

*CORRESPONDENCE
He Zhang
✉ orthobot85@gmail.com

RECEIVED 02 January 2024
ACCEPTED 20 March 2024
PUBLISHED 12 April 2024

CITATION
Li A, Ying Y, Gao T, Zhang L, Zhao X, Zhao Y, Song G and Zhang H (2024) MF-Net: multi-scale feature extraction-integration network for unsupervised deformable registration.
Front. Neurosci. 18:1364409.
doi: 10.3389/fnins.2024.1364409

Deformable registration plays a fundamental and crucial role in scenarios such as surgical navigation and image-assisted analysis. While deformable registration methods based on unsupervised learning have shown remarkable success in predicting displacement fields with high accuracy, many existing registration networks are limited by the lack of multi-scale analysis, restricting comprehensive utilization of global and local features in the images. To address this limitation, we propose a novel registration network called multi-scale feature extraction-integration network (MF-Net). First, we propose a multiscale analysis strategy that enables the model to capture global and local semantic information in the image, thus facilitating accurate texture and detail registration. Additionally, we introduce grouped gated inception block (GI-Block) as the basic unit of the feature extractor, enabling the feature extractor to selectively extract quantitative features from images at various resolutions. Comparative experiments demonstrate the superior accuracy of our approach over existing methods.

KEYWORDS

deformable image registration, unsupervised learning, convolutional neural network, multi-scale, gating mechanism

1 Introduction

Deformable image registration involves obtaining non-rigid spatial transformations from a moving image to a fixed image, representing a crucial step in tasks such as surgical navigation and image-assisted analysis (Nakajima et al., 2020; Drakopoulos et al., 2021; Geng et al., 2024). For instance, Drakopoulos et al. (2021) introduced the deformable registration method into the AR neuro-navigation system to assist brain tumor resection in functional areas of the brain. Geng et al. (2024) used deformable registration to obtain brain templates for Chinese babies, which can be used for investigating neural biomarkers for neurological and neurodevelopmental disorders in Chinese populations. The significance of deformable registration in influencing the outcomes of these tasks cannot be overstated, as it plays a crucial role in ensuring their success.

Learning-based methods for deformable registration involve modeling the registration process as a neural network. This approach entails iteratively optimizing the network parameters across the entire dataset to obtain a shared registration function. Learning-based registration can be categorized into supervised and unsupervised learning methods.

Supervised learning registration uses the true spatial transformations as labels, wherein neural networks are utilized to learn the spatial relationships between moving and fixed images. Obtaining these labels through manual annotation is impractical; hence, they are commonly obtained through traditional algorithms (Cao et al., 2017, 2018; Yang et al., 2017). For instance, Yang et al. (2017) proposed a Large Deformation Diffeomorphic Metric Mapping (LDDMM) model to register brain MR scans by using results from optimizing the LDDMM shooting formulation as labels. Cao et al. (2018) used the SyN algorithm (Avants et al., 2008) and Demons algorithm (Vercauteren et al., 2009; Lorenzi et al., 2013) to obtain displacement fields as labels for training the model, resulting in a model for aligning brain MR scans. However, this method for obtaining labels has limitations. Specifically, the use of traditional algorithms can potentially constrain the model's performance due to the accuracy limitations inherent in these algorithms. Consequently, the performance of supervised registration is limited by the restrictions of label acquisition.

Due to the limitation of supervised registration, current research has shifted toward unsupervised registration. These models incorporate a differentiable Spatial Transformer Network (STN) module (Jaderberg et al., 2015) to apply the displacement fields generated by neural networks to the moving images, resulting in warped images. The similarity between the warped images and fixed images serves as the loss function guiding the optimization of model parameters (Balakrishnan et al., 2018; Hu et al., 2019; Mok et al., 2020; Ma et al., 2023). VoxelMorph (Balakrishnan et al., 2018), a representative unsupervised registration network, used a U-shaped network as its backbone to align brain MR scans. Huang et al. (2022) proposed a network for brain registration, which enhanced the model's capabilities by introducing an inception block and a hierarchical prediction block based on the U-shaped network. Additionally, Chen et al. (2022) proposed a brain registration network utilizing transformer modules and adopting a U-shaped structure. The aforementioned work addressed the deformable registration issue to some extent. However, these registration models only extract features from the original resolution image pairs, which overlooks the analysis of multi-scale semantic information and constrains the comprehensive utilization of global and local features by the model. As a result, these methods fail to achieve finer registration.

Several studies have addressed unsupervised registration task from the multi-scale perspective, such as LapIRN (Mok and Chung, 2020), Dual-PRNet (Kang et al., 2022), and Symmetric pyramid network (Zhang et al., 2023). These methods achieve multi-scale registration by progressively warping images through the acquisition of multiple upsampled displacement fields. However, upsampling and composition of displacement fields can lead to error accumulation, resulting in deviation between the final registration outcome and the true transformation, especially when noise or distortions are introduced at multiple stages. In addition, the lack of control over information flow prevents these models from adequately filtering out valid information.

To improve the model's multi-scale analysis capability, we introduce a new registration network called the multi-scale feature extraction-integration network (MF-Net). This work's main contributions are:

- Our novel unsupervised deformable registration network is based on a multi-scale feature extraction-integration strategy and comprehensively models both global and detailed information of images, thereby enhancing the deep representation of the registration model. The network is comprised of three main components: an image pyramid, a selective feature extractor (SFE), and a feature integration path (FIP). This design allows for the comprehensive capture of image features at different scales while also integrating them effectively to enhance the overall registration performance.
- The grouped gated inception block (GI-Block) was specifically designed as the basic unit of the SFE in order to facilitate the selective extraction of different features from images of varying resolutions. By employing filters with various receptive fields and utilizing gating mechanism to regulate feature flow, the GI-Block is able to effectively extract quantitative information from images at different resolutions. Furthermore, the implementation of grouped convolution operations within the GI-Block contributes to the efficient processing of information.
- Comparative experiments show that our model achieves higher accuracy than existing models. Ablation studies also confirm the effectiveness of the multi-scale strategy and gating mechanism.

2 Methods

2.1 Formalized description

For a pair of fixed image $F:\Omega\rightarrow R$ and moving image $M:\Omega\rightarrow R$ defined in the subspace Ω of R^3, the objective of deformable registration is to predict a displacement field $\phi:\Omega\rightarrow R^3$ to warp the moving image so that the warped image $M\circ\phi$ is aligned with the fixed image F, as shown in Equation (1).

$$F(x)\approx M\left(x+\phi(x)\right),x\in\Omega \tag{1}$$

Where "$\approx$" denotes that $M\circ\phi$ and F achieve the highest anatomical similarity, and x denotes any point in the image. We model deformable registration as Equation (2).

$$f_\theta(F,M)=\phi \tag{2}$$

where θ represents the parameters of the function. We employ a neural network to learn this registration function.

2.2 Multi-scale feature extraction-integration network (MF-Net)

Figure 1 illustrates the overall architecture of the proposed MF-Net. For clarity, we use 2D slices instead of the original 3D images.

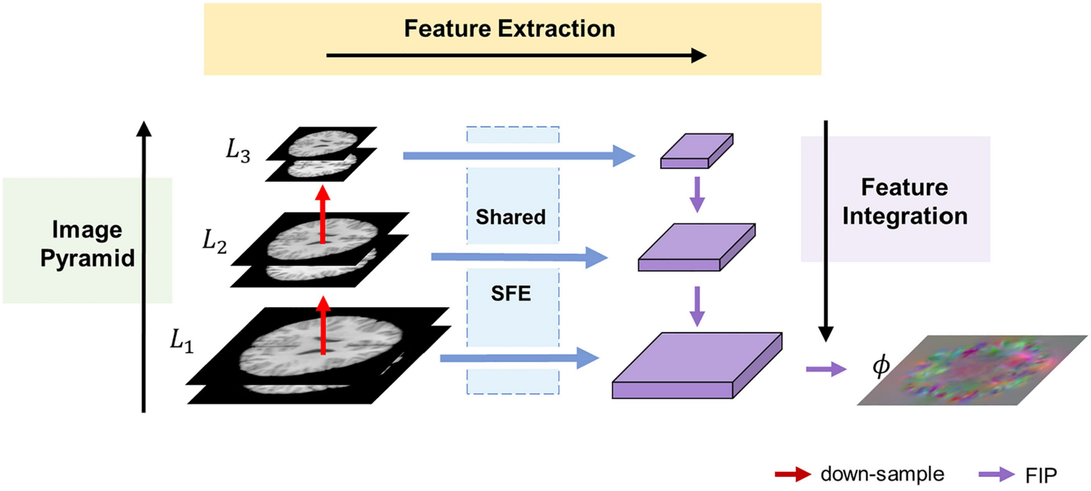

FIGURE 1
Overview of the proposed MF-Net framework. Our MF-Net consists of three main modules: an image pyramid, a shared SFE, and a FIP. Firstly, the image pyramid is used to create multi-resolution sub-bands of the original image. Then, the shared SFE is employed to extract features from the different sub-bands generated by the pyramid. Finally, the FIP performs the crucial task of integrating the multi-scale features extracted by the SFE and utilizing the integrated features to produce the displacement field.

Rather than employing an encoder-decoder strategy like U-shaped structure, our method utilizes a multi-scale feature extraction-integration strategy. Specifically, our model is composed of an image pyramid, a selective feature extractor (SFE), and a feature integration path (FIP). To begin, an image pyramid is generated from an image pair consisting of a fixed image F and a moving image M. Following this, the different levels of the image pyramid are input into a shared SFE to extract features at corresponding scales. Ultimately, the extracted multi-scale features are integrated by FIP to generate the displacement field ϕ, which includes the displacement of each pixel in the x, y, and z directions.

2.2.1 Image pyramid

To address the limitations of the U-shaped structure, which only extracts features from the original resolution images, an image pyramid component is introduced into our network. This component follows the multi-resolution strategy employed in traditional image algorithms. Specifically, the fixed image and the moving image are concatenated along the channel dimension and down-sampled using trilinear interpolation to generate an N-layer image pyramid $\{L_1, L_2, \ldots, L_N\}$, where L_1 is the original image pair. For simplicity, N is set to 3 in this paper.

2.2.2 Selective feature extractor

To adaptively extract quantitative information from various levels of the image pyramid, we propose the SFE. The SFE utilizes grouped gated inception blocks (GI-Blocks) with a gating mechanism, allowing for adaptive feature extraction from images at varying resolutions. For various levels of the image pyramid, features are extracted using a shared SFE. This design ensures versatile feature extraction capabilities tailored to the varying resolutions of the image pyramid.

2.2.2.1 Architecture of SFE

The proposed SFE architecture is shown in the top half of Figure 2. SFE is comprised of densely connected GI-Blocks. The decision to use dense connections for feature extraction is rooted in the idea that these connections continually amalgamate features at various levels, thereby allowing the model to seamlessly integrate semantic information from different levels and synthesize semantic cues for the generation of a registration displacement field.

We start by feeding a specific level L_n from the set $\{L_1, L_2, \ldots, L_N\}$ into a strided convolutional layer to halve the size of the feature map, as shown in Equation (3).

$$Y_n^1 = StridedConv_{3\times3\times3}^{2\to C_1}\left(L_n\right) \tag{3}$$

Where $StridedConv_{3\times3\times3}^{2\to C_1}$ represents a $3\times3\times3$ kernel size convolutional layer with input channels of two, output channels of C_1, and a stride of two. Next, the feature map is fed into a dense path comprised of densely connected GI-Blocks, as shown in Equation (4).

$$Y_n^2 = DensePath\left(Y_n^1\right) \tag{4}$$

Where the *DensePath* represents a densely connected path consisting of M GI-Blocks. We fix the output channel number of the GI-Blocks as K, which is also referred to as the growth rate (Huang et al., 2017).

According to the structure of the dense connection, the channel number of Y_n^2 is $C_1 + M \times K$. To simultaneously fix the input channel number of the GI-Blocks, we linearly scale the channel number of the feature map to $4K$ before feeding it into the GI-Block. Finally, we linearly scale the channel number of the output from the densely connected path to $4K$ and feed it into a transposed convolutional layer with an output channel number of C_2 to restore the size of the feature map, as shown in Equations (5, 6).

$$Y_n^3 = LinearScale^{(C_1+M\times K)\to 4K}\left(Y_n^2\right) \tag{5}$$

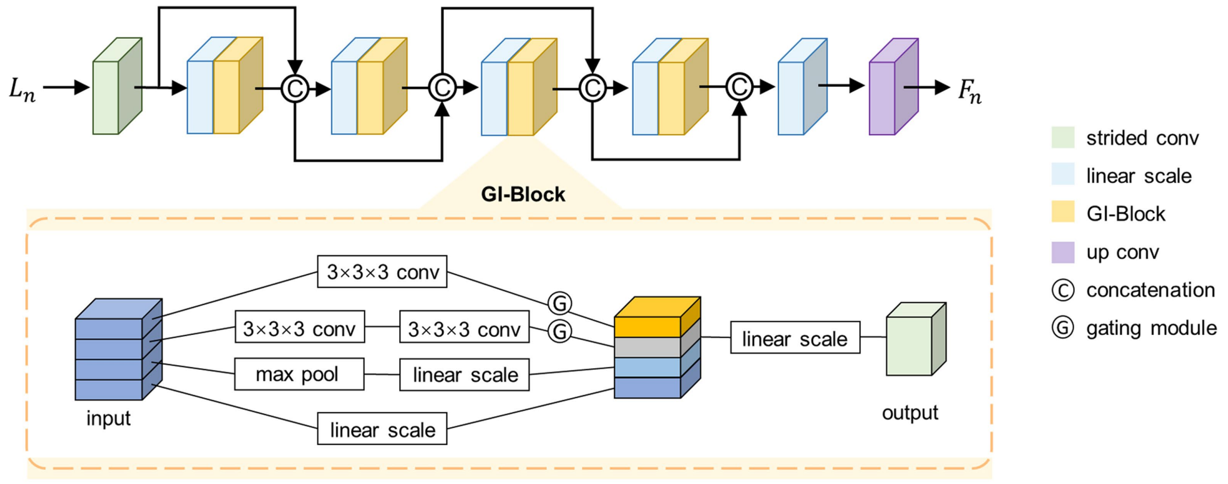

FIGURE 2
Architecture of the SFE. For simplicity, only four GI-Blocks are shown.

$$F_n = TransposeConv_{4\times4\times4}^{4K \to C_2}\left(Y_n^3\right) \tag{6}$$

We set K and C_1 to 32, C_2 to 16, and M to 5. Note that for simplicity, only four GI-Blocks are shown in Figure 2.

2.2.2.2 GI-Block

To adaptively extract quantitative information from images at various resolutions, we propose the GI-Block. The structure of the GI-Block is shown in the lower part of Figure 2. The proposed GI-Block consists of four parallel branches. The first branch employs a $3\times3\times3$ convolutional layer to extract features with a smaller receptive field. The second branch uses two $3\times3\times3$ convolutional layers to approximate a $5\times5\times5$ convolution (Szegedy et al., 2016), extracting features with a larger receptive field. The third branch includes a max-pooling layer and a linear scaling layer (i.e., a $1\times1\times1$ convolutional layer). The max-pooling layer is responsible for extracting representative information from the input feature map, and the linear scaling layer scales the extracted representative information. Finally, the fourth branch utilizes only a linear scaling layer to preserve the features of the original input. We split the input feature map into four parts along the channel dimension, and then input each part into each of the four branches mentioned above.

To enhance the differentiation of receptive field weights for feature maps at varying resolutions in GI-Block, we introduce the gating mechanism. This mechanism addresses the need for distinct receptive field weights for images with different resolutions. Specifically, information extracted from a smaller image should include more features extracted using a smaller receptive field filter, while information extracted from a larger image should include more features extracted using a larger receptive field filter. To achieve this, the gating mechanism is incorporated. We feed the features extracted by the first two branches into a convolutional layer with a kernel size of $3\times3\times3$ and an activation function of SoftSign to obtain weights in the range of 0–1. These weights are then multiplied with the original features, resulting in the gated features. The formula for the gating mechanism is described as Equation (7).

$$Y = X \times Sigmoid\left(Conv_{1\times1\times1}^{C \to C}\left(X\right)\right) \tag{7}$$

Where X represents the input to the gating mechanism, and Y represents the output of the gating mechanism.

Finally, the feature maps extracted by different branches are merged along the channel dimension and fused through a $1\times1\times1$ convolutional layer to prevent potential feature disintegration caused by group convolution.

2.2.3 Feature integration path

To integrate the extracted multi-scale semantic information and generate a registration displacement field using the integrated semantic information, we propose the FIP module. Figure 3 illustrates the structure of the FIP. The lower resolution feature map is doubled in size through transpose convolution and then connected to the feature map at a higher resolution via residual connection. The resulting feature map then undergoes the same process iteratively until reaching the feature map at the highest resolution, as shown in Equation (8).

$$F_n' = TransposeConv_{4\times4\times4}^{C2 \to C2}\left(F_{n+1}'\right) + F_n, n \in \left[1, N-1\right] \tag{8}$$

When $n = N$, $F_N' = F_N$. Finally, the integration features pass through the output layer, a convolutional layer with a SoftSign activation function, to produce the registration flow field, as shown in Equation (9).

$$\phi = R \times SoftSign\left(Conv_{3\times3\times3}^{C \to 3}\left(F_N'\right)\right) \tag{9}$$

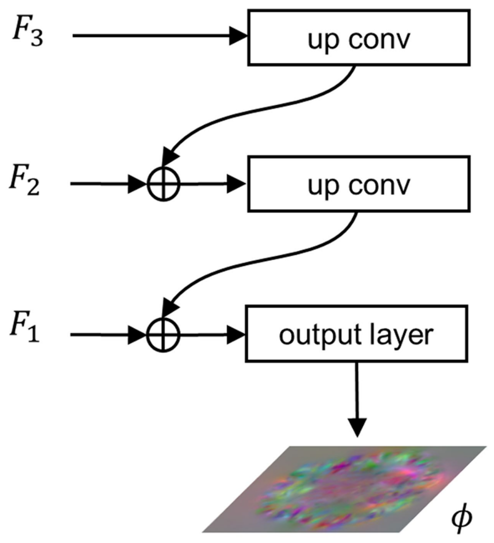

FIGURE 3
Architecture of the FIP. F_1, F_2, and F_3 represent features extracted from L_1, L_2, and L_3, respectively. ϕ denotes the final output of the network, i.e., the displacement field.

where R is the scale factor and we set R to 20.

2.3 Loss functions

To guide the optimization of the neural network, we employ an intensity-based similarity metric between $M \circ \phi$ and F. Our method is unsupervised as the loss function does not necessitate the introduction of labels. In order to mitigate folding in the displacement field that deviates from anatomical constraints, we utilize the gradient norm of the displacement field as a regularization term.

2.3.1 Similarity loss

We use normalized cross-correlation (NCC) to measure the similarity between $M \circ \phi$ and F. The NCC function yields values ranging from 0 to 1, with higher values indicating higher similarity. We take the negative of the similarity metric so that as the loss function decreases, the similarity measure between the images increases, as shown in Equation (10).

$$L_{sim}\left(M \circ \phi, F\right) = -NCC\left(M \circ \phi, F\right) \tag{10}$$

2.3.2 Grad loss

If the optimization of the neural network is guided solely by the similarity metric between $M \circ \phi$ and F, it may lead to results that do not conform to anatomical constraints, such as abrupt changes or folding of the displacement field. To mitigate this situation, we introduce the norm of the displacement field gradient as a regularization term in the loss function, as shown in Equation (11).

$$L_{grad}\left(\phi\right) = \frac{1}{\left|3\Omega\right|} \sum_{x \in \Omega} \left\|\nabla \phi\left(x\right)\right\|^2 \tag{11}$$

We combine the similarity metric and the regularization term into the overall loss function, as shown in Equation (12).

$$L_{total} = L_{sim}\left(M \circ \phi, F\right) + \lambda L_{grad}\left(\phi\right) \tag{12}$$

Where λ is a hyperparameter used to balance the contributions of the two terms.

3 Experiments

3.1 Dataset and preprocessing

We conducted atlas-based registration experiments on the publicly available OASIS dataset (Marcus et al., 2007). OASIS comprises 416 3D brain MR scans from participants aged 18–96. We utilized a processed version of OASIS (Balakrishnan et al., 2019), where the brain scans underwent skull stripping and subcortical structure segmentation. For our experiments, we randomly selected 200, 35, and 35 scans as the training, validation, and test sets, respectively. We randomly chose five scans from each of the validation set and test set as fixed images, with the remaining scans serving as moving images. That is, each method was optimized on a training set containing 10×200 image pairs during training, and each method registered 5×30 image pairs during validation or testing.

We cropped unnecessary regions around the brain and resample the images to $96 \times 112 \times 96$. Subsequently, intensity normalization was applied to each scan, mapping pixel intensities to the range [0,1] to facilitate network convergence. Finally, we conducted affine pre-registration on the moving and fixed images in the dataset using ANTs toolkit (Avants et al., 2011).

3.2 Baseline methods and implementation

We compared the proposed MF-Net with three baseline methods, namely VoxelMorph, SYMNet (Mok et al., 2020), and LapIRN. VoxelMorph is a classic unsupervised registration model utilizing a U-shaped convolutional network to predict the displacement field. We evaluated two variants proposed in their paper: VoxelMorph-1 and VoxelMorph-2. SYMNet predicts both forward and inverse transformations simultaneously through a U-shaped network, and provides diffeomorphic properties. LapIRN combines displacement fields at multiple scales to obtain the final registration displacement field. This study also predicts diffeomorphic transformations. We conducted evaluation on both LapIRN and its variant, LapIRN$_{\text{disp.}}$, the latter of which abandons the diffeomorphic property while enhancing registration accuracy. All the mentioned methods were used for brain MR registration in their respective original papers. We used the official implementations of these methods and followed the recommended guidelines, adjusting hyperparameters to ensure the best registration performance.

We implemented MF-Net using PyTorch (Paszke et al., 2017) and employed the AdamW optimizer (Loshchilov and Hutter, 2017) with a learning rate of 0.0001 for training over 100 epochs. The hyperparameter λ is set to 1. All experiments were conducted on a personal workstation equipped with an RTX 3080 GPU and an Intel(R) i7-10700KF CPU.

3.3 Evaluation metrics

3.3.1 Dice score

We quantified the degree of overlap between the fixed image and the warped image using the dice score, Dice (1945) computed from the anatomical tissue segmentation masks of the fixed image and the warped image, as shown in Equation (13).

$$Dice = 2 \cdot \frac{\left| F^{msk} \cap \left(M^{msk} \circ \phi \right) \right|}{\left| F^{msk} \right| + \left| M^{msk} \circ \phi \right|} \tag{13}$$

Where F^{msk} and M^{msk} denote the subcortical segmentation masks of the fixed image and the moving images, respectively. The dice score, ranging from 0 to 1, signifies the degree of overlap, with a higher score reflecting increased registration accuracy.

3.3.2 Jacobian determinant

We evaluated the smoothness of the deformation field by computing the percentage of voxels with a non-positive Jacobian determinant ($|JD \le 0|$). The formula for the Jacobian determinant of the displacement field is given by Equation (14).

$$J_\phi(p) = \begin{vmatrix} \frac{\partial \phi_x(p)}{\partial x} & \frac{\partial \phi_x(p)}{\partial y} & \frac{\partial \phi_x(p)}{\partial z} \\ \frac{\partial \phi_y(p)}{\partial x} & \frac{\partial \phi_y(p)}{\partial y} & \frac{\partial \phi_y(p)}{\partial z} \\ \frac{\partial \phi_z(p)}{\partial x} & \frac{\partial \phi_z(p)}{\partial y} & \frac{\partial \phi_z(p)}{\partial z} \end{vmatrix} \tag{14}$$

A smaller percentage suggests a higher level of smoothness.

3.4 Comparative evaluation

Table 1 provides the average dice score and the percentage of voxels with non-positive Jacobian determinants ($|JD \le 0|$) for all subjects and structures, encompassing VoxelMorph-1, VoxelMorph-2, SYMNet, LapIRN, LapIRN$_{disp}$, and our MF-Net. We also include affine transformation for comparison purposes. It is evident that our MF-Net achieves better registration accuracy with few folding voxels. While SYMNet and LapIRN achieved entirely smooth displacement fields through diffeomorphic transformation, this achievement comes at the expense of registration accuracy.

Figure 4 illustrates registration example slices of brain MR scans under different methods. As evident from the difference map between the fixed image and the warped image obtained by various methods, our method yielded a warped image that is most similar to the fixed image. Both quantitative and qualitative evaluations demonstrate the effectiveness of our multi-scale feature extraction-fusion strategy. Additionally, to improve comprehension of the registration process, we display the slices of the displacement field output by each method in Figure 5.

TABLE 1 **Comparison of different methods on the dataset, with affine registration used for reference.**

Method	Dice (%)	$\lvert JD \le 0 \rvert$
Affine Only	56.33±0.04	-
VoxelMorph-1	73.07±0.04	186±38
VoxelMorph-2	73.94±0.05	392±69
SYMNet	71.89±0.31	0.5±0.4
LapIRN	71.43±0.04	**0**
LapIRN$_{disp}$	74.89±0.18	1757±259
MF-Net (ours)	**75.38±0.05**	332±22

Dice measures registration accuracy (higher values are better), and $|JD \le 0|$ indicates the number of folding voxels that do not conform to the anatomical structure. Please note that the best-performing results are highlighted in bold.

3.5 Ablation analysis

To further validate the effectiveness of the multi-scale feature extraction-fusion strategy, we omitted the multi-scale strategy of MF-Net and predicted the displacement field solely based on images at the original resolution. We label this network as MF-Net-1. Table 2 displays the registration metrics of MF-Net and MF-Net-1 on the test set. It can be observed that MF-Net exhibits higher registration accuracy than MF-Net-1. This experiment demonstrates that our network, employing the multiscale analysis strategy, can more efficiently capture features at various scales, thereby improving the model's registration performance.

To verify the effectiveness of the proposed gating mechanism, we omitted the gating mechanism of GI-Block in our variant MF-Net-2. Table 3 presents the quantitative evaluation results before and after the removal. It is evident that MF-Net demonstrates better registration accuracy compared to MF-Net-2. This experiment demonstrates that the gating mechanism can efficiently extract meaningful information from redundant cascade features, automatically learning the weights of different sensory field features, and thereby improving the model's registration performance.

4 Discussion

Although both utilize multi-scale information from images, MF-Net differs from existing models represented by LapIRN. Like most existing registration networks based on multi-scale strategies, LapIRN achieves multi-scale information fusion by continuously compositing the generated multi-scale displacement fields. In contrast, MF-Net extracts multi-scale features, then fuses these features, and finally, obtains the registration displacement field from the fused features. In other words, MF-Net fuses the multi-scale information

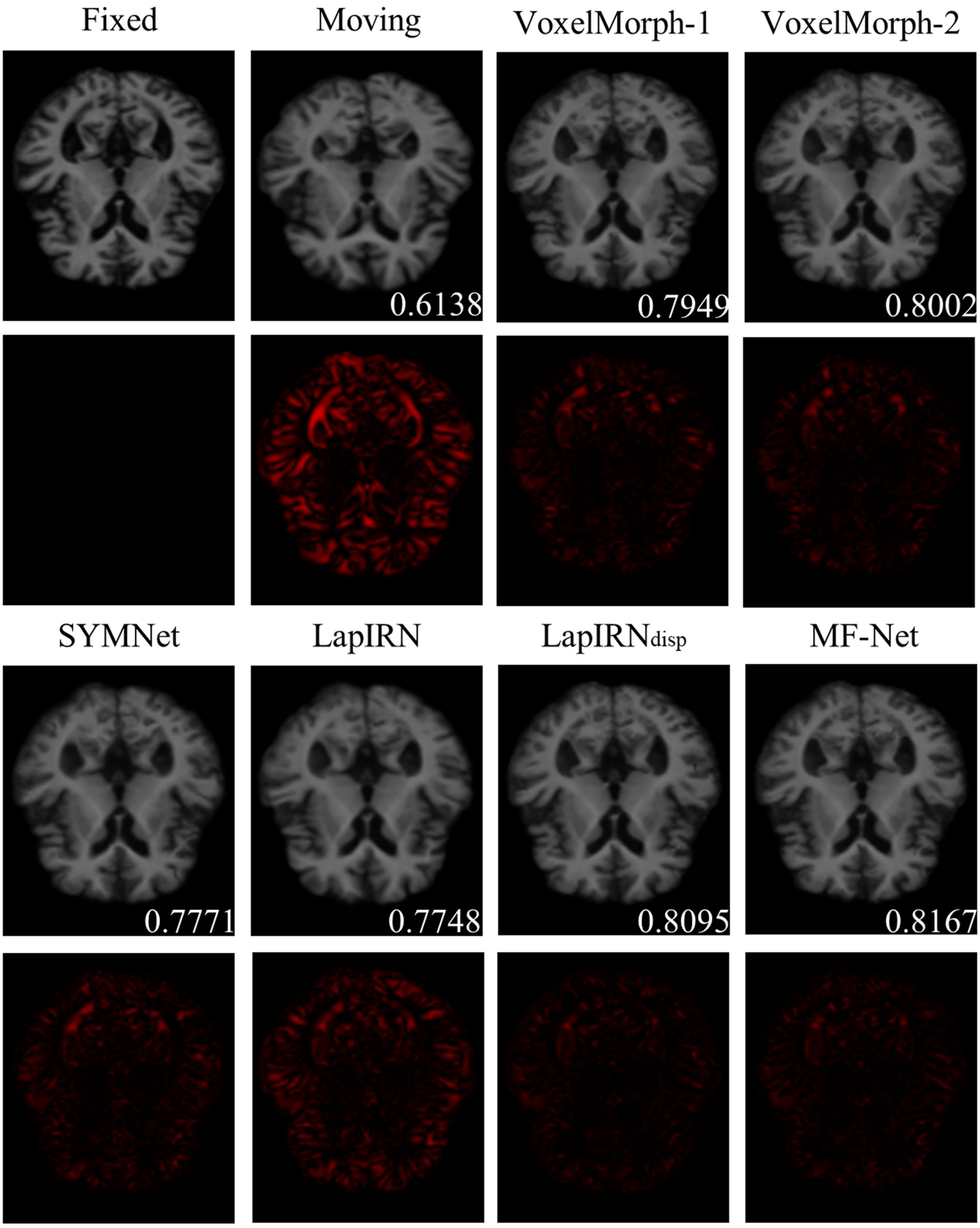

FIGURE 4
The registration results for a representative sample within the dataset employing six distinct methods. The second and fourth rows show the heat maps, which illustrate the absolute differences between the warped image and the fixed image. Notably, the lower right corner of the warped image shows the dice score, which indicates the degree of similarity between the warped image and the fixed image.

earlier than LapIRN, which may be one of the reasons for the better accuracy of our method, considering that LapIRN uses multiple displacement fields that may cause the accumulation of errors. Furthermore, our feature extractor adjusts the flow of feature information through gating mechanism, which may be another contributing factor.

In addition, we changed the resolution of images in the preprocessing stage through resampling, potentially impacting the model's performance due to the loss of image information. It is important to note that while our manipulation has affected the results of individual models, it does not alter the comparison of different models, as our comparisons of different models were conducted under the same conditions. The disparity between MF-Net and the baselines might become more apparent when training and testing are conducted using images at their original resolution. Given our model's better feature extraction abilities, it is expected to more effectively analyze

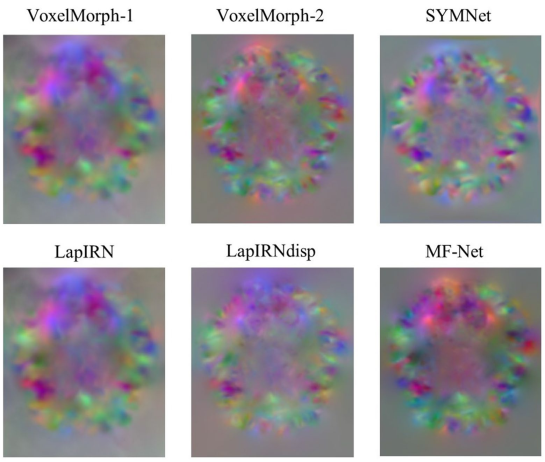

FIGURE 5
Slices of the displacement field. The red, green, and blue colors in the image show voxel displacement in three directions.

TABLE 2 Ablation analysis of the multiscale strategy on the MF-Net.

Method	Dice (%)	$\|JD \leq 0\|$
MF-Net	75.38±0.05	332±22
MF-Net-1	75.18±0.01	268±11

MF-Net is the proposed model, and MF-Net-1 is based on MF-Net but eliminates the multi-scale feature extraction-integration strategy.

TABLE 3 Ablation analysis of the gating mechanism on the MF-Net.

Method	Dice (%)	$\|JD \leq 0\|$
MF-Net	75.38±0.05	332±22
MF-Net-2	75.02±0.05	168±8

MF-Net is the proposed model, and MF-Net-2 is based on MF-Net but eliminates the gating mechanism.

the additional information available at the original resolution. Therefore, the gap between our model and the baselines may expand in such scenarios.

5 Conclusion

In this study, we introduced a novel 3D image deformation registration network named MF-Net, which is built upon the multi-scale feature extraction-fusion strategy. MF-Net enhances the model's analytical ability by integrating multi-scale information, thereby balancing image texture and detail registration. Within our network, we design the GI-Block as the basic unit of the feature extractor, which adaptively extracts quantitative information through gating mechanism. Compared with existing registration approaches, our network demonstrated better registration accuracy. Ablation experiments further indicated that the proposed multi-scale strategy can improve registration performance. Our work has potential applications in the fields of neuronavigation and brain image-assisted analysis. This expands the scope for future research and applications in the realms of neurosurgery and neuroscience.

Data availability statement

Publicly available datasets were analyzed in this study. This data can be found here: https://www.oasis-brains.org/.

Author contributions

AL: Writing – review & editing, Writing – original draft, Software, Methodology, Conceptualization. YY: Visualization, Writing – review & editing, Writing – original draft. TG: Writing – review & editing, Writing – original draft. LZ: Writing – review & editing, Writing – original draft. XZ: Writing – review & editing, Writing – original draft. YZ: Writing – review & editing, Writing – original draft. GS: Supervision, Resources, Funding acquisition, Writing – review & editing, Writing – original draft. HZ: Investigation, Visualization, Writing – review & editing.

Funding

The author(s) declare that financial support was received for the research, authorship, and/or publication of this article. This work was partially supported by National Key R&D Program of China under grant 2022YFB4700702, the National Natural Science Foundation of China under grant agreement no. 62073314 and 92048203, and Liaoning Provincial Natural Science Foundation of China (2022-YQ-06).

Conflict of interest

The authors declare that the research was conducted in the absence of any commercial or financial relationships that could be construed as a potential conflict of interest.

Publisher's note

References

Avants, B. B., Epstein, C. L., Grossman, M., and Gee, J. C. (2008). Symmetric diffeomorphic image registration with cross-correlation: evaluating automated labeling of elderly and neurodegenerative brain. *Med. Image Anal.* 12, 26–41. doi: 10.1016/j.media.2007.06.004

Avants, B. B., Tustison, N. J., Song, G., Cook, P. A., Klein, A., and Gee, J. C. (2011). A reproducible evaluation of ANTs similarity metric performance in brain image registration. *NeuroImage* 54, 2033–2044. doi: 10.1016/j.neuroimage.2010.09.025

Balakrishnan, G., Zhao, A., Sabuncu, M.R., Dalca, A.V., and Guttag, J. (2018). "An unsupervised learning model for deformable medical image registration" in 2018 IEEE/CVF Conference on Computer Vision and Pattern Recognition, 9252–9260.

Balakrishnan, G., Zhao, A., Sabuncu, M. R., Guttag, J., and Dalca, A. V. (2019). VoxelMorph: a learning framework for deformable medical image registration. *IEEE Trans. Med. Imaging* 38, 1788–1800. doi: 10.1109/tmi.2019.2897538

Cao, X., Yang, J., Zhang, J., Nie, D., Kim, M., Wang, Q., et al. (2017). "Deformable image registration based on similarity-steered CNN regression" in Medical Image Computing and Computer Assisted Intervention—MICCAI 2017: Springer International Publishing, 300–308.

Cao, X., Yang, J., Zhang, J., Wang, Q., Yap, P.-T., and Shen, D. (2018). Deformable image registration using a Cue-aware deep regression network. *IEEE Trans. Biomed. Eng.* 65, 1900–1911. doi: 10.1109/tbme.2018.2822826

Chen, J., Frey, E. C., He, Y., Segars, W. P., Li, Y., and Du, Y. (2022). TransMorph: transformer for unsupervised medical image registration. *Med. Image Anal.* 82:102615. doi: 10.1016/j.media.2022.102615

Dice, L. R. (1945). Measures of the amount of ecologic association between species. *Ecology* 26, 297–302. doi: 10.2307/1932409

Drakopoulos, F., Tsolakis, C., Angelopoulos, A., Liu, Y., Yao, C., Kavazidi, K. R., et al. (2021). Adaptive physics-based non-rigid registration for immersive image-guided Neuronavigation systems. *Front. Digit. Health* 2:613608. doi: 10.3389/fdgth.2020.613608

Geng, X., Chan, P. H., Lam, H. S., Chu, W. C., and Wong, P. C. (2024). Brain templates for Chinese babies from newborn to three months of age. *NeuroImage* 289:120536. doi: 10.1016/j.neuroimage.2024.120536

Hu, X., Kang, M., Huang, W., Scott, M.R., Wiest, R., and Reyes, M. (2019). “Dual-stream pyramid registration network” in *10th International Workshop on Machine Learning in Medical Imaging (MLMI)/22nd International Conference on Medical Image Computing and Computer-Assisted Intervention (MICCAI)*, 382–390.

Huang, G., Liu, Z., Maaten, L.V.D., and Weinberger, K.Q. (2017). "Densely connected convolutional networks" in *2017 IEEE Conference on Computer Vision and Pattern Recognition (CVPR)*, 2261–2269.

Huang, M., Ren, G., Zhang, S., Zheng, Q., and Niu, H. (2022). An unsupervised 3D image registration network for brain MRI deformable registration. *Comput. Math. Methods Med.* 2022, 1–10. doi: 10.1155/2022/9246378

Jaderberg, M., Simonyan, K., Zisserman, A., and Kavukcuoglu, K. (2015). "Spatial transformer networks" in Advances in Neural Information Processing Systems. Curran associates, Inc.

Kang, M., Hu, X., Huang, W., Scott, M. R., and Reyes, M. (2022). Dual-stream pyramid registration network. *Med. Image Anal.* 78:102379. doi: 10.1016/j.media.2022.102379

Lorenzi, M., Ayache, N., Frisoni, G. B., and Pennec, X. (2013). LCC-demons: a robust and accurate symmetric diffeomorphic registration algorithm. *NeuroImage* 81, 470–483. doi: 10.1016/j.neuroimage.2013.04.114

Loshchilov, I., and Hutter, F. (2017). "Decoupled weight decay regularization" in *International Conference on Learning Representations*.

Ma, M., Liu, G., Song, L., and Xu, Y. (2023). SEN-FCB: an unsupervised twinning neural network for image registration. *Appl. Intell.* 53, 12198–12209. doi: 10.1007/s10489-022-04109-8

Marcus, D. S., Wang, T. H., Parker, J., Csernansky, J. G., Morris, J. C., and Buckner, R. L. (2007). Open access series of imaging studies (OASIS): cross-sectional MRI data in young, middle aged, nondemented, and demented older adults. *J. Cogn. Neurosci.* 19, 1498–1507. doi: 10.1162/jocn.2007.19.9.1498

Mok, T.C.W., and Chung, A.C.S. (2020). "Large deformation diffeomorphic image registration with Laplacian pyramid networks" in *Medical Image Computing and Computer Assisted Intervention—MICCAI 2020.* (Springer International Publishing), 211–221.

Mok, T.C.W., Chung, A.C.S., and IEEE (2020). "Fast symmetric diffeomorphic image registration with convolutional neural networks" in *IEEE/CVF Conference on Computer Vision and Pattern Recognition (CVPR)*, 4643–4652.

Nakajima, Y., Sohma, Y., and Jiang, J. (2020). Laser-beam projection mapping with compensation for soft-tissue deformation. *Sensors Mater.* 32:935. doi: 10.18494/sam.2020.2630

Paszke, A., Gross, S., Chintala, S., Chanan, G., Yang, E., DeVito, Z., et al. (2017). Automatic differentiation in pytorch.

Szegedy, C., Vanhoucke, V., Ioffe, S., Shlens, J., Wojna, Z., and Ieee, (2016). "Rethinking the inception architecture for computer vision" in *2016 IEEE Conference on Computer Vision and Pattern Recognition (CVPR)*, 2818–2826.

Vercauteren, T., Pennec, X., Perchant, A., and Ayache, N. (2009). Diffeomorphic demons: efficient non-parametric image registration. *NeuroImage* 45, S61–S72. doi: 10.1016/j.neuroimage.2008.10.040

Yang, X., Kwitt, R., Styner, M., and Niethammer, M. (2017). Quicksilver: fast predictive image registration—a deep learning approach. *NeuroImage* 158, 378–396. doi: 10.1016/j.neuroimage.2017.07.008

Zhang, L., Ning, G., Zhou, L., and Liao, H. (2023). Symmetric pyramid network for medical image inverse consistent diffeomorphic registration. *Comput. Med. Imaging Graph.* 104:102184. doi: 10.1016/j.compmedimag.2023.102184

Frontiers in
Neuroscience

Provides a holistic understanding of brain function from genes to behavior

Part of the most cited neuroscience journal series which explores the brain - from the new eras of causation and anatomical neurosciences to neuroeconomics and neuroenergetics.

Discover the latest Research Topics

See more →

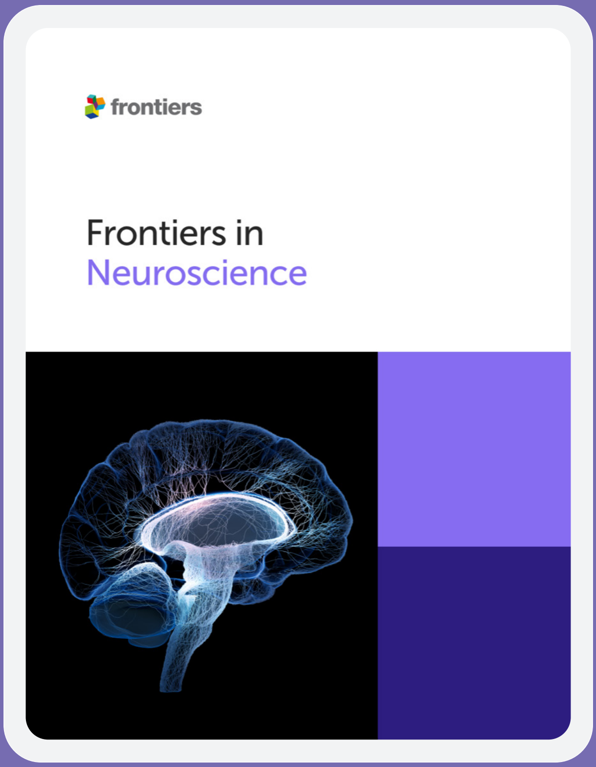

frontiers

Frontiers in
Neuroscience

Frontiers

Avenue du Tribunal-Fédéral 34
1005 Lausanne, Switzerland
frontiersin.org

Contact us

+41 (0)21 510 17 00
frontiersin.org/about/contact